Structural studies of the *Vibrio cholerae* chromosome segregation system

By Alexandra Parker

A thesis submitted in part fulfilment for the degree of Doctor of Philosophy

Department of Molecular Biology and Biotechnology
The University of Sheffield, United Kingdom
November 2021

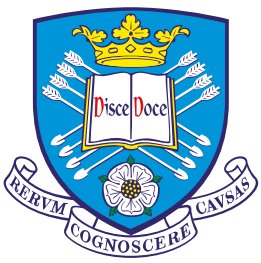

The University Of Sheffield.

Abstract

The efficient segregation of replicated genetic material is an essential step for cell division. In eukaryotic cells, sister chromatids are separated via the mitotic spindles. In contrast, bacterial cells use several evolutionarily-distinct genome segregation systems. The most common of these is the type I Par system. It consists of an adapter protein, ParB, that binds to the DNA cargo via interaction with the parS DNA sequence; and an ATPase, ParA, that binds nonspecific DNA and mediates cargo transport. However, the molecular details of how this system functions are not well understood.

Using the human pathogen *Vibrio cholerae*, which possesses two chromosomes each encoding its own Par system, I first determined a purification protocol for its ParA proteins (ParA1 and ParA2, respectively). I then used negative-stain TEM to investigate the oligomerization of ParA2, in the presence of nucleotide as well as DNA. I also determined its crystal structure, in both apo and ADP-bound states. Finally, I used cryo-EM to determine its structure bound to DNA, the first structure of a ParA filament.

Collectively, these structures offer insight into its conformational changes from dimerization through to DNA binding and filament assembly. Specifically, it is shown that the ParA dimer is stabilized by nucleotide binding, and forms a left-handed filament using DNA as a scaffold. The structural analyses also reveal dramatic structural rearrangements upon DNA binding and filament assembly. Finally, through negative-stain electron microscopy, I show how filament formation is controlled via C-terminal basic residues of ParA2, with nucleotide binding and hydrolysis being key to filament assembly and disassembly along DNA. The data reported here provides the structural basis for ParA's cooperative binding to DNA and the formation of high ParA density regions on the nucleoid, and suggest a role for its filament formation in DNA segregation in bacteria.

Acknowledgments

I would firstly like to thank my first first-supervisor, Dr Ling Chin Hwang, for giving me this opportunity and taking me on as a PhD student, and with her I would like to thank the fellow lab members, Adam Brooks and Satpal Chodha.

Despite abandoning me for the allure of London, I would like to give an immense thank you to my second first-supervisor, Dr Julien Bergeron, whose support, encouragement, and many pints of beer have played such a vital role during my past 3 years. Most importantly, I thank Julien for introducing me to the field of structural biology, which has been such a joy to learn despite the many ups and downs of research.

I give my greatest appreciation to all the members/alumni of the Bergeron and Bullough labs along with other members of the EM group, in particular Dr Svetomir Tzokov (notably for his incredible patience), Dr Jason Wilson and Dr Daniel Mann. It has been such a privilege to work alongside such kind-hearted and supportive people, whose help has been invaluable during my project and there has never been a dull moment.

It goes without mention that I would like to thank my friends and family, who have been incredibly supportive over the years. Particularly to Ainhoa, Lucia, Ruairidh, Shauna and Ash, for making my time at Sheffield so enjoyable and continuously picking me up when times have been hard.

I would like to express my gratitude to my current and third first-supervisor, Dr Daniel Bose, for taking me under his wing and guiding me through the uncertainty that's been the past 20 months.

Lastly, I give my greatest thanks to Ava the Arctica, for never losing her *cool* with me despite the amount of work I've put her through.

List of abbreviations

2D	Two-dimensions
3D	Three-dimensions
Å	Angstrom
a, b, c	Real space unit cell dimensions
Abs	Absorbance
ADP	Adenosine diphosphate
ATP	Adenosine triphosphate
ATPγS	Adenosine 5'-(γ-thiotriphosphate)
B-factor	Temperature factor
BME	β-Mercaptoethanol
bp	Base pairs
ChrI	Chromosome 1
ChrII	Chromosome 2
Cryo-EM	Cryogenic electron microscopy
CTD	C-terminal domain
CTF	Contrast transfer function
CV	Column volume
DBD	DNA-binding domain
DED	Direct electron detector
dsDNA	Double stranded DNA
DTT	Dithiothreitol
e^-	electron
EDTA	Ethylenediaminetetraacetic acid
EM	Electron microscopy
FEG	Field emission gun
FFT	Fast Fourier transform
HDR	High-density chromosomal region
HEPES	4-(2-hydrxyethyl)-1-piperazineethanesulfonic acid
HTH	Helix-turn-helix
IPTG	Isopropyl β-D-thiogalactoside
Kb	Kilo base pair
kDa	Kilo-Dalton
keV	Kiloelectron volts
LB	Luria-Bertani broth
M	Molar concentration
Mb/kb	Megabase pairs/kilobase pairs
Mw	Molecular weight
NCS	Non-crystallographic symmetry
nsDNA	Non-specific DNA
NTD	N-terminal domain
°C	Degrees Centigrade

OD	Optical density
Ori	Chromosome macrodomain that encompasses the oriC
ori/oriC	Origin of replication/chromosomal origin of replication
Par	Partitioning
ParPD	Propagation defective
PCR	Polymerase chain reaction
PDB	Protein Data Bank
PEG	Polyethylene Glycol
pI	Isoelectric point
PISA	Protein Interfaces, Surfaces and Assemblies
Rfree	Free-R factor
RMSD	Root mean square deviation
Figure	Revolutions per minute
s	second
SDS	Sodium dodecyl sulphate
SDS-PAGE	Sodium dodecyl sulphate polyacrylamide gel electrophoresis
SEC-MALS	Size exclusion chromatography-multiple angle light scattering
sssDNA	Sonicated salmon sperm DNA
TEM	Transmission electron microscopy
ter	Replication terminus
TIRF	Total internal reflection fluorescence
Tris	Tris (hydroxymethyl) aminomethane
UV	Ultraviolet
V	Volt
Vc	*Vibrio cholerae*
Vm	Matthews coefficient
w/v, v/v	weight/volume, volume/volume
WT	Wild type
xg	Relative centrifugal force
α, ß, γ	Real space unit cell angles

List of Figures

List of Tables

List of Movies

Table of Contents

1 Introduction

1.1 Introduction to the Par system

DNA replication and segregation are essential in all life forms. In eukaryotic cells, the mechanism of chromosome segregation is conserved among diverse species, following a well-established cell-cycle utilising essential features such as the formation of a mitotic kinetochore and spindle apparatus (Yanagida, 2005). François Jacob proposed one of the first models for bacterial chromosome segregation in the 1960's, suggesting that newly replicated origins of replications are anchored to the cell membrane at the pole whereby chromosomes are then segregated passively throughout the cell growth and elongation (Jacob et al., 1963). However, upon discovery that chromosomes segregate much faster than the rate of cell growth, this model was superseded (Fiebig et al., 2006; Viollier et al., 2004; Webb et al., 1998). In prokaryotes, segregation mechanisms can vary substantially between species, however, many utilise the Par partitioning system. First discovered and studied in low-copy-number plasmids, *Par* loci have been found in the chromosomes of 70% of sequenced bacteria for the efficient segregation of replicated genetic material to the daughter cell (Baxter & Funnell, 2015; Brooks & Hwang, 2017; Gordon & Wright, 2000; Livny et al., 2007; Ogasawara & Yoshikawa, 1992; Reyes-Lamothe et al., 2012), while high-copy-number plasmids segregate via random diffusion (Hu et al., 2017). The tripartite system encodes a cis-acting centromere-like site along with two *trans*-acting Par proteins, an adapter which binds to the centromere-like cite, and a NTPase "motor" protein (Austin & Abeles, 1983a, 1983b; Gerdes et al., 1985; Ogura & Hiraga, 1983). The *Par* loci are divided into three different types (**Figure 1.1**), classified by their motor protein: Type I *par* loci encode a P loop ATPase, ParA, which possesses a deviant Walker-type motif; the Type II ATPase, ParM, is actin-like; and the Type III GTPase, TubZ, is tubulin-like. The mechanisms of type II and III systems have been extensively characterized (Brooks & Hwang, 2017; Schumacher, 2008). In contrast, the mechanism of the Type I segregation system remains elusive, with in particular discrepancy regarding ParA's action during segregation (Jalal & Le, 2020).

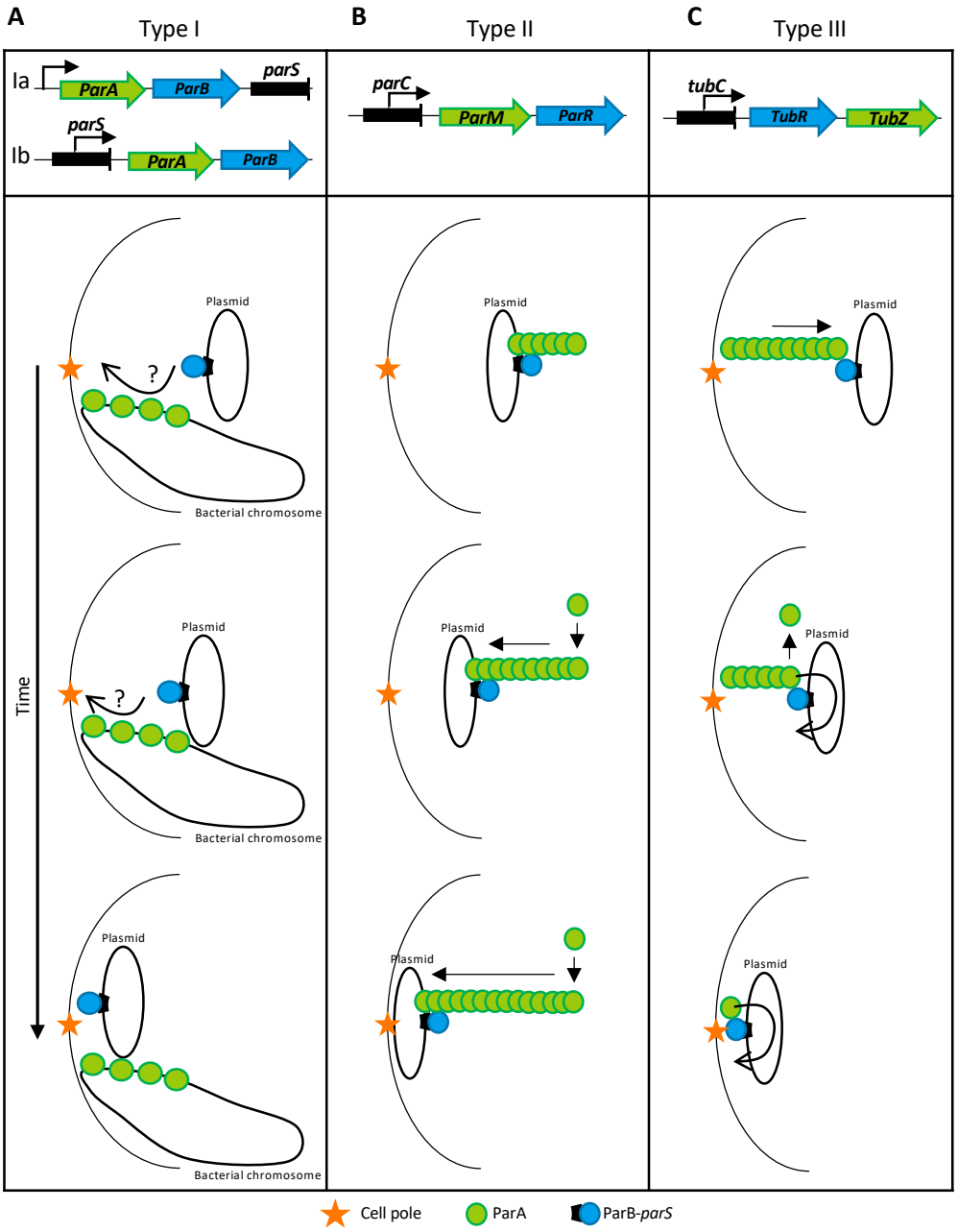

Figure 1.1. Types of par loci and mechanism of segregation.
Showing the movement over time of each type of par mediated model. ***A)*** *Type Ia and Ib par operon and hypothesized ParA activity in plasmid segregation, ParA binding non-specifically to DNA.* ***B)*** *Type II par operon and actin-like ParA mechanism of action in plasmid segregation, the ParM polymerizing pushing the segregation complex towards the cell pole.* ***C)*** *Type III par operon and tubulin-like mechanism of action in plasmid segregation, TubZ polymer disassembly pulling the segregation complex towards the cell pole.*

1.2 Types of *par* loci

1.2.1 Type III

Unlike eukaryotic cells, bacterial cells are generally thought to lack tubulin-like polymers during DNA segregation mechanisms. The most common relative protein is the distant tubulin homolog, FtsZ, which assembles a cytokinetic ring at the mid-cell position and is essential for cell division (Dajkovic & Lutkenhaus, 2006). The type III par loci, however, encodes a GTPase motor protein (TubZ), that shows structural similarity to FtsZ. The gene encoding the TubZ protein was first discovered on the pBtoxis plasmid of *Bacillus thuringiensis*, with Type III loci later being found in various plasmids across the Bacillus genus (Akhtar et al., 2009). TubZ assembles into linear polymers, however, the TubZ polymer is not dynamically unstable like tubulin, undergoing polymerisation/depolymerisation at their plus ends (Gerdes et al., 2010). The linear polymer has polarity and therefore shows directional stability, having a leading end to which monomers bind and a trailing end where there is disassembly occurs (Larsen et al., 2007). The Type III locus also encodes an adaptor protein (TubR) and its cognate centromeric site (*tubC*) (**Figure 1.1C**). Biochemical data has shown that TubR binds specifically to *tubC* and also interacts with the distal end of the TubZ filament, promoting its GTPase activity, causing a treadmilling mechanism of the filament, with GTP binding and hydrolysis being key to filament extension and contraction (Fink & Löwe, 2015; Hoshino & Hayashi, 2012; Ni et al., 2010) . When the TubR-*tubC* complex assembles, it associates with the trailing end of the filament. It has been suggested that the treadmilling action of the TubZ filament causes a pulling force from the trailing end, pulling the TubR/*tubC* complex from mid-cell towards the cell poles (Fink & Löwe, 2015).

1.2.2 Type II

The actin-like plasmid partition systems are perhaps the most well understood, with thorough *in-vivo* and *in-vitro* research revealing the mechanism involved in the *E.coli* R1 plasmid segregation. The par system responsible for segregation is the ParMRC system, consisting of the actin-like ATPase ParM, an adaptor protein ParR and its cognate partition site *parC* (**Figure 1.1B**). This type II plasmid segregation system is

described to show mechanistic similarity to the eukaryotic method of DNA segregation, with ParM being structurally similar to eukaryotic actin and forming filament bundles (Van den Ent et al., 2002). The lifecycle of these filaments are dependent on the binding and hydrolysis of ATP. When bound to ATP, ParM polymerises, forming its characteristic filaments. Subsequent hydrolysis of the nucleotide triggers disassembly of the filament. This dynamic therefore allows the filament to grow and shrink during their process of search and capture of the ParR-*parC* complex (Garner et al., 2004). Upon capture, the ParM filaments become stabilised and undergo insertional polymerisation, a mechanism where ATP bound ParM is added to the ParMR-*parC* interface (Møller-Jensen et al., 2003). This expansion of filament between two connected plasmids separates them to opposite cell poles. Once the plasmids have reached the poles, the filament undergoes catastrophic disassembly to complete division (Garner et al., 2007).

1.2.3 Type I

The mechanisms involved in type II and III par loci encoded segregation has been extensively researched, with their pushing and pulling actions being well understood and generally accepted. However, the Type I loci encoded mechanism is less well understood, with discrepancies in many different areas and varying proposed mechanisms. The Type I segregation system locus encodes a deviant walker-box P loop ATPase ParA; an adapter protein, ParB; and centromere-like *parS* site(s) (**Figure 1.1A**). ParB binds specifically to its cognate *parS* site (Funnell, 2016) in addition to non-specifically along DNA, and was shown recently to have CTPase activity (Jalal et al., 2020; Osorio-Valeriano et al., 2019; Soh et al., 2019), although the role of this activity remains unclear. ParA also binds to DNA in the presence of nucleotide, but unlike ParB this interaction is sequence-independent. Biochemical studies have shown that ParB stimulates ParA's ATPase activity, promoting its dissociation from DNA (Baxter et al., 2020; Caccamo et al., 2020; Vecchiarelli et al., 2010; Volante & Alonso, 2015).

Type I segregation systems can be subdivided into two families, Ia and Ib, based on the ParA sequence (Gerdes et al., 2000) and the organization of the locus (**Figure**

1.1A). Type Ia ParAs possess an additional N-terminal helix-turn-helix domain (NTD) that is absent in type Ib ParAs(Ebersbach & Gerdes, 2005). The additional HTH NTD has been suggested to be involved in site-specific DNA binding for *par* gene transcription repression, binding to its own promoter to repress transcription of the locus (Baxter et al., 2020; Boudsocq et al., 2021; Castaing et al., 2008; Hayes et al., 1994). The organization of the locus and the transcriptional control also differs between these two subtypes. In type Ia, the *parA* gene is located directly after the promoter sequence, followed by *parB* and *par*S. In contrast, in type Ib systems, *par*S is located after the promoter, followed by *parA* and *parB*, showing a closer similarity to Type II loci (Gerdes et al., 2010)(Gerdes et al., 2000). In this locus, transcription control is carried out by ParB, the ParB protein binds to its upstream *par*S site and undergoes spreading. This is the process by which ParB recruits more ParB proteins to bind, thereby obstructing and repressing genes located nearby (Rodionov et al., 1999). The mechanisms of segregation differ extensively depending on whether the system is segregating a plasmid or a chromosome, and on the organism itself. First discovered and studied in the *E.coli* mini-plasmids (Austin & Abeles, 1983a), the Type Ia Par segregation system is mostly encoded by low-copy number plasmids, the model systems for study including the *E.coli* F, P1 and P7 plasmids. In contrast, Type Ib systems are predominantly present in native bacterial chromosomes (Livny et al., 2007). However, chromosomes within the same organism can also show difference in their segregation systems. For example, *V. cholerae*; its larger chromosome segregating more similarly to that of other bacterial species (e.g Caulobacter), and its smaller being more similar to segregation systems seen on plasmids, even though both are encoded by Type I *par* loci (Gerdes et al., 2000).

The components of the Type I segregation system show functional similarity to those encoded by Type II and III, the NTPase motor-like protein being stimulated by a recognition site binding adaptor protein, resulting in hydrolysis and driving segregation. However, there is no defining consensus on the mechanism involved in plasmid/ chromosome segregation encoded by the Type I system, unlike the well-studied models involved in Type II and III.

1.3 Models of Type I chromosome segregation

1.3.1 Filamentous model

A mitotic-like filament model was initially suggested (Ebersbach et al., 2006; Fogel & Waldor, 2006; Ptacin et al., 2010; Ringgaard et al., 2009), similarly to type II and type III segregation systems. According to this model, ParA polymerises to form filaments in the presence of ATP along the length of the cell, its leading edge towards the ParB-*parS* complex (Ringgaard et al., 2009) (**Figure 1.2A**). Filament dissociation is then triggered upon interaction with ParB, stimulating the intrinsic ATPase activity of ParA to hydrolyse bound ATP to ADP, disassembling the filament and causing a pulling of the chromosome towards the cell pole (Hui et al., 2010). Support for this model came in the form of various studies over a range of organisms, including work on ChrI of *V. cholerae* and *in vitro* and *in vivo* studies in *C. crescentus* (Fogel & Waldor, 2006) (Ptacin et al., 2010). In *V. cholerae,* the origin of replication of chromosome I ($OriI_{vc}$) was seen moving across the cell to its opposing pole, while following a leading edge of ParA1 as it retracts to its new pole (Fogel & Waldor, 2006). A significant factor of this proposed mechanism is the filament formation capabilities of type II and type III systems, since the motor protein actions in these systems are well known to form filaments, it was initially thought that those of type I would also follow suit. For example, ParM encoded by the type II *par* operon of the R1 plasmid (**Figure 1.1B**) described in 1.2.2 (Garner et al., 2004, 2007; Gerdes & Molin, 1986). In addition, it was observed that Soj from *Thermus thermophilus,* a Type Ib ParA protein, is able to form ATP-dependent nucleoprotein filaments with DNA (Leonard et al., 2005). Studies carried out on *C. crescentus*, an organism whose chromosome that shows similarity to *V. cholerae*'s ChrI revealed continual formations of ParA filaments *in vitro*, giving rise to the hypothesis that retracting ParA filaments enabled segregation (Ptacin et al., 2010). These nucleotide dependent nucleoprotein filaments have also been observed with $ParA2_{vc}$ using negative stain electron microscopy (Hui et al., 2010). However, a range of evidence, including the fact that these *in vitro* studies were performed using higher than physiologically relevant concentrations of ParA, and the contradicting data on whether ParA form filaments *in vivo*, has led to questioning of this model (Ptacin et al., 2010; Szardenings et al., 2011).

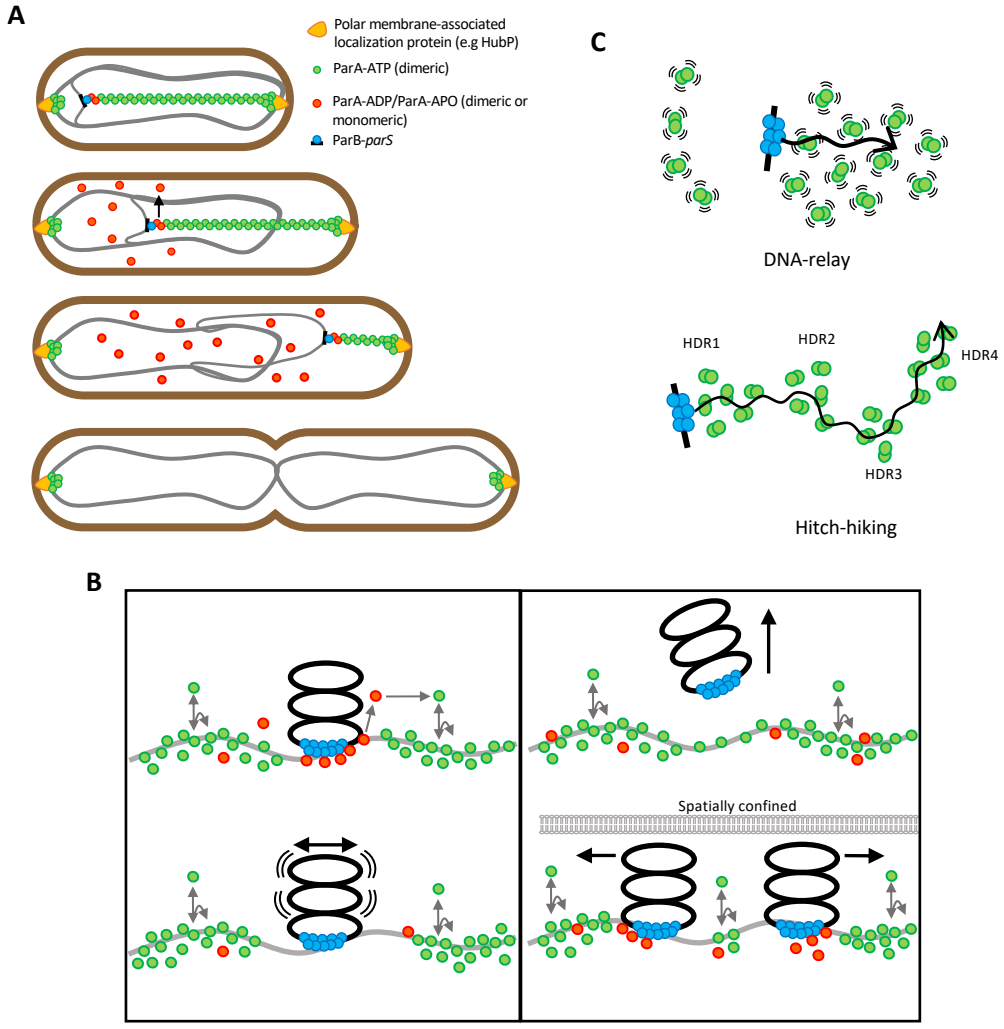

Figure 1.2. Proposed models of chromosome/ plasmid segregation.
A) *Filamentous model for chromosome segregation, ParA forms a polymer, pulling the partition complex across the cell to the new cell pole.* ***B-C)*** *Models for low-copy number plasmid segregation.* ***B)*** *The diffusion ratchet model left panel shows the general mechanism features, the right panel visualizes the aspect of special confinement (adapted from* (Hwang et al., 2013)*).* ***C)*** *The DNA-relay and Hitch-hiking diffusion ratchet models, HDR referring to high density regions (adapted from* (Jalal & Le, 2020)*.*

1.3.2 Diffusion ratchet

The most recent and currently accepted mechanism is the "diffusion ratchet" model whereby ParA coats the bacterial chromosome, binding non-specifically to DNA (Hwang et al., 2013). The increase in ATPase activity of ParA upon binding to ParB causes its dissociation from the DNA and an uneven distribution of ParA across the nucleoid; The partition complex then chases the ParA concentration gradient across the nucleoid (**Figure 1.2B**). This model explains the directional movement of the segregating DNA and is supported by recent evidence using reconstituted systems and single-molecule measurements (Havey et al., 2012; Taylor et al., 2015;

Vecchiarelli et al., 2010); however, the molecular details of how it allows the diffusion of entire DNA molecules across the bacterial cell is currently not understood.

The diffusion ratchet model is based on ParA's increased binding affinity to non-specific DNA (nsDNA), when in its ATP bound state (Hui et al., 2010). The model states that, upon binding of ParB to the *parS* site, a dense partition complex is formed as the ParB protein bridges multiple DNA molecules together (Taylor et al., 2015). In addition to binding non-specifically along the nucleoid, ParA also binds to the partition complex, forming an intermediate partition complex (Havey et al., 2012). The ParB-mediated DNA bridging, in addition to the non sequence-specific DNA binding of ParA, is thought to be the basis of tethering the complex to the nucleoid (Fisher et al., 2017; Kleckner et al., 2014). As described above, the increase in in ATPase activity of the ParA upon ParB interaction causes dissociation from the DNA and an uneven distribution of ParA across the nucleoid. Directional movement is achieved via the partition complex (ParB-*parS*) diffusing up the gradient and by Brownian motion chasing the ParA concentration gradient across the nucleoid (Hu et al., 2017) whilst under confinement by the inner membrane, preventing diffusion of the partition complex into the cytosol (**Figure 1.2B right panel**) (Hwang et al., 2013). Directionality may also be introduced through interaction with polarly localised proteins, for example the polar trans-membrane protein, HubP. In the case of *V. cholerae* ChrI, ParA interaction with HubP helps with origin localisation during segregation (Yamaichi et al., 2012) but studies focusing on the polar trans-membrane protein of *C. crescentus* (PopZ,) show a sequestering of apo-ParA/ParA-ADP, allowing for ParA-ATP regeneration to take place at the cell pole (Ptacin et al., 2014; Schofield et al., 2010). As mentioned for the filamentous model, *in vivo* studies of ParA during segregation have been carried out using fluorescence microscopy, showing "cloud-like" formations and leading edges towards cell poles, which were previously thought to be filaments (Fogel & Waldor, 2006; Szardenings et al., 2011). However, more recently using super-resolution microscopy, it has been shown that Par proteins locate within the chromosome, with partition complexes and ParA showing localization to dense chromosomal regions (HDRs). This suggests that the partition complex uses the nucleoid as a scaffold to guide proper segregation (Le Gall et al., 2016) and these "cloud like" formations are ParA binding the nucleoid at a gradient

towards the cell pole, potentially clustering at HDRs. This model is thereby able to provide insight into the molecular mechanisms seen *in vivo* (Le Gall et al., 2016; Vecchiarelli et al., 2012; Vecchiarelli, Hwang, et al., 2013), which have previously been assumed to be filamentous ParA polymers (Fogel & Waldor, 2006).

1.3.2.1 DNA relay and Hitch-hiking model

Due to argument that the short-range diffusion of ParB-*parS* would be insufficient to maintain unidirectionality during segregation, two extensions to the diffusion-ratchet model have been suggested (Chu et al., 2019; Jalal & Le, 2020). The first extension incorporates features of DNA elasticity, known as the DNA-relay mechanism (Lim et al., 2014; Surovtsev et al., 2016) (**Figure 1.2C**). This model proposes that the chromosome plays a mechanical role, relaying the partition complex from one location to another across a dimer gradient through DNA-bound ParA-ATP dimers transiently tethering and harnessing the elastic dynamics of the chromosome (Lim et al., 2014; Surovtsev et al., 2016). The second model focuses on ParA clustering at regions of high DNA density, labelled the hitch-hiking model (Le Gall et al., 2016) (**Figure 1.2C**). In this model ParA assembles into small patches at regions of high DNA density (HDRs), partition complexes are recruited to these high-density regions of ParA within the nucleoid. These small patches and oligomers are more stable than their ns-DNA bound counterparts in lower concentration regions, not jumping on and off the nucleoid, meaning dissociation of ParA is prevented at these HDRs unless under proximity with ParB or partition complexes stimulating ATP hydrolysis (Bouet et al., 2007; Vecchiarelli, Hwang, et al., 2013). Introduction of the partition complex into these ParA patches triggers progressive dissociation of ParA from HDRs and release of the partition complex, which using Brownian diffusion “hitch-hikes” to the next ParA clustered HDR (Le Gall et al., 2016).

1.4 *Vibrio cholerae* and its chromosomes

V. cholerae is a gram-negative bacterium, and the aetiological agent of cholera, a severe diarrheal disease affecting an estimated 3-5 million worldwide (Faruque et al., 1998)**.** *V*. *cholerae* is among 10% of known bacteria species to have a divided genome (Ramachandran et al., 2014), possessing two chromosomes: chromosome 1 (Chr I) and chromosome 2 (Chr II), that are ~3Mbp and ~1Mbp, respectively (Heidelberg et al., 2000) (**Figure 1.3A**). Each chromosome encodes its own segregation complex, with Chr I encoding a chromosomal Type Ib system, and Chr II encoding a plasmid-like Type Ia system (**Figure 1.1A**). During cell division, both chromosomes segregate synchronously. ChrI initiates segregation first, from the old cell pole to new in an asymmetric manner (**Figure 1.3B**). Once Chr I reaches the mid-cell region, ChrII commences segregation. ChrII segregates symmetrically moving from the mid-cell to quarter cell positions, both chromosomes terminating segregation in unison (Fiebig et al., 2006; Fogel & Waldor, 2005; Yamaichi, Fogel, Mcleod, et al., 2007).

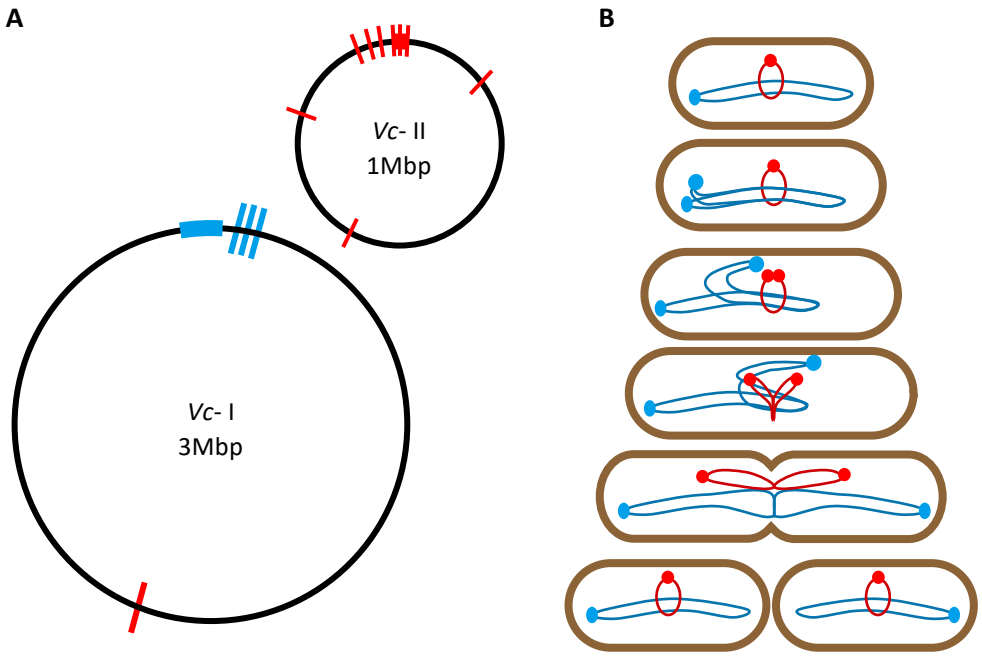

Figure 1.3. Vibrio cholerae chromosomes and segregation synchronization.
A) *Chromosomes I and II (not to scale) annotated with their corresponding par operon/origin of replication (bold coloured line) and parS sites, blue for ChrI and red for ChrII.* ***B)*** *Model of segregation of the two chromosomes, chromosome I in blue and chromosome II in red, with the origins indicated (Adapted from* (Egan et al., 2005)*.*

1.4.1 Chromosome I

Chromosome I (ChrI) is the larger (2.96Mbp) and the primary chromosome of *V. cholerae*, encoding the majority of the essential genes needed for cell growth (**Figure 1.3A**). The Par system of ChrI belongs to the Type Ib par loci family, encoding for ParA1, ParB1 and *parS1* (Livny et al., 2007), showing similarity in particular with the segregation system of *C. crescentus* (Toro & Shapiro, 2010).

Despite carrying the majority of genes essential for cell growth, the ParABS system is not essential for segregation of ChrI. (Yamaichi, Fogel, & Waldor, 2007). Substantial evidence suggests that instead, the parABS system functions in the polar localisation of the chromosome. Upon deletion of parABS1, ChrI is still able to undergo segregation, however, there is mis-location of the origin of replication ($oriCI_{vc}$) to the mid-cell position (Possoz et al., 2012). Research regarding the positioning of the *parS* sites also provides a basis for this hypothesis. Using fluorescently labelled ParB1 and sequence analysis, three putative *parS1* sites were identified based on fluorescent ParB1 foci formation and similarity to a parS 8 bp consensus sequence. All three of the parS1 sites identified were located within an 8kbp region on ChrI, 60kbp from ChrI's $oriCI_{vc}$ and 80kbp from parAB (Yamaichi, Fogel, Mcleod, et al., 2007) (**Figure 1.3A**). These findings agree with the suggestion that *parS1* may act as a chromosomal centromere, as it has been previously shown that *parS1*, like in *C. crescentus*, segregates ahead of $oriI_{vc}$ (Fogel & Waldor, 2006). In regard to *Caulobacter*, segregation becomes delayed when the *parS* site is moved further away from the origin of replication (Toro et al., 2008). As ChrI shows a similar segregation pattern to *Caulobacter*, this suggests that ChrI may also not begin segregation until *parS* is duplicated (Toro & Shapiro, 2010). Deletion of parABS may cause origin mis-location due to ParA1's direct interaction with HubP. As briefly introduced above, HubP, is a landmark protein located at both cell poles, it's interaction with ParA1, which in turn interacts with the *parS* ParB complex, anchors the centromere-like site to the cell pole (Yamaichi et al., 2012). Fluorescently labelled $oriCI_{vc}$ and ParA show the movement of $oriCI_{vc}$ asymmetrically across the cell to the new pole following a "cloud" of ParA (Ramachandran et al., 2014), suggesting that the ParA1 and B1 proteins form an apparatus that pulls the $oriCI_{vc}$ across to the cell (Fogel & Waldor,

2006). However, clear spindle or filament formation of ParA1 have yet to be seen *in vivo*, with only ParA2 proteins having been shown to form filaments at high concentrations in vitro (Ptacin et al., 2010).

1.4.2 Chromosome II

ChrII is the smaller of the two circular chromosomes (1.07Mbp), however it does encode some essential genes such as ribosome proteins, a translation initiation factor and an aminoacyl tRNA. It has been proposed that the chromosome originated as a mega-plasmid, containing 13 toxin-antitoxin loci, similar to those found in plasmids, for example, the shiga toxin of *Shigella flexneri*, carried on the pIWR501 plasmid (Heidelberg et al., 2000; Venkatesan et al., 2001). ChrII's par loci and pattern of origin segregation also shows similarity to that of plasmids. It encodes a Type I par locus, producing ParA2, ParB2 and *parS2*. Showing similarity to that in the *E.coli* P1 and F plasmids, its ParA protein categorising the loci into the Type Ia subtype, due to the presence of the additional N-terminal DNA binding domain (Ebersbach & Gerdes, 2005). In vivo fine-scale origin movements revealed the dynamics of origin arrangement during the cell cycle, showing that ChrII localises to the mid-cell and segregates symmetrically to the quarter cell position (Fiebig et al., 2006; Fogel & Waldor, 2005; Yamaichi, Fogel, & Waldor, 2007) (**Figure 1.3B**).

Although ChrII contains only few essential genes, its correct segregation is crucial to the cell, meaning unlike ChrI, in ChrII the ParABS system is essential. ParAB2 deletion mutants show mis-location of the chromosome, resulting in a failure of segregation and eventually death of daughter cells, as they are not viable in the presence of ChrI alone (Yamaichi, Fogel, & Waldor, 2007). These experiments also provide evidence that the ParABS segregation system in *V. cholerae* is chromosome specific, as no defect was seen in the segregation of ChrI (Kadoya & Chattoraj, 2012). Yamaichi et al in 2007 provided evidence of the secondary chromosome's evolution from plasmids through sequence analysis. This analysis shows that like its Par protein sequences, the *parS* sites located on *V. cholerae* ChrII lack relation with the "universal" chromosomal *parS* sequence. Instead, the *parS* sites show similarity to those found

on some plasmids. This sequence analysis identified ten ParB2-binding *parS* sites in the *V. cholerae* genome, one of which being located near are located within 70Kbp from ChrII's origin of replication (*oriCIIvc*) (Yamaichi, Fogel, Mcleod, et al., 2007), suggesting that ParB2 binding may influence the subcellular localisation of *oriCIIvc* (Yamaichi, Fogel, & Waldor, 2007).

Although deletion mutations have concluded that the two *V. cholerae* chromosomes segregate independently of one another, a parS2 site located near the $terI_{vc}$ suggests that the segregation of ChrII may influence the termination of ChrI segregation (Yamaichi, Fogel, Mcleod, et al., 2007). A site identified on ChrI, called ChrII replication-triggering site (*crtS*) has been shown to control the initiation of ChrII replication. The site produces a RctB protein that binds to 12-mer site on ChrII that promotes replication, instead of the 39-mer site that causes inhibition (Baek & Chattoraj, 2014; Ramachandran et al., 2017).

1.5 Understanding the Par-ticipants

1.5.1 MinD/ParA family

The P loop GTPase superfamily is extensive, with the P-loop NTPase fold characterized by an N-terminal Walker A motif, a phosphate binding loop. Typically adopting the sequence pattern GxxxxGK [T/S] (Saraste et al., 1990) (**Figure 1.4**), the motif's conserved lysine residue has been identified as key for nucleotide binding. The superclass is firstly split into two classifications according to shared structural and sequence features, TRAFAC (after translation factors) and SIMIBI (after signal recognition particle, MinD and BioD) (Leipe et al., 2002; Lutkenhaus, 2012)(**Figure 1.4**). The first group, TRAFAC, includes enzymes involved in translation, signal transduction, cell motility and intracellular transport. The second group, SIMIBI, includes signal recognition particle (SRP) GTPases and ATPases involved in localization, chromosome partitioning and membrane transport (Leipe et al., 2002).

SIMIBI is then furtherly split into three, the largest subgroup, the Mrb/MinD family, adopting a 'deviant Walker A motif – KGGXXGKT' whereby there are two conserved lysines, allowing for dimerization through forming contacts with the adjacent molecule (Koonin, 1993). This Mrb/MinD family differs considerably from members of the TRAFAC subclass also by lacking conservation of the [NT]KxD motif which provides specificity for guanine, among the eight Mrb/MinD subfamilies subdivided by sequences homology (Lutkenhaus & Sundaramoorthy, 2003), there is a great deal of variation (Leipe et al., 2002). These subfamilies include: Mrp/NBP35, AF2380, MinD, MotR/FlhG, ParA/Soj, NifH, ChlL/FrxC and ArsA, however more recently new members have been recognised (**Figure 1.4**).

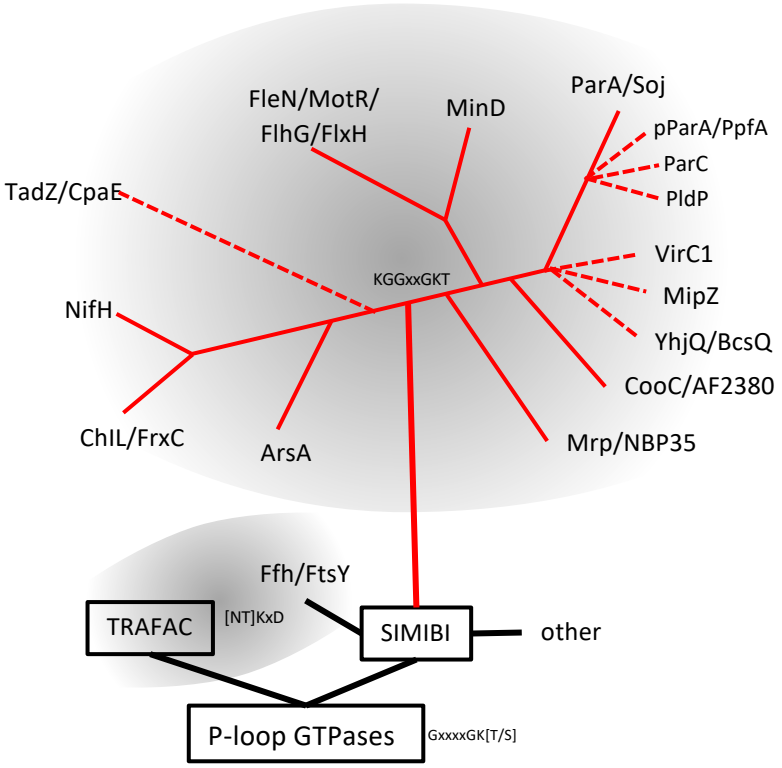

Figure 1.4. Phylogenetic tree of the MinD/ParA family from the GTPase superfamily.
The MinD/ParA/Mrp family lined in red, more recently recognized members with dotted lining. Grey clouding indicating families containing conserved sequences (Adapted from (Lutkenhaus, 2012) *).*

1.5.2 Biochemistry of ParA proteins

Plasmid ParAs, both Type Ia and Ib have been studied biochemically extensively over many years, including ParAs such as pSM19035, pB171, TP228, P1 and F (Baxter & Funnell, 2014) . From these studies general characteristics of Type I ParAs have been determined, showing how although ParA dimerises upon ATP-binding, the intrinsic ATPase activity is relatively weak, with a specific activity of 0.1 mol ATP $min^{-1}mol^{-1}$ (Chodha et al., 2021), requiring stimulation by ParB and binding of non-specific DNA to enhance this activity **(Figure 1.5A)** (Ah-Seng et al., 2009; Barillà et al., 2007; Davis et al., 1992; Ebersbach et al., 2006; Pratto et al., 2008; Watanabe et al., 1992).

The N-terminal arginine residue aka “arginine-finger” of ParB has been proposed to be responsible for the interaction resulting in ATPase stimulation (Ah-Seng et al., 2009; Barillà et al., 2007). Although dimerization is triggered upon ATP or ADP

binding, the effects of binding differ between ParAs. TP228 ParF and Soj along with MinD are monomeric when bound to ADP and dimeric with ATP, while with other Type Ib and Type Ia ParAs dimerization is stimulated with both ADP and ATP and can even occur in the absence of nucleotide altogether (Castaing et al., 2008; Davey & Funnell, 1997; Dunham et al., 2009; Pratto et al., 2008; Vecchiarelli et al., 2010). With P1 ParA, a monomer-dimer equilibrium has been proposed, which shifts towards dimer with the introduction of ADP or ATP (Davey & Funnell, 1997; Vecchiarelli et al., 2010). Along with this, an intermediate stable state of ParA upon ATP-binding and dimerization of ParA monomers, $ParA^*_2{:}ATP_2$, has been proposed (Vecchiarelli et al., 2010). This conformational change is a slow multi-step transition, allowing for reversible binding of DNA, which in turn increases the intrinsic ATPase activity of the ParA. This time delay coupled with hydrolysis stimulation exerted by ParB would cause an uneven distribution of ParA across the nucleoid, causing a concentration related motive force for segregation (Vecchiarelli et al., 2010).

ParA have been shown to be able to bind to DNA while in different nucleotide states **(Figure 1.5B**), however with a significant favour towards the ATP bound state, showing a much higher affinity. This DNA binding biochemical data gives evidence towards a cooperative binding affinity of ParA proteins, due to the sigmoidal curve produced over an increase in ParA concentration (Baxter et al., 2020; Chodha et al., 2021; Ebersbach et al., 2006; Jindal & Emberly, 2015; Leonard et al., 2005).

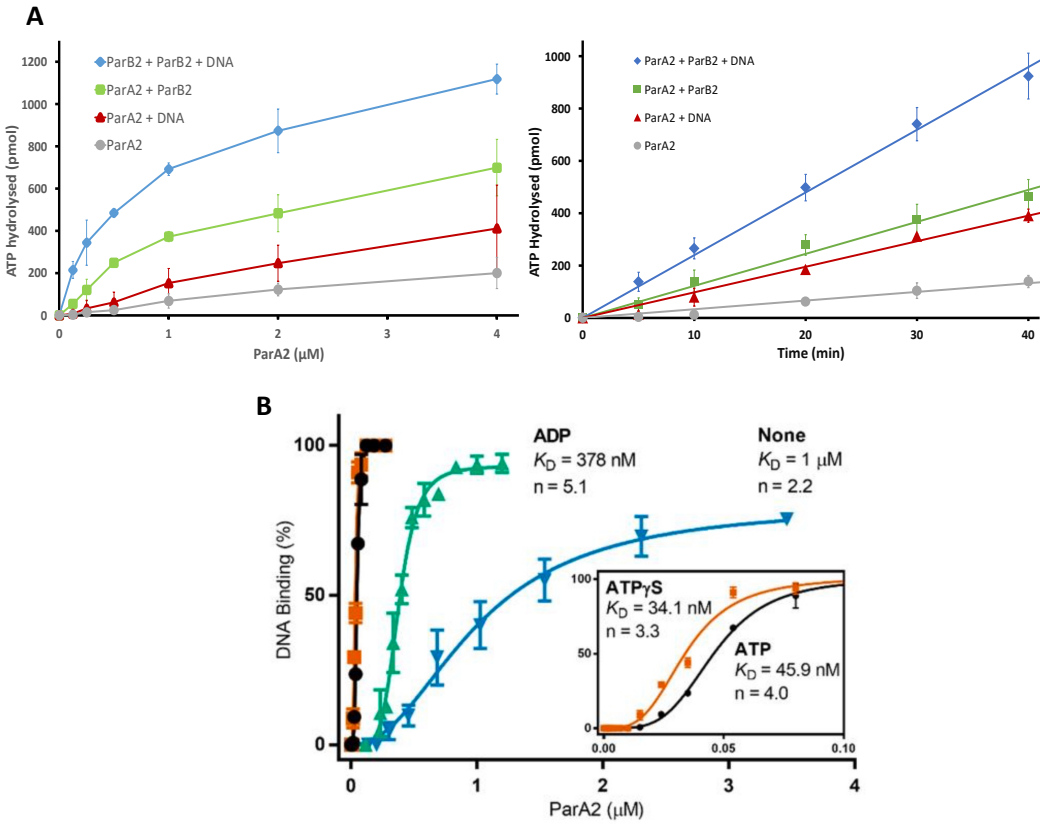

Figure 1.5. ATPase and DNA binding activity of ParA2$_{vc}$.
A) *Change in ATPase activity of ParA2 while in the presence of ParB2 and DNA over an increase in ParA2 concentration (Left) and at a constant concentration over time (right).* ***B)*** *DNA binding activity of ParA2 in the presence of different nucleotides over an increase in ParA2 concentration. All work was carried out by Satpal Chodha* (Chodha et al., 2021).

The ParA protein's catalytic activity has been characterised, focusing on the conserved residue K122 in P1 ParA, involved in ATP-binding and hydrolysis, specifically how activity is related to *par* operon repression (Davis et al., 1996; Fung et al., 2001; Vecchiarelli, Havey, et al., 2013). Three of the mutants observed were K122Q, K122E, and K122R, classed with the phenotypes "super-repressor", null and ParPD (worse than null) (Davis et al., 1996; Fung et al., 2001). While all three mutants are defective for plasmid partitioning, K122R shows a "worse than null" phenotype, meaning the defect is worse than the lack of ParA (Fung et al., 2001). Regarding nucleotide binding and hydrolysis, K122Q is shown to be able to bind to both ADP and ATP but is unable to undergo the conformational change required for DNA binding (ATP-ATP to [ATP-ATP]*) (Vecchiarelli et al., 2010). K122R is shown to be able to bind ATP and undergo the change needed for DNA binding, but however has

reduced ATP hydrolysis efficiency. K122E however, is unable to bind nucleotide altogether (Vecchiarelli, Havey, et al., 2013).

1.5.3 Structural characterization of ParAs

As introduced above, ParA is part of the MinD/ParA subfamily of the GTPase superfamily, the majority of which are able to form homodimers (Koonin, 1993). Despite being distant relatives with a wide range of functions, they share a similar fold and oligomerisation mode (**Figure 1.6**).

Although there is low sequence identity between homologues, core conserved regions are vital amongst ParAs, particularly the dimerization and nucleotide binding and DNA binding sites (Hester & Lutkenhaus, 2007). The crystal structures of ParA has been solved in a range of bacterial species and plasmids (Chu et al., 2019; Dunham et al., 2009; Leonard et al., 2005; Schumacher, 2008), which revealed that the overall structure is conserved, and that they form dimers along the same interface (**Figure 1.6**). Negative-stain electron microscopy of several ParA orthologues, both of the Type Ia and type Ib families, claim the formation of filaments in the presence of nucleotide and/or DNA (Chu et al., 2019; Hui et al., 2010; Leonard et al., 2005; Ptacin et al., 2010)**;** However, crystal structures of ParA proteins bound to DNA did not provide any support for filamentous architecture (Chu et al., 2019). Whether ParA proteins form filaments, and the molecular basis for filament assembly, remained controversial prior to the work reported here.

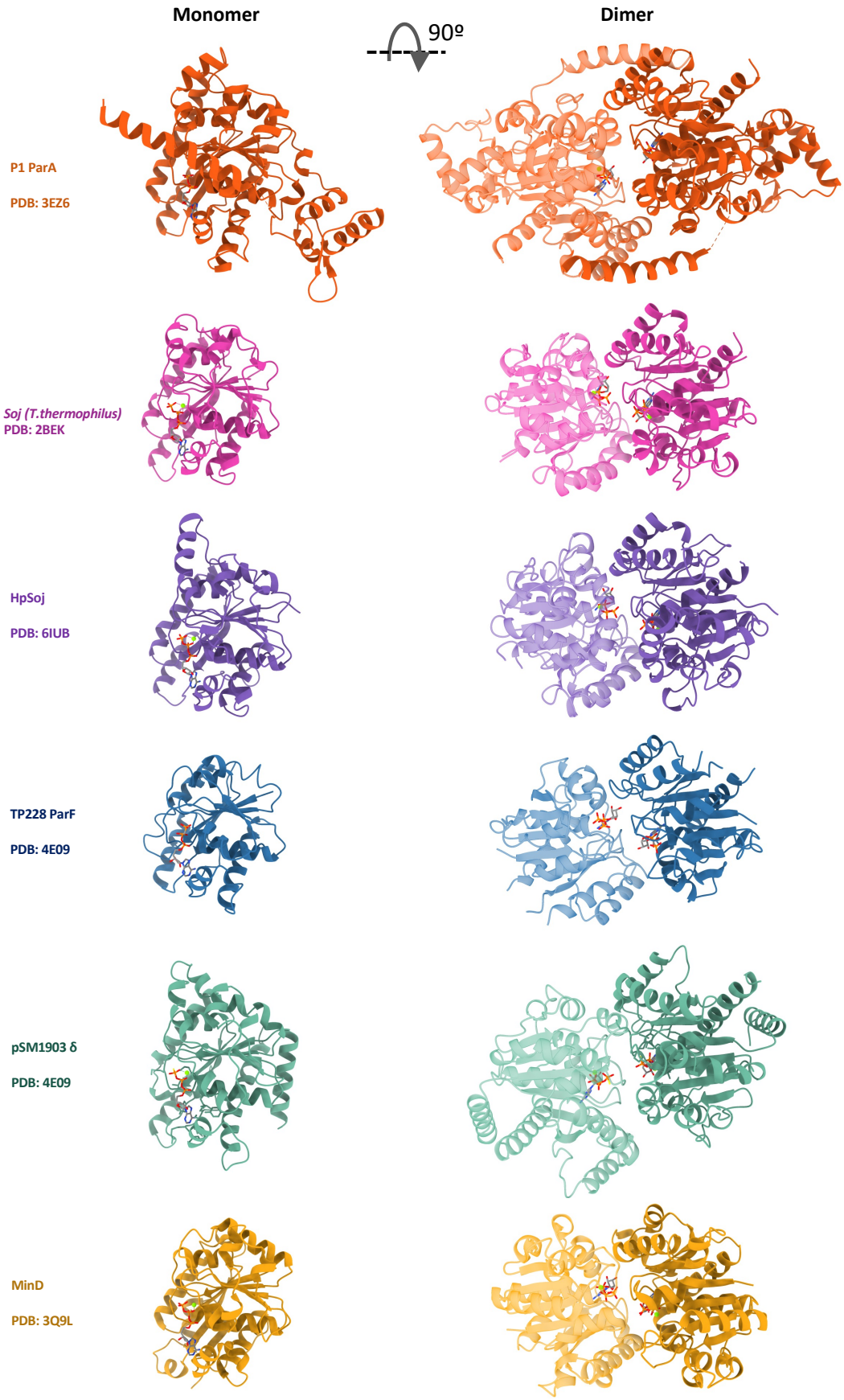

Figure 1.6. Comparison of ParA/MinD crystal structures.
Monomers indicated on the left and dimers on the right having been rotated 90° in the X axis with one monomer slightly more transparent and nucleotides coloured via element.

The filamentous model was initially proposed based on negative stain EM images of filaments (**Figure 1.7**) forming with ATP independent of DNA. Filaments have been observed not just with Par proteins, but also in the wider GTPase family, including MinD. However, the quality of many of these images is concerning for several reasons. Firstly, some of these images are significantly under or over-focused, using unsuitable magnifications and even having confusing contrasts in the context of the staining methods used (**Figure 1.7**). Secondly, many of these filaments forming in the absence of DNA do not show much resemblance to tradition protein filaments shown with negative stain, whereby the protein filament is viewed as white on the dark stain background, with patterning seen for monomers/dimers along the filament. As seen on Figure 1.7 where there is a collection of images of differing ParAs/MinD, a lot of these filaments lack resemblance from their dimeric counterparts and resemble more like crystals seen from salt or even from the heavy metal stain itself.

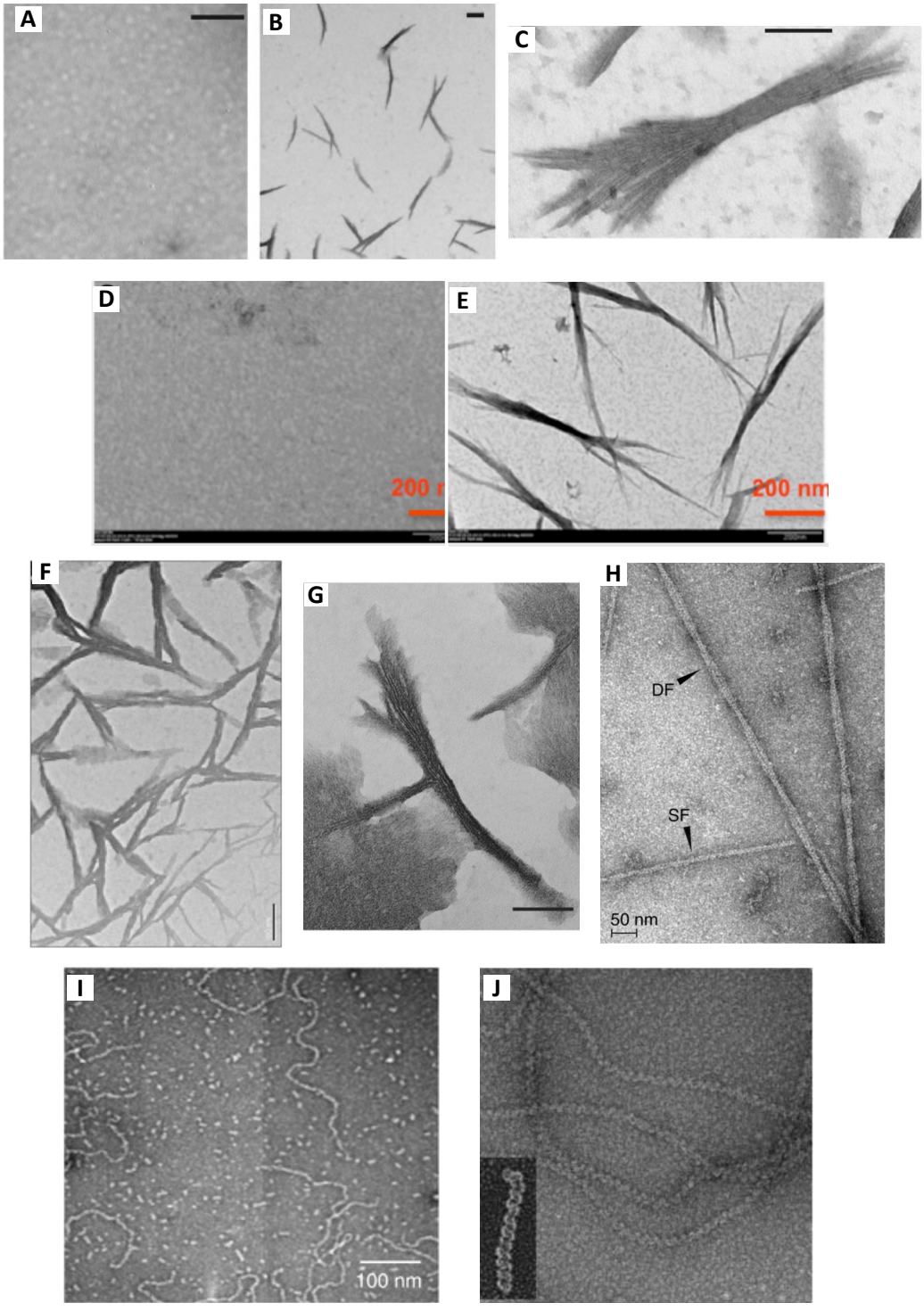

Figure 1.7. Negative stain electron microscopy of ParA and MinD filaments.
A-C) *Negative stain micrographs of E.coli F-plasmid SopA, scale bars= 100 nm.* ***A)*** *SopA in the absence of ATP.* ***B-C)*** *differing magnification of fibres formed by SopA in the presence of ATP* (Bouet et al., 2007). ***D-E)*** *Micrograph of pNOB8 ParA* (Zhang & Schumacher, 2017). ***D*** *showing ParA (5 µM) in the presence of AMPPNP (2 mM), $MgCl_2$ (1 mM) and DNA (10 µM), not forming polymers while* ***E*** *states the presence of polymers in the absence of DNA.* ***F)*** *Negative stain EM micrograph of C. Crescentus ParA forming polymers in the presence of ATP, Scale bar = 100 nm* (Ptacin et al., 2010). ***G)*** *Reverse contrast negative stain electron micrograph of TP228 ParF forming filaments in the presence of ATP* (Barillà et al., 2005). ***H)*** *Micrograph of MinCD copolymer filaments showing a single filament (SF) and a double filament (DF)* (Szewczak-Harris et al., 2019). ***I)*** *Micrograph of T.thermophilus Soj forming nucleoprotein filaments with DNA in the presence of ATP* (Leonard et al., 2005). ***J)*** *Micrograph of V. cholerae ParA2 nucleoprotein filaments with DNA in the presence of ATP* (Hui et al., 2010).

Despite these poor examples of negative-stain microscopy, some clear negative-stain micrographs of protein filaments, and low resolution3D reconstructions, have also been published showing filaments, including Soj from *T. thermophilus* and $ParA2_{vc}$ (**Figure 1.7 and 1.8**), proving that these filaments can be formed *in vitro*. Regarding MinD, of which there are multiple papers showing bundle like filaments (**Figure 1.7**), more recently copolymer filament structures of MinCD have been solved using cryo-EM (**Figure 1.8**), showing MinC stimulating polymerisation MinD and giving doubt to the ability of MinD to be able to polymerise with ATP in the absence of MinC.

Biochemical experiments support the hypothesis that ParA filaments may be formed under high concentration. ParA proteins are intrinsically weak ATPases **(Figure 1.5A)** with a slow conformational change from ATP-binding to a DNA-binding state, this licenses ParA-ATP dimers to cooperatively bind onto DNA **(Figure 1.5B)** to form higher order complexes (Baxter et al., 2020; Chodha et al., 2021; Jindal & Emberly, 2015).

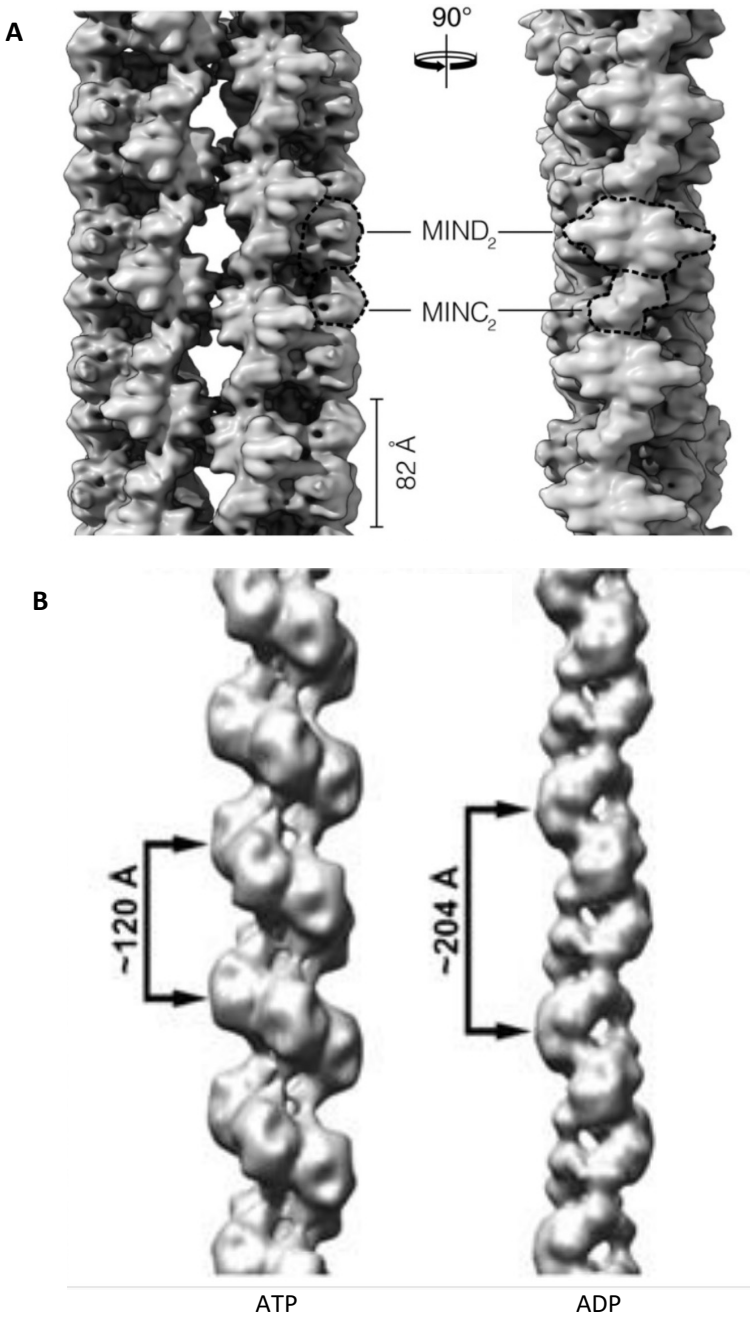

Figure 1.8. Structures of MinCD and ParAvc-DNA filaments.
(A) *3.1 Å cryo-EM structure of the MinCD copolymeric double filament from Pseudomonas aeruginosa* (Szewczak-Harris et al., 2019). ***B)*** *The low-resolution negative stain EM structure of ParA2$_{vc}$-ATP (left) and ADP (right) nucleofilaments* (Hui et al., 2010).

1.5.4 ParB- biochemistry and structural biology

As introduced previously, ParB is a crucial member of the par tripartite system. When bound to DNA, ParB stimulates the ATPase activity of ParA, which drives the ParB-*parS* complex to the opposite pole, carrying the whole nascent chromosome with it (Hwang et al., 2013; Lim et al., 2014; Taylor et al., 2021). ParB carries out this activity in the form of a higher-order nucleoprotein complex, first nucleating on *parS* and then spreading to neighbouring non-specific DNA (Funnell, 2016). ParB proteins share common domain architecture (Jalal & Le, 2020), consisting of an N-terminal domain (NTD) containing a highly conserved arginine-rich motif required for protein-protein and protein-ligand interactions (Osorio-Valeriano et al., 2019; Soh et al., 2019). A central DNA-binding domain (DBD) containing a helix-turn-helix motif for specific *parS* binding (Chen et al., 2015) and a C-terminal domain (CTD) important for ParB homodimerization through a leucine zipper motif (Fisher et al., 2017; Funnell, 2016; Leonard et al., 2004; Schumacher & Funnell, 2005) (**Figure 1.9A**). Like with ParA mechanisms, there is controversy over ParB activity, and four main models are proposed for ParB-DNA nucleoprotein assembly. (1) One dimensional filamentation of ParB, whereby a ParB filament grows nucleating from the *parS* site, mediating gene silencing (Rodionov et al., 1999). (2) Bridging and condensing DNA, based on ParB binding and bridging across to different segments of DNA (Graham et al., 2014). (3) Caging ParB and DNA, the *parS* site acting as a nucleation centre, while protein-DNA and protein-portein interactions cage ParB into a confined volume (Sanchez et al., 2015). (4) Lateral sliding of a ParB-CTP clamp on DNA, whereby the CTP-induced dimerization of ParB confirms a clamp-like conformation, entrapping DNA in the cavity, ParB is then able to slide and self-load onto the *parS* site (Jalal & Le, 2020; Soh et al., 2019).

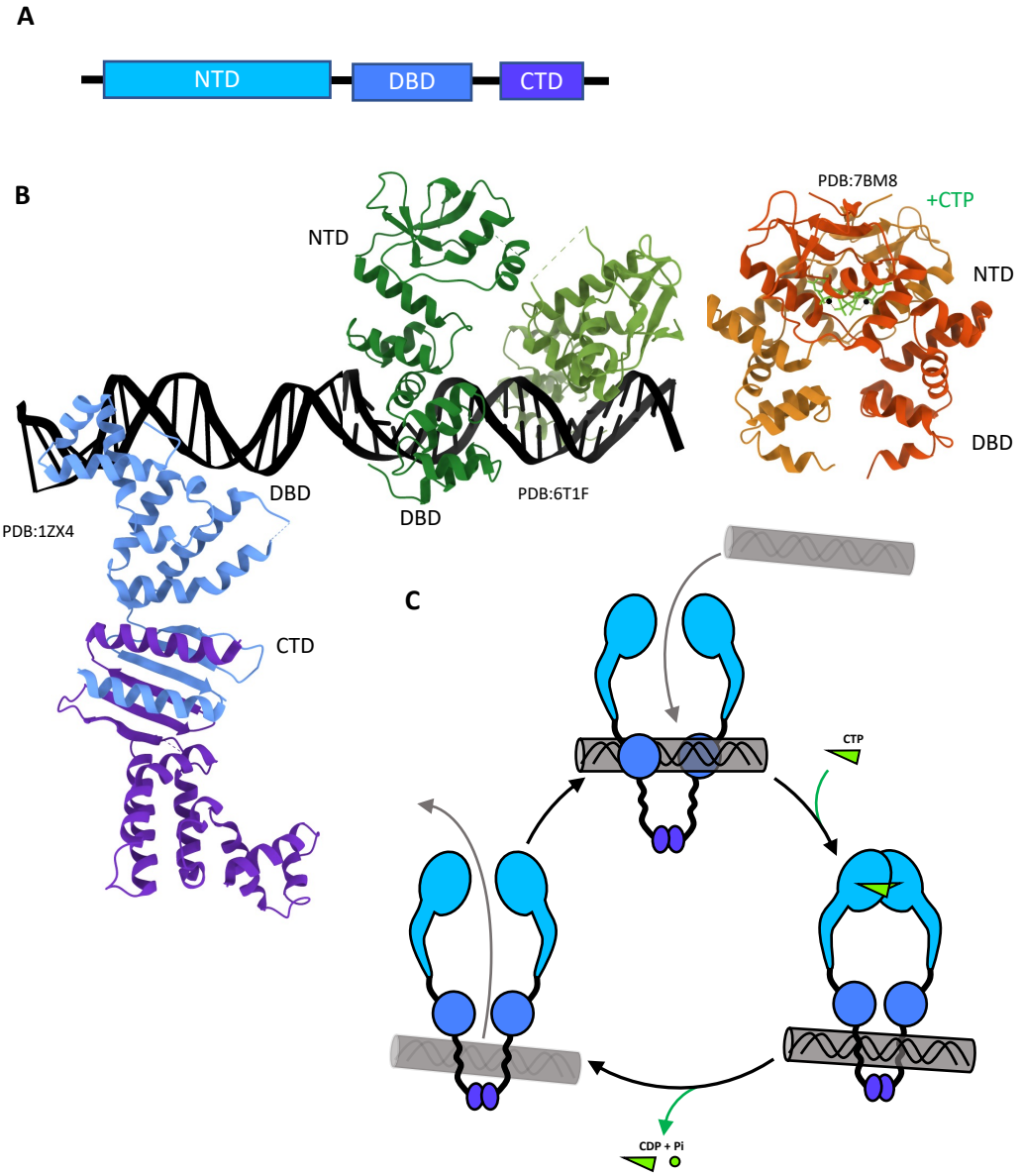

Figure 1.9. The domains of ParB and CTP-dependent gating mechanism.
A) *The three domains of ParB, The N-terminal domain, the DNA binding domain and the C-terminal domain, coloured to match the schematic in C.* ***B)*** *Crystal structures showing differing domains of ParB, each chain coloured differently. Chains with NTD truncations (blue and purple), showing dimerization with the CTD and the BDB binding to DNA. Structures with CTD truncations (light green, dark green, orange and yellow) bound to DNA through the DBD (light and dark green) and self-dimerization through the NTD bound to CTP (yellow and orange).* ***C)*** *The DNA gating mechanism of ParB upon CTP binding via the NTD* (Jalal et al., 2021).

Although ParB proteins have been studied biochemically and structurally for many years, due to the flexibility of the protein, the structure of a full length ParB has not been solved (Jalal & Le, 2020). The first solved structure of a truncated ParB was achieved with the *E. coli* P1 plasmid system (Schumacher & Funnell, 2005). Missing the NTD (first 141 residues) bound to *parS,* this structure showed how ParB forms an asymmetric dimer with individual DNA-binding modules that rotate freely around a flexible linker, enabling contacts to be made with differing arrangements of DNA motifs surrounding the *parS* site (**Figure 1.9B**) (Schumacher & Funnell, 2005) .

However, recently the CTPase enzymatic activity of ParB has been elucidated (Jalal et al., 2020; Osorio-Valeriano et al., 2019; Soh et al., 2019), showing how *parS* binding stimulates cooperative ParB binding of CTP and hydrolysis to CDP (Soh et al., 2019). In *Myxococcus xanthus*, CTP has been suggested to modulate *parS* binding of ParB (MxParB) (Osorio-Valeriano et al., 2019), while in *C. crescentus,* CTP was shown to be required for ParB spreading during *parS* nucleation (Jalal et al., 2020). With this surge in biochemical data also came advances in ParB crystallization. Although still truncated, various species of ParB have been crystallised bound to CTP, CDP, and *parS*, showing changes in the NTD upon CTP binding and hydrolysis (**Figure 1.9B**) (Jalal et al., 2021; Osorio-Valeriano et al., 2021). As described by Jalal et al in eLife, nucleating ParB is said to capture *parS* at the DNA binding-domain (DNA-gate) while in an "open-clamp position", the NTD then self-dimerises upon CTP binding, closing the NTD-gate of the clamp along with the DNA-gate, therefore moving *parS* into a compartment between the DNA-gate and the CTD and the DNA-gate, CTP hydrolysis and/or phosphate release then re-opens the gates (Jalal et al., 2021) (**Figure 1.9C**).

1.6 Thesis rationale

Despite years of research, very little is understood about chromosome/plasmid partitioning in type I systems. Since the majority of research has been focused on the type Ia system in *E.coli* plasmids, studying the Par system in *V. cholerae*, specifically in chromosome II, allows us to understand more about how the system is adapted for native chromosomes and how the mechanism has evolved from plasmids. With this in mind, the objectives of this work and the questions I am trying to address involve elucidating ParA protein interactions with DNA and other ParA molecules, and how this could orchestrate segregation. I intend to resolve the controversy of whether ParA proteins can form filaments and determine the molecular basis of ParA interacting with DNA and cooperative binding. Using structural biology methods, such a X-ray crystallography and electron microscopy, I aim to understand the conformational changes involved in ParA dimerization, DNA binding and filament formation. I will then be able to use his information to propose a molecular mechanism for type I DNA segregation.

2 Materials and Methods

Materials

2.1 Buffers and media

2.1.1 Bacteria culture media

	Composition
Lysogeny Broth (LB)	25g of LB broth Miller 1L of double-distilled Milli-Q water (DDW)
LB Agar	35g of LB broth with agar (Lennox) 1 of double-distilled Milli-Q water (DDW)
Super Optimal broth with Catabolite repression (SOC) media	2%Tryptone 0.5% Yeast Extract 10 mM NaCl 2.5 mM KCl 10 mM MgCl2 10 mM MgSO4 20 mM Glucose

2.1.2 Purification and protein buffers

2.1.2.1 Sonication Buffers

Buffer	**Composition**
HEPES Sonication Buffer (pH 7.5)	50 mM HEPES 50 mM $(NH_4)_2SO_4$ 1 mM EDTA 0.5 mM DTT
Tris Sonication Buffer (pH 7.5 and 8)	50 mM Tris 50 mM $(NH_4)_2SO_4$ 1 mM EDTA 0.5 mM DTT

2.1.2.2 Purification Buffers

	Buffer A	**Buffer B**
HEPES S Buffer (pH 6)	25 mM HEPES 25 mM Imidazole 0.1 mM EDTA 10% Glycerol 25 mM KCl 1 mM DTT	25 mM HEPES 25 mM Imidazole 0.1 mM EDTA 10% Glycerol 1 M KCl 1 mM DTT

Affinity Buffer (pH 7.5 and 8)	50 mM Tris 0.1 mM EDTA 10% Glycerol 100 mM NaCl 2 mM DTT	50 mM Tris 0.1 mM EDTA 10% Glycerol 1 M NaCl 2 mM DTT
HEPES Q Buffer (pH 6 and 7.5)	25 mM HEPES 0.1 mM EDTA 10% Glycerol 25 mM KCl 1 mM DTT	25 mM HEPES 0.1 mM EDTA 10% Glycerol 1 M KCl 1 mM DTT
HisTrap Buffer (pH 7.5)	30 mM Tris pH 7.5 20 mM Imidazole (pH 7.5) 10% Glycerol 500 mM NaCl 2 mM DTT	30 mM Tris pH 7.5 1 M Imidazole (pH 7.5) 10% Glycerol 500 mM NaCl 2 mM DTT
Mono S Buffer (pH 8)	50 mM MES (pH 6) 0.1 mM EDTA 10% Glycerol 80 mM NaCl 2 mM DTT	50 mM MES (pH 6) 0.1 mM EDTA 10% Glycerol 80 mM NaCl 2 mM DTT
ParB Buffer (pH 8)	20 mM Tris 0.1 mM EDTA 10% Glycerol 500 mM NaCl 2 mM DTT	

2.1.2.3 General buffers

Buffer	**Composition**
HEPES Storage Buffer (pH 7.5 and 8)	25 mM HEPES pH 7.5 0.1 mM EDTA 10% Glycerol 300 mM KCl 10 mM DTT
Tris Storage Buffer (pH 7.5 and 8)	30 mM Tris pH 7.5 0.1 mM EDTA 10% Glycerol 500 mM NaCl 2 mM DTT

TE Buffer (pH 8)	10 mM Tris pH 8 1 mM EDTA
10x SDS running buffer	250 mM Tris base 1.92 M Glycine 1% SDS
2x Laemmli buffer	4% SDS (0.14M) 120 mM Tris-Cl pH 6.8 20% glycerol 0.02% (w/v) bromophenol blue

2.2 Strains, plasmids, and oligonucleotides

2.2.1 Plasmids

E.coli	**Genotype**	**Supplier**
BL21 (DE3)	*fhuA2 [lon] ompT gal (λ DE3) [dcm] ΔhsdS λ DE3 = λ sBamHIo ΔEcoRI-B int::(lacI::PlacUV5::T7 gene1) i21 Δnin5*	New England Biolabs
NEB 5-alpha	fhuA2 [lon] ompT gal (λ DE3) [dcm] ΔhsdS λ DE3 = λ sBamHIo ΔEcoRI-B int::(lacI::PlacUV5::T7 gene1) i21 Δnin5	New England Biolabs

Plasmids	**Source**	**Inducer**	**Antibiotic resistance**
pET28b-A1	LCH	IPTG	Kanamycin
pBAD-A1	LCH	Arabinose	Ampicillin
pET15b-HisB1	LCH	IPTG	Ampicillin
pET28b-ParA2	LCH	IPTG	Kanamycin
pET28b-ParA2-Δ4-37	This thesis	IPTG	Kanamycin
pET28b-ParA2-K338	This thesis	IPTG	Kanamycin
pET28b-ParA2-K338_L291_R395A	This thesis	IPTG	Kanamycin
pET28b-ParA2-K124E	SC	IPTG	Kanamycin
pET28b-ParA2-K124Q	SC	IPTG	Kanamycin
pET28b-ParA2-K124R	SC	IPTG	Kanamycin

LCH- plasmid designed and cloned by Ling-Chin Hwang
SC- plasmid designed and cloned by Satpal Chodha

2.2.2 Oligonucleotides

Mutation	Sequence (5'-3')	
ParA2$_{vc}$-Δ4-37	gatataccatggcaatggacgaacactttccgcc	Fwd
	ggcggaaagtgttcgtccattgccatggtatatc	Rev
ParA2$_{vc}$-Δ4-108	aggagatataccatggcaatggaaaacaaaccgtggattatc	Fwd
	gataatccacggtttgttttccattgccatggtatatctcct	Rev
ParA2vc-K388A	ccagtgcgcttgcttgaacggcatcctgggccg	Fwd
	cggcccaggatgccgttcaagcaagcgcactgg	Rev
ParA2$_{vc}$-L391A	tgccgttcaaaaaagcgcagcggaactggaacgcg	Fwd
	cgcgttccagttccgctgcgctttttttgaacggca	Rev
ParA2$_{vc}$-R395A	aagcgcactggaactggaagccgtcctgcattc	Fwd
	gaatgcaggacggcttccagttccagtgcgctt	Rev
ParA2vc-K338A_L391A_R395A	aatgcaggacggcttccagttccgctgcgcttgcttgaacggcatcctgggc	Fwd
	gcccaggatgccgttcaagcaagcgcagcggaactggaagccgtcctgcatt	Rev

2.3 Purification columns

Column	Volume	Type	Loading Volume	Pressure Limit (MPa)
HisTrap	5 ml	Affinity	< 150 ml	0.5
HiTrap Heparin	5 ml	Affinity	< 150 ml	0.5
HiTrap SPHP	5 ml	Cation	< 150 ml	0.5
Mono Q	1 ml	Anion	< 20 ml	4
Mono S	1 ml	Cation	< 20 ml	4
HiPrep desalting 26/10	53 ml	Size exclusion	< 10 ml	0.15
Superdex 200 HiLoad 16/600	120 ml	Size exclusion	< 2 ml	0.5
Superdex 75 HiLoad 16/600	120 ml	Size exclusion	< 2 ml	0.5
Superdex 75 HiLoad 10/300	24 ml	Size exclusion	< 2 ml	1.8

Methods

2.4 Cell and protein manipulation

2.4.1 Transformation

50 µl of BL21/ DH5α competent cells were taken from -80°C storage and thawed on Ice. Once thawed ~60-80 ng of plasmid DNA was added and mixed by flicking, the mixture was then left on ice for 30 minutes. The cells were then heat shocked for 20 seconds by being placed in a 42°C water bath, followed by being placed back on ice for 5 minutes. 450 µl of SOC media was added to the mixture, and placed in a 37°C incubator to shake (200 Figure) for 1 hour. 100 µl of the cell mixture was then pipetted and spread onto an antibiotic selective LB agar plate and placed at 37°C overnight.

2.4.2 Protein expression

A starter culture was prepared by inoculating 15 ml of LB in a 50 ml falcon with the required concentration of antibiotic to which the plasmid holds resistance, while under sterile conditions. A single transformed colony grown on the antibiotic selective LB agar plate was picked and dropped into the media, the culture was then placed in a 37°C incubator (Gallenkamp 10x400.xx1.c orbital incubator) to shake at 200 rpm overnight.

The next day the 15 ml of starter culture was split equally over 5 x 2L flasks containing 400 ml of antibiotic inoculated LB. The flasks were placed into 37ºC, shaking at 200 rpm, until they reached an OD600 of 0.4-0.6. Once reached they were induced with 0.4 mM of IPTG (or 0.1% arabinose for a pBAD plasmid), and put into 25ºC, shaking at 200 rpm. For ParA1 the cells were induced for 2 hours, while ParA1-GFP cells were placed into 16°C and left overnight.

The culture was then centrifuged at 4000 rpm (Beckman Avanti J25I) for 20 minutes at 4°C, the supernatant discarded, and the pellet resuspended in 50 ml of fresh LB. The resuspension was split across 2x 50 ml falcon tubes and centrifuged at 4000 rpm (Thermo Scientific Sorvall ST 16R Centrifuge) for 20 minutes at 4ºC, the supernatant of each was discarded and the pellets frozen in liquid nitrogen and stored at -80ºC.

2.4.3 Protein Purification

2.4.3.1 Cell lysis and ammonium sulphate precipitation

The cell pellet was taken out of -80°C storage, weighed and thawed on Ice. 10 ml/g of pellet was added of Sonication buffer, along with ½ a crushed (Roche) protease inhibitor tablet and 1 mg/ml of lysozyme. The mixture was left to rock on ice for ~20 minutes to dissolve the lysozyme and protease inhibitor tablet. The cell mixture was then lysed by sonication (Sonics Vibra-Cell VCX130 ultrasonic processor) for a total of 6-7 minutes, 30 seconds ON and 30 seconds OFF at 75% amplitude. The lysate was then centrifuged at 20,000 rpm on a Beckman Avanti J25I centrifuge, using a JA-25.50 rotor, for 25 minutes at 4ºC. The supernatant was kept and 0.35 g of ammonium sulphate was added per ml before being centrifuged again at 20,000 rpm for 25 minutes at 4ºC. The supernatant was discarded, and the pellet was resuspended in 10-15 ml of Affinity Buffer A, the resuspension was then dialysed against Affinity Buffer A overnight at 4°C while stirring.

2.4.3.2 5 ml HiTrap & HisTrap column chromatography

The following method was used on the affinity columns and the 5 ml HiTrap SPHP cation exchange column in **Section 2.3**

Lines A and B of the AKTA were first washed with DDW. The column was then attached while there is ddH20 being flown through and the column was washed with at least 5 column volumes (CV) of DDW at a flow rate of 3 ml/min, not exceeding the pressure limit of the column (**see section 2.3**). Line A was then washed in HisTrap Buffer A and line B in Buffer B, before equilibrating the column with 10 CV of HisTrap Buffer A at 3 ml/min. The superloop was loaded with the sample (haven taken it out of the dialysis tubing) and attached onto the AKTA. The following method was run:

Flow Rate	**3 ml/min**
Column equilibration	**2CV**
Wash column	**2CV**
Linear gradient length	**12CV**

100% B wash	**5CV**
Re-equilibration	**5CV**
Flow through fraction size	**10 ml**
Elution fraction size	**2 ml**

Table 2.1. 5 ml HiTrap/HisTrap column run parameters.

2.4.3.3 Ion exchange chromatography

The following method were used on the Mono Q and Mono S ion exchange columns in **section 2.3**

The Lines of the AKTA were washed as described above (**2.4.3.2**), the ion exchange column was then washed with 10CV of DDW at 1 ml/min (see pressure limit in table x). Lines A and B are then washed in Purification Buffers A and B, respectively. The column was washed with 10CV of ion exchange Buffer A at 1 ml/min. The superloop was loaded with sample and attached onto the AKTA. The method was run:

Flow Rate	**1 ml/min**
Column equilibration	**2CV**
Wash column	**2CV**
Linear gradient length	**20CV**
100% B wash	**5CV**
Re-equilibration	**5CV**
Flow through fraction size	**10 ml**
Elution fraction size	**1 ml**

Table 2.2. Ion exchange column run parameters.

2.4.3.4 Size-exclusion chromatography

The lines of the AKTA were washed as described above (**2.4.3.2**), the size exclusion column was then washed with 1.2CV of DDW at 1 ml/min for the Superdex 16/600 columns and 0.5 ml/min for the Superdex 75 10/300 column (see pressure limit in table x). Line A was then washed with Purification Buffer (see results section for which buffers). A 2 ml loop was attached to the AKTA and was washed with 10 ml of Buffer with a syringe. The method was run:

Flow Rate	**1 ml/min (16/600), 0.5 ml/min (10/300)**
Column equilibration	**0.2 CV**
Elution length	**1.2 CV**

Elution fraction size	**0.5 ml (10/300), 1-2.5 ml(16/600)**

Table 2.3. Gel filtration column run parameters.

While the column is equilibrating during the method run, the sample was manually injected into the loop by the syringe.

2.4.3.5 Buffer exchange and Protein concentration

Buffer exchange was carried out using a HiPrep 26/10 desalting column.

The lines of the AKTA were washed as described in (**2.4.3.2)**, the column was then washed in 3CV of DDW at 8 ml/min. Line A was then washed in with Purification Buffer before the column was washed with Buffer also (3CV) at 7 ml/min. The method was run:

Flow rates	**During equilibration**	**7 ml/min**
	During Run	**6 ml/min**
	During sample injection	**4 ml/min**
	Column equilibration	**5 CV**
	Elution length	**1.2 CV**
	Elution fraction size	**2 ml**

Table 2.4. Desalting column run parameters.

Pooled elution fractions and final purification products were concentrated using VivaSpin 20 columns (Sartorius 10,000 MWCO PES), all centrifugation was carried out at 4000 rpm. The column was washed by adding 5ml of DDW and being centrifuged until less than 100 µl remains. 3 ml of ethanol was added and centrifuged, this step was repeated. 3 ml of DDW as added and centrifuged, this step was repeated until less than 100 µl remains.

2.4.3.6 Sodium Dodecyl Sulfate Polyacrylamide Gel Electrophoresis (SDS-PAGE) analysis

2-Mercaptoethanol (BME) was added to Laemmli sample buffer (2x) to 5% (v/v). An equal volume of the 2x Laemmli sample buffer was added to the protein sample, resulting in a 1x solution. 15 µl of the protein- sample buffer solution was loaded into each well of SDS-PAGE gel, with PageRuler protein ladder loaded into the first lane.

All SDS-PAGE gels were made followed the recipe:

SDS-PAGE 2 gel recipe

Component	Resolving			Stacking	
	10%	12%	14%	4%	6%
1.5M Tris pH 8.8	2.5 ml	2.5 ml	2.5 ml	-	-
0.5M Tris pH 6.8	-	-	-	1.25 ml	1.25 ml
40% acrylamide	**2.5 ml**	**3 ml**	**3.5 ml**	**500 µl**	**750 µl**
10% SDS	100 µl	100 µl	100 µl	50 µl	50 µl
10% APS	50 µl	50 µl	50 µl	25 µl	25 µl
DDW	**4.84 ml**	**4.34 ml**	**3.84 ml**	**3.17 ml**	**2.92 ml**
TEMED	10 µl	10 µl	10 µl	5 µl	5 µl
TOTAL	10 ml	10 ml	10 ml	5 ml	5 ml

Table 2.5. SDS-PAGE gel recipe.

All gels were run at 200V for 42 minutes in 1x SDS running Buffer.

2.4.4 Measuring protein and DNA concentration

Concentrations were measured for protein and DNA samples and products using a BioDrop Duo+ (Biochrom), pipetting 1 µl of sample onto the port. For dsDNA, absorbance was read at 260 nm, giving the concentration as ng/µl. For protein, absorbance was read at 280 nm, the concentration was calculated from the measured absorbance using the extinction coefficient of the protein.

2.5 nsDNA extraction and purification

In order to obtain DNA to a high enough concentration suitable for electron microscopy, two methods were applied.

2.5.1 Sonicated salmon-sperm DNA (sssDNA)

Salmon sperm DNA (Sigma) was dissolved to 10 mg/ml in TE buffer pH 8 and distributed to 250 µl aliquots. For a target length of 1Kb fragments, each aliquot was sonicated at 50% intensity for 10 second pulses for a total of 1 minute 50 seconds. The aliquots were centrifuges at 12,000 g for 3 minutes to pellet titanium particles from the sonicator probe, the supernatant was transferred to another Eppendorf. 1/10 of the DNA volume was added of 3M sodium acetate (pH 5.2) followed by 2.5x the DNA volume of ice cold 100% ethanol and the mixture was vortexed for 2 minutes. The samples were then placed at -20°C for 1 hour prior to centrifugation at 12,000 g at 4°C for 30 minutes. The supernatant was carefully aspirated and 200 ul

of 70% ice cold ethanol was added followed by centrifugation at the same conditions as above. The supernatant was aspirated, and the pellet was left to air dry at 30°C for 20 minutes. The pellet was then resuspended in TE buffer (pH 8) and the concentration is measured.

As much as possible of the attained sssDNA was loaded onto a 1% agarose gel, which was run at 90V for 45 minutes. The gel was then soaked in SYBR safe (Invitrogen), diluted 10,000x for 30 minutes before imaging under UV light. Across all lanes of the agarose gel, the required DNA length was cut out using a razor blade (~1Kb) and gel extraction was using a GeneJET Gel Extraction Kit.

2.5.2 PBSKII plasmid midi prep

pBSKII plasmid was transformed into DH5α and grown on ampicillin selective agar overnight. A single colony was selected and inoculated into 200 ml of ampicillin selective LB broth for overnight growth at 37°C shaking at 200 Figure. The culture was then centrifuged and the DNA was purified from the pellet using a Promega PureYield Plasmid Midiprep System kit, eluting into 50°C warmed ddH_20. The yield is then measured using a BioDrop.

2.6 Mutagenesis

Primers were designed using the Aligent QuikChange Primer Design programme and ordered from IDT. PCR was then carried out using the QuikChange II site-directed mutagenesis kit, following the included protocol for sample reaction and thermo-cycling parameters. The template strand was digested with the restriction enzyme DpnI (NEB), adding 1µl to each reaction.

2.7 X-ray crystallography

2.7.1 Crystallisation

$ParA2_{vc}$ was purified to 20 mg/ml in 50 mM Tris buffer with 200 mM NaCl. For apo ParA2, 5 mM $MgCl^{2+}$ was added and for the nucleotide co-crystallisation trials, 5 mM of ATP, ADP or ATPγS was added in addition. The protein solutions were set-up for crystallisation trials in sitting drop 96-well plates (Hampton Research), in standard crystallization screens (QIAgen) using a mosquito protein crystallisation robot (sptlabtech). Crystallisation reactions were set up in a ratio of 1:1 and 1:3 of protein

to crystallisation solution, with the screen solutions JCGS+, PACT and Morpheous. For each nucleotide state, apo, ADP, ATP and ATPγS, two 96 well plates were generated for each screen solution to be grown at 4°C and 20ºC.

Crystals grew in all screens used, at both temperature conditions, for all the nucleotide states, showing a range in morphology. Selected wells containing crystals were carefully cut open, through the clear plastic film, using a razor. Matching the size of the target crystal to the loop size, crystals were picked up in 0.1-0.5 micron cryo-base mounted litholoops (Molecular Dimensions) and cryo-cooled in liquid nitrogen. The crystals grown in screens containing PEG 3000 (**table 2.1**), were soaked in the crystallisation condition supplemented with 10% glycerol, for cryo-protection, before cryo-cooling. The loops were placed into Diamond Light Source (DLS) standard sample containers for shipping to the MX beamline at DLS, Oxfordshire.

2.7.2 Data collection

Data collection was carried out at the Diamond Light Source beamline io3, with a fixed wavelength of 0.9762 Å. 3600 images were collected for each experiment, with an oscillation of 0.20° and a 20% beam intensity with an 0.01s exposure, under cryo conditions (100K). All images were collected on a Dectris Eiger2 XE 16M detector, with data collection carried out for diffracting crystals from each nucleotide state (**table 2.6**).

Nucleotide state	Screen conditions	Space Group	Estimated Resolution
Apo	0.1M MIB buffer pH 4, 25% (w/v) PEG 1500	P32 1 2	2.88 Å
ADP	24% w/v PEG 1500 with 20% w/v glycerol – 4ºC	P61 2 2	3.18 Å
ATPyS	0.1M tri-Sodium citrate pH 5.5, 20% w/v PEG 3000	P32 1 2	3.82 Å
ATP	0.1M tri-Sodium citrate pH 5.5, 20% w/v PEG 3000	P32 1 2	2.41 Å

Table 2.6. Collection details of each nucleotide state which diffracted.

2.7.3 Data processing

The autoPROC automated pipeline was used for immediate processing of collected data (Vonrhein et al., 2011). AutoProc utilises XDS/XSCALE, CCP4, POINTLESS and AIMLESS for spot detection, indexing, deciding on the space grouping, scaling and merging the data, and data reduction (Evans, 2005; Kabsch et al., 2010).

2.7.3.1 Apo conformation

The data collected from the ATP co-crystallised crystal (**table 2.6**), later discovered to be in the apo conformation, was further processed using the staraniso pipeline included with the autoPROC automated processor (Tickle et al., 2018). Phases were obtained by molecular replacement with Phaser (McCoy et al., 2007) implemented in the Phenix package, using a homology model of $ParA2_{vc}$ based on the P7 ParA structure (3ezF), and missing of the N-terminal residues 1-107. The N-terminal domain was then manually built into the electron density map using *Coot* (Emsley et al., 2010). The Matthews Coefficient analysis predicted only 1 molecule per asymmetric unit (ASU), so only this was trialled during phasing (**section 5.2.2**).

2.7.3.2 ADP bound

Molecular replacement was carried out on the autoPROC processed diffraction data using the structure obtained from the data set of the apo conformation, manually editing sections of the atomic model deviating from the electron density map using *Coot.* The Matthews Coefficient analysis predicted 4 to 9 molecule copies per ASU, therefore each number was trialled during phasing. 4 component copies found the best Top LLG (log-likelihood gain) and TFZ (Translation function) (**section 5.3.2.1**).

2.7.4 Structure refinement

2.7.4.1 Apo conformation

The obtained atomic model was refined through multiple cycles of manually building in *Coot* and refinement, using phenix.refine (Afonine et al., 2012). Over the course of refinement, secondary structure and TLS restraints were applied, until the Rwork/Rfree values had converged.

2.7.4.2 ADP bound

Similarly to the apo conformation, the structure was refined through iterative cycles of manually building regions into electron density using *Coot*, and refinement using phenix.refine. Ramachandran angles, side chain rotamers bond angles were refined using Isolde (Croll & Read, 2021). The same refinement strategy was applied as above (**2.7.4.1**), however, NCS (non-crystallographic symmetry) was applied for the first couple of rounds of refinement. The model was completed once the Rwork/Rfree values were as low as possible.

2.8 Electron Microscopy

2.8.1 Negative-stain Electron microscopy

2.8.1.1 Sample preparation of ParA2

For the $ParA2_{vc}$ samples, 1 mg/ml of protein was incubated with 3.5 mM nucleotide and $MgCl_2$ at 30°C for 15 minutes. 1/100 dilutions were made for each nucleotide state (ATP, ATPγS, ADP and without nucleotide) into sample buffer containing 100 mM NaCl, 50 mM Tris pH 7.5, 2.5 mM nucleotide (or distilled water for the apo state) and 2.5 µM $MgCl_2$.

2.8.1.2 Sample preparation of ParA2-DNA

Initially, $ParA2_{vc}$ was incubated with pBSKII plasmid to a final concentration of 0.68 mg/ml of ParA2 to 0.022 mg/ml of DNA, in the presence of 4.5 µM of ATP and $MgCl_2$. After optimisation, $ParA2_{vc}$-DNA filaments samples were prepared as above (**2.8.1.1**) with their respective nucleotide, except with 2 mg/ml of $ParA2_{vc}$. Each sample was then spiked with pBSKII plasmid to a final concentration of 0.2 mg/ml and left at 30°C for a further 10 minutes, leaving a $ParA2_{vc}$:DNA ratio of ~6:1 and nucleotide and $MgCl_2$ at 3 mM. A 1/10 dilution for each state was made using sample buffer and staining was done as above. For the ATPγS nucleotide state, $ParA2_{vc}$ at 1 mg/ml was incubated with $MgCl_2$ and ATPγS at 4.5 mM and incubated at 30°C for 15 minutes. The sample was then spiked with sssDNA (1kb) to a final concentration of 0.14 mg/ml and incubated again, resulting in a ParA:DNA ratio of ~3.5:1. From this stock a 1/10 dilution was made for negative staining.

2.8.1.3 Sample preparation of ParB

For ParB-ParS imaging, $ParB2_{vc}$ was incubated with ParS2 DNA with a final concentration of 0.65 mg/ml of ParB to 0.3 mg/ml of DNA, in a buffer containing 100 mM NaCl, 50 mM Tris and 5 mM $MgCl_2$. 1/30 dilution was prepared for negative staining.

For ParB-*parS* ParA2-DNA experiments, $ParA2_{vc}$ was first incubated with sssDNA following the methods outlined in **2.8.1.1** with a final concentration of 1.39 mg/ml of $ParA2_{vc}$, 1.27 mg/ml of DNA, 3.8 mM of $MgCl_2$ and ATPγS and 0.069% Tween20. Separately from ParA2, ParB2 and *parS*DNA was pre-incubated together at 30ºC, with a final concentration of 0.6 mg/ml of ParB2 and 0.44 mg/ml of *parS*DNA with 0.069% tween20. 6 µl of the ParA2-DNA solution was then mixed with 3 µl of the ParB-*parS* solution, and ten-fold serial dilutions were prepared for negative staining.

2.8.1.4 Negative staining

Carbon-coated copper grids (Agar scientific) were glow discharged for 30 seconds using a Cressington 208 carbon coater. 4 µl of the prepared sample was applied to the grid and left to incubate, after 2 minutes excess sample was removed by holding a piece of filter paper gently against the edge of the grid. The grid was then dipped into 3 small pools of distilled water (blotting in between), followed by 3 pools of 0.75% uranyl formate, blotting between each. Filter paper was held gently against the grid where it meets the tweezers followed by waving over a vacuum pump to remove any left-over moisture (Ohi et al., 2004).

2.8.1.5 Imaging and data collection

All negative-stain data was collected manually at a defocus range of ~-1 µm to -3.5 µm on a CM100 TEM (Phillips) with a MSC 794 camera (Gatan) at 27,500x with a pixel size of 7.2 Å. For 2D classification, the micrographs were processed using cisTEM 58, and 2D classes were generated using a box size of 24 pixels.

2.8.2 Cryo-EM data collection

2.8.2.1 Sample preparation

ParA2$_{vc}$ at 4 mg/ml was incubated with ~ 6 mM ATPγS and $MgCl_2$ at 30°C for 15 minutes, and was then spiked with sssDNA to a final concentration of ~0.8 mg/ml of DNA, ~1.9 mg/ml of ParA, and ~4 mM of ATPγS and $MgCl_2$. The sample was then incubated again for 10 minutes at 30ºC. Tween 20 was then added to a final concentration of 0.1% before grid preparation, to facilitate incorporation of the filaments into the holes of the carbon grid.

2.8.2.2 Grid preparation

3 µl of the ParA2$_{vc}$-DNA sample was applied to a glow discharged (for 15 seconds) 300 mesh Quantifoil R2/2 grid, and left for 30 seconds before manually blotting with filter paper. The grid was then loaded into a Leica EM-GP plunge freezer at 80% humidity and 4°C where a further 3 µl was applied for a 10 second incubation followed by a 4 second blot before being plunged into liquid ethane.

2.8.2.3 Imaging and data collection

Screening of grids was performed on a 200kV Technai Arctica cryo-electron microscope, with a Falcon III camera. Micrographs of ParA2$_{vc}$-ATPγS-DNA filaments were recorded using EPU (Thermo Fischer), on a 300KV Titan Krios FEG microscope with a Gatan K2 Summit detector in counting mode. For the initial data collection, 3665 movies were recorded with a pixel size of 1.35 Å over 48 frames, with a total dose of 49.92 $e^-/Å^2$ and over a defocus range of -3.25 µm to -1.5 µm. For the improved collection, 5785 movies were recorded with a pixel size of 1.047 Å over 50 frames with a total dose of 52.02 $e^-/Å^2$, at a defocus range of -2.3 µm to -1.3 µm.

2.8.3 Data processing and atomic model building

Frames were aligned using MotionCor2 (Zheng et al., 2017), and CTF estimation was obtained using CTFFIND4.1 (Rohou & Grigorieff, 2015). Filaments were then manually picked in Relion (He & Scheres, 2017), and helical segments were extracted with a box size of 200 pixels, a tube diameter of 140 Å and a helical rise of 30 Å. 2D classification, 3D classification, and 3D refinement was performed in Relion-3

(Zivanov et al., 2018), with a tube density used as an initial reference map. For 3D classification, 6 classes were generated over 25 iterations with a mask diameter of 200 Å over a local helical search range of -70° to -90° for twist and 20 Å to 40 Å for rise. A chosen class was then selected and put into 3D refinement following the same parameters, and the resulting map was post-processed in Phenix (Afonine, Klaholz, et al., 2018). The local resolution was determined with ResMap (Kucukelbir et al., 2014).

To build the atomic model, a polyA-polyT dsDNA molecule was generated in Coot, and placed in the map. A $ParA2_{vc}$ dimer from the ADP-bound structure (see above) was fitted into the EM map using ChimeraX (Goddard et al., 2018), and helix 1 was re-built manually in Coot. Multiple copies of the resulting dimer were then generated, and placed in the corresponding density in ChimeraX. The final model was then subjected to real-space refinement in Phenix (Afonine, Poon, et al., 2018) and refinement using ISOLDE on each chain at a time (Croll & Read, 2021).

3 Results Chapter 1: Par Protein Purification

3.1 Introduction

Efficient purification of protein is vital for structural and biochemical studies. In the case of Par proteins, various protocols have been outlined in brief among previous publications. Some of these methods utilise His tags to help with the process, while others have purified the WT protein, without modification. In this chapter, I am going to outline the purification steps I took to purify the proteins for both biochemical experiments, particularly enzymatic assays, and structural characterisation. Therefore, there is the upmost importance that the product is as pure as possible.

Despite being native to their respective chromosomes of *V. cholerae*, ParA and ParB have differing properties which require changes in the methods used in purification, specifically between ParA of ChrI (ParA1), and ParA of ChrII (ParA2), and of course between ParB and ParA in general. Regarding the ParA proteins, ParA2 is of similar size to other Type Ia ParAs, with a molecular weight of 46.3kDa and amino acid length of 407,. In comparison, P1 ParA (44kDa) and F plasmid SopA/$ParA_F$ (43.7kDa), have a sequence identity of 28.5% (63.2% similar) and 28% (62.7% similar) to $ParA2_{vc}$, respectively (Dunham et al., 2009; Watanabe et al., 1992). However, ParA1 is a Type Ib ParA, therefore is more similar in size to that of *T.thermophilus* Soj (~27kDa) (Leonard et al., 2005), consisting of 257 amino acids with a molecular weight of 28kDa and having a sequence identity of just 22.5% (58.3% similar) to ParA2. In addition, ParA2 has an extinction coefficient of 47900 and a theoretical pI of 5.45, while ParA1 has a ext. coefficient of 14900 and a theoretical pI of 6.83, much closer to neutral pH. A major difference between the two which may affect their purification is also the number of tryptophan residues in their amino acid sequence. While ParA2 has 6, ParA1 doesn't have any, which may affect UV measurements of the protein.

ParBs between chromosomes I and II also have very low sequence similarity, being just 19.2% identical (55.4% similar), despite being closer in size. ParB1 is 323 amino acids long with a molecular weight of 32.3kDa, while ParB2 is 323 amino acids long with a molecular weight of 35.9kDa. Similarly to ParA1, both ParBs have a theoretical pI close to neutral, at 6.94 for ParB1 and 6.99 for ParB2, which could make purification without a His tag difficult.

3.2 Optimisation of ParA1 purification

3.2.1 Purification of ParA1$_{vc}$ in pBAD vector using ion exchange chromatography

It had previously been identified that a plasmid encoding the ParA1$_{vc}$ gene could not be transformed and expressed when a His tag was cloned onto the N or C terminal, therefore non-tagged ParA1 was used. Expression and purification was carried out following the protocol outlined in **Figure 3.1** (including step A), transforming the pBAD-A1 plasmid into BL21 competent *E.coli* cells (**methods**). 1L pellet of pBAD-A1 was resuspended into HEPES pH 7.5 Sonication Buffer for ammonium precipitation to precipitate out protein that binds to nucleotide, (see **methods)** and dialysed into HEPES S Buffer A (pH6). The dialysed sample was loaded on a 5 ml HiTrap SPHP column for cation exchange chromatography (**Methods**), using HEPES S Buffer A and B at pH 6.

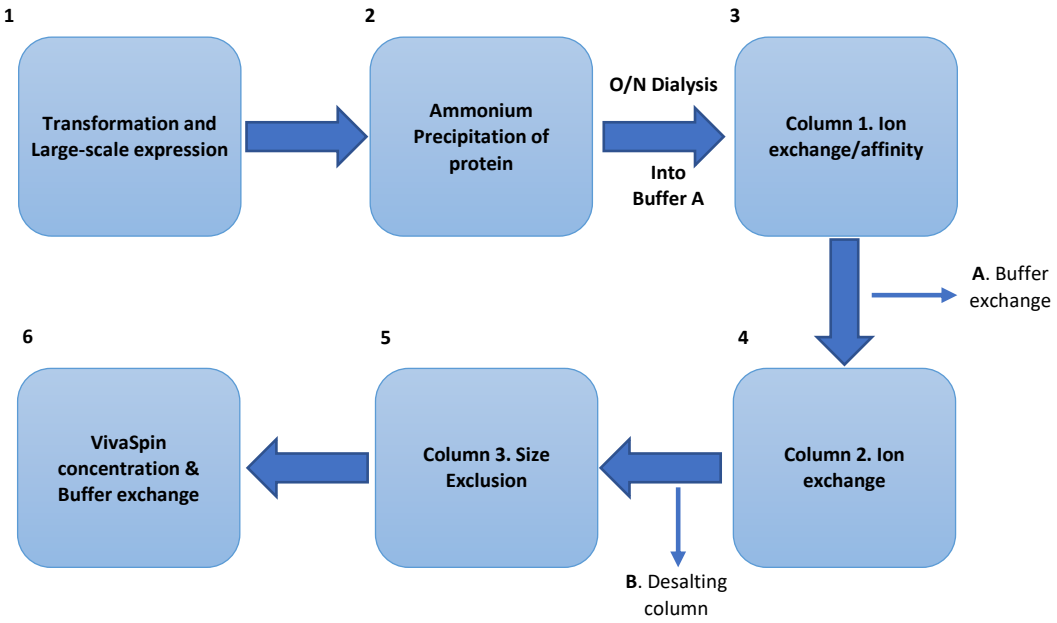

Figure 3.1. Flowchart overview of ParA1 purification.
(1) *The chosen plasmid is transformed into BL21 competent cells and expressed at a large-scale following the methods outlined in* ***Methods****.* ***(2)*** *The cell pellet from expression undergoes lysis, resuspension and ammonium precipitation, dialysing the* $(NH_4)_2SO_4$ *out overnight (****Methods****).* ***(3-5)*** *Protein samples are loaded onto their designated column following the methods outlined in* ***Methods****.* ***(6)*** *Following the 3 columns outlined, the final sample is concentrated using a VivaSpin column, while exchanging the Buffer to a Storage Buffer.*
Additional steps:
(A)*- Method 1 of ParA1 purification: dialysing into the ion exchange buffer.*
(B)*- Method 2 of ParA1 purification: Using the HiPrep desalting column for buffer exchange (****Method****).*

ParA1 eluted into fractions A7 to B12 at ~312 mM of NaCl (**Figure 3.2A**). Because of the high contamination seen (**Figure 3.2B**), only fractions A6-A11 were pooled. The pooled fractions were put into dialysis overnight against HEPES Q Buffer A at pH 7.5.

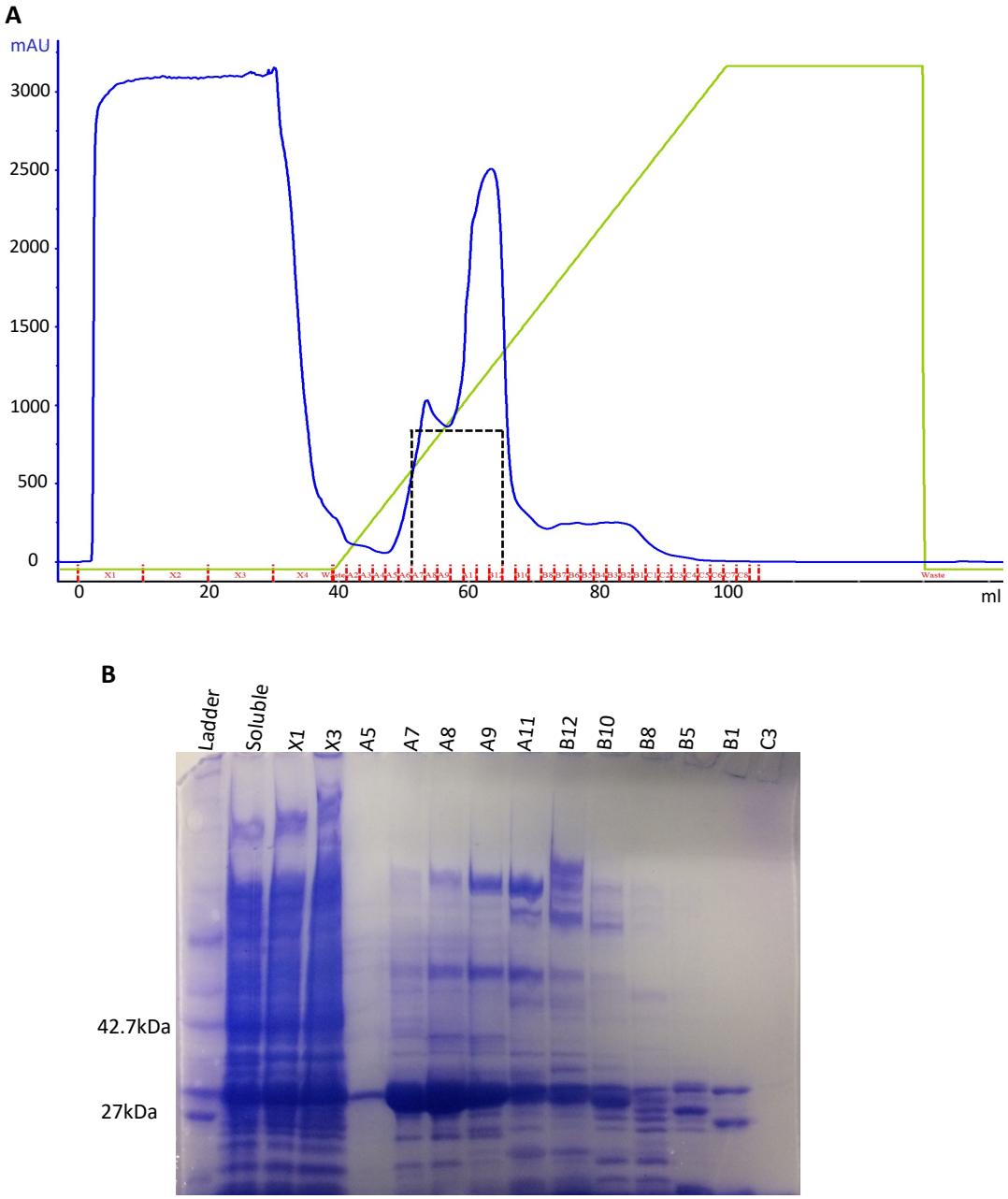

Figure 3.2. ParA1 method 1 chromatogram and SDS-PAGE of HiTrap SPHP column chromatography.
(A) *Chromatogram of the purification run. The X axis is the measured mL, the Y axis is the % of Buffer B, peak protein elution is at 23.6% B. Dark blue is UV measured at 280 nm in mAU, Green is conc of B% and red is fractions. The dotted region indicates pooled fractions.* ***(B)*** *10% SDS-PAGE analysis of column fractions, X1 and X3 are the flow through fractions, A5-C3 are the elution fractions.*

However, the dialysis was not successful, with a lot of precipitation. The sample was centrifuged to pellet the precipitant, and the supernatant diluted up to 37 ml with

HEPES Q Buffer A (pH 7.5) to lower the salt concentration, before loading onto a Mono Q column (column 2) **methods)** using HEPES Q Buffer A and B at pH 7.5. No clear ParA1 peak is seen in the chromatograph (**Figure 3.3A**), as there are multiple peaks throughout. However, **Figure 3.3B** shows that the protein did not bind to the column and was eluted into the flow through. Despite this, some contamination did bind, cleaning up the sample. This could be due to the close to neutral pI of ParA1, reducing the attraction to the mono Q column, or there could be a too high of a concentration of salt in the sample loaded onto the column.

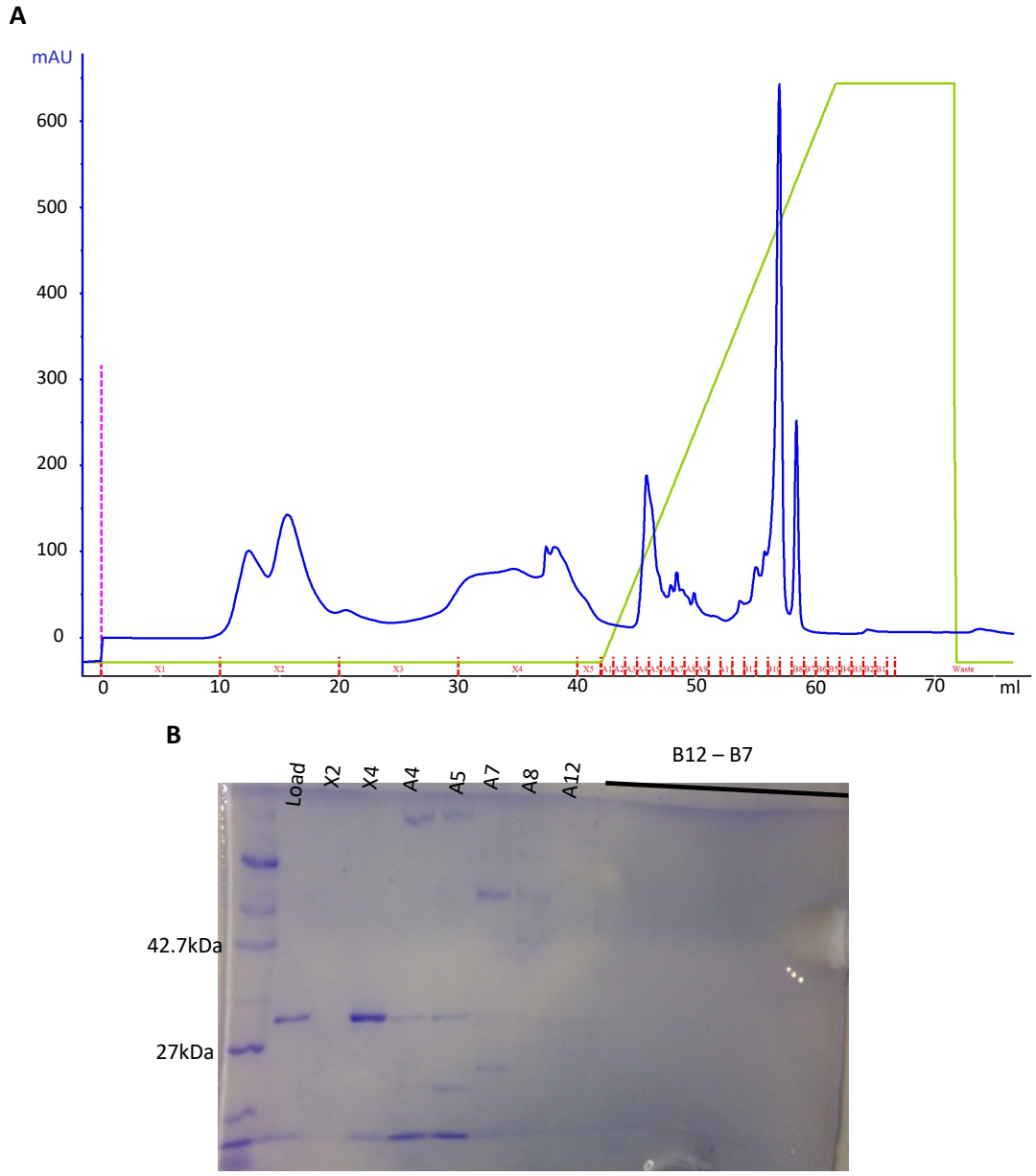

Figure 3.3. ParA1 method 1 chromatogram and SDS-PAGE of Mono Q ion exchange column chromatography. ***(A)*** *Chromatogram of the Mono Q protein purification column, from the chromatograph it is unclear to see where the protein eluted. Dark blue is UV measured at 280 nm in mAU, Green is conc of B% and red is fractions.* ***(B)*** *10% SDS-PAGE analysis of column fractions, X2 and X4 are the flow through fractions, A4 – B7 are the elution fractions.*

The flow through fraction was concentrated (**methods**) to be loaded onto the Superdex 75 10/300, eluting with HEPES Q Buffer A (pH 7.5) (**Methods**). ParA1 eluted at around 10 ml (**Figure 3.4A**), which is expected due to its molecular weight of 28kDa. Fractions containing ParA1 appear to be pure, however, the amount of protein is very low (**Figure 3.4B**). The fractions B12 to B10 were pooled, concentrated, and exchanged into the HEPES Storage Buffer to a final volume of ~150 ul. The

concentration of protein was calculated by measuring the absorbance at 280 nm, showing a concentration of 13µM.

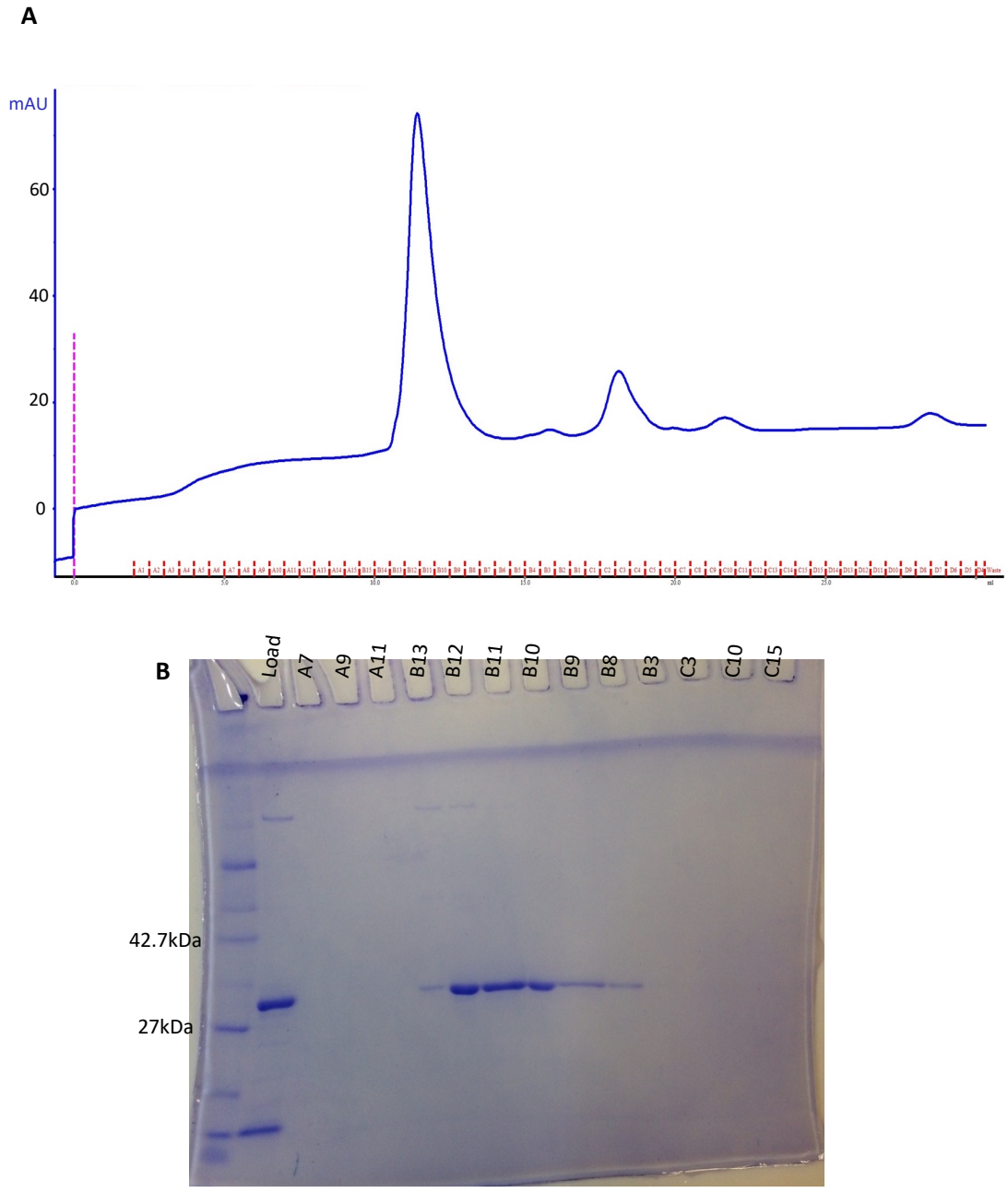

Figure 3.4. ParA1 method 1 chromatogram and SDS-PAGE of size exclusion column chromatography.
(A) *Chromatogram of the Superdex 75 10/300 purification column run, a suspected peak is seen after 10 ml across fractions B13 to B8* ***(B)*** *10% SDS-PAGE analysis of elution fractions, the load fraction indicates the sample loaded onto the column.*

From this purification protocol I concluded that a significant amount of protein was lost due to dialysis during buffer exchange. This could be because the pH of the buffers being exchange from and to meant that the pH was passing the isoelectric

point (pI) of ParA1, which is 6.8. Because of the slow buffer exchange, this could have meant the protein was in an unsuitable environment for too long, causing it to precipitate out of solution. The yield was also expected to be low due to a low induction during large-scale expression.

3.2.2 Purification of ParA1$_{vc}$ in pET28b vector

To help to improve induction of the protein, ParA1 was expressed in the pET28b (IPTG inducible) plasmid for the second round of purification. Cell lysis and ammonium precipitation was carried out the same as in **3.2.1**. The dialysed sample was loaded on a 5 ml HiTrap SPHP column (see **methods**) and was eluted against HEPES Q Buffer B (pH6) at ~300 mM NaCl (**Figure 3.5A**). However, protein is also seen in the flow through, along with contamination by a protein weighing ~42.7kDa in eluted fractions (**Figure 3.5B**).

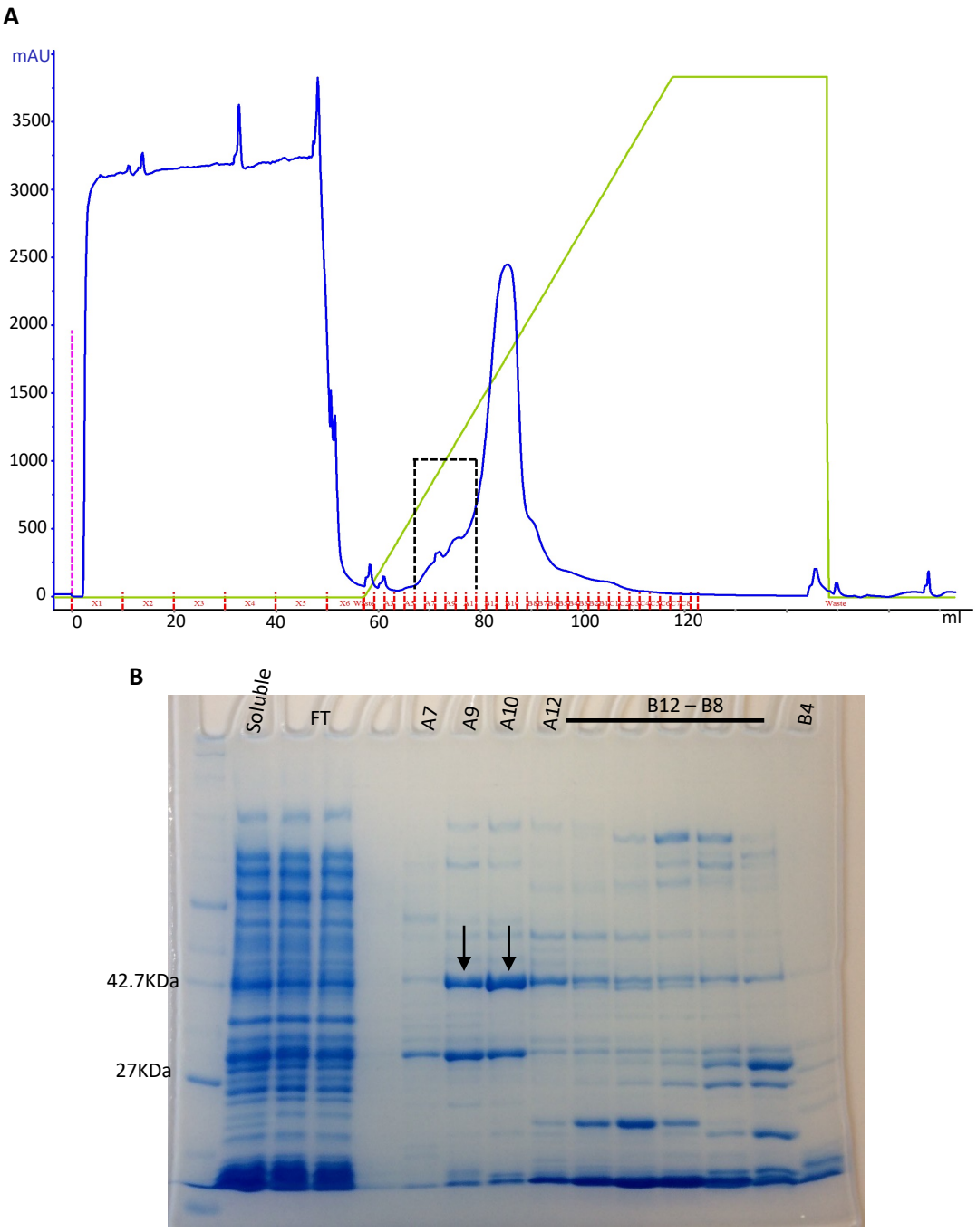

Figure 3.5. ParA1 method 2 Chromatogram and SDS-PAGE of HiTrap HPSP column chromatography.
(A) *Chromatogram of the purification run. The X axis is the measured mL, the Y axis is the % of Buffer B, peak protein elution is at 23% B. Dark blue is UV measured at 280 nm in mAU, Green is conc of B% and red is fractions. The dotted section indicates pooled fractions* ***(B)*** *10% SDS-PAGE analysis of column fractions and soluble sample from large-scale expression, FT lanes are X2 and X4 from the chromatograph, A5-B4 are the elution fractions. The black arrows indicate the contaminant.*

Fractions A6 – A11 were pooled and loaded onto the Mono Q column, using HEPES Q Buffer A and B at pH 6. Again, ParA1 eluted into the flow through (**Figure 3.6**), however, the same contamination seen in the HiTrap SPHP column eluted alongside.

The Flow through fraction X1 was concentrated to be loaded onto the Superdex 75 10/300, using HEPES Q Buffer A at pH 6 to run the method.

A peak is shown at ~10 ml (**Figure 3.7A**), the expected volume for ParA1. However, as it isn't a clean symmetrical peak, it may be 3 proteins eluting at the same point. This is confirmed in the SDS-PAGE (**Figure 3.7B**), as the fractions containing ParA1 also show an abundance of the same contaminant seen throughout this round of purification (42.7kDa), along with other little contaminants.

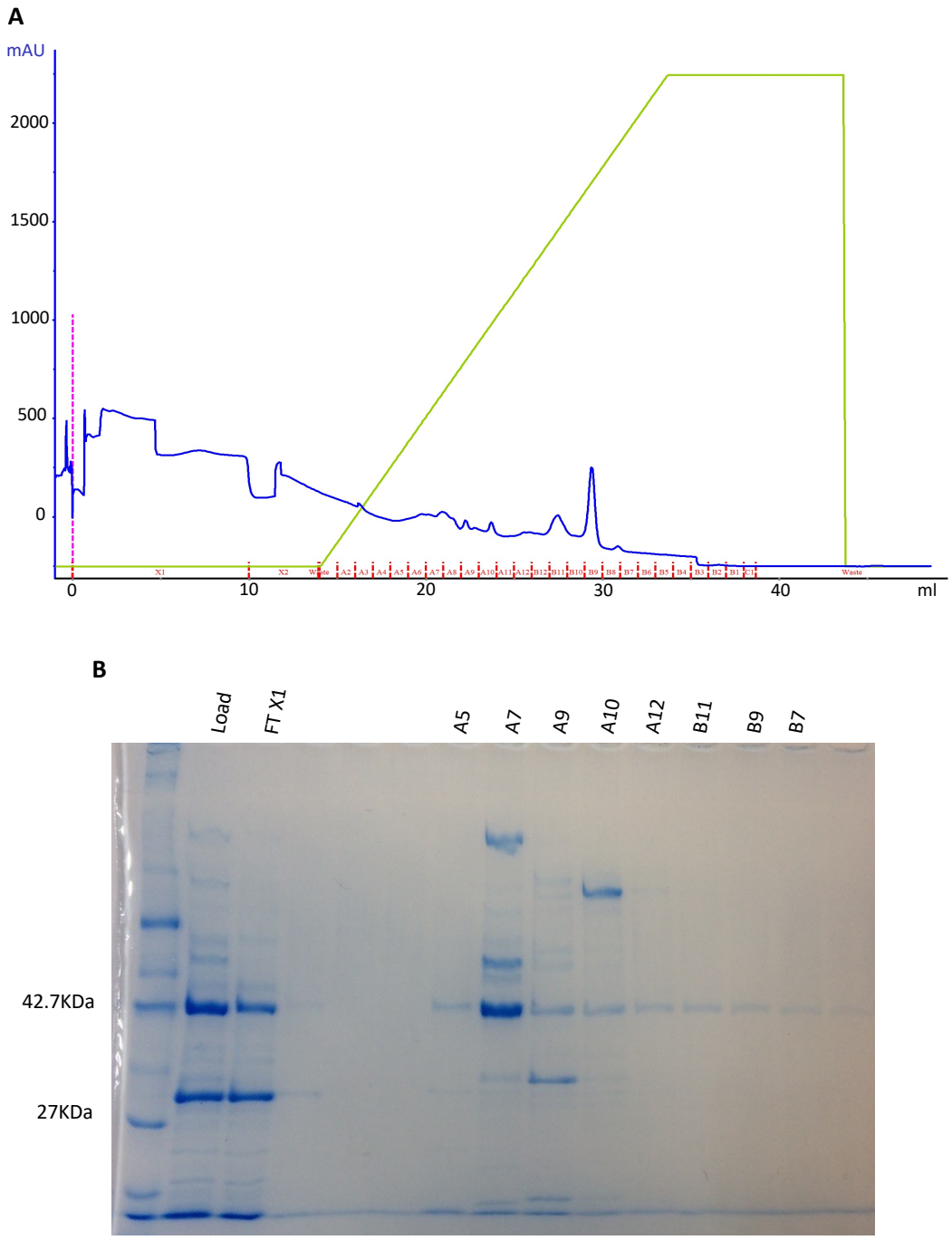

Figure 3.6. ParA1 method 2 Chromatogram and SDS-PAGE of Mono Q ion exchange column chromatography. ***(A)*** *Chromatogram of the purification run. The X axis is the measured mL, the Y axis is the UV measured at 280 nm in mAU. dark blue line is the measured UV at 280 nm, Green is conc of B% and red is fractions.* ***(B)*** *10% SDS-PAGE analysis of column fractions. The Load lane shows what was loaded onto the column, FT is the flow through. A7 is the only fraction that showed a significant amount of protein, but this is a contamination.*

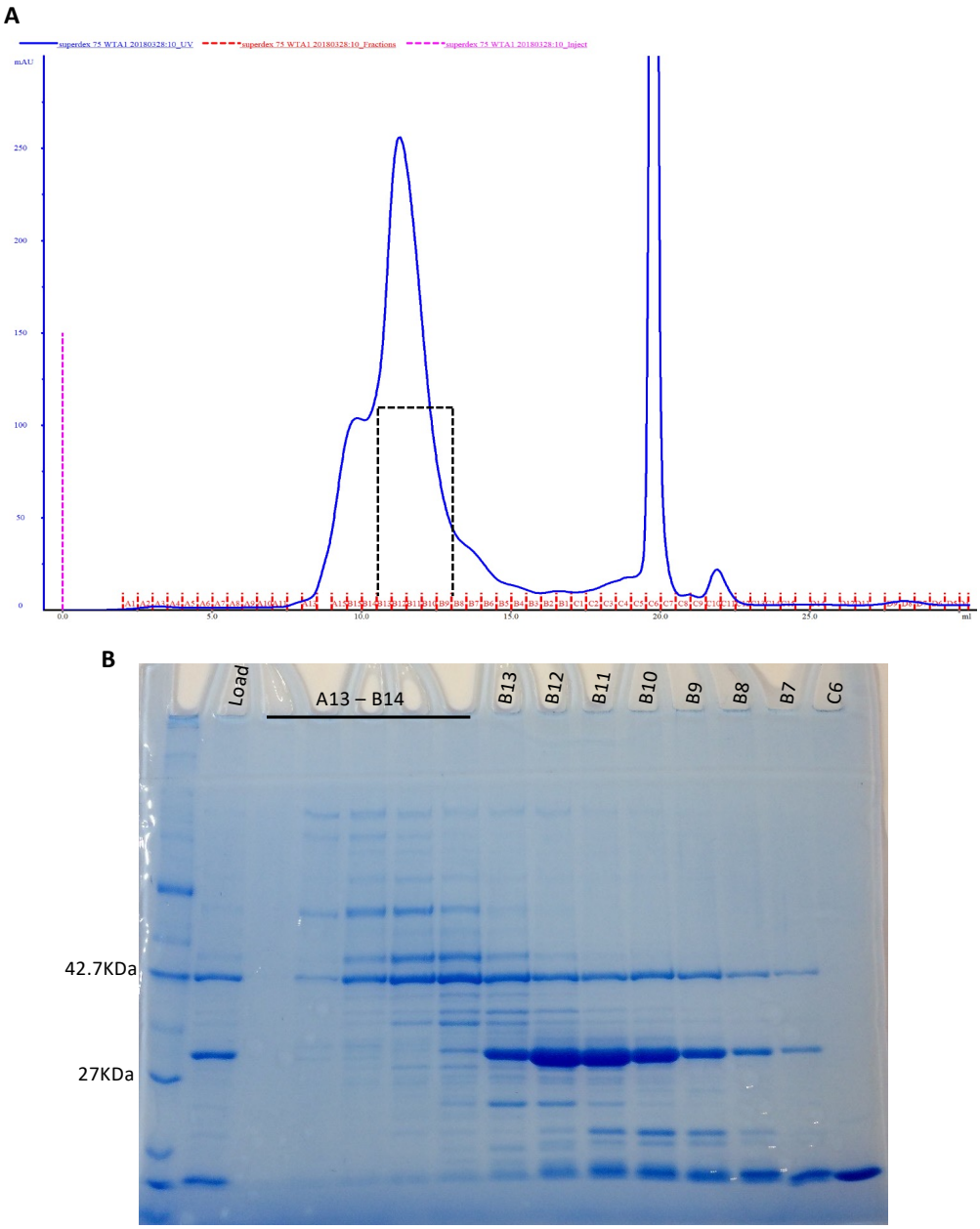

Figure 3.7. ParA1 method 2 chromatogram and SDS-PAGE of size exclusion column chromatography.
(A) *Chromatogram of the Superdex 75 10/300 purification column run, the dotted section indicates the fractions pooled (B13-B9).* ***(B)****10% SDS-PAGE analysis of elution fractions, the 'Load' lane shows what was loaded onto the column.*

Although a much higher yield of ParA1 has been obtained from this purification, the yield is not pure enough, so further steps were needed. Fractions B13 – B9 were pooled, diluted up to 5 ml with HEPES S Buffer A at pH 6 and loaded onto the HiPrep 26/10 desalting column (see **methods**) to exchange into HEPES Q Buffer A at pH 7.5. Fractions A6-A8 (**Figure 3.8A**) were pooled and concentrated to <5 ml to be loaded onto the Superdex 75 16/600 (see **Method**), using HEPES Q Buffer A at pH 7.5.

ParA1 eluted after 60 ml (**Figure 3.8B**), as expected and the column was successful in removing the contaminants. However, the final yield of ParA1 is very low, even after concentration of the pooled fractions (B8-B6).

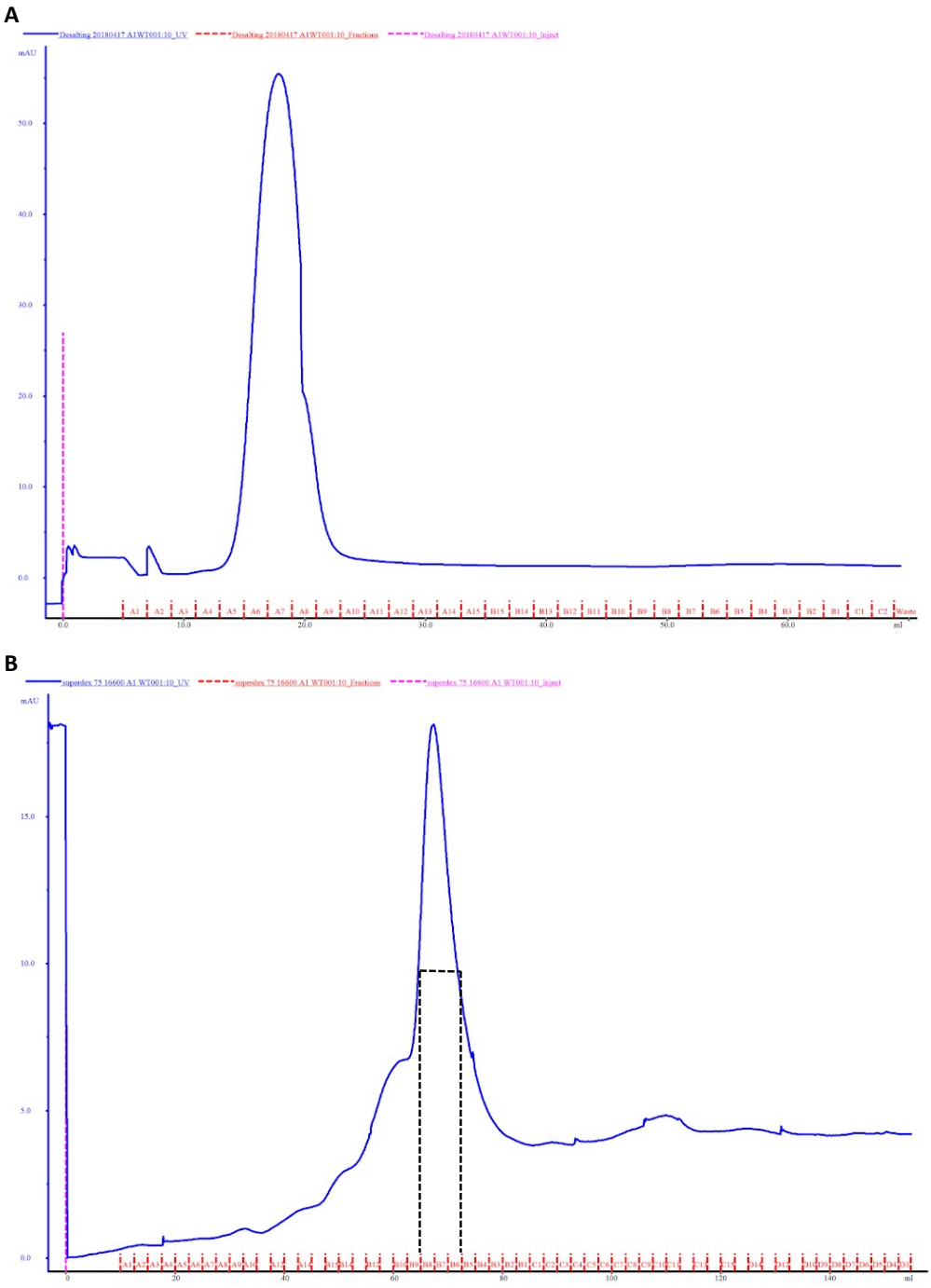

Figure 3.8. ParA1 method 2 chromatograms of desalting and size exclusion column chromatography.
(A) *desalting column ran to carry out buffer exchange. A clear peak is seen between fractions A6 and A8.* ***(B)*** *Chromatogram of the superdex 75 16/600 purification column run, the dotted section indicates the fractions pooled (B8-B6).*

3.2.3 ParA1 purification using affinity chromatography

As ParA1 is a DNA binding protein with a positively charged surface, a heparin affinity column was used instead of the previously used HPSP cation exchange column. This meant that the same Buffer could be used for all the columns and no buffer exchange is needed. A 0.5L pellet of pET28b-A1 was resuspended into Tris Sonication Buffer (pH 8) and ammonium precipitation was carried out, resuspending and dialysing overnight against Affinity Buffer A at pH 8 containing 50 mM NaCl. The dialysed sample was loaded on a 5 ml HiTrap Heparin column, using Affinity Buffer A and B at pH 8 (50 mM NaCl).

ParA1 was able to bind to the heparin column and was eluted at 235 mM NaCl (**Figure 3.9A**), fractions A6-9 were pooled and loaded onto the Mono Q column. As expected, ParA1 did not bind to the Mono Q column and was eluted into the flow through (**Figure 3.9B**). The flow through was therefore concentrated before loading onto a Superdex 75 16/600 for size exclusion chromatography, using Affinity Buffer A (pH8 50 mM NaCl).

Again, ParA1 eluted after 60 ml (**Figure 3.9C**), however, a contaminant only slightly smaller than ParA1 has not been separated, which could potentially be a degradation product. Fractions D2-E2 were pooled for concentration and exchange into Tris Storage Buffer, as they contained the most ParA1 compared to the contaminant. Although a better yield of ParA1 has been obtained than previously, the concentration is still too low for enzymatic assays (300µl of 12.6µM) with the amount of the contaminant being too high.

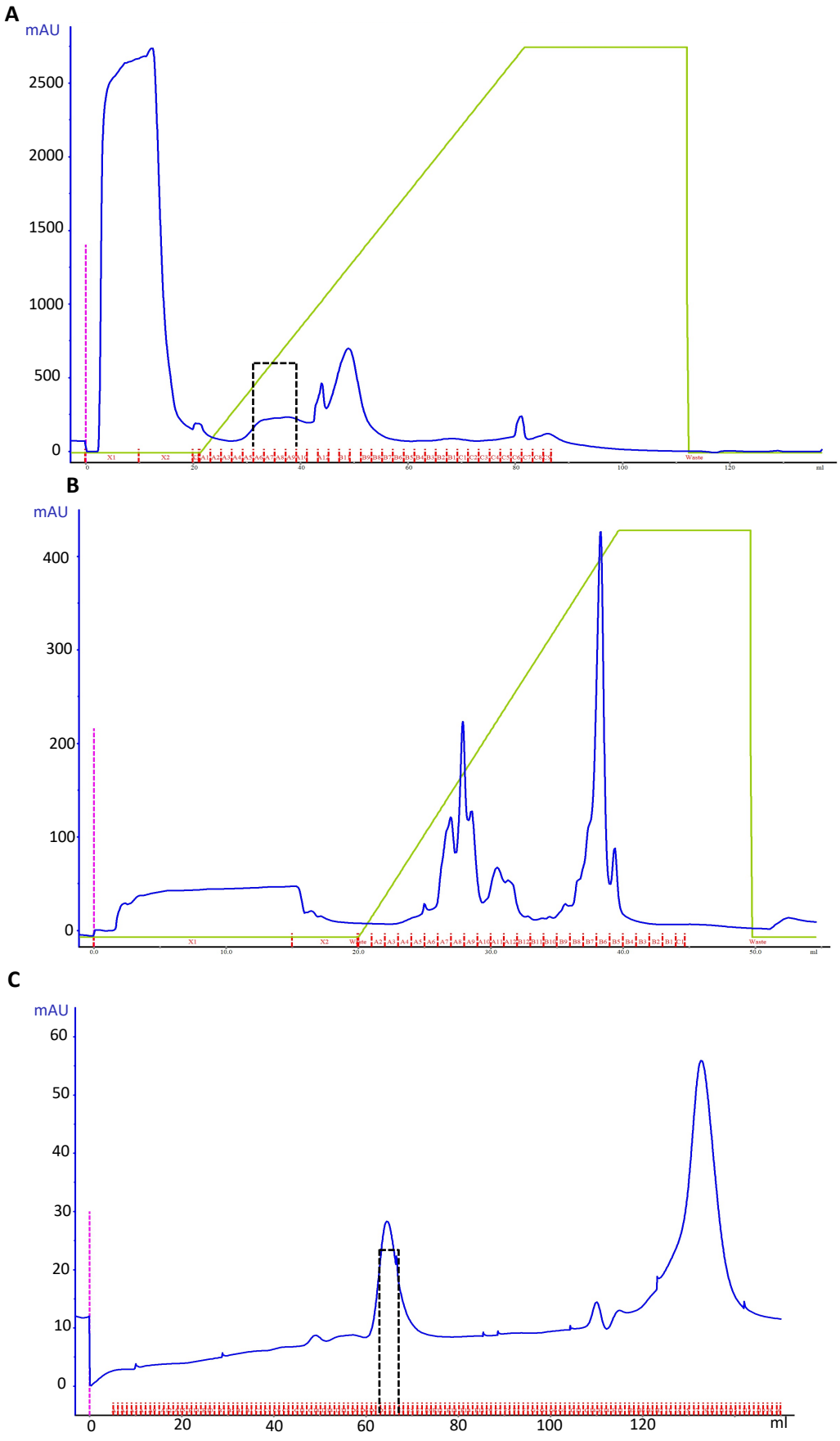

Figure 3.9. Chromatograms of ParA1 method 3 column chromatography.

The dark blue line is the measured UV at 280 nm, the green line represents the percentage of buffer B and the fractions are shown in red. ***(A)*** *Chromatogram of the 5 ml HiTrap heparin column chromatography, X1-X3 are the sample loading and column wash steps, fractions A1-B2 are the fractions collected in a serpentine fashion from elution. The dotted section indicates the fractions pooled.* ***(B)*** *Chromatogram of the Mono Q ion exchange column chromatography run, the purification steps are the same as in A.* ***(C)*** *Chromatogram of the Superdex 75 16/600 size exclusion column chromatography run. 1 ml fractions are collected with the dotted line indicating the fractions pooled (D2-E2).*

Each step of purification was successful in cleaning up the protein sample (**Figure 3.10**), from this concluding SDS-PAGE gel shows that ParA1 again has not been induced to a high extent. This could also be why the yield was too low for biochemical applications.

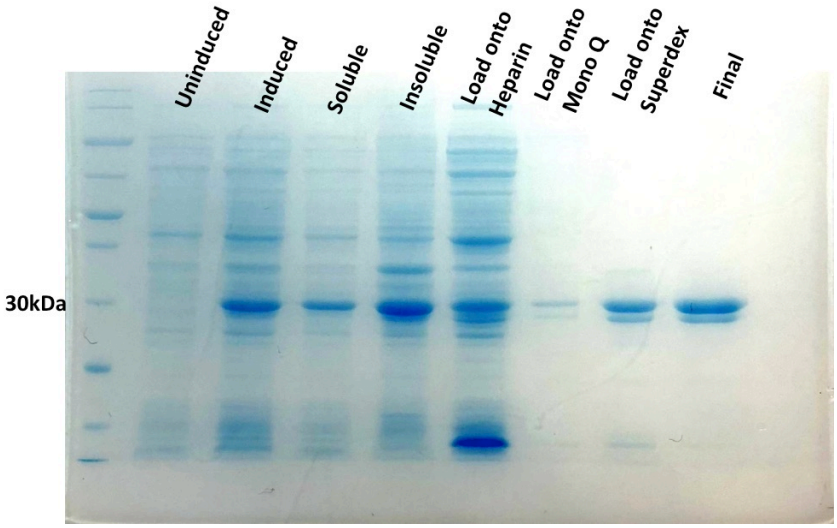

Figure 3.10. Concluding SDS-PAGE of ParA1 protein purification method 3.
12% SDS-PAGE gel with a PageRuler Broad Range Unstained Protein Ladder, the uninduced, Induced, soluble and insoluble samples were taken during large-scale expression.

3.2.4 Purification at pH 7.5

It seemed to be that different contaminants elute with ParA1 at different pH values, therefore a pH needed to be selected that where there the contaminating protein has the largest difference of molecular weight to ParA1, which could be separated using the size exclusion column. From previous purification runs, pH 7.5 led to the contaminant that would be easiest to separate, so therefore the next purification protocol ran was carried out at this pH.

A 1.5L pellet of ParA1 overexpressed in BL21 *E. coli* was resuspended into Tris Sonication Buffer (pH 7.5) and ammonium precipitation was carried out,

resuspending, and dialysing overnight against Affinity Buffer A (25 mM NaCl pH7.5). ParA1 eluted from the Heparin column between 235-415 mM NaCl , fractions A7-A12 (**Figure 3.11**) were pooled, concentrated and exchanged back into Buffer A (low salt) to be ran on the Mono Q.

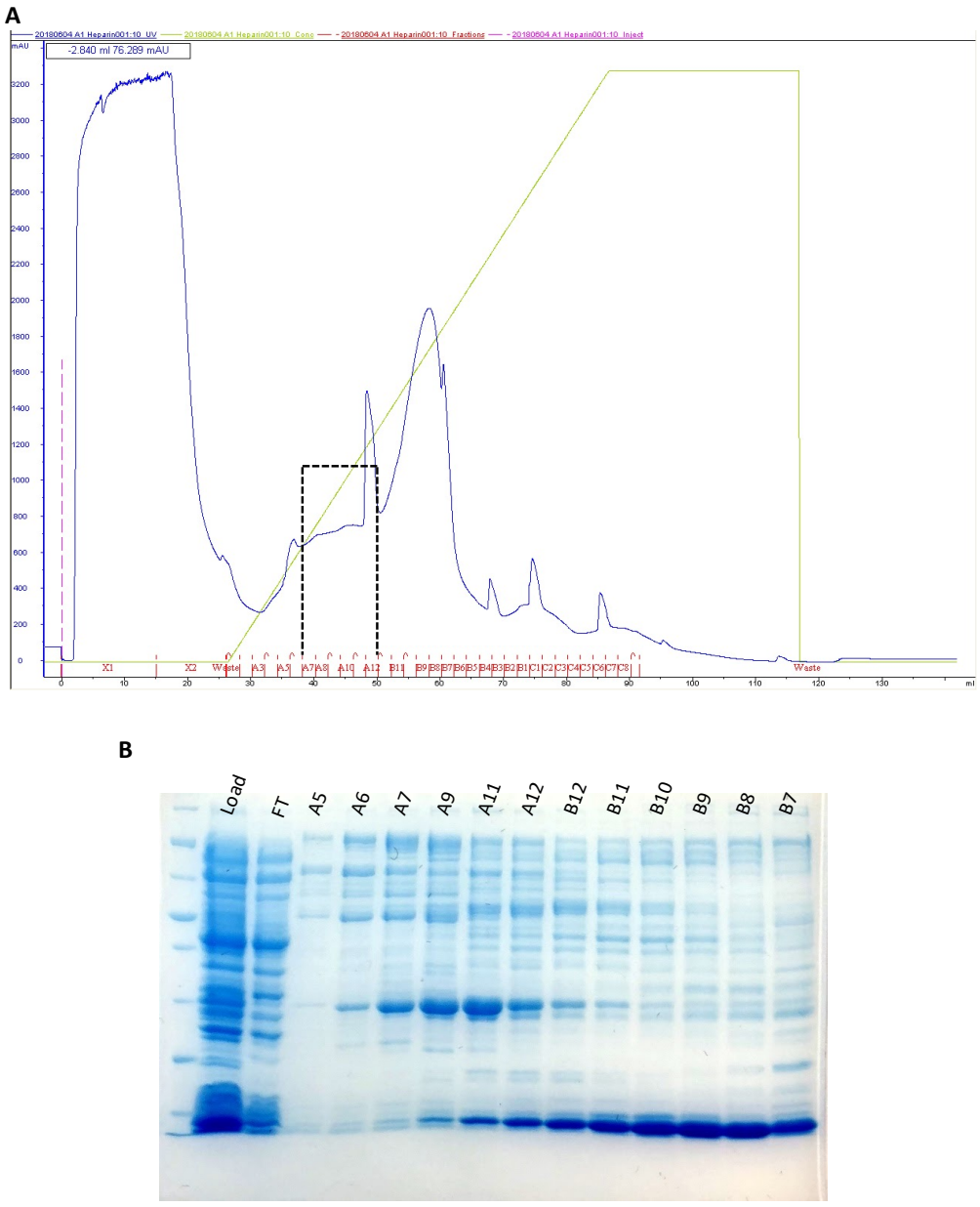

Figure 3.11. ParA1 method 4 chromatogram and SDS-PAGE of HiTrap heparin column chromatography. ***(A)*** *Chromatogram of the purification run, the X axis is the measured mL, the Y axis is the UV measured at 280 nm in mAU, correlating to the dark blue line. The light blue line shows the conductivity %, the green is the percentage of buffer B ranging from 0-100%, and in red is fractions. The dotted section indicates the fractions pooled.* ***(B)*** *12% SDS-PAGE analysis of column fractions FT lanes are X1 and X2 from the chromatograph, the load lane showing the sample loaded onto the column.*

Despite lowering the salt concentration even more than the previous methods during buffer exchange, ParA1 still did not bind to the column and was seen to elute into the

flow through fraction (**Figure 3.12**). Furtherly, during concentration of the flow through, precipitation was observed, potentially due to the low salt concentration in the buffer (25 mM NaCl). However, since ParA1 was seen to elute from the Superdex 75 16/600 at the expected volume of 60 ml, it was suggested that only a small amount of ParA1 may have been lost during precipitation, with a contaminant being the bulk of the precipitation (**Figure 3.13**).

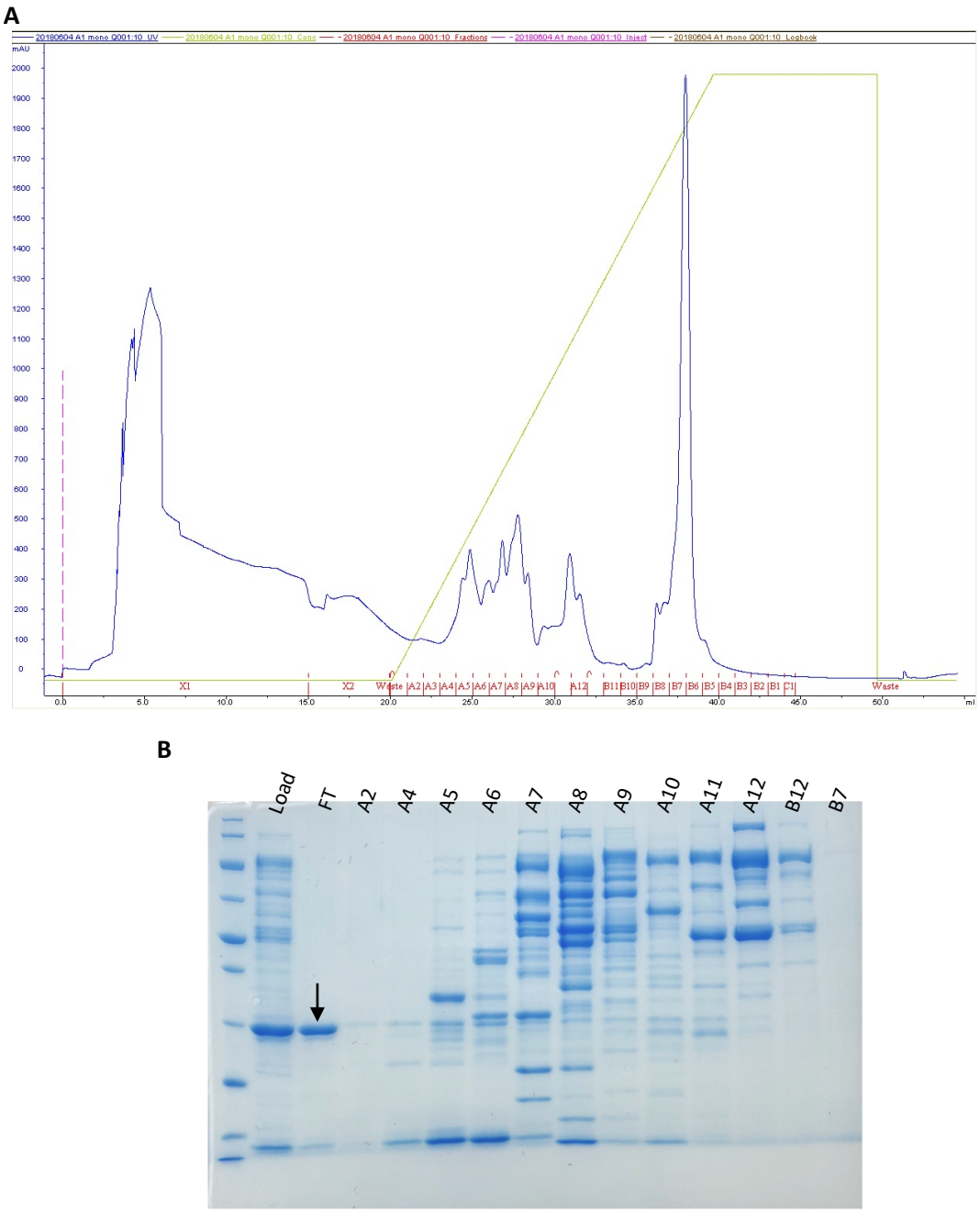

Figure 3.12. ParA1 method 4 chromatogram and SDS-PAGE of Mono Q ion exchange column chromatography. ***(A)*** *Chromatogram of the purification run, the X axis is the measured mL, the Y axis is the UV measured at 280 nm in mAU, correlating to the dark blue line. The conductivity %, the green is the percentage of buffer B ranging from*

0-100%, and in red is fractions. ***(B)*** *12% SDS-PAGE analysis of column fractions FT lanes are X1 from the chromatogram, the load lane showing the sample loaded onto the column. The black arrow indicates ParA1.*

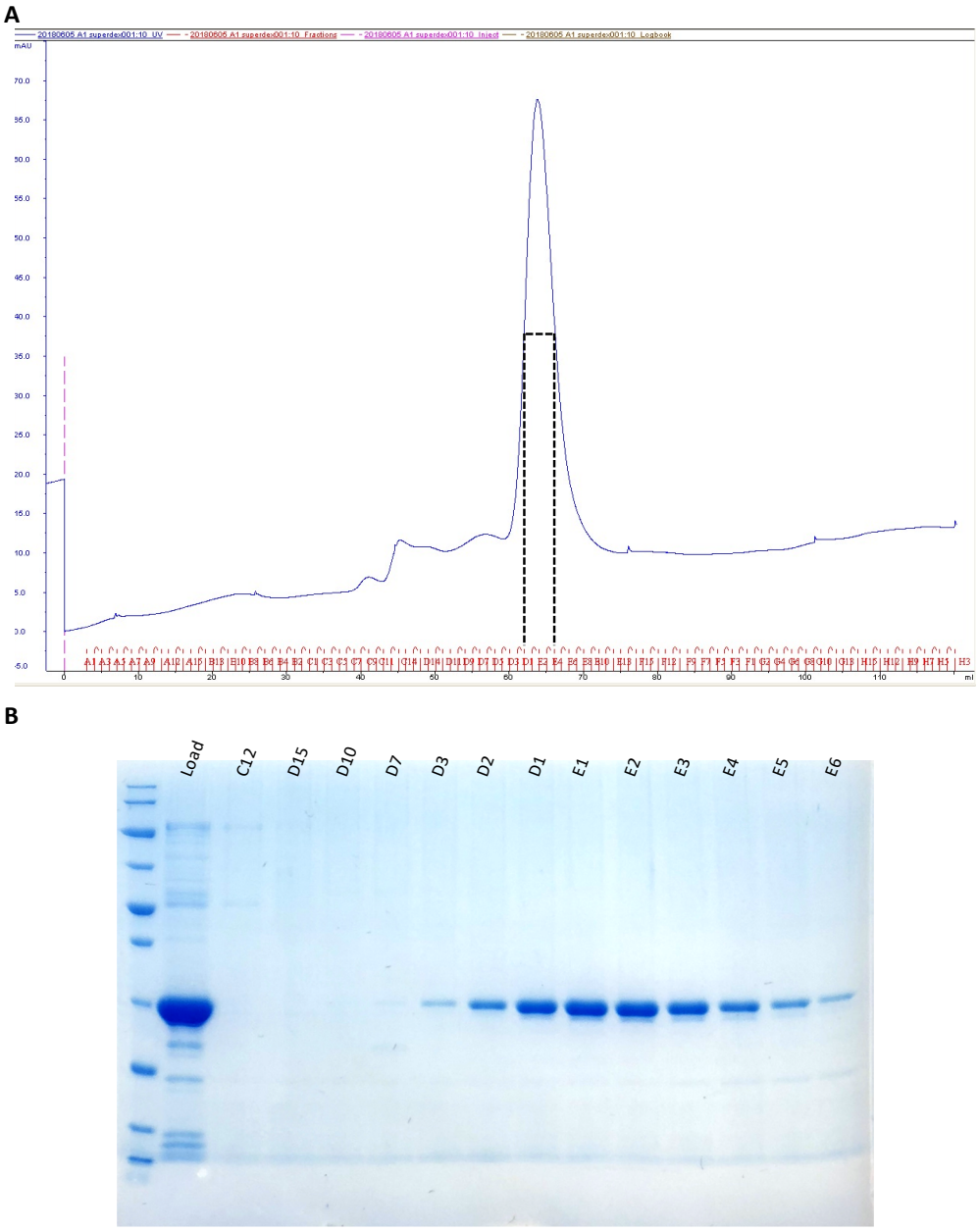

Figure 3.13. ParA1 method 4 chromatogram and SDS-PAGE of Superdex 75 16/600 column chromatography*.* ***(A)*** *Chromatogram of the purification run, the X axis is the measured mL, the Y axis is the UV measured at 280 nm in mAU, correlating to the dark blue line and in red is fractions with the dotted section indicating the fractions pooled.* ***(B)*** *12% SDS-PAGE analysis of column fractions, the load lane showing the sample loaded onto the column, the labelled fractions correspond to the dotted section in A.*

Fractions D1-E3 were concentrated and exchanged into Tris Storage Buffer and when ran on the concluding SDS-PAGE analysis, a much better amount of protein has been obtained (**Figure 3.14**), the final concentration of protein being 85µM (450µl). However, the purity is still not suitable for biochemical studies, with the contaminant that is slightly smaller than ParA1 seen again along with a lot of smaller proteins.

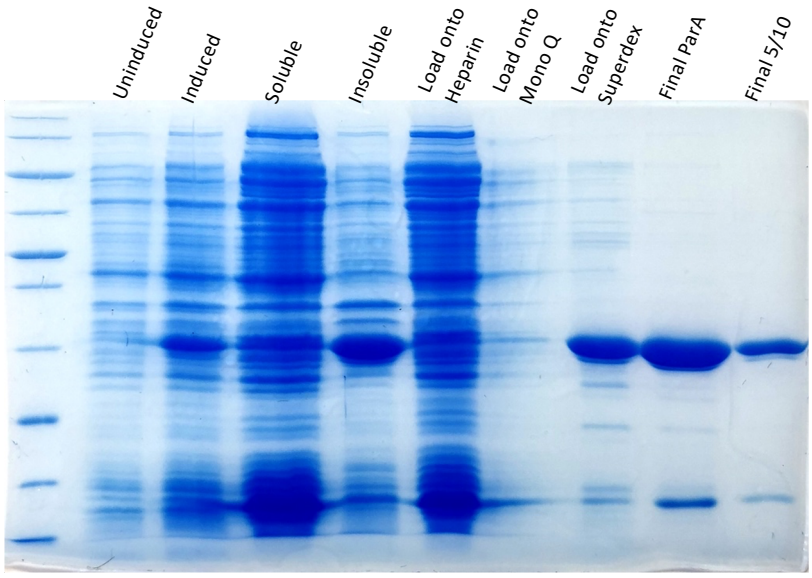

Figure 3.14. Concluding SDS-PAGE of ParA1 protein purification method 4.
12% SDS-PAGE gel with a PageRuler Broad Range Unstained Protein Ladder, the uninduced, Induced, soluble and insoluble samples were taken during large-scale expression.

From these 4 rounds of purification, ParA1 was seen to bind to the Sepharose anion exchange column better than the heparin affinity column, with the contaminant at a similar size to ParA1 not being present when the ion exchange column was used.

3.3 Purification of tagged ParA1

3.3.1 ParA1-GFP-His

Unlike a plasmid encoding for WT ParA1, GFP tagged ParA1 can be transformed and overexpressed with a His tag on the C-terminal of the GFP. Purification therefore follows the same steps as in 3.2.4 but using a Nickle affinity column instead (**Method**). From the HisTrap column, ParA1-GFP eluted at ~350 mM imidazole, fractions A7-A10 were pooled for loading onto the ion exchange column (**Figure 3.15A**). Before loading onto the Mono Q anion exchange column, the pooled fractions were exchanged into MonoQ buffer A to reduce the concentration of imidazole and NaCl in the sample loaded.

However, ParA1-GFP looked to have eluted into the flow through, obvious since it was luminous green. A large amount of protein is seen to elute into fraction A7 however this looks too large to be ParA1-GFP (**Figure 3.15B**), similarly to fraction A10 where a less heavy band is seen but this is slightly too small. Since A7 and A10 didn't look green at all, the flow through was concentrated to 1 ml.

The 1 ml sample was loaded onto the Superdex 200pg 16/600 gel filtration column where ParA1-GFP was seen to elute after 70 ml. However, the fractions from this column were deemed to be too contaminated for the protein to be used in enzymatic assays so the resulting fractions were not pooled and concentrated (**Figure 3.15C**). All chromatograms can be viewed in **appendix Figure 8.1**.

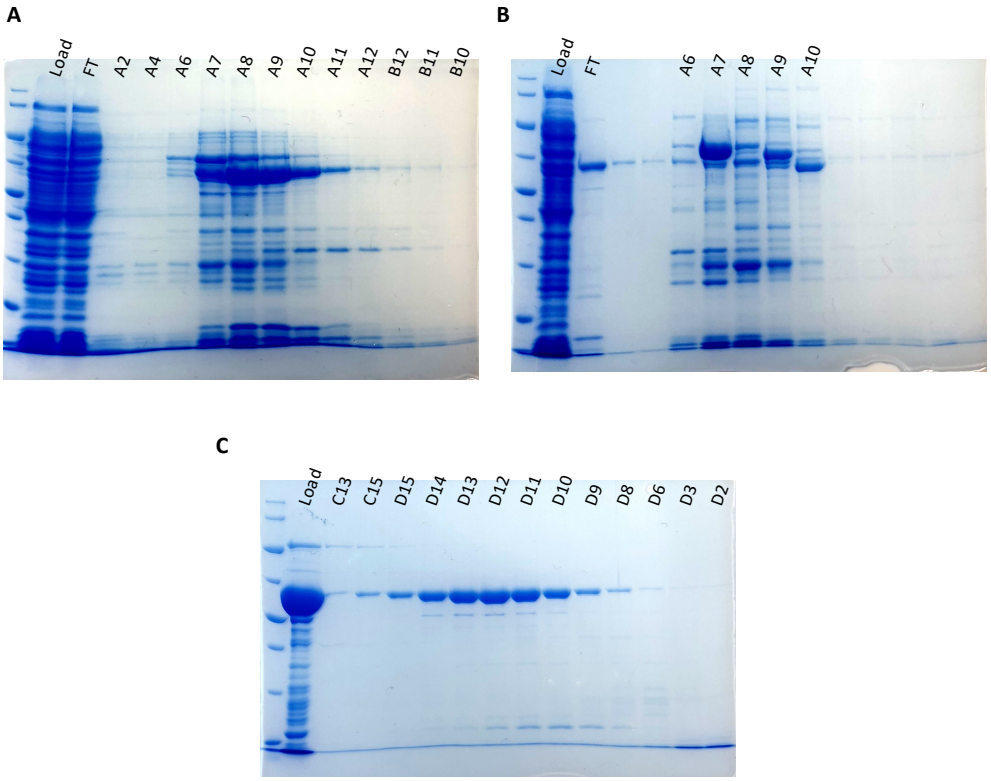

Figure 3.15. SDS-PAGE of ParA1-GFP-His protein purification.
(A) *HisTrap nickel column chromatography gel, FT refers to the flow through fraction, the Load lane shows the sample that was loaded onto the column.* ***(B)*** *Mono Q ion exchange column chromatography gel, the Load lane indiciates to the sample loaded onto the column, the FT fraction is the flow through.* ***(C)*** *Superdex 16/600 gel filtration column chromatography gel, the load fraction indicates the sample that was loaded onto the column.*

3.4 Insights into ParA1 purification

Despite optimising ParA1 purification to an acceptable standard for structural biology, the protocol could be improved further. The next steps I would take to improve purification further would be to try a variety of protein affinity tags, such as a Glutathione S-transferase (GST) tag or a SUMO tag, which may also help increase expression levels which are normally low. The advantages of this step could mean that an affinity purification step could be used and replace the ion exchange column whereby a lot of protein is normally lost. The chosen tag could then be cleaved after purification since ParA1 is small (27kDa) and such a large tag could affect the protein's actions and interactions. Similarly, since ParA1 was able to be purified with a C-terminal GFP and His tag, this purified sample could then undergo tag cleavage to result in pure WT protein.

3.5 Purification of ParA2

3.5.1 Nucleotide binding and/or hydrolysis mutants

Prior to this work, a protocol was already established for WT ParA2 purification, carried out by purification technician. Based on ParA2's properties (size, pI and DNA binding ability), a protocol was designed to purify 3 mutant ParA2 proteins: K124R, K124Q and K124E. All 3 mutants followed the same protocol and behaved the same, eluting at the same points during each step. Because of this, I have chosen to show only one chromatograph for each step as a representative of all 3 proteins (K124E) (all can be seen in the appendix). The only difference between each purification being the size of the fractions collected from the Superdex 200 16/600.

Like with ParA1, K124R/Q/E-ParA2 1L pellets underwent sonication to lyse the cells and ammonium precipitation to precipitate out nucleotide binding proteins, in Tris Sonication Buffer at pH 8 due to the pI of 5.45. The dialysed samples were loaded onto the HiTrap Heparin affinity column, since ParA2 is a DNA binding protein with a positively charged surface. All 3 eluted against Affinity Buffer B at ~325 mM NaCl (**Figure 3.16, appendix Figure 8.2**), fractions A8-A12 were therefore pooled to be loaded onto the Mono Q column to be ran with the same buffers (Affinity Buffer A and B pH 8).

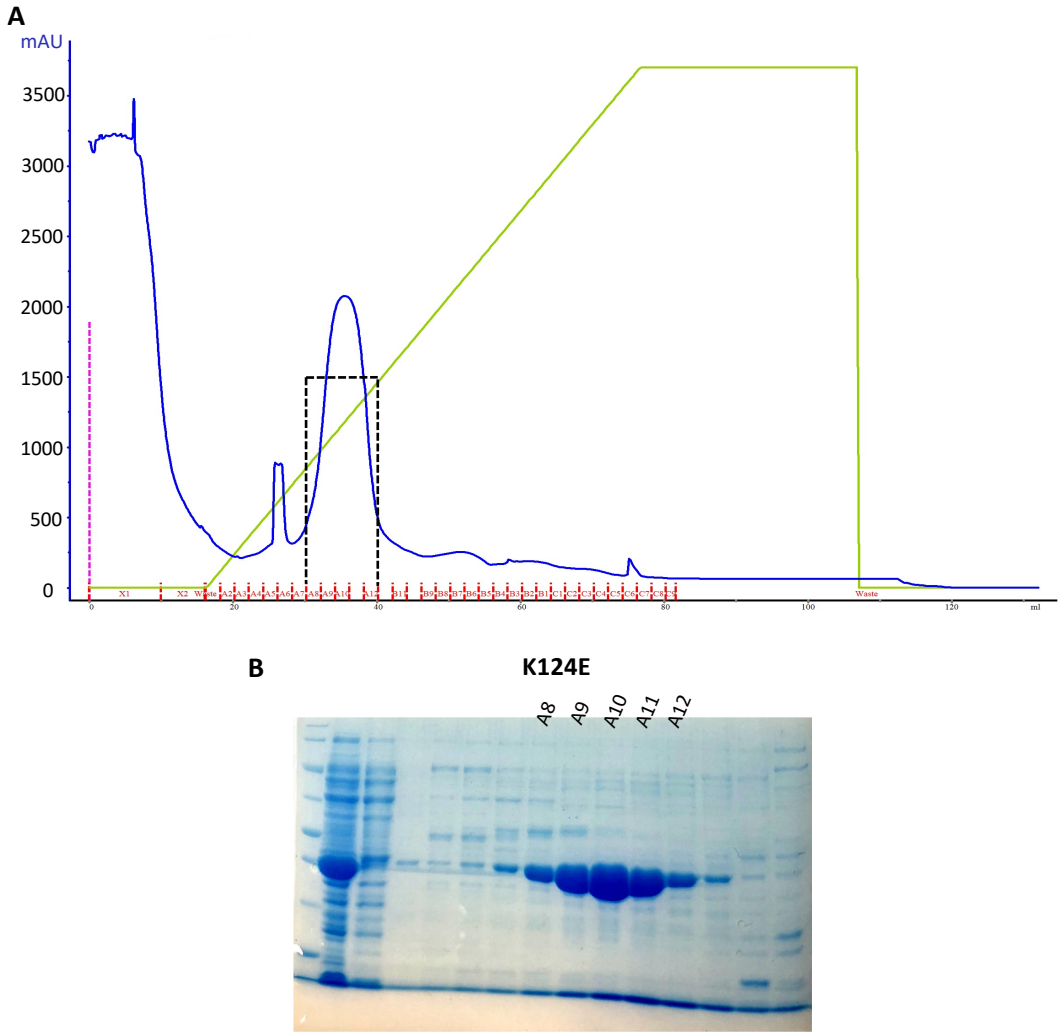

Figure 3.16. Representative chromatogram and SDS-PAGE of heparin column chromatography of ParA2$^{K124R/E/Q}$. ***(A)*** *A representative chromatogram of the purification run, the X axis is the measured mL, the Y axis is the UV measured at 280 nm in mAU, correlating to the dark blue line, the green is the percentage of buffer B ranging from 0-100%. The fractions are shown in red with the dotted section indicating the fractions pooled.* ***(B)*** *12% SDS-PAGE analysis of column fractions, the load lane showing the sample loaded onto the column, with the lane immediately to the left being the FT fraction X1.*

ParA2's surface is more positively charged than ParA1 having a pI of ~5.8, therefore the mutants bound to the Mono Q anion exchange column really well at pH8, all eluting at 300-450 mM NaCl (**Figure 3.17, appendix Figure 8.3**). Fractions A6-A8 were pooled for concentration, even though A9 contained a lot of protein it also contained more contamination, so it wasn't pooled.

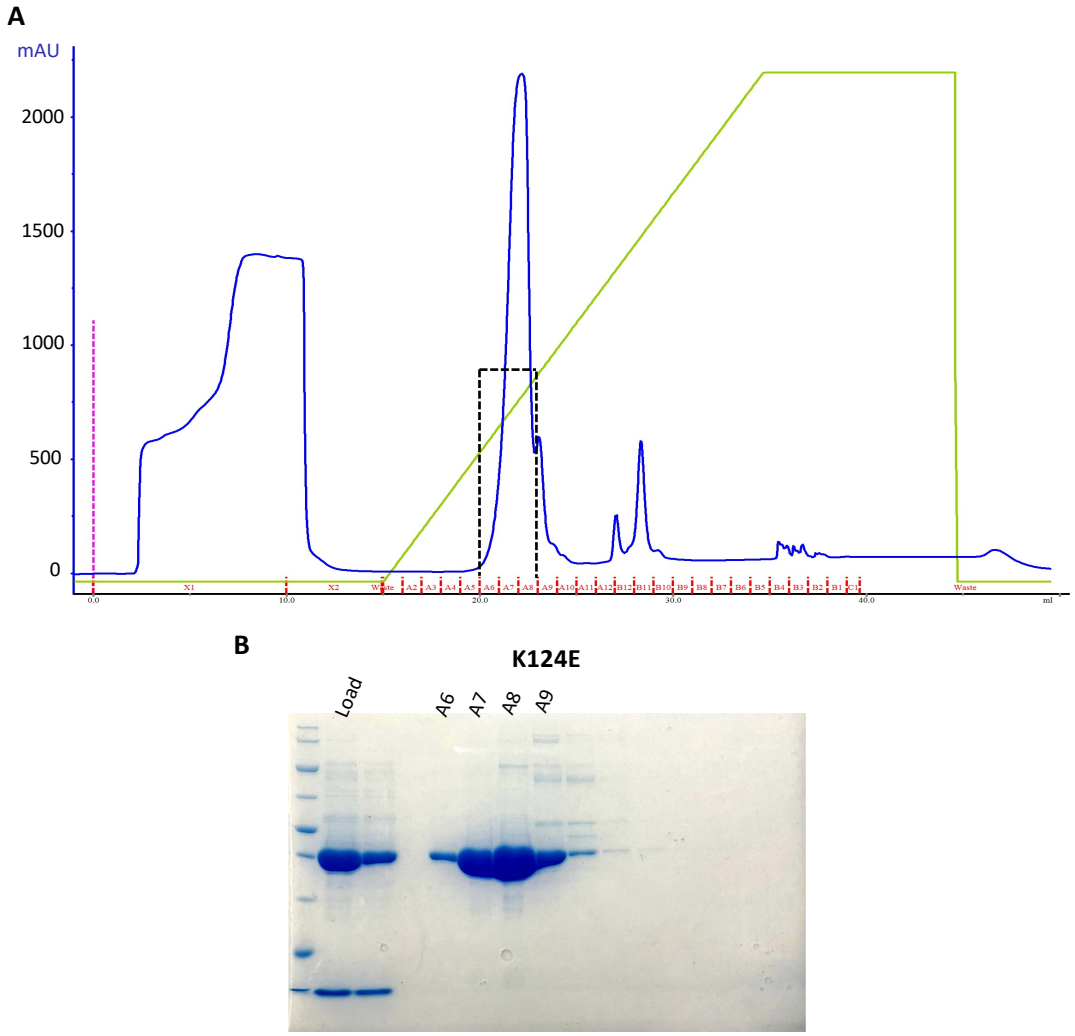

Figure 3.17. Representative chromatogram and SDS-PAGE of Mono Q ion exchange column chromatography of ParA2$^{K124R/E/Q}$.

(A) *A representative chromatogram of the purification run, the X axis is the measured mL, the Y axis is the UV measured at 280 nm in mAU, correlating to the dark blue line, the green is the percentage of buffer B ranging from 0-100%. The fractions are shown in red with the dotted section indicating the fractions pooled.* ***(B)*** *12% SDS-PAGE analysis of column fractions, the load lane showing the sample loaded onto the column, with the lane immediately to the left being the FT fraction X1.*

Once the samples were <2 ml they were loaded onto the Superdex 200 16/600 and ran with Tris Buffer A (pH 8). As expected, the ParA2 mutants eluted at ~65 ml, suggesting that the proteins elute as dimers (~92kDa) (**Figure 3.18, appendix Figure 8.4**). For K124R fractions B7-B4 were pooled for concentrating and exchanged into Tris Storage Buffer, for K124Q and K124E, fractions E5-E11 and B1-C3, respectively, were pooled and concentrated.

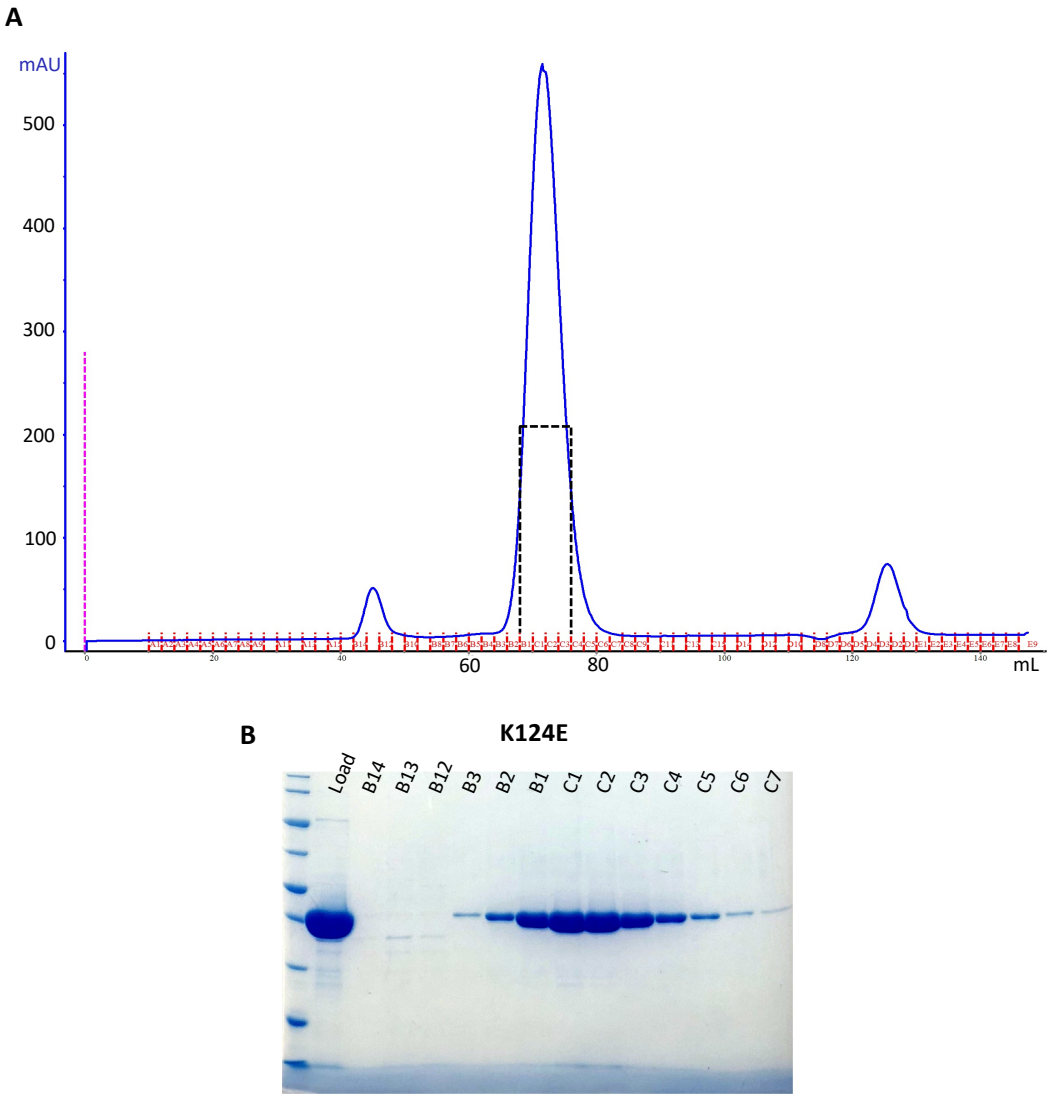

Figure 3.18. Representative chromatogram and SDS-PAGE of size exclusion column chromatography of ParA2$^{K124R/E/Q}$.

(A) *A representative chromatogram of the purification run on the Superdex 200pg 16/600 , the X axis is the measured mL, the Y axis is the UV measured at 280 nm in mAU, correlating to the dark blue line, the fractions are shown in red, those that were pooled are shown as the dotted section.* ***(B)*** *12% SDS-PAGE analysis of column fractions, the load lane showing the sample loaded onto the column.*

A concluding SDS-PAGE was ran showing each step of purification for each mutant (**Figure 3.19**) with the final concentrations being 76µM, 63µM and 213µM for K124R, K124Q and K124E, respectively. Due to the success of this protocol in purifying these modified ParAs, it became the standard method for WT ParA2 purification.

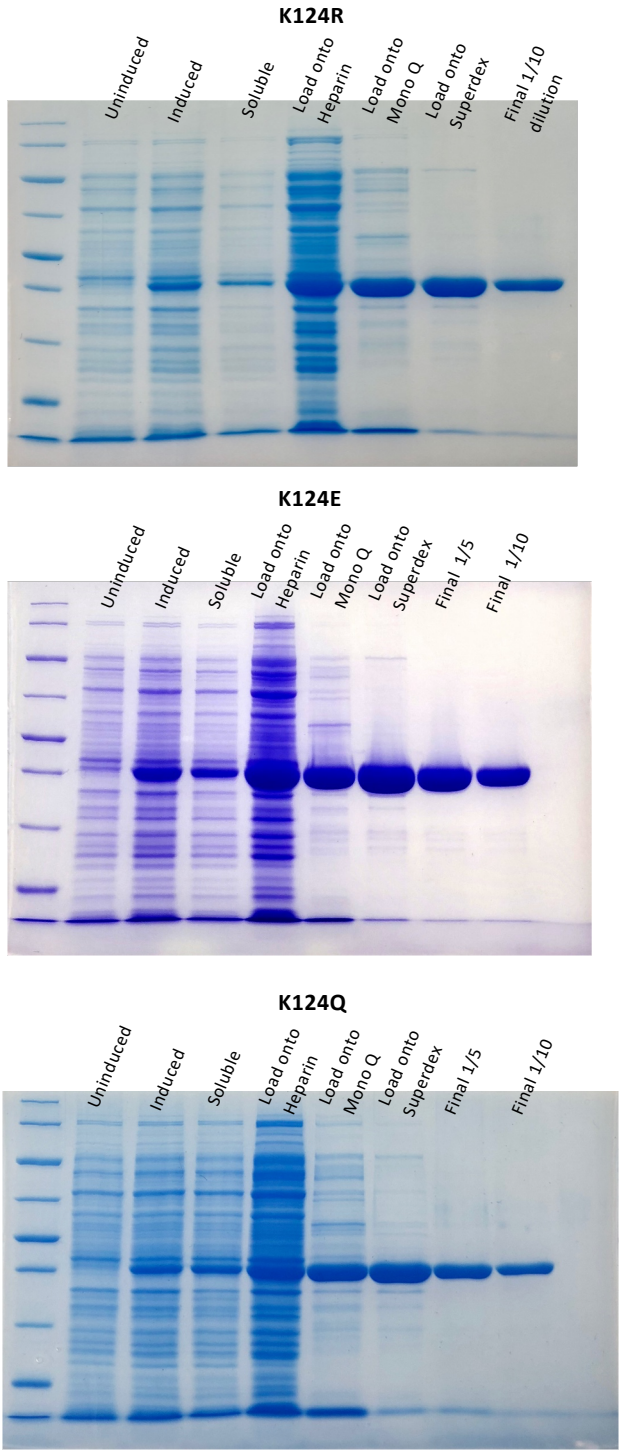

Figure 3.19. Concluding SDS-PAGE of ParA2$^{K124R/E/Q}$ protein purification.
12% SDS-PAGE gel with a PageRuler Broad Range Unstained Protein Ladder, the uninduced, Induced, soluble and insoluble samples were taken during large-scale expression for each mutant.

3.5.2 Non-conserved residue mutants

Multiple mutant constructs were prepared via Quick Change mutagenesis (**Method 2.6**) based on the results seen in chapter 6 (**6.4.2**). These included an N-terminal helix deletion (Δ4-35), an N-terminal HTH domain deletion (Δ4-106), and finally 3 separate

C-terminal polar residues (K388, L391, R395) to alanine along with a triple mutation to alanine of all 3. However, due to limited time only a subset was over-expressed and purified.

3.5.2.1 ParA2-Δ4-35

pET28b-ParA2-Δ4-35, lacking the N-terminal helix (helix 1) is slightly smaller than WT, at a predicted molecular weight of 42.5kDa (46kDa for wild-type), with the deletion causing minimal change to the theoretical pI at 5.49 (5.45 for wild-type). Following the same protocol as the previous ParA2 mutants, the soluble protein lysate obtained after dialysis (**Figure 3.20**) is loaded onto a Heparin HiTrap column. Eluting at ~400 mM NaCl into fractions A10 to B2, which were pooled, of which fractions A10 and 11 can be seen in **Appendix Figure 8.5-6**

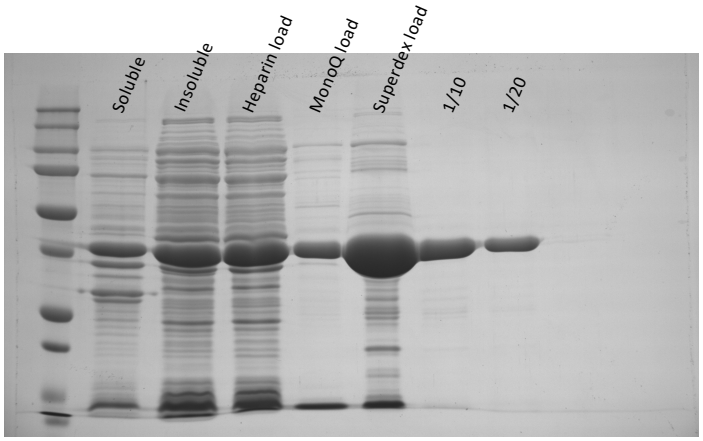

Figure 3.20. Concluding SDS-PAGE of Mutant 4 ParA2Δ4-35 protein purification.
12% SDS-PAGE gel with a PageRuler Broad Range Unstained Protein Ladder, the soluble and insoluble fraction were taken during cell lysis. The load lanes for each column shows the sample that was loaded onto that column, the 1/10 and 1/20 are the dilutions of the concentrated final protein sample.

The pooled fractions were concentrated and re-diluted into a low salt buffer (**Methods**) prior to loading onto the 1 ml Mono Q (**Figure 3.19**) to make sure they would adequately bind to the column. Eluting at ~420 mM NaCl, fractions A7- A9 were pooled, concentrated to 1 ml and loaded onto the Superdex 16/600 200pg (**Figure 3.19**) and were subsequently eluted at ~80 ml into fractions G10-H4 which were pooled concentrated to 16 mg/ml before flash freezing in Liquid nitrogen (**Figure 3.19**).

3.5.2.2 *ParA2Δ-4-106*

pET28b-ParA2-Δ4-106, a deletion mutant missing the N-terminal winged HTH domain was successfully overexpressed in BL21 (DE3)(**Appendix Figure 8.7**). After pellet lysis and ammonium precipitation, the sample was loaded onto the Heparin column, however no clear band is seen from the elution, apart from a small amount in the flow through (**appendix Figure 8.7**). The flow through was then loaded onto the Mono Q, of which there was again no clear band for the protein. However, from SDS-PAGE analysis, only a very faint band is seen at the expected weight (34.4kDa) in the lanes for the load onto the column and the flow through (**appendix Figure 8. 7**). In the overall gel ran with a lane for each step of the purification process, a large band at the expected weight (34.4kDa) is seen in the insoluble fraction, taken from the pellet after cell lysis (**Figure 3.21)**.

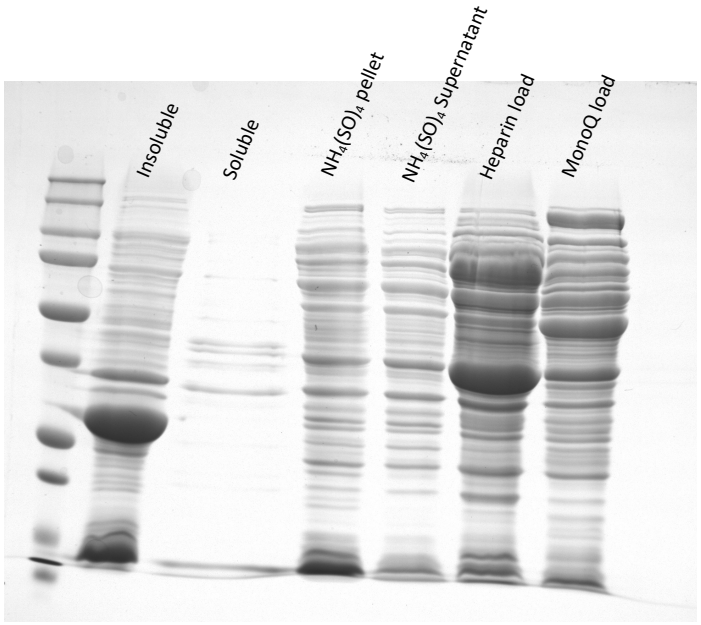

Figure 3.21. SDS-PAGE of ParA2-Δ4-106 protein purification.
The concluding SDS-PAGE of all the steps taken during protein purification, the soluble and insoluble fraction were taken during cell lysis.

3.5.2.3 *ParA2-K388A*

pET28b-ParA2-K388A was successfully overexpressed in BL21 (DE3). After pellet lysis and ammonium precipitation the sample was loaded and eluted from a heparin HiTrap column. However, the protein was shown to have eluted into the flow

through and the wash steps (**Appendix Figure 8.8)**, these fractions were consequently pooled and concentrated briefly before loading onto the MonoQ. From this column a significant amount of protein eluted into the flow through and the wash, however, a considerable amount also bound and eluted in early fractions (A4-8) at ~300 mM NaCl, which were then pooled and concentrated for loading on the gel filtration column. ParA2-K388A eluted at ~75 ml into fractions G4-G8 (**Figure 3.22A**) therefore fractions G4-G9 were pooled.

Due to the large amount of protein seen to elute into the flow through of the Mono Q, the flow through was then taken and re-run on the Mono Q. Although again a large amount eluted into the flow through, fractions A5-A8 (~300 mM NaCl) also contained an acceptable amount (**Appendix Figure 8.8**) so these fractions were selected and pooled to be concentrated and loaded onto the superdex. The protein eluted across fractions G2 to G9 (**Figure 3.22B**) at ~75 ml (**Appendix Figure 8.9**), from which fractions G3-7 were pooled and added to G4-9 from the first gel filtration column. The pooled fractions were concentrated to 10 mg/ml and frozen in liquid nitrogen.

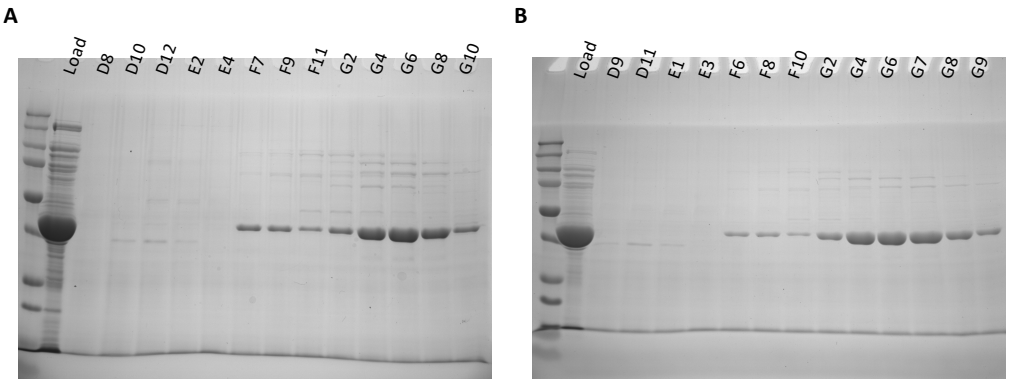

Figure 3.22. SDS-PAGE of mutant 6 ParA2^{K388A} size exclusion chromatography.
(A) *Superdex 16/600 gel filtration column run 1, the load fraction indicates the sample that was loaded onto the column.* ***(B)*** *Superdex 16/600 gel filtration column run 2, the load fraction indicates the sample that was loaded onto the column.*

3.5.2.4 ParA2-K388A_L391A_R395A

pET28b-ParA2-K388A_L391A_R295A was successfully overexpressed in BL21 (DE3). The protein was seen to completely insolubilize during the ammonium precipitation step (**Figure 3.23**), and following resuspension of the pellet and overnight dialysis, the sample was loaded and eluted from a heparin HiTrap column. However, the protein eluted into the flow through fractions ,suggesting the mutations applied have affected ParA2's ability to adequately bind to DNA through disrupting the surface charge. These fractions were pooled and loaded onto the Mono Q anion exchange column, from which the protein was seen to elute at ~460 mM NaCl, into fractions D6-8 , which were pooled, concentrated and loaded onto the gel filtration column. The protein was seen to elute into fractions C9-D3, at ~ 75 ml, which were pooled and concentrated to 14 mg/ml. Each step of purification is shown in **Figure 3.23**, chromatograms and SDS-PAGE analysis can be seen in appendix Figures 8.10-11 for each step.

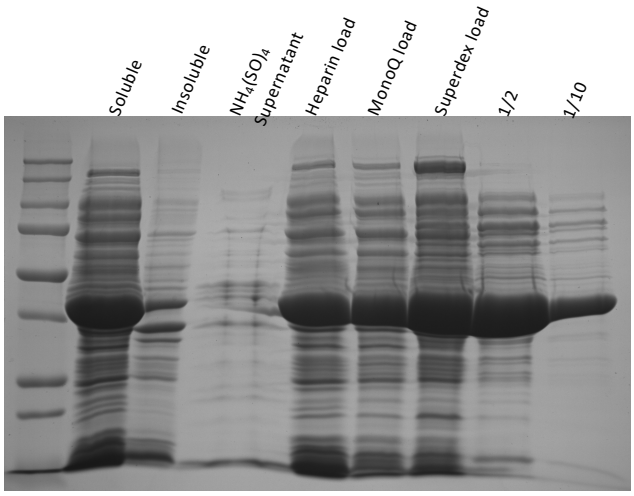

Figure 3.23. Concluding SDS-PAGE of Mutant 9 ParA2^{K388A_L391A_R395A} protein purification.
12% SDS-PAGE gel with a PageRuler Broad Range Unstained Protein Ladder, the soluble and insoluble fraction were taken during cell lysis. The load lanes for each column shows the sample that was loaded onto that column, the 1/2 and 1/10 are the dilutions of the concentrated final protein sample.

3.6 Discussion

Protein purification of *V. cholerae* ParA varies a considerable amount between ParA1 and ParA2, and between ParA2 mutants. Since ParA2 and ParA1 have previously shown difficulty expressing with either N-terminal or C-terminal His tags, this further limits the available methods of which to use in order to separate out a large proportion of contaminants. As ParA is a non-specific DNA binding protein, this means basic residues must be present on the outer surface of the protein as either a monomer or a dimer. Using this logic, the heparin column was chosen as the first step, this allows for a large amount of protein lysate to be loaded using the superloop and for a quick column run on the FPLC.

In the case of ParA2, purification is a straightforward process. ParA2 has a pI of 5.45, meaning there is a strong chance it will bind successfully to an anion exchange column using a buffer with a pH of at least 7. Native ParA2 has shown to bind as expected to the heparin columns used and then furtherly binds successfully to the anion exchange column used. ParA2 then elutes sometimes as a monomer or as a dimer on the gel filtration column and a high yield of reasonably pure protein can be collected from the overall process.

However, ParA1 is a much more difficult protein to handle. ParA1 doesn't express in as large amounts as ParA2 and is also more unstable upon cell lysis. ParA1 has a pI of 6.8, close to neutral. This could be the reason why ParA1 had difficulty binding to the ion exchange columns used and why the protein precipitated during buffer dialysis, as the buffer was needing to change pH across ParA1's pI. Concluding SDS-PAGE was originally decided to be ran at the end of each purification protocol for ParA1 in order to determine when in the purification process ParA1 was lost or failed to be separated from contaminants (**Figure 3.10 and 3.14**). This helped to design each purification method as it was now more clear which steps weren't suitable and needed adjusting. Despite difficulty expressing ParA1 with a His tag, the plasmid encoding for ParA1 was able to be transformed, expressed, and purified with a C-terminal GFP-His fusion. Following the purification it was deemed that the product had too much contamination for its intended purpose of enzymatic assays and

ultimately flow-cell TIRF (total internal reflection fluorescence) microscopy. However, reviewing this purification, ParA1-GFP-His would have been suitable for structural biology.

The ParA2 mutants also varied in purification success, the conserved catalytic lysine mutants K124E, Q and R behaving similarly to native ParA2, while the non-conserved deletion and/or surface charge abrogation mutants showed an altered behaviour during purification. ParA2Δ4-106 was unable to be purified as the protein remained in the insoluble pellet after cell lysis (**Figure 3.20D)**, this suggests that the large N-terminal deletion may be too disruptive to the viability of the protein. Deleting such a large region may affect the folding of the protein after translation, rendering it unstable and/or insoluble. ParA2K388A also didn't purify as straightforward as the native protein, despite still binding to the heparin and ion exchange column, a much larger proportion of protein was eluted into the flow through. This suggested that the mutation from lysine to alanine may have affected the surface charge of ParA2, allowing still for sufficient binding but at a lower efficiency. To account for the protein lost, the flow through from the Mono Q column was reapplied for a second round on the ion exchange portion of purification before loading onto the Superdex gel filtration column, resulting in two Mono Q and Superdex runs (**Figure 3.22**).

3.7 Conclusion

Despite extensive efforts, Wild-Type ParA1 was unable to be purified to the level required for biochemical assays. ParA1 is able to be purified when fused to a GFP tag, however, it is uncertain whether the tag alters the function of the protein. In contrast, ParA2 was able to be purified easily to a high purity for multiple mutants as well as wild-type. Since the protocol designed for ParA2 mutant purification was so successful, it became the standard protocol for purification of wild-type ParA2, showing no deviation between the different conserved catalytic lysine ParA2 constructs. ParA2 was therefore used for subsequent structural work.

4 Results Chapter 2: Characterisation of ParA2$_{vc}$ oligomerisation by negative stain transmission electron microscopy

4.1 Introduction

ParA family members' nucleotide binding activity has been extensively studied, giving insight how binding and hydryolysis may alter ParAs conformation. For P1 ParA, circular dichroism (CD) has been used to understand how the structure of ParA alters upon binding ATP compared to other nucleotides (ADP or ATPγS), and furthermore the effects of hydrolysis (Davey & Funnell, 1997). Along with nucleotide binding, ParA's interaction with DNA has been a focus of research in many species. ParAs ability to bind to DNA non-specifically has been observed using negative stain TEM across many orthologues. *Helicobacter pylori* Soj ($_{Hp}$Soj), *T. thermophilus* Soj, and *V. cholerae* ParA2 are examples of ParAs observed coating DNA using this technique (Chu et al., 2019; Hui et al., 2010; Leonard et al., 2005). However, the arrangement of ParA dimers in these assemblies is difficult to distinguish, as only ParA2$_{vc}$ out of imaged ParAs has been reconstructed in 3D (Hui et al., 2010). Without reconstruction, the details of dimer-dimer interaction remain unresolved, not allowing for ParA coating of DNA and assembly of higher-order complexes, such as filaments, to be distinguished between. Since nucleoprotein filaments have been reported across type Ia and Ib ParAs (see **Chapter 1**) and little biochemical and structural characterisation of these polymers has been published, the understanding of why ParAs may or may not form filaments along DNA is still to be elucidated.

In this chapter I will investigate how filament formation differs with ParA2$_{vc}$ in different nucleotide states and describe the process whereby ParA2$_{vc}$-DNA samples were optimised for negative stain TEM, to collect preliminary data on filament formation. I will also show the effects of various mutations in the N-terminal and C-termini, as well as in the nucleotide binding pocket, on filament formation.

4.2 ParA2$_{vc}$ forms dimers in all nucleotide states

Purified ParA2$_{vc}$ was diluted and incubated at 30°C with various nucleotides in the presence of Mg^{+2} as per **section 2.8.11**, the samples were then applied to glow-discharged carbon coated copper grids following **section 2.8.1.4**. Varying concentrations of ParA2$_{vc}$ were optimised to find the best condition to view monomers and dimers. Once this was found, ~0.01 mg/ml, grids of ParA2$_{vc}$ with ATP, ADP, ATPγS and without nucleotide were negatively stained. Small data sets were collected on each state, followed by 2D particle picking and 2D classification using cisTEM (**section 2.8.1.5**). From this I was able to see that ParA2$_{vc}$ forms dimers in all nucleotide states imaged (**Figure 4.1**), including in the absence of nucleotide. From the 2D classes obtained, different views of dimers over the different nucleotide states are observed. Regarding ParA2$_{vc}$ in the absence of nucleotide, dimers were present, however, monomers could also be seen in the micrographs (**Figure 4.1**). 2D classes of the monomer conformation cannot be clearly seen, however, on the micrographs themselves, the protein density is much higher than the other grids imaged in the presence of nucleotides, despite being at the same concentration (~0.01 mg/ml). Smaller proteins can also be seen dotted around the micrographs which are suggested to be the monomer conformation (**Figure 4.1D)**.

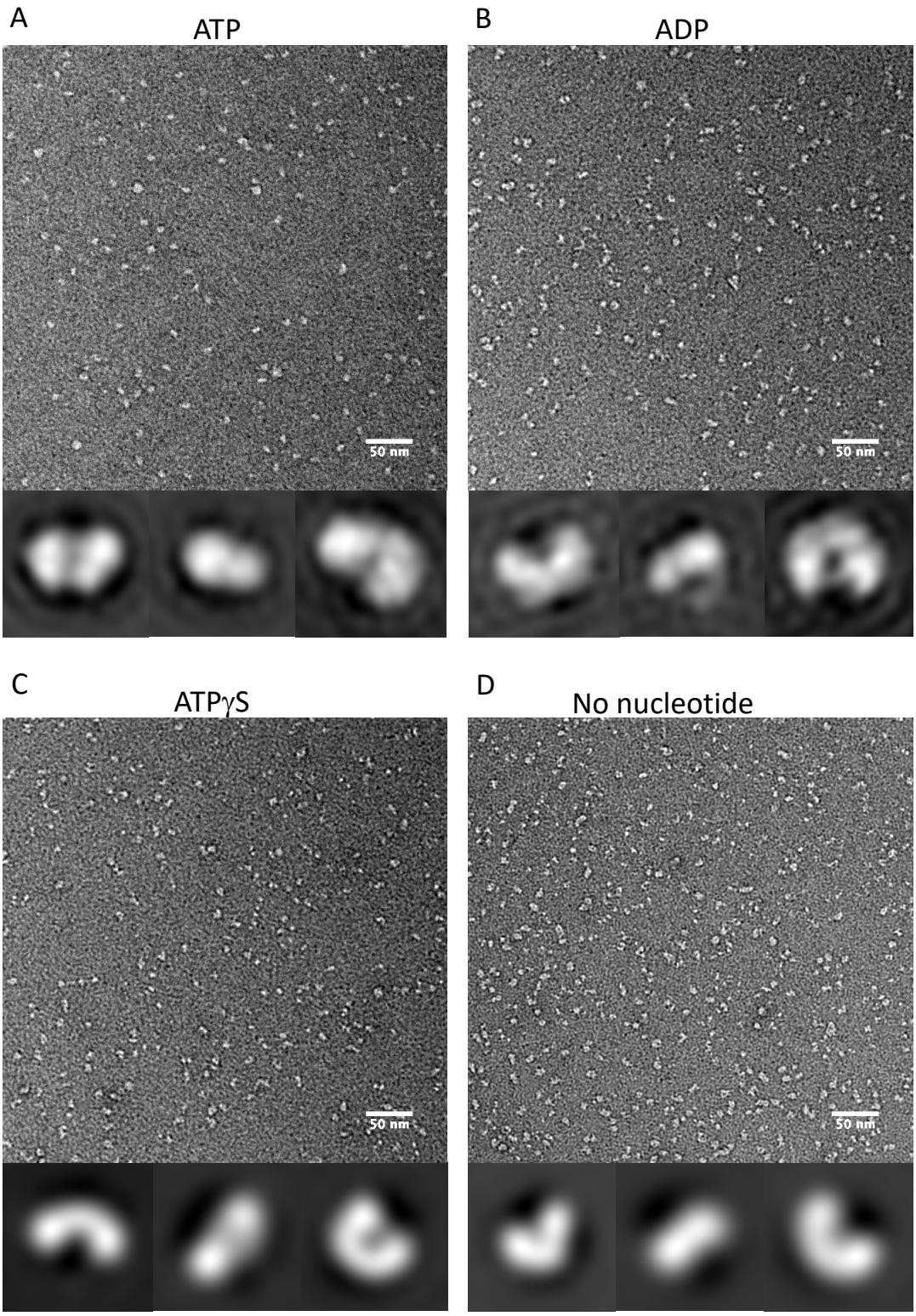

Figure 4.1. Representative micrographs and 2D classes of ParA2$_{vc}$ in different nucleotide states.
Negatively stained electron microscopy micrograph of native ParA2$_{vc}$ in the presence of **(A)** ATP **(B)** ADP **(C)** ATPγS and **(D)** no nucleotide. Each state is paired with the 3 top 2D classes from 2D classification carried out using cisTEM.

4.3 ParA2$_{vc}$ binding to DNA and filament formation

4.3.1 Optimisation of ParA2$_{vc}$-DNA filaments

To view ParA2$_{vc}$ protein-protein and protein-DNA interactions, samples of ParA2$_{vc}$ were incubated with nsDNA along with nucleotide as per **section 2.8.1.2**. To begin with, ParA2$_{vc}$ was incubated with plasmid DNA in the presence of ATP and $MgCl_2$. The sample then followed serial dilution by 10fold to create grids before imaging. From this a clear filament could be seen from the sample diluted 10x (**Figure 4.2A**), forming a chain like patterning along the plasmid. However, the background of protein is far too high, completely coating the grid and the occurrence of ParA2$_{vc}$-DNA complexes is also far too low for negative stain data processing. When the 100x dilution is imaged, clear ParA2$_{vc}$-DNA complexes like previously seen couldn't be found. However, the sparse ParA2$_{vc}$ coating of the grid allows for homodimers to be clearly seen (**Figure 4.2B**).

A

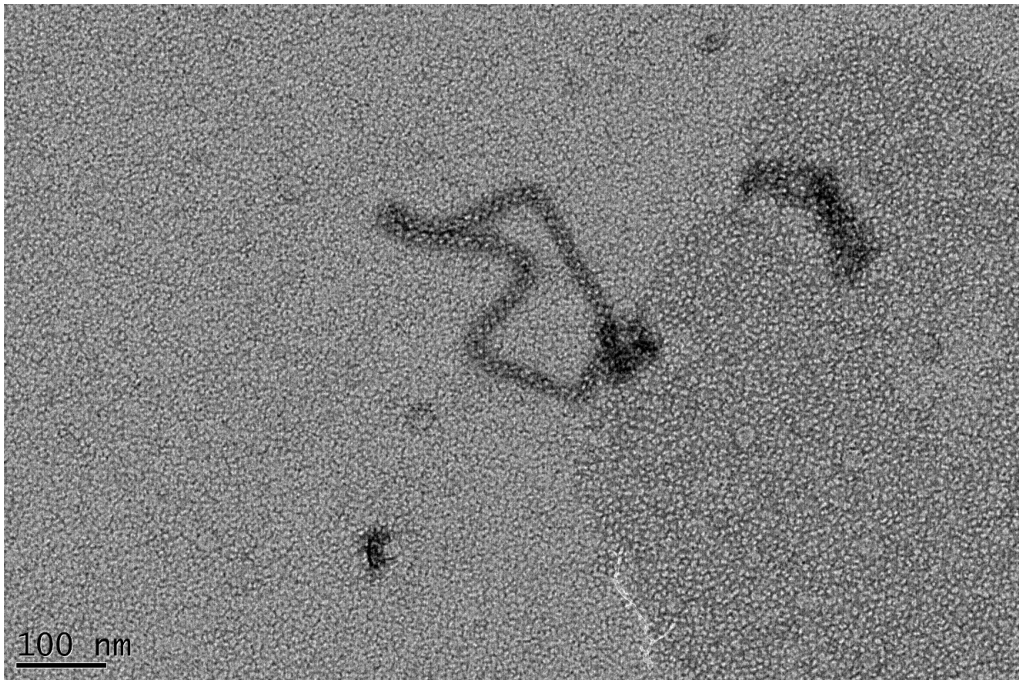

B

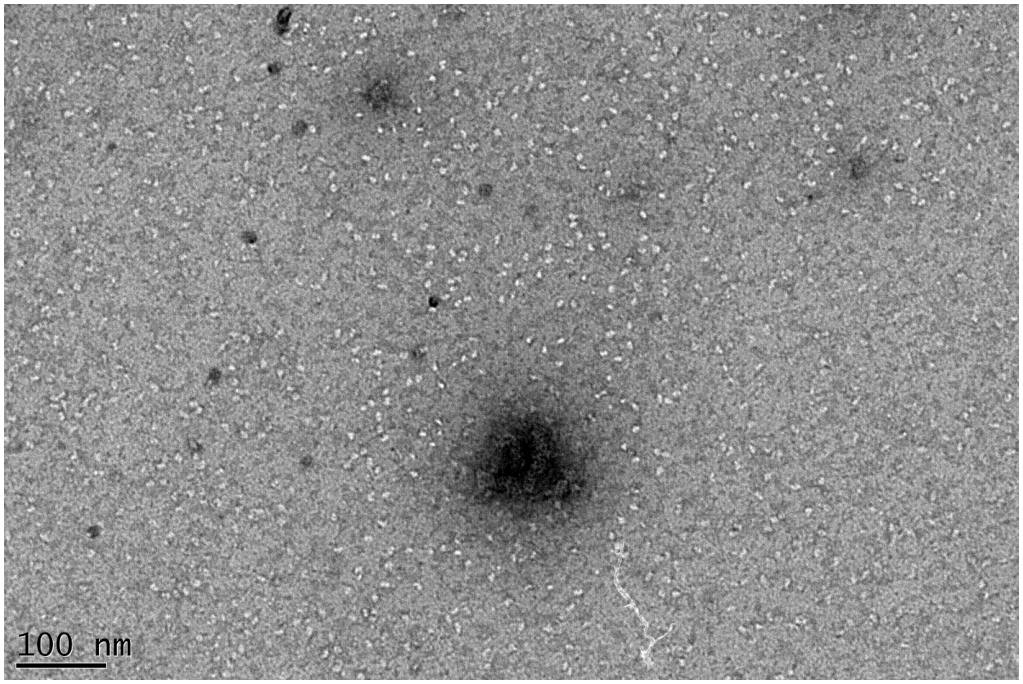

Figure 4.2. Electron micrographs of ParA2$_{vc}$-ATP with DNA.
(A) *Negative stain electron micrograph of 10-fold dilution of ParA2-ATP-DNA.* ***(B)*** *Negative stain electron micrograph of 100-fold dilution of ParA2-ATP-DNA.*

Following optimisation, it was observed that the density of ParA2$_{vc}$-DNA complexes is far too low to allow for data analysis. To increase this, the concentration of the nsDNA needs to be higher, to avoid diluting the concentration of ParA2$_{vc}$ in the

incubation. It was also attempted to use a slow hydrolysing analogue of ATP, ATPγS, instead of ATP, to try to reduce dissociation of the ATPase from the DNA when diluted from the concentrated incubated sample. This led to a new protocol of DNA preparation (**2.5.1**) from sonicated salmon sperm DNA, to obtain a higher yield. This protocol for DNA preparation was successful in increasing the density of $ParA2_{vc}$-DNA complexes, the ratio of ParA:DNA being 3.4:1 (mg/ml) (**Figure 4.3A**), forming clear filaments of around ~1Kb in length. Furtherly, the addition of ATPγS allowed for complexes to remain intact when the sample was diluted another 2-fold to reduce the background coating of protein (**Figure 4.3B**). This increased occurrence of filaments and lowered background noise allowed for a small data set over varying defocus to be collected (~-1 μm - -3 μm), and 2D classes to be generated using relion from particles picked using cisTEM (**Figure 4.3B**). The low resolution 2D classes produced allow for observation of the filament helical properties, showing there is an order to the $ParA2_{vc}$ binding along the DNA. When you compare the two classes, the one to the right (shorter) appears slightly wider between the white subunits that can be seen. This is suggestive that there is a differential binding and could be where some dimers are not contributing to a full filament along the DNA, maybe at the end of the strand or on a bend in the DNA.

A

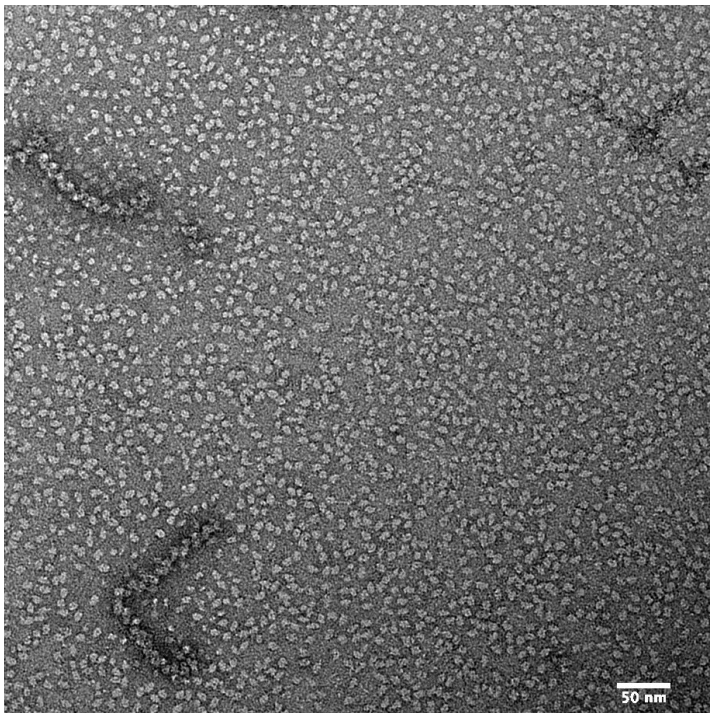

B

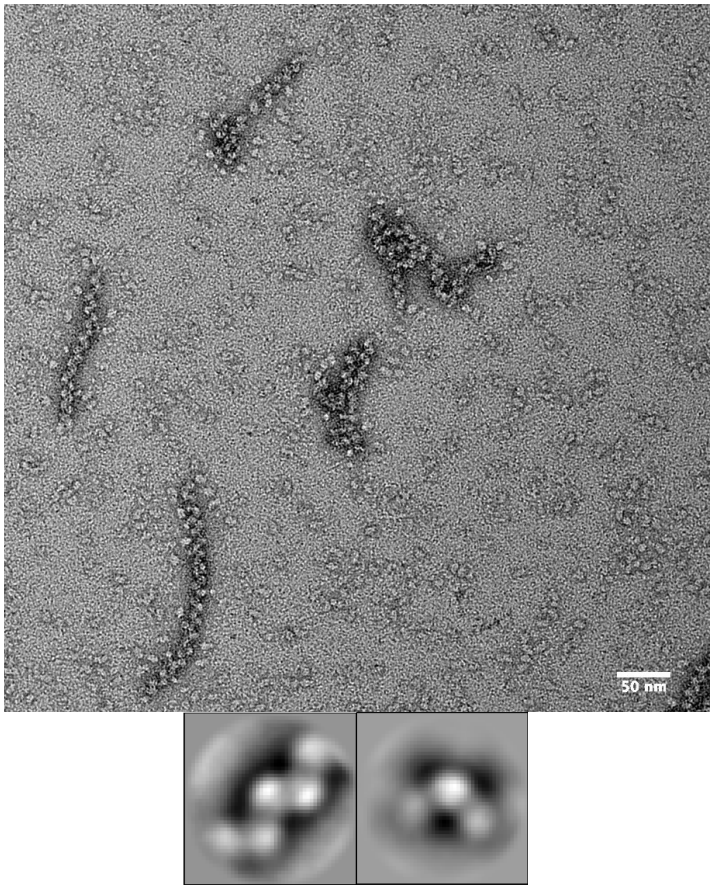

Figure 4.3. Micrographs and 2D classification of ParA2$_{vc}$-DNA with ATPγS.
(A) *10-fold dilution following* ***methods****.* ***(B)*** *Representative micrograph from small-scale data collection of 20-fold dilution following* ***methods****, paired with 2D classes obtained (below) from 2D classification carried out using Relion 2.1.*

4.3.2 ParA2$_{vc}$-DNA with ATP

Since optimising and analysing the ParA2$_{vc}$-ATPγS-DNA filaments, the DNA sample has changed again, back to pBSKII plasmid (**method 2.5.2**), as purification and gel extraction of sssDNA produced very varied results, with lots of DNA getting stuck in the agarose gel wells. With a ratio of 10:1, ParA2$_{vc}$-ATP is able to form filaments along DNA resembling those seen in **5.3.1** (**Figure 4.4A**). The filaments formed vary between straight singular stretches of ParA2$_{vc}$-DNA and jumbled sections of filaments interacting with other complexes, an array can be seen in **appendix 8.12**.

4.3.3 ParA2$_{vc}$-DNA with ADP

Following the same method as with ATP (**2.8.1.2**), native ParA2$_{vc}$ was incubated with DNA in the presence of ADP. However, filament formation is difficult to distinguish (**Figure 4.4B**). Jumbled masses of what could be ParA bound to DNA can be seen, however the complexes aren't as ordered as those observed with ATP. ParA2 is binding to the DNA while bound to ADP, however whether there is interaction between the dimers is not clear, more examples from the image collection can be seen in **appendix 8.13**.

4.3.4 ParA2$_{vc}$-DNA with no nucleotide

It has previously been determined that ParA2$_{vc}$ is able to form transient dimers in the absence of nucleotide (**4.2**), it was investigated to see whether it would be able to form filaments. However, upon incubation with DNA, no filaments or protein-coated DNA can be observed (**Figure 4.4C**). Unlike the grids made with ADP (**4.3.3**), no DNA can be visualised with sporadic ParA binding, due to unbound protein coating the grid and covering the free DNA. This suggests that there is not only no filament formation, but also no DNA binding at all (**appendix 8.14**).

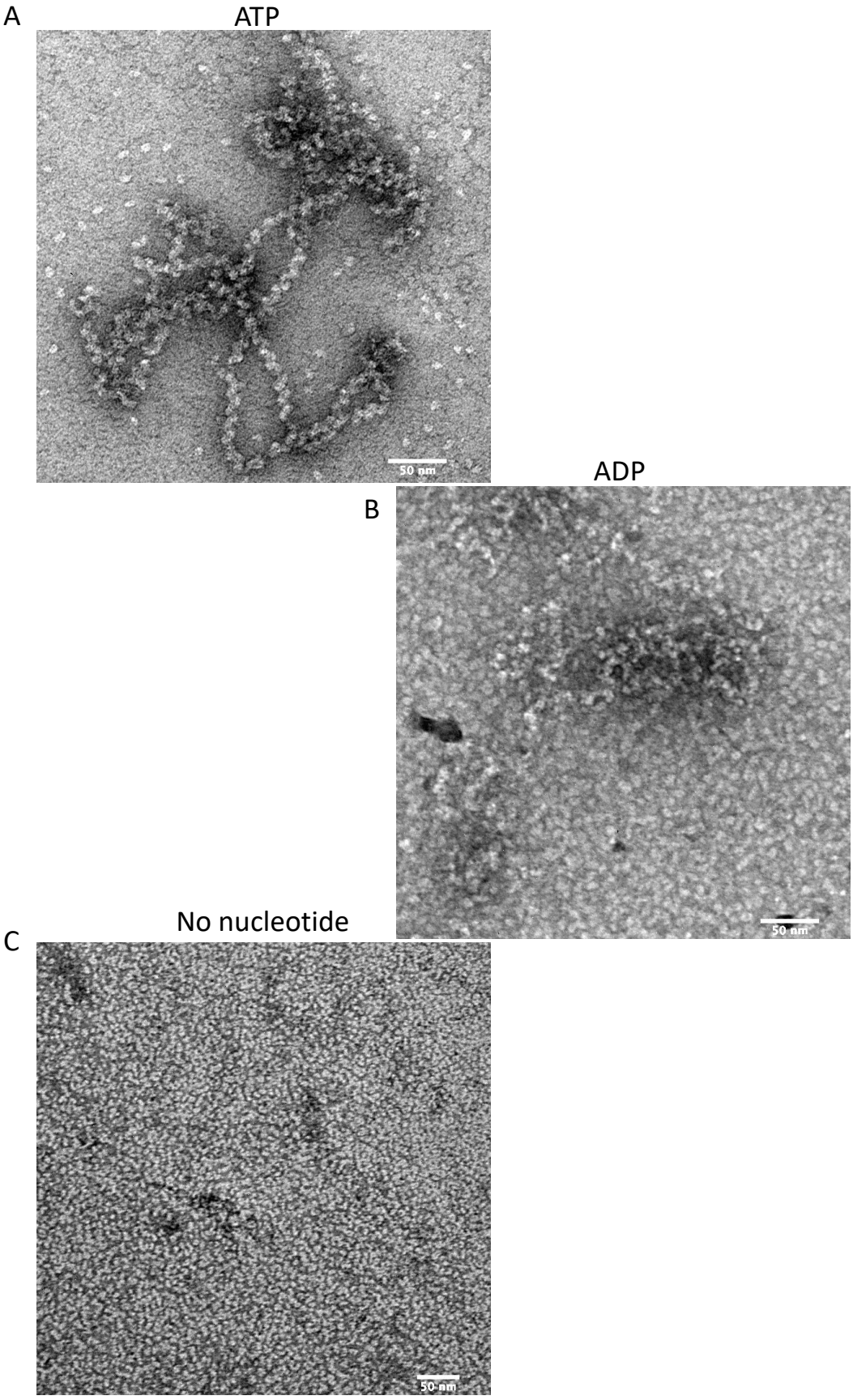

Figure 4.4. Electron micrographs of ParA2$_{vc}$-DNA with different nucleotides.
(A) *In the presence of ATP.* ***(B)*** *In the presence of ADP.* ***(C)*** *In the absence of nucleotide. For more images please see* ***appendix****.*

4.4 How mutating ParA2$_{vc}$ affects filament formation with DNA

To further investigate filament formation of ParA2$_{vc}$ with DNA, a range of mutants were engineered. Firstly, to see how the surface facing features of ParA2$_{vc}$ are involved in filament formation and secondly to investigate the properties of nucleotide binding.

4.4.1 ParA2$_{vc}$Δ4-36

Since the N-terminal helix stretches across the adjacent ParA2 molecule in the dimer, it was suggested this could play a role in filament formation. When incubated with DNA and ATP as by **2.8.1.2**, ParA2$_{vc}$Δ4-36 is still able to form filaments with DNA (**Figure 4.5A**). Despite missing helix 1, there is no clear difference between the filaments formed by this truncation than by wild-type ParA2 (**appendix 8.15**).

4.4.2 ParA2$_{vc}$K388A and ParA2$_{vc}$K388A_L391A_R395A

From results presented in **Chapter 6**, a few residue-specific mutations to alanine were engineered along the C-terminal helix, since this helix also lies along with what could be the dimer-dimer interface. Two mutants, a single point mutation K388 to alanine (K388A), and the triple mutant K388A, R395A and L391A were engineered (**2.6**). When incubated with ATP and DNA, following the method outlined in **2.8.1.2,** ParA2$_{vc}$K388A caused some filament formation disruption in comparison to wild-type ParA2 (**Figure 4.5B**). Likewise, to what was observed with wild-type ParA2 in the presence of ADP, clumps of DNA with protein binding are observed, however, no filament patterning, or straight complex formation can be seen (**appendix 8.16**).

ParA2$_{vc}$K388A_L391A_R395A when incubated with ATP and DNA, was also not able to form filaments (**Figure 4.5C**). Dimers can be viewed coating the micrograph, but DNA binding seems to be minimal, with no sign of filament formation (**appendix 8.17**).

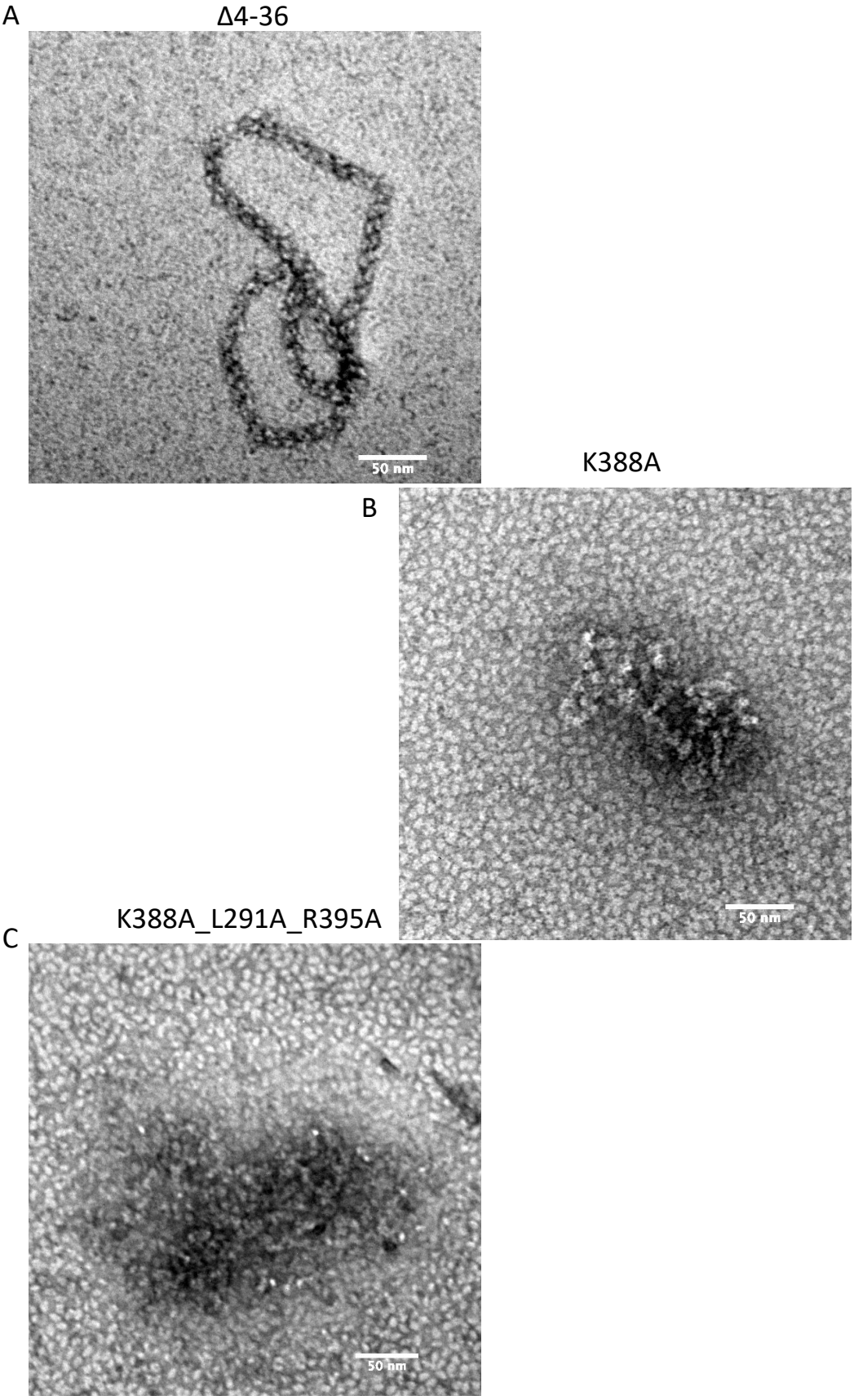

Figure 4.5. Electron micrographs of ParA2$_{vc}$ mutants with DNA and ATP.
*10-fold dilutions following **methods**, negatively stained following **methods (A)** ParA2$_{vc}^{\Delta 4\text{-}36}$ with DNA In the presence of ATP. **(B)** ParA2$_{vc}^{K388A}$ with DNA in the presence of ATP. **(C)** ParA2$_{vc}^{K388A_L391_R395}$ with DNA in the presence of ATP. For more images please see **appendix**.*

4.4.3 Nucleotide binding mutants

Since WT ParA2 binding to DNA and forming filaments changes depending on the nucleotide bound, 3 nucleotide binding and hydrolysis mutants were engineered (See chapter 2 for purification details). ParA2$_{vc}$K124E caused a disruption in filament formation and DNA binding, as no filaments could be observed (**Figure 4.6A, appendix 8.18**). This is expected since a similar mutation in P1 ParA (Davis et al., 1996; Vecchiarelli et al., 2010; Vecchiarelli, Havey, et al., 2013) inhibits nucleotide binding, therefore it was expected that ParA2 would behave like in **4.3.4**. In contrast, the K124R and K124Q mutations had no negative impact on ParA2's ability to form filaments, as large complexes were easy to see and abundant (**Figure 4.6**, **appendix 8.19-20**). Although both ParA2$_{vc}$K124R and ParA2$_{vc}$K124Q are seen to form nucleoprotein filaments **(Figure 4.6B-C)**, there is a dramatic difference between the two. While ParA2$_{vc}$K124Q forms clear straight filaments similar to those formed by WT ParA2, multiple complexes were seen entangling for ParA2$_{vc}$K124R **(Figure 4.6B)**, forming large masses of aggregating filaments. This suggests that being unable to hydrolyse ATP altogether might cause aggregations or higher-order assemblies with nearby DNA-bound ParA filaments.

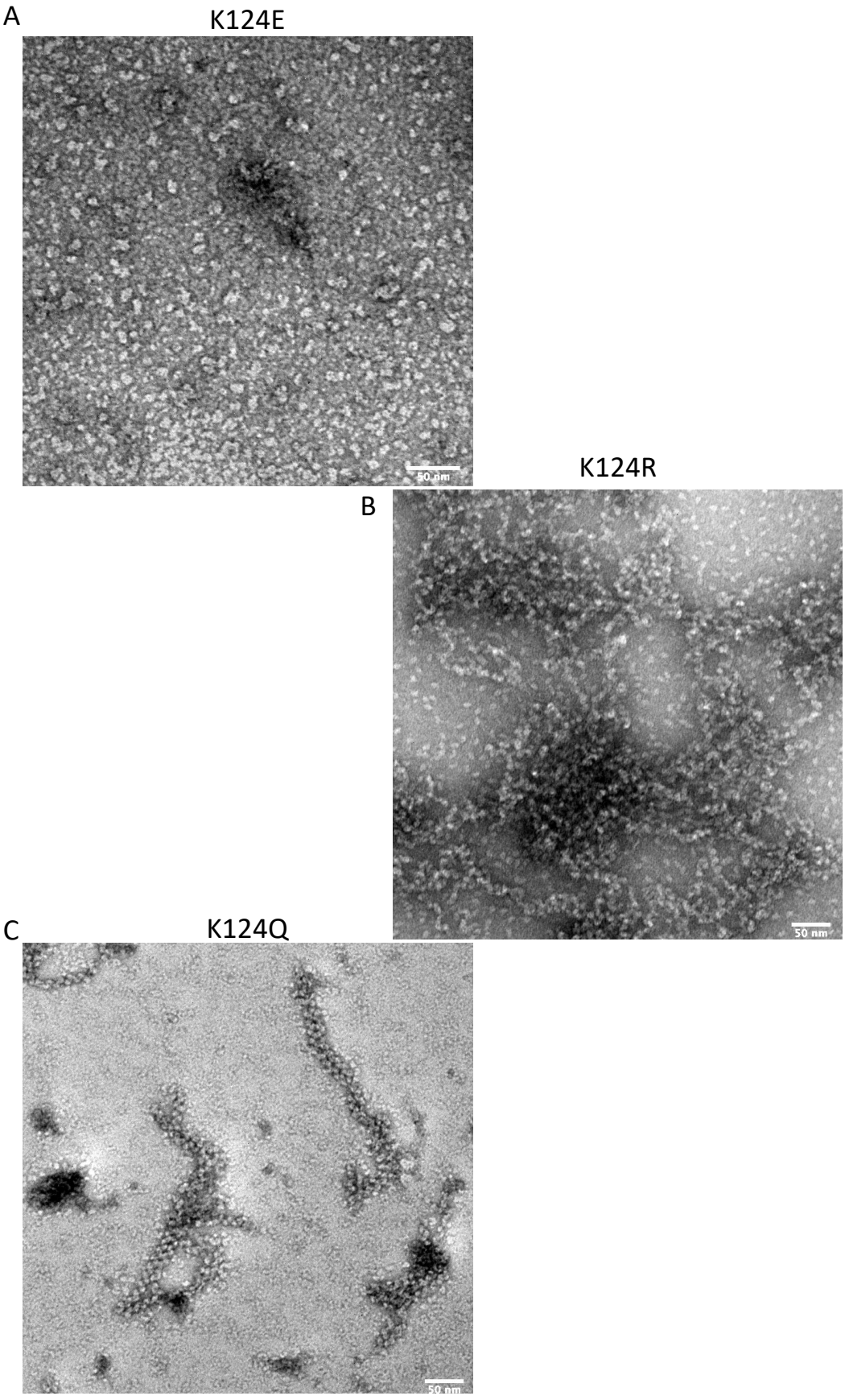

Figure 4.6. Micrographs of nucleotide binding and hydrolysis mutants of ParA2$_{vc}$ with DNA.
*10-fold dilutions following **methods**, negatively stained following **methods**. **(A)** ParA2$_{vc}^{K124E}$ with DNA in the presence of ATP. **(B)** ParA2$_{vc}^{K124R}$ with DNA in the presence of ATP. **(C)** ParA2$_{vc}^{K124Q}$ with DNA in the presence of ATP.*

4.5 ParB

To see if the partition complex consisting of ParB bound to *parS* interacting with ParA could be captured, ParB and *parS*-DNA were introduced to the incubation for grid preparation by negative stain. Before preparing grids with ParB and ParA together, I sought to initially characterise the ParB-*parS* complex in isolation. Therefore, ParB was incubated with *parS* DNA, in the absence of nucleotide, by **method 2.8.1.3** to view ParB binding to the *parS* site. From this, coating of ParB along the short sections of DNA including the 14bp *parS* site can be seen (**Figure 4.7**). However, no binding patterning, like with ParA-DNA, is observed, suggesting that ParB may not be binding to DNA and forming well-ordered higher-order complexes.

When grids were prepared with ParA and ParB, alongside *parS* DNA and 1kbp nsDNA (**2.8.1.3**), no clear partition complex could be observed (**Figure 4.8**). Some ParA-DNA filaments can be seen; however, they are quite flexible and missing sections of bound ParA. Surrounding the ParA-DNA complexes are short stretches of protein, which could potentially be ParB bound to *parS*-DNA. However, with the lack of resolution provided by negative stain, there is no confirmation on the identity of the protein, and this could be ParB, ParA, or a contaminant.

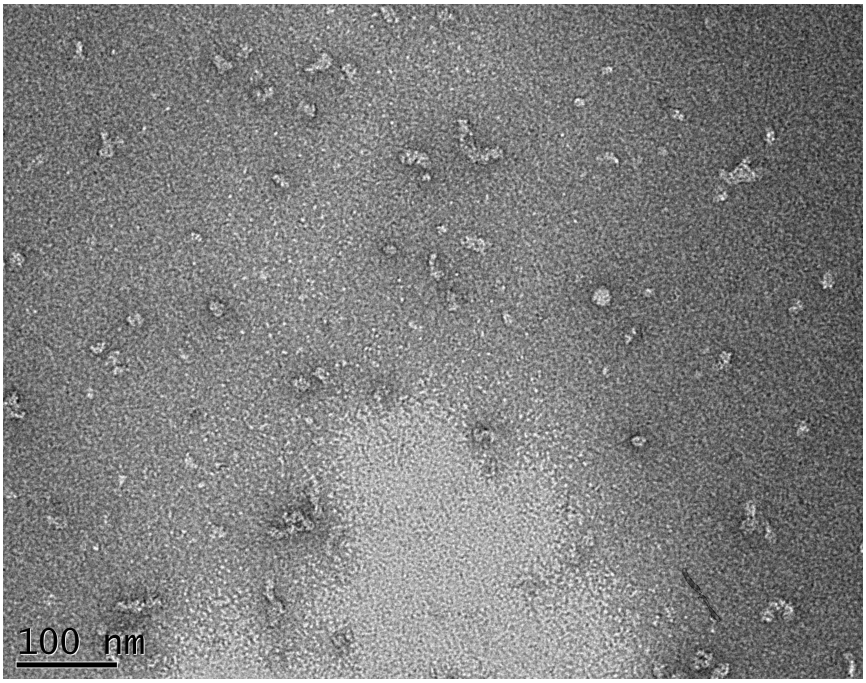

Figure 4.7. Micrograph of ParB2-parSDNA.
*Negatively stained ParB2 incubated with parSDNA followed by 30x dilution (**methods**).*

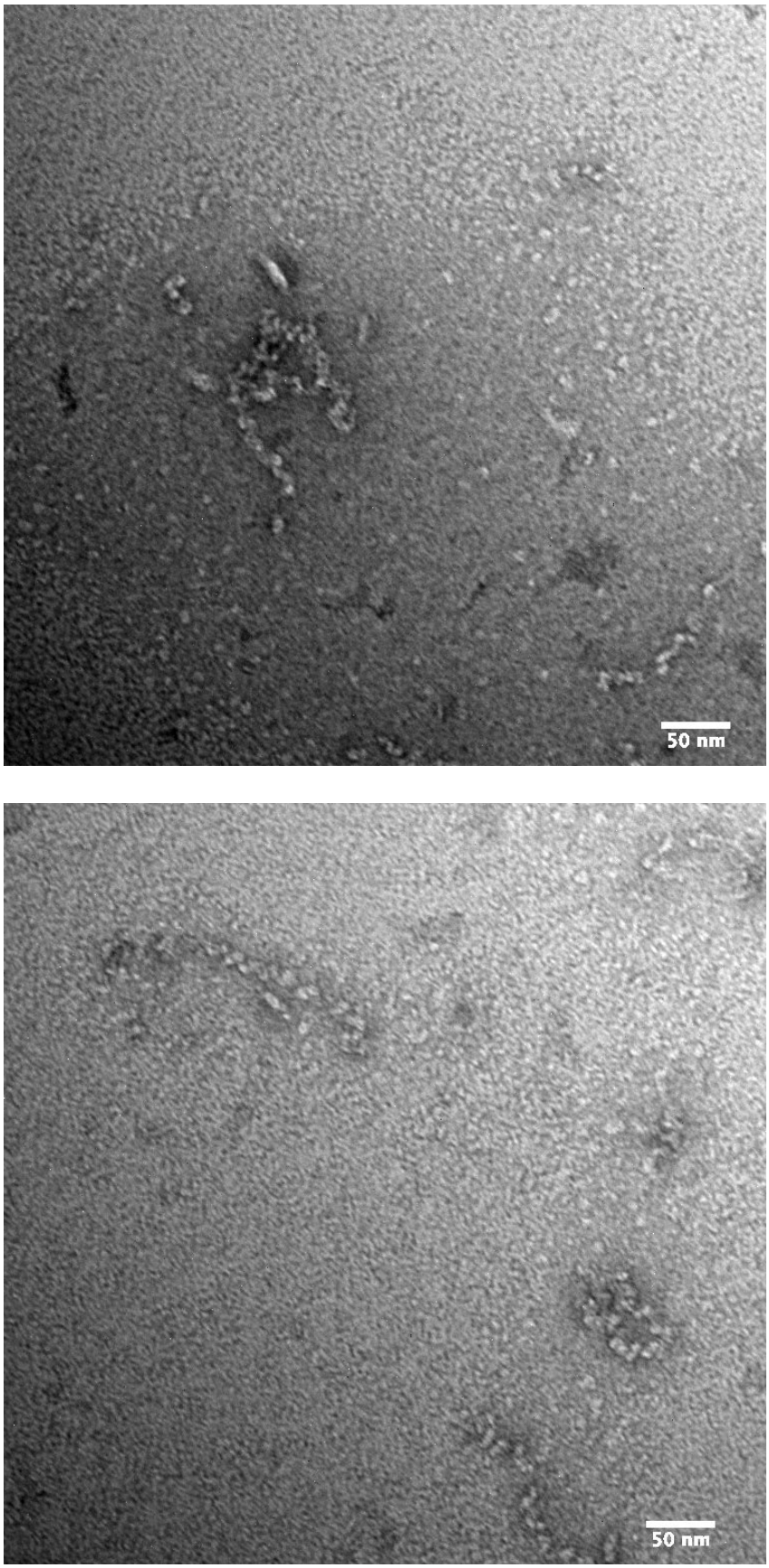

Figure 4.8. Micrographs of ParA2-ATP-DNA with ParB2-parSDNA.
*Two micrographs showing the result of mixing $ParA2_{vc}$-ATP-DNA with ParB2-parS following their individual incubations (**methods**). Larger complexes seen are $ParA2_{vc}$-DNA filaments, small sections of ParB bound to parS can be seen laying near ParA-DNA complexes.*

4.6 Discussion

Sample preparation of ParA:DNA is a very challenging process. Despite following the same protocol multiple times, the process of grid preparation was not consistently reproducible. This could be because of damage on the grid, tearing the carbon between grid-bars, therefore finding a patch where protein-complexes are laying is much more difficult. In other times where filaments could be found, however, the quality of the staining is very poor, and the details of the filaments are not suitable for further analysis (Kepiro et al., 2020). Throughout optimisation of filament formation, I noticed fewer filaments were forming when ParA2 was incubated with ATP (along with DNA) prior to dilution during sample preparation. When the slowly hydrolysable analogue, ATPγS, was used instead of ATP, filaments were more prevalent after dilution. From this, it suggests that one of the reasons why ParA2-DNA filaments disassemble so readily is due to the turnaround between the binding of nucleotide and DNA by ParA2 and hydrolysis of ATP.

A feature of filament formation observed throughout this process is that there are either complete stretches of protein filament along the DNA strand or no binding at all. Sporadic binding of $ParA2_{vc}$ could be seen in some cases, in some of the mutant samples viewed and when native ParA2 is in the presence of ADP as a nucleotide. This suggests that $ParA2_{vc}$ may be binding cooperatively to form these filaments, whereby once one dimer binds, it promotes binding of further dimers. This is consistent with biochemical assays that have been carried out, showing sigmoidal binding of ParA to nsDNA (Chodha et al., 2021).

However, the observed lack of filament patterning of ParA2 while in the presence of ADP disagrees with previous negative stain literature. In the case of $ParA2_{vc}$, filaments have been studied using negative stain TEM, forming the same chain-like patterned filament with ATP observed during this work (Hui et al., 2010). However, a low-resolution negative stain electron microscopy reconstruction showed that ParA forms a filament with ADP but with different helical symmetry to that with ATP (Hui et al., 2010). It is unclear why my micrographs look so different and disordered compared to this previous study. It could be that with the higher concentration of ParA2 used in sample preparation from this previous study, ParA binding was easier

to obtain. The map seen in **Figure 1.7B(right)** could be a reconstruction of ParA dimers bound to DNA, but without any higher-order interactions between them, as the low resolution produced from negative stain would not allow for proper helical symmetry parameters to be produced.

Although it would be advantageous to quantify filament formation across the different nucleotides and ParA2 mutants imaged, due to the challenging nature of sample preparation as described above, quantification would be unsuitable and therefore unreliable.

4.6.1 The role of the N-terminal and C-terminal helices on filament formation

Viewing the effects of mutations on filament formation allows for some characteristics of ParA2 cooperativity to be elucidated. Interestingly, the first mutant observed, ParA2$_{vc}$Δ4-36 was still able to form filaments (**Figure 4.5A**). This mutant lacks the N-terminal helix, which stretches across the partner monomer in the ParA2 dimer (**3.5.2.1**). Since this helix lies across the side of the dimer when bound to DNA, it was suggested that it may have a function in filament formation. However, now it can be observed that ParA2 is able to cooperatively bind without having the N-terminal helix, we can conclude that it is not necessary for filament formation. However, the C-terminal mutations observed were successful in disrupting filament formation. ParA2$_{vc}$K388A, disrupting a positive charge, was able to abrogate filament formation, with no distinctive filaments to be seen. Some ParA2$_{vc}$K388A binding to DNA could be observed (**Figure 4.5B**), forming clumps of DNA with what looks like protein bound to the surface. This suggests that ParA2$_{vc}$K388A is still able to bind to DNA non-specifically but may not induce cooperative binding or be able to interact with neighbouring dimers. Furtherly, the triple mutant ParA2$_{vc}$K388A_L391A_R395A could be seen potentially disrupting cooperativity even more (**Figure 4.5C**). It is unclear to what extent this mutant is able to bind to DNA, with balled up clumps of DNA observed surrounded by dimers, the lack of protein binding could therefore be a feature of variable quality of staining. To allow further understanding of how subtle changes in hydrophobicity can affect interactions with neighbouring dimers, it would be advantageous to view the L391A mutation alone, since there would be no net

change in charge of the residue, both being hydrophobic. A major limitation of negative stain electron microscopy is the lack of quantifiability due to the variability of the staining. Therefore, biochemical measurements of DNA binding activity will be required to confirm this interpretation.

4.6.2 The role of ATP-binding and hydrolysis on filament formation

To investigate the role of ATP-binding and hydrolysis on filament formation, 3 mutations were engineered on conserved lysine K124, analogous to K122 of *E.coli* P1 ParA. Filaments are observed resembling those seen in WT with ParA2$_{vc}$K124R (**Figure 4.6B**), this mutation being a "ParPD" dominant-negative (worse-than null) phenotype, allowing for ATP-binding and for conformational change but having a reduced ATP hydrolysis efficiency (Vecchiarelli, Havey, et al., 2013). Therefore, filament formation like that observed with ATPγS was expected, however, the filaments observed with this mutation are much more clumped. This could be due to a more reduced efficiency of hydrolysis compared to the slowly hydrolysable ATP analogue, ATPγS, therefore causing large nucleoprotein complexes across multiple DNA templates to form. ParA2$_{vc}$K124E, was not able to form filaments with DNA, which was expected from the mutant phenotype. Since the K124E mutation disrupts nucleotide binding altogether, a phenotype similar to the ParA2$_{vc}$ experiments in the absence of nucleotide was hypothesised (**Figure 4.6A**). However, ParA2$_{vc}$K124Q unexpectedly formed filaments with DNA. According to the mutation phenotype in P1 ParA, K124Q is able to bind both ADP and ATP but is unable to undergo the conformational change required for DNA binding (Vecchiarelli et al., 2010) . However, this is the opposite of what is observed in **4.4.3** (**Figure 4.6C)**, as ParA2$_{vc}$K124Q-DNA complexes are clearly observed, resembling those of native ParA2$_{vc}$ with ATP (**Figure 4.4**). Therefore, further characterisation of this catalytic mutant is required in *V. cholerae* via biochemical methods.

4.6.3 Chemical fixation to stabilise ParA2-DNA complexes

As previously discussed, during sample optimisation ParA2-DNA complexes suffered from disassembly over dilution. To resolve this issue, the slowly hydrolysable

analogue ATPγS was used. However, chemical fixation of the protein to the DNA could have helped with sample preparation in the form of crosslinking. A major disadvantage of using glutaraldehyde for chemical fixation is the formation of artifacts, making particle imaging more difficult (Hayat, 1986). A glycerol gradient method has been developed to entitled GraFix (Kastner et al., 2007), whereby aggregation can be avoided while improving homogeneity of the sample and reducing artifacts induced from fixation. While this would be a great solution to view protein-DNA complexes by negative stain, a disadvantage would be losing the array of native structures and changes of interactions you can obtain during cryo-EM data collection. A major appeal of cryo-EM is that you can view proteins and their interactions under natural conditions, allowing you to distinguish between different conformations which may be important in their interaction. If you were to chemically fix the protein to the DNA you would therefore be missing out on this subtlety of the technique which is afforded to you.

4.7 Conclusion

$ParA2_{vc}$ forms complete stable filaments with DNA at a high concentration and a ratio of ~10:1 (mg/ml) with ATP. However, the dynamic properties of ParA mean that dissociation is triggered upon dilution. Nucleotide binding is a crucial feature of filament formation, which is not permitted in the absence of ATP. This is also evidenced via the nucleotide binding mutants observed, showing how when unable to hydrolyse ATP, $ParA2_{vc}$ exhibits binding similarly to when incubated with ATPγS. Equally, when mutated to be unable to bind nucleotide, DNA binding and therefore filament formation is completely abrogated. $ParA2_{vc}$'s N-terminal helix 1 (residues 4-36) isn't required for filament formation, however basic residues on the C-terminal helix are, as shown by mutating to alanine, causing a disruption to $ParA2_{vc}$-DNA filament assembly.

5 Results Chapter 3: Structure determination of ParA2$_{vc}$ via X-ray crystallography

5.1 Introduction

ParA2$_{vc}$ has low sequence similarity to other ParA homologues, the *E. coli* P1/P7 plasmid ParAs being the closest orthologue of known structure (29% identity). I therefore sought to characterize the ParA2$_{vc}$ structure, to verify that it adopts a similar architecture to other ParA proteins, and to identify any differences with other ParA orthologues.

Other ParA orthologues have been studied following their population dynamics upon the addition of nucleotides, revealing that ParAs are able to form dimers transiently in the absence of nucleotide as well as when bound (Vecchiarelli et al., 2010). This feature has also been studied in ParA2$_{vc}$, observed by SEC-MALS (Chodha et al., 2021) and negative-stain electron microscopy (**section 4.2)**. This previous work has shown that ParA2$_{vc}$ is also able to form dimers in all nucleotide states as well as in the absence of nucleotides like it's relatives, although not to the level of equilibrium like with P1 ParA (Chodha et al., 2021; Vecchiarelli et al., 2010).

ParA2$_{vc}$ was therefore purified with the goal to elucidate its dimeric structure in the presence of different nucleotides. This chapter describes the structural determination of ParA2$_{vc}$ in two nucleotide states, apo and ADP bound, by x-ray crystallography.

5.2 Structure of the APO ParA2

5.2.1 Crystallisation and data collection

Crystallisation screening assays were set up for $ParA2_{vc}$ in the apo state and co-crystalised with nucleotides, ATP, ADP, and ATPγS (**methods**). The purified protein crystallized readily across screening conditions used, with ~20 hits per screen across all the nucleotide states, at both 4°C and 20°C. However, the crystal morphology obtained varied significantly between the wells of each screening plate of the same crystallisation condition, the majority forming sharp spike-like crystals (**Figure 5.1**).

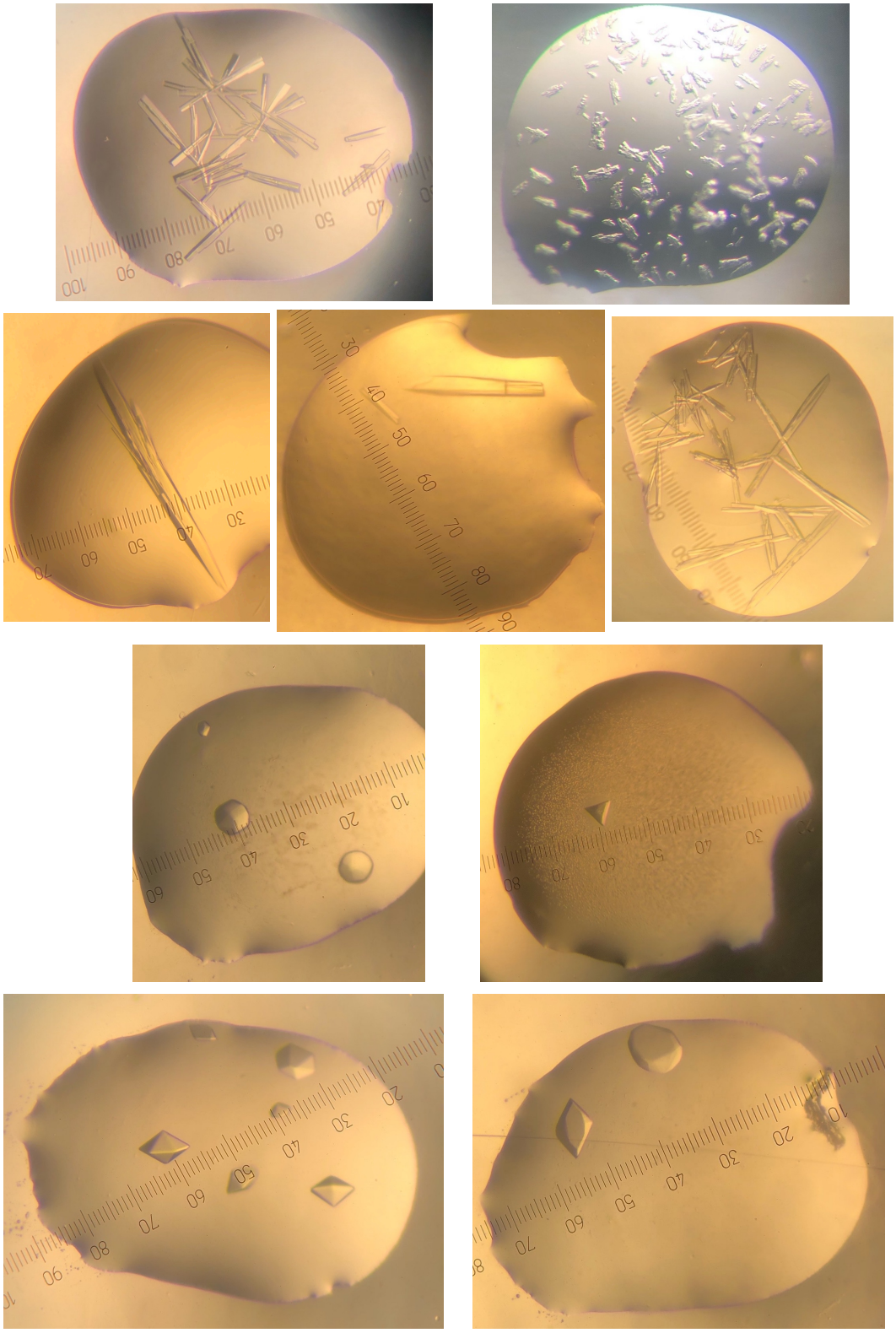

Figure 5.1. Range of crystal morphologies observed.
A selection of each of the different morphologies of crystals obtained during screening, across the crystallization conditions JCSG+, PACT and Morpheous for all the nucleotide co-crystallisation trials set up. Spike-like needle morphology at the stop with dipyramidal and triangular below.

Crystals were looped from a range of conditions and morphologies and cryo-cooled for shipment to the Diamond Light Source, However, upon testing for diffraction, it was apparent that the crystals with the spike morphology did not diffract. Despite this, a few datasets were collected across the nucleotide states (**table 2.6**) from crystals which bipyramidal morphology (**Figure 5.1**). Despite crystals fished from the apo, ATP, ADP, and ATPγS crystallisation screens diffracting (although not to very high resolution), the auto-processing pipeline allowed us to see that the collections for apo, ATP and ATPγS all showed the same space group (**table 5.1**). During phasing of the data, it was discovered that they are all in fact apo $ParA2_{vc}$. Because of this, the data collected from an ATP co-crystallisation assay crystal was chosen to be processed for the apo structure, grown in JCSG+ well A2 at 4ºC, diffracting to ~ 2.5 Å (**Figure 5.1**) . From the auto-processing pipeline, the data was indexed to the space group $P3_2$ 1 2 with the unit cell dimensions of a=63.247 b=63.247 c=214.373 Å and 90 90 120° (**Table 5.1**). The Matthews coefficient was calculated to be 3.01 $Å^3Da^{-1}$, which could only accommodate one molecule of $ParA2_{vc}$ per asymmetric unit **(Figure 5.3**), with a solvent content of 59%.

Nucleotide state	Unit Cell	Space Group	Estimated Resolution
Apo	62.85 62.85 213.03 90.00 90.00 120.00	P32 1 2	2.88 Å
ADP	199.19 199.19 260.02 90.00 90.00 120.00	P61 2 2	3.18 Å
ATPyS	63.25 63.25 214.74 90.00 90.00 120.00	P32 1 2	3.82 Å
ATP	63.25 63.25 214.37 90.00 90.00 120.00	P32 1 2	2.41 Å

Table 5.1. Diffraction statistics

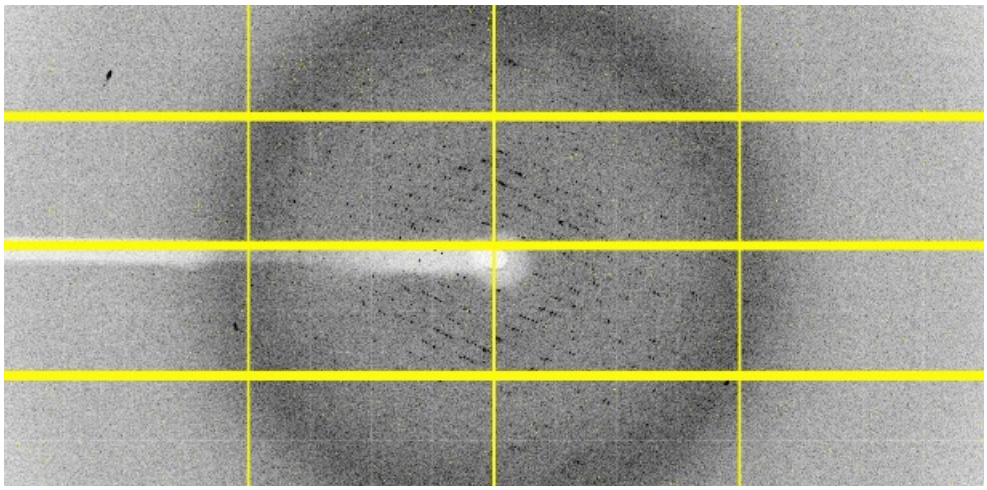

Figure 5.2. ParA2$_{vc}$-apo diffraction pattern.
A diffraction pattern collected from the crystal which was analysed for the apo data set.

N(mol)	Prob(N) for resolution	Prob(N) overall	Vm A**3/Da	Vs % solvent	Mw Da
1	0.9996	0.9996	3.01	59.09	46388.00
2	0.0004	0.0004	1.50	18.19	92776.00

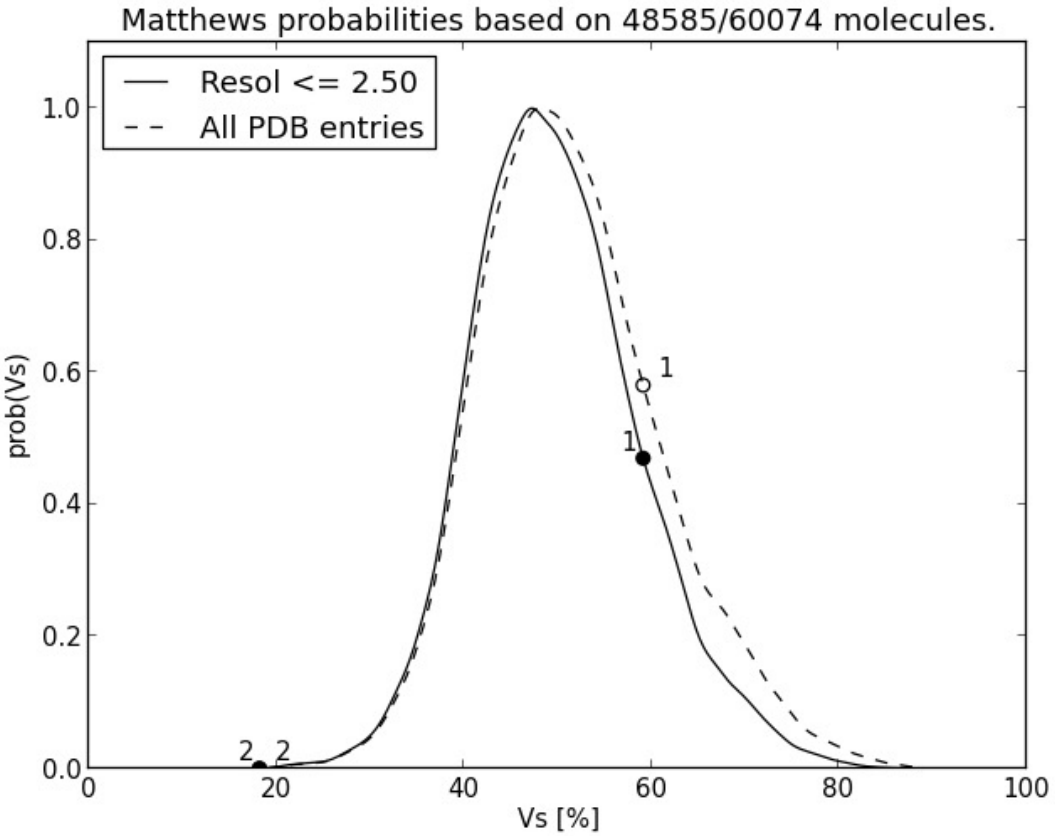

Figure 5.3. Matthews coefficient analysis and plot of ParA2$_{vc}$-apo crystal form from data collection.
The Matthews coefficient analysis predicts that 1 molecule are most likely to be present in the asymmetric unit. With a probability of 0.9996, the Vm is ~3 with a solvent content of 59.1%. The other possibility predicted is 2 molecules per asymmetric unit, with a Vm of 1.5 and solvent content of 18.2%, however the probability is extremely low at > 0.001%.

5.2.2 Phasing of ParA2-APO

Starting with the P1 ParA crystal structure as a template, various molecular replacement models were produced with differing N-terminal truncations, as molecular replacement failed with the whole molecule. From these, Phaser found a molecular replacement solution from a model of P7 ParA (3EZ9) missing the first 107 amino acids (**Figure 5.4**), producing an initial top LLG of 63.2, a TFZ of 9.6 with 1 $ParA2_{vc}$ molecule per asymmetric unit (asu), as previously estimated by the Matthews coefficient. From this starting point, an iterative process began whereby robetta and swiss-model servers homology models' N-termini were selected and fused onto successful Phaser models, to help build the N-terminal domain removed from the original molecular replacement model (**Figure 5.4**). Once the model was improved, this was used to phase the diffraction data for the ADP co-crystallised data set.

While there being only 1 molecule per asu, when we generate the crystal packing (**Figure 5.5**), we can see that $ParA2_{vc}$ forms a symmetry related pair with another monomer, resulting in a crystallographic dimer (see below).

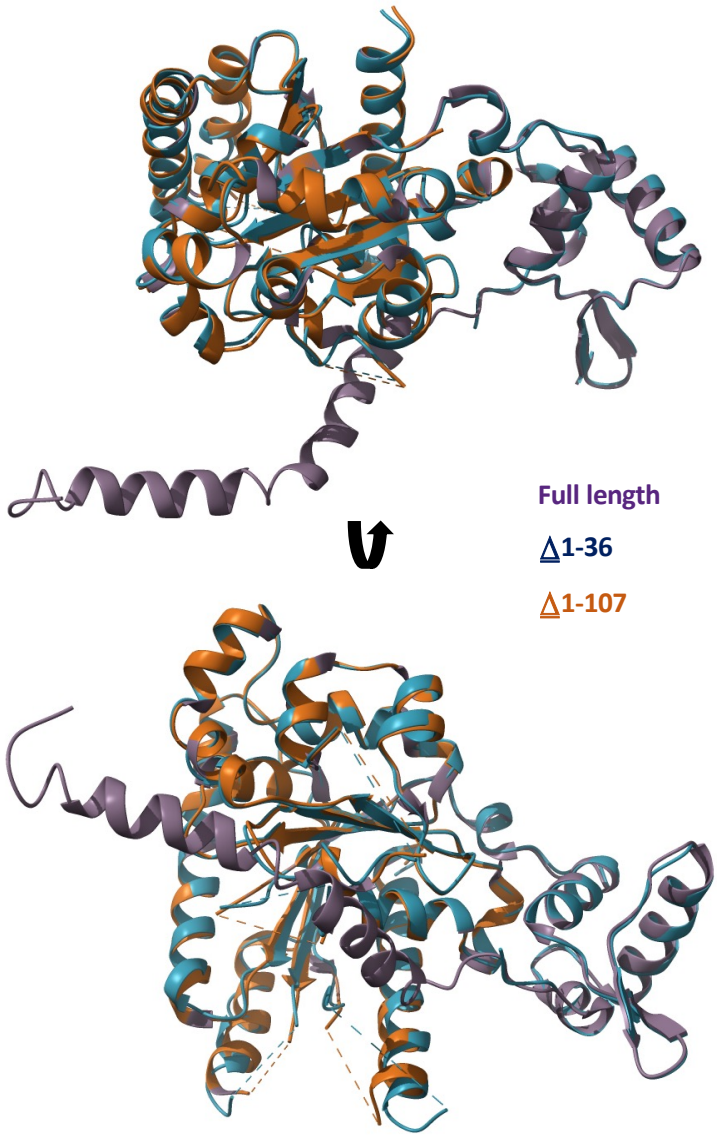

Figure 5.4. N-termini truncations on molecular replacement model P7 ParA (3EZ9).
Each truncation in a different colour and aligned to the full length (purple). The Blue truncation is the removal of the N-terminal helix alone (first ~36aa), the orange truncation is the removal of the N-terminal domain found in type Ia ParAs (first ~107aa).

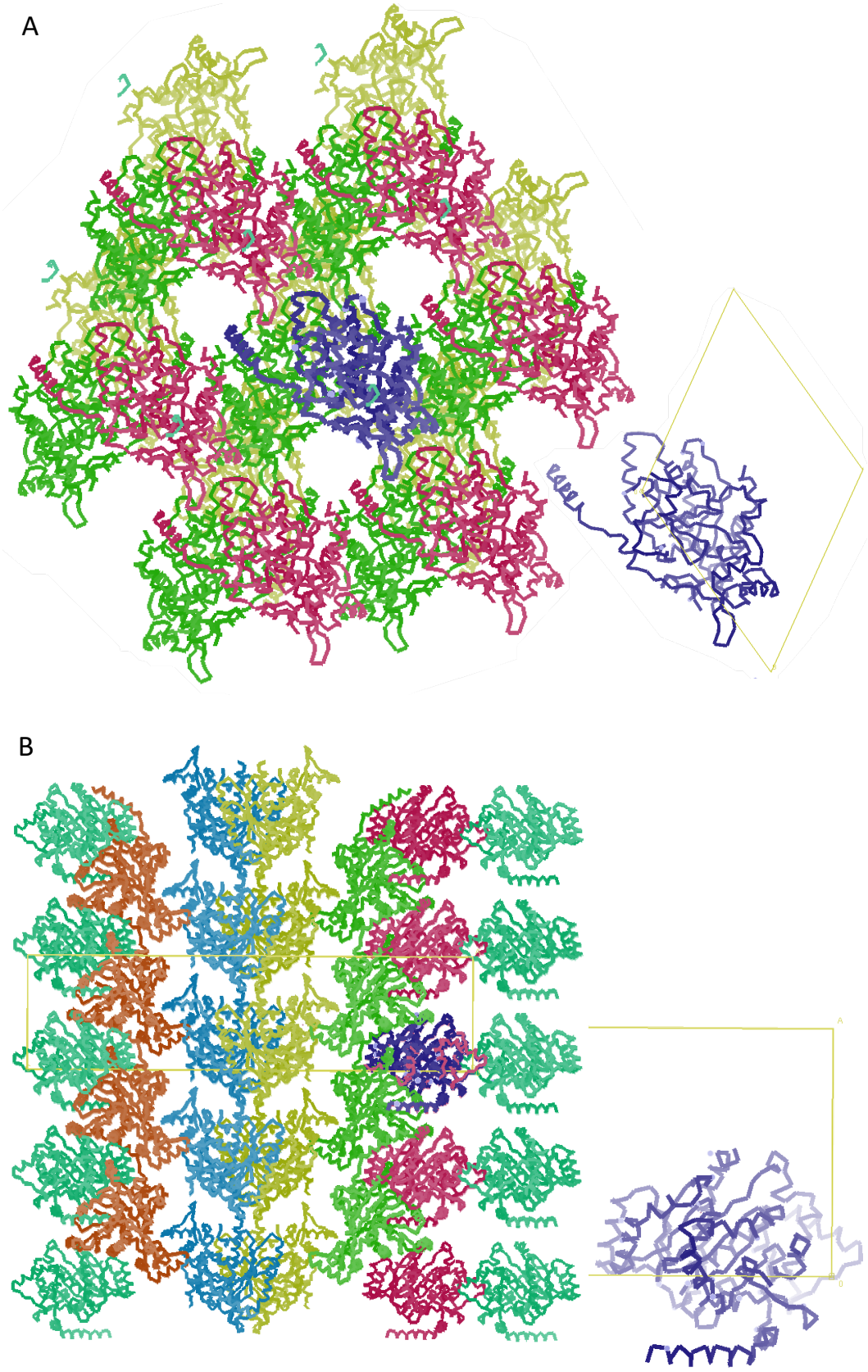

Figure 5.5. Unit cell crystal packing of ParA-apo with asymmetric unit.
(A) *Along the C axis, showing P3 symmetry, with the asu (left) showing the orientation of the one molecule, the crystallographic dimer can be seen in green and pink (or purple).* ***(B)*** *Along the B axis with 2-fold symmetry, the unit cell (left) showing the one molecule per asu.*

5.2.3 Building and refinement

Throughout the process of phasing (5.2.2), the N-terminal domain was slowly built into the free density manually using Coot along with iterative cycles of refinement, auto-building, and Phaser. Refinement began by refining with grouped B-factors and as the map improved the B-factors were refined individually along with restraining using secondary structure restrains and TLS parameters, resulting in final Rwork/Rfree values of 27.5%/33.5%, respectively (**Table 5.2**).

Throughout the refinement process, the atomic model generated was used to attempt at phasing and refining against the 2.8 Å data set from the apo crystal diffraction (**table 5.1**), to see if there were any improvements. However, this proved to be unsuccessful, with the refinement statistics often being worse while still at a lower resolution.

5.2.4 Structure of ParA2$_{vc}$ in the apo conformation

The overall structure of the ParA2$_{vc}$ monomer (**Figure 5.6a)** is similar to that of P7 ParA, with an overall RMSD of 2.2 Å for CA atoms. In particular, the N-terminal HTH domain resembles that of P1 and P7 ParA, confirming that ParA2$_{vc}$ belongs to the type Ia family (**Figure 5.6**). No ligand density was observed in the active site, confirming that this structure corresponds to the apo state of the protein. It is worth noting that the nucleotide binding site is generally poorly resolved, and in particular, the P-loop could not be built in this structure.

As mentioned above, SEC-MALS and negative stain EM data (**Chapter 3**) has shown that ParA2$_{vc}$ is able to form dimers in the absence of nucleotide, at least at high concentration. Therefore, it was questioned if crystallographic symmetry-related ParA2$_{vc}$ molecule pairs might recapitulate the biological dimer. As shown on **Figure 5.6b**, one of the symmetry-related pairs is consistent with a biological dimer, and largely resembles the P7 ParA dimer structure. This suggests that the structure of the ParA2$_{vc}$ dimer has been obtained through crystallographic symmetry, having an interface area of 2326 Å with a 32260sq Å and a 4650sq Å surface and buried area, respectively (calculated via PDBePISA (Krissinel & Henrick, 2007)).

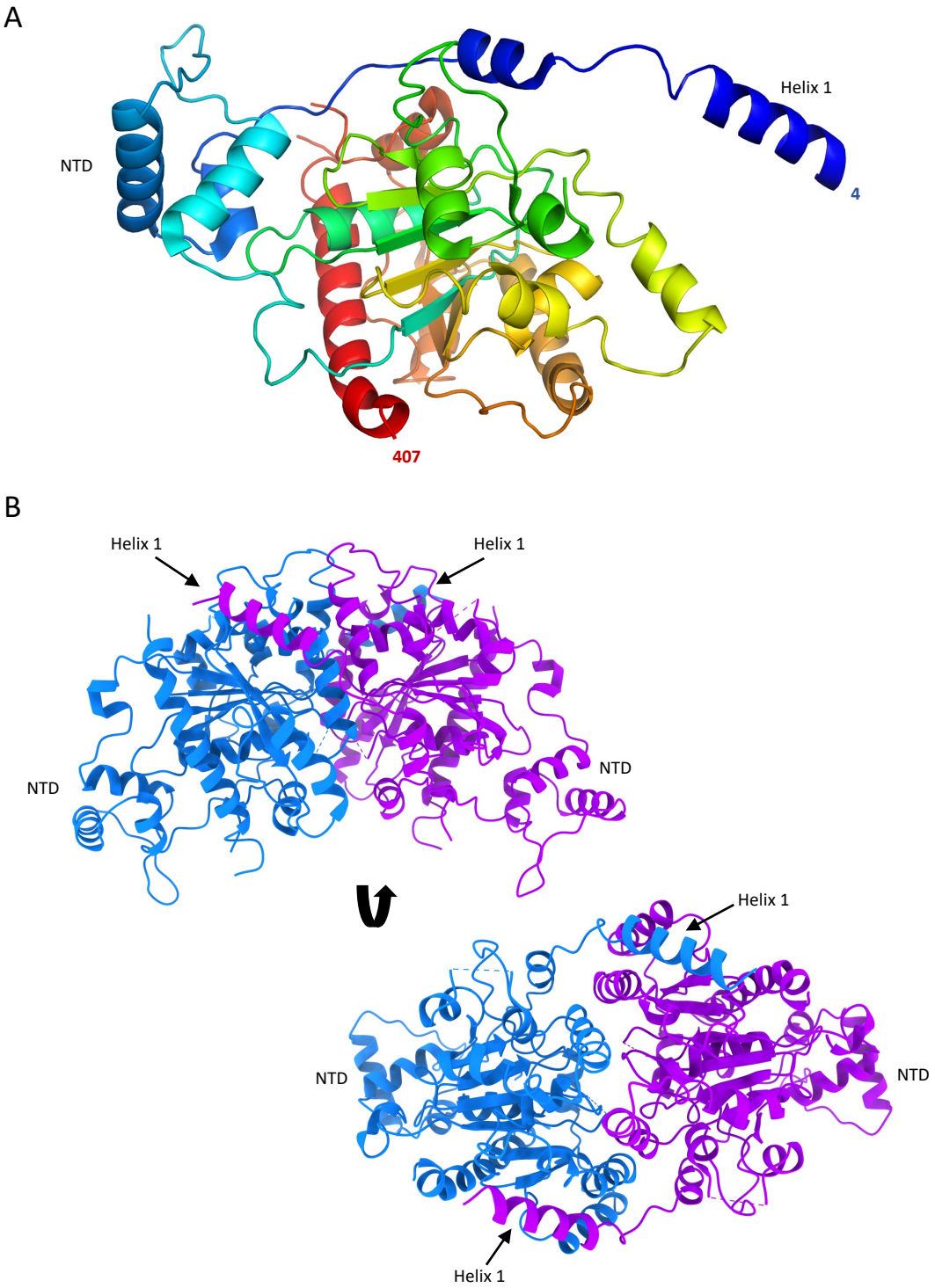

Figure 5.6. Structure of the ParA2$_{vc}$ monomer and dimer.
(A) *Cartoon representation of the ParA2$_{vc}$ crystal structure, in rainbow coloring, starting from blue at the N terminus, to red at the C terminus.* ***(B)*** *The crystallographic dimer of ParA2$_{vc}$ shown from the side (left) and top (right), with the two symmetry-related pairs in blue and magenta, respectively. The NTD and helix 1 are indicated.*

What is apparent about the $ParA2_{vc}$ apo structure is that the quality of the data is very poor. Despite diffracting to a moderate resolution (2.5 Å), the refinement statistics are substandard (**table 5.1, table 5.2**). The bond angles (º) are above 1 at 2.33 which is high, along with the favoured Ramachandrans being low at 83.11%, 13.19% being allowed and 3.69% outliers. This could be due to the poor electron density at various regions of the map, particularly where there may be unstructured regions and flexible loops of the sequence.

Nonetheless, overall, this structure confirms the common architecture of ParA proteins, and is consistent with the fact that the *V. cholerae* chromosome 2 is plasmid-like, as suggested previously (Kirkup et al., 2010), since the $ParA2_{vc}$ structure confirms that it belongs to the type Ia family.

5.3 Crystallography of ParA2 with nucleotide

Previous studies on the type Ia P1/P7 ParA suggested structural rearrangements of the ParA dimer upon binding to ATP (Dunham et al., 2009). We therefore sought to identify if the $ParA2_{vc}$ structure was altered in the presence of nucleotide. As indicated above, crystallization trials were also performed in the presence of ADP, ATP, and the non-hydrolysable ATP analogue ATPγS. While crystals grew and diffracted in all co-crystallization experiments, for ATP and ATPγS the crystals possessed the same crystal form as the apo structure described above, and no nucleotide was observed in the active site for these.

5.3.1 Crystallisation and data collection

Nonetheless, one dataset collected on a crystal obtained in the presence of ADP showed a different space group. Data was collected from a crystal grown in the ADP co-crystallisation trial from well D1 of JCSG+ at 4ºC, diffracting to ~3.1 Å (**Figure 5.7**).

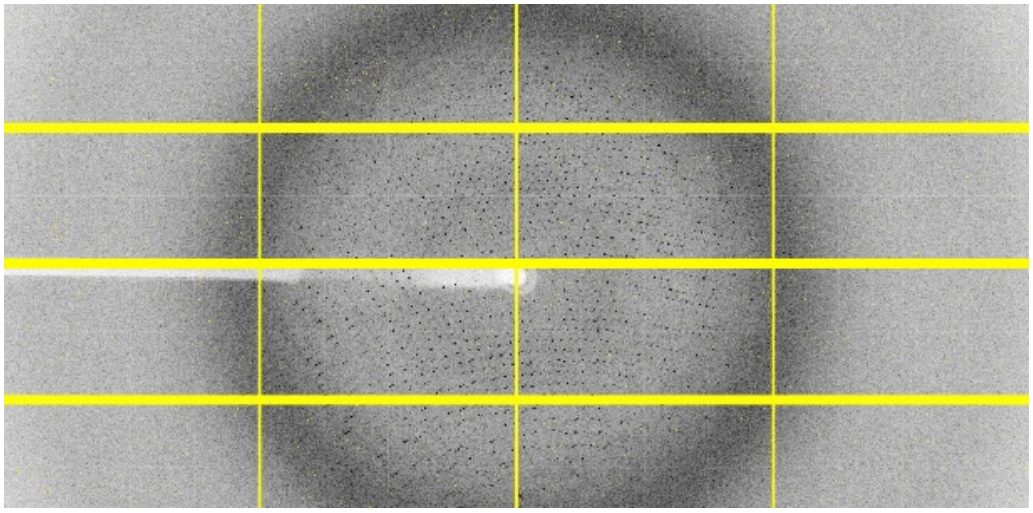

Figure 5.7. $ParA2_{vc}$-ADP diffraction pattern.
A diffraction pattern collected from the crystal which was analysed for the ADP data set.

From the auto-processing pipeline, the data was indexed to the space group $P6_1$ 2 2 with the unit cell dimensions of a=199.21 b=199.21 c=260.07 Å, 90 90 120° (**table 5.1**). When the collection parameters were applied to calculate the Matthews probability, 4 to 10 molecules were predicted as probable component numbers, 6 to 8 being the highest (**Figure 5.8**). Because of this, molecular replacement using a range

of numbers of molecules for the search were attempted. Through this, 4 molecules per asu were determined, with The Matthews coefficient calculating 4.63 $Å^3Da^{-1}$ for the volume of the ASU, with a 73.45% solvent content (**Figure 5.8**).

N(mol)	Prob(N) for resolution	Prob(N) overall	Vm A**3/Da	Vs % solvent	Mw Da
1	0.0000	0.0000	18.53	93.36	46388.00
2	0.0006	0.0014	9.27	86.73	92776.00
3	0.0065	0.0090	6.18	80.09	139164.00
4	0.0267	0.0311	4.63	73.45	185552.00
5	0.0663	0.0717	3.71	66.82	231940.00
6	0.1465	0.1487	3.09	60.18	278328.00
7	0.2542	0.2516	2.65	53.54	324716.00
8	0.2857	0.2785	2.32	46.91	371104.00
9	0.1682	0.1637	2.06	40.27	417492.00
10	0.0384	0.0374	1.85	33.63	463880.00
11	0.0059	0.0058	1.68	27.00	510268.00
12	0.0010	0.0010	1.54	20.36	556656.00
13	0.0000	0.0000	1.43	13.73	603044.00

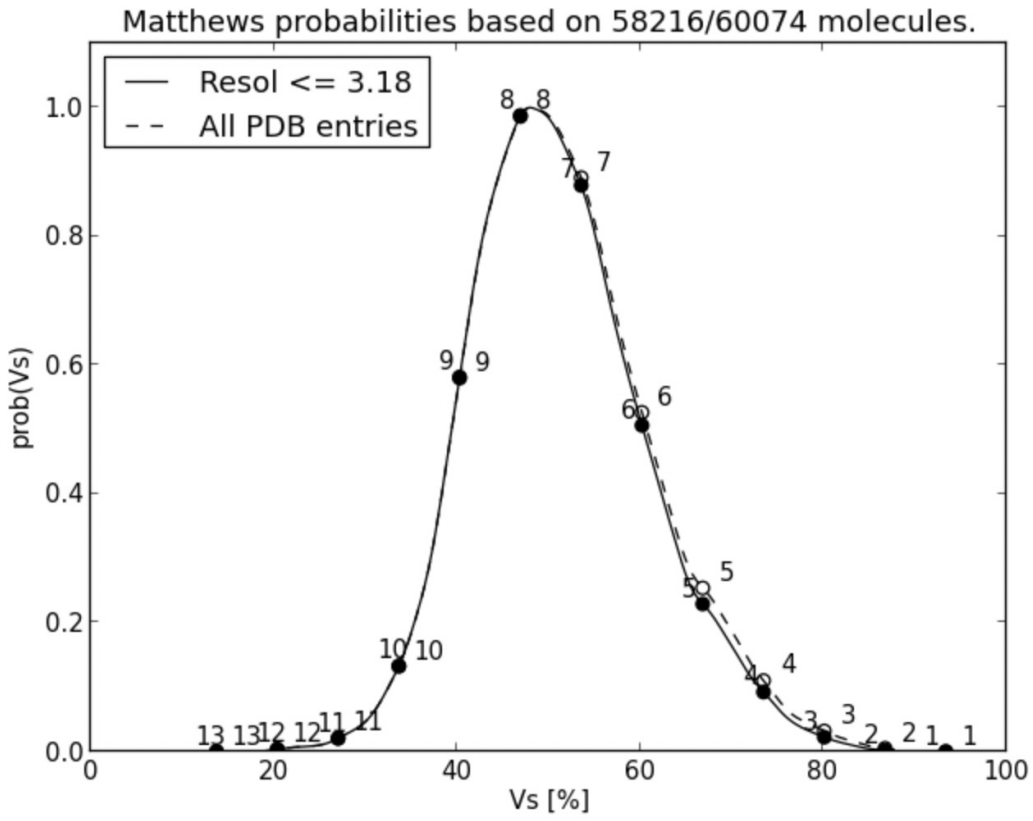

Figure 5.8. Matthews coefficient analysis and plot of ParA2$_{vc}$-ADP crystal form from data collection.
The Matthews coefficient analysis predicts from 1 to 13 molecules to be present in the asu, with 6 to 9 molecules having the highest probability. The highest probability, at ~28%, is 8 molecules per asu, having a Vm of 2.32 and solvent content of 46.91%. From molecular replacement, 4 molecules per ASU was found. Having a Vm of 4.63 and solvent content of 73.45%, despite the probability being ~2.6%.

5.3.2 Phasing, building and refinement

5.3.2.1 Processing using anisotropic correction

Initial diffraction statistics provided by the auto-processing pipeline during diffraction collection showed an improvement in resolution upon anisotropic correction, therefore, phasing began on the AutoProc +StarAniso auto processed data set. Since The Matthews coefficient did not permit to unambiguously determine how many molecules were in the ASU (see above), a variety of component copy numbers for trialled using the $ParA2_{vc}$ atomic model (**5.2.4**) as the molecular replacement template. Using this template, a molecular replacement solution was found with a top LLG of 3035.185 and TFZ of 45.4 when 4 component copy numbers were searched for. The phasing step therefore revealed that the asymmetric unit consists of two $ParA2_{vc}$ dimers (**Figure 5.9**). Alike to the $ParA2_{vc}$-apo data set, the atomic model was built and refined through an iterative process, manually deleting and rebuilding sections of each molecule chain between refinement cycles. The refinement process began with B-factors being grouped and using NCS (non-crystallographic symmetry) to refine all 4 molecules the same way. As the refinement statistics improved, the B-factors were refined individually, and NCS was turned off so each molecule could be refined separately, allowing for comparisons to be made between chains. The final atomic model with the data collection cut to 3.2 Å produced the Rwork/Rfree values of 0.213/0.268 with Ramachandran statistics of 85.63%/11%/3.37% for favoured, allowed, and outlier conformations respectively. Despite the lower resolution, the refinement statistics aren't as polished as we would like (**Table 5.2**). For example, the completeness of the data is low at 82.64% with only 20.50% in the high-resolution shell, and a Ramachandran favoured of 85.63% is too low, especially with 3.37% being outliers.

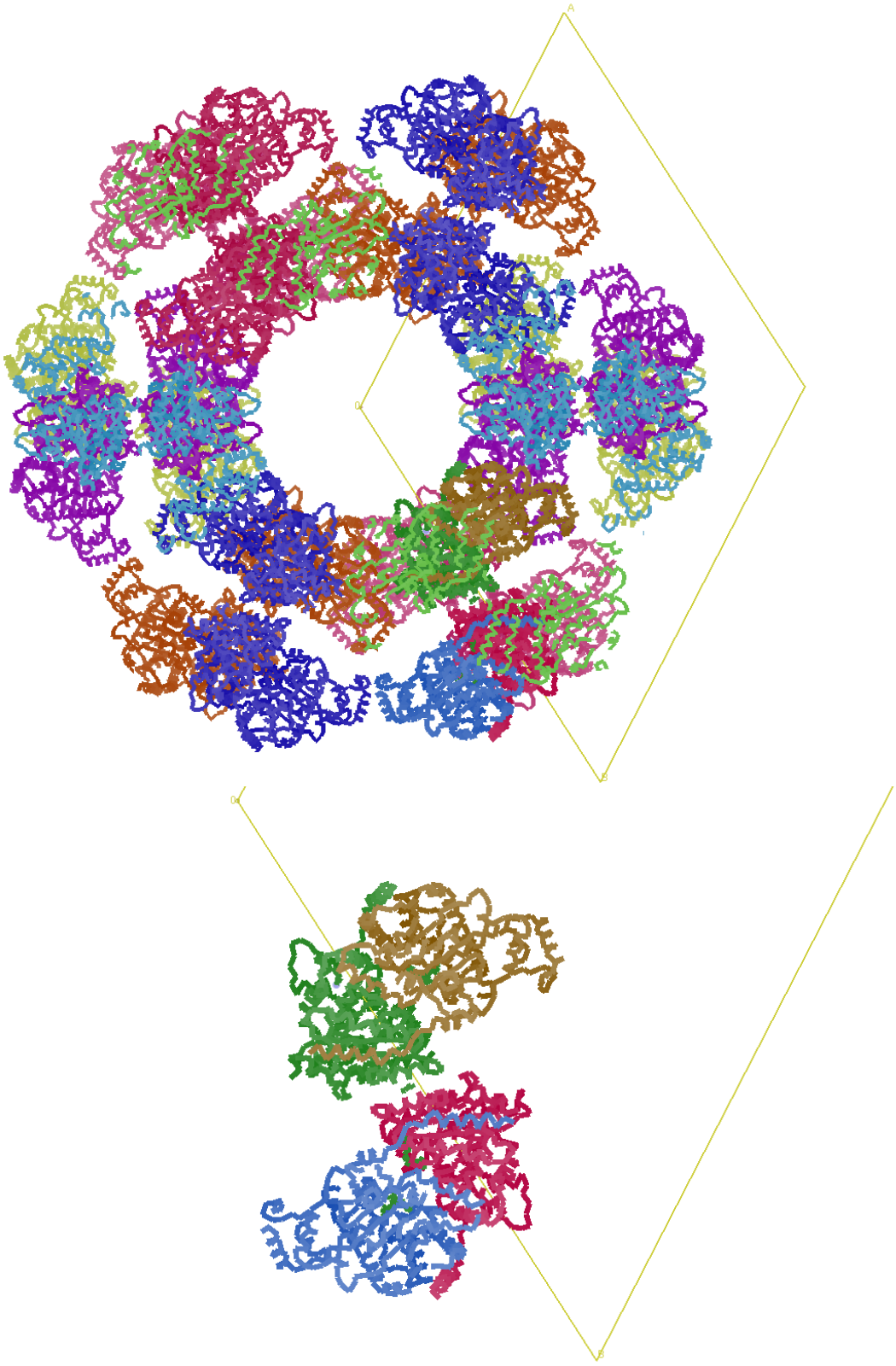

Figure 5.9. Unit cell crystal packing of ParA-ADP with asymmetric unit.
Along the C axis, showing P6 symmetry, with the asu (left) showing the orientation of the one molecule, the crystallographic dimer can be seen in green and pink (or purple). ***(B)*** *Along the B axis with 2-fold symmetry, the unit cell (left) showing the one molecule per asu.*

5.3.2.2 Processing without anisotropic correction

Since the final refinement statistics from the AutoProc + StarAniso auto indexed data collection seemed too poor, despite much refinement and manual editing, the AutoProc auto-processed data collection was retrieved to see if it would be of any better quality. This auto-processing pipeline was chosen as the resolution was similar at 3.18 Å and the completeness at collection is higher than that from the AutoProc + StarAniso pipeline, due to data being lost during anisotropic correction. Molecular replacement was performed using the final refinement from the previous data collection and produced a top LLG of 12252.898 and TFZ of 129.3. The atomic model went through some iterative rounds of real-space and regular refinement while being manually edited in coot. The final model refined against this auto-processed data collection was an improvement from the previous (see above). Although there is no improvement regarding the Rwork/Rfree (0.2395/0.2812), the completeness of the data is much better at 96.38%, with 66.68% in the high-resolution shell. There are also minor improvements with the Ramachandran statistics, increasing to 88.85% favoured conformation with 9.57% allowed and 1.58% outliers. The clashscore was also improved from 24.36 to 15.05.

5.3.3 Fixing the geometry using ISOLDE

Once it was deemed that the geometry statistics couldn't be improved anymore through refinement on Phenix, Isolde was used through ChimeraX to see if this could amend poor residue conformations (**2.7.4.2**). Running on each chain separately, the final refinement statistics were improved for the Ramachandran plot. The favoured increased to 91.51%, allowed to 6.84% and outliers still being a little too high at 1.65%. The clashscore was also slightly improved, lowering from 15.05 to 12.07. All of the final refinement and data collection statistics can be seen on **Table 5.2**.

	apo	ADP-bound		
Data collection		**AutoProc + Santariso**	**AutoProc**	
Resolution range (Å)	38.31 - 2.601 (2.694 - 2.601)	48.91 - 3.2 (3.314 - 3.2)	48.91 - 3.184 (3.298 - 3.184)	
Space group	P 32 1 2	P 61 2 2		
Unit cell	63.247 63.247 214.373 90 90 120	199.205 199.205 260.066 90 90 120		
Total reflections	28240 (1378)	83924 (2044)	99408 (6728)	
Unique reflections	14120 (689)	41962 (1022)	49704 (3364)	
Multiplicity	2.0 (2.0)	2.0 (2.0)		
Completeness (%)	91.02 (44.89)	82.64 (20.50)	96.38 (66.68)	
Mean I/sigma(I)	36.81 (1.85)	25.61 (1.75)	21.69 (0.98)	
R-merge	0.01654 (0.3752)	0.02751 (0.3801)	0.02072 (0.5636)	
CC*	1 (0.932)	1 (0.933)	1 (0.891)	
Refinement				**ISOLDE refined**
R-work/R-free	0.2743/0.3353	0.2130/0.2683	0.2395/0.2812	0.2380/0.2779
Number of non-hydrogen atoms	2946	12382	12065	12065
macromolecules	2899	12251	11941	11941
ligands	0	129	124	188
Water	47	0	0	0
Protein residues	388	1600	1608	1602
R.M.S deviation				
Bond length (Å)	0.017	0.011	0.004	0.0031
Bond angle (◦)	2.33	1.39	0.8	0.78
Ramachandran plot				
Favored (%)	83.11	85.63	88.85	91.51
Allowed (%)	13.19	11	9.57	6.84
Outliers (%)	3.69	3.37	1.58	1.65
Average B-factor	85.4	98.49	124.17	124.12
macromolecules	85.74	98.77	124.61	124.56
ligands	/	71.84	81.66	81.66
water	64.4	/	/	/
Clashscore	44.07	24.36	15.05	12.07

Table 5.2. X-ray crystallography data collection and refinement statistics.
The apo data collection shows the statistics from collection to the final refinement. The ADP collection shows the different auto-processed collection and refinement statstics as well as the geometry refinement statistics.

5.3.4 ParA2-ADP structure

The final structure of the ParA2$_{vc}$ dimer can be seen in **Figure 5.10**, each monomer coloured differently with the ADP nucleotide in view. There is very little difference (RMSD ~ 0.3 Å) between the two ParA2$_{vc}$ dimers contained in the ASU (**Figure 5.11a**), as well as in the relative subunit orientation between both dimers. Ligand density was observed in the active site of all four molecules (**Figure 5.12a**), confirming that this structure corresponds to the ADP-bound state of the protein, with the position of the nucleotide being largely similar to that of other ParA orthologues (**Figure 5.12b**).

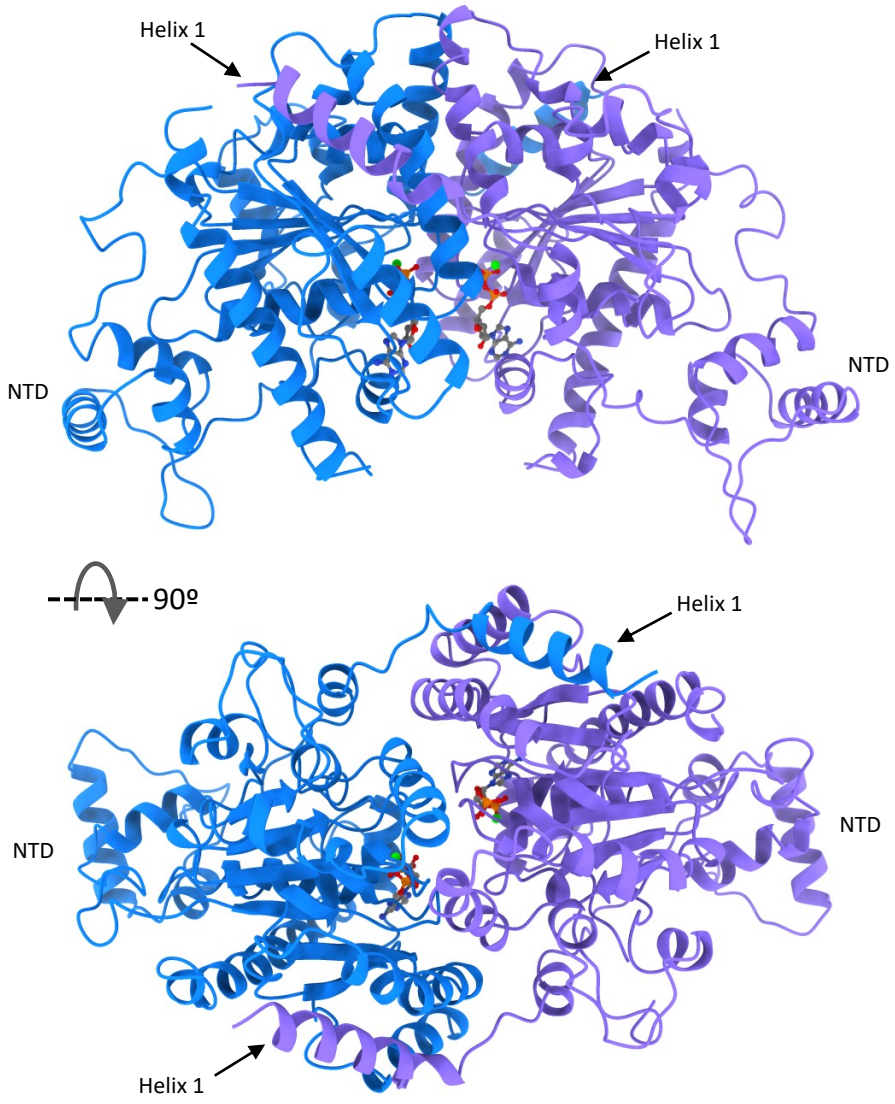

Figure 5.10. Structure of ParA2$_{vc}$ bound to ADP.
Cartoon representation of the ParA2$_{vc}$-ADP crystal structure, the NTD and helix 1 are indicated. The ADP and Mg are present in each ParA2$_{vc}$ molecules' binding site, shown in sticks and sphere representations respectively.

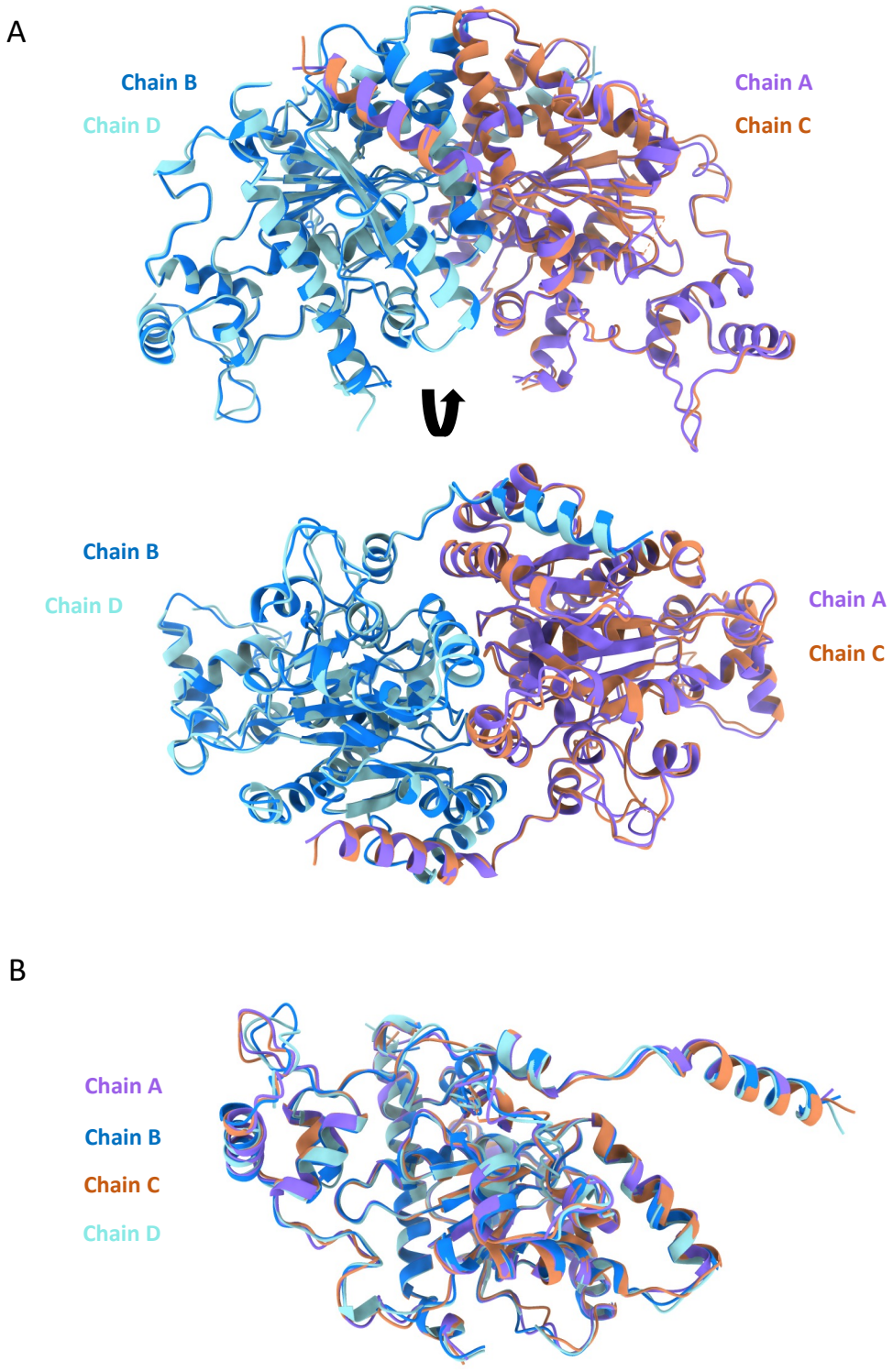

Figure 5.11. Comparison of chains in the ParA2$_{vc}$-ADP asymmetric unit.
(A) *Cartoon representation of ParA2$_{vc}$-ADP dimers. Side (top) and top (bottom) views of the two dimers in the ASU overlayed, dimer 1 consisting of chains A and B (Purple and deep blue), dimer 2 C and D (orange and light blue).* ***(B)*** *Overlay of all 4 chains, coloured as in (A). All four chains only show minor variations in loop regions, and the dimeric architecture is the same for the two dimers.*

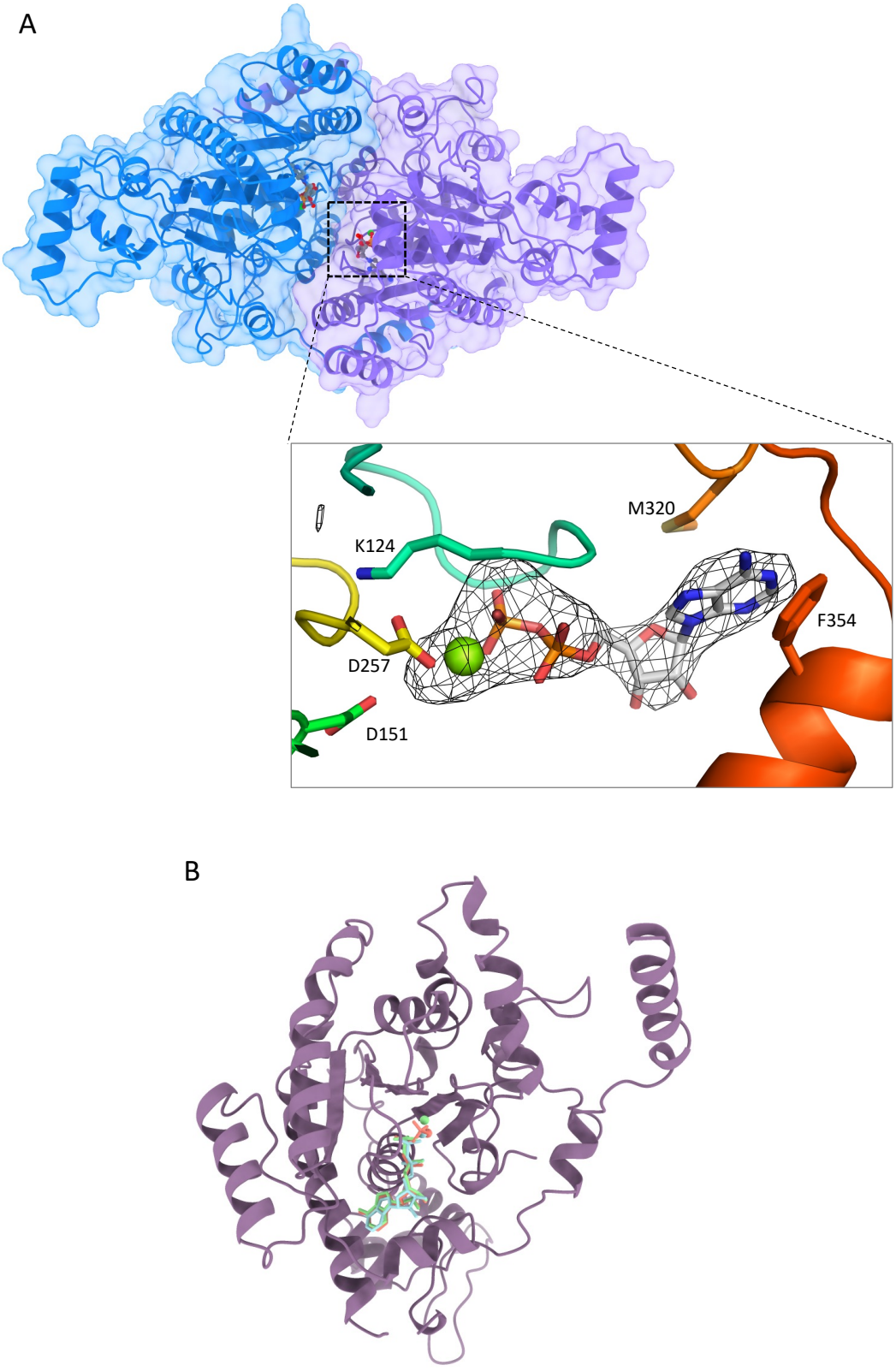

Figure 5.12. ADP binding of ParA2$_{vc}$.
(A) *Cartoon representation of ParA2$_{vc}$-ADP dimer inside a transparent surface representation, the ADP and Mg molecules are shown In sticks and sphere representation, respectively. A close-up view of the ADP and Mg in one molecule with the composite omit map (below) is shown. Residues that interact with the nucleotide and Mg are shown in sticks.* ***(B)*** *Comparison of nucleotide binding with ParA orthologues. The structure of ParA2$_{vc}$ is in purple, with the bound ADP molecule in cyan. The nucleotide in overlaid P1 ParA structure (ADP:PDB ID 3ZE6) and in hpSoj (ATP:PDB ID 6IUB) are in green and orange, respectively. The nucleotide is positioned similarly in all three structures.*

As expected, the overall structure of the ParA2$_{vc}$ monomer in the ADP-bound state is similar to that of the apo structure (**Figure 5.13**), with a RMSD of ~ 0.8 Å. I do note some changes in the nucleotide binding site, with the P-loop being better ordered in the ADP-bound conformation. In addition, a change in the positioning of the helix 1 is observed, which is closer to that of P1/P7 ParA in the ADP-bound structure. As indicated above, helix 1 forms a domain-swapping interaction with the adjacent molecule in the ParA dimer (**Figure 5.10**). Because of the difference in the position of this helix, the architecture of the ParA2$_{vc}$ dimer differs between the ParA2$_{vc}$ apo and ADP-states (**Figure 5.13**), with a slight shift in the relative subunit position between the two states, indicated by the arrow.

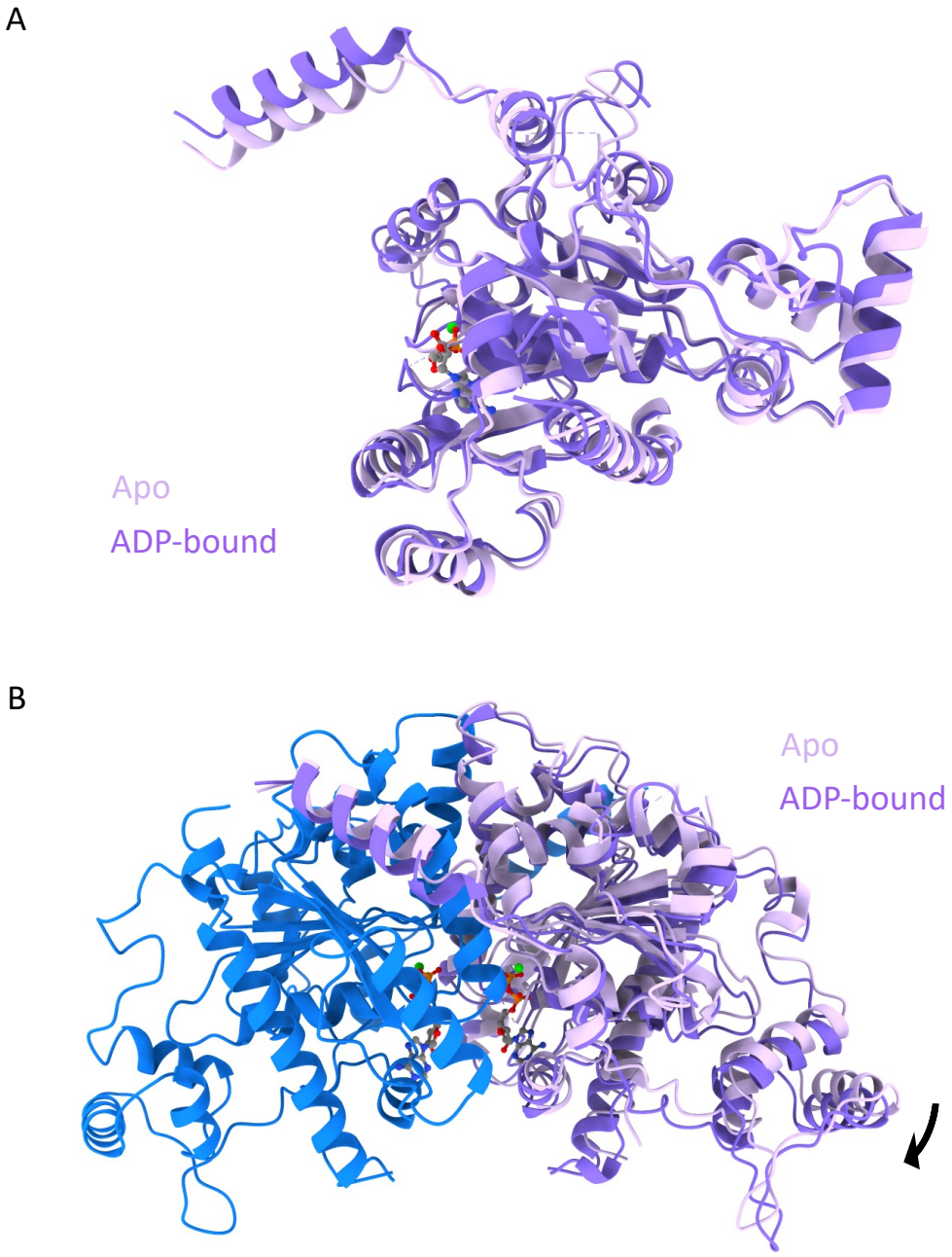

Figure 5.13. Comparison of the ADP bound and apo ParA2$_{vc}$ structures.
(A) *Aligned monomers from apo ParA2$_{vc}$ (light pink) and ADP bound (purple).* ***(B)*** *Aligned dimers, overlaid on the blue subunit (apo), the light pink and purple subunits show the change in molecule conformation between nucleotide states against the other molecule (blue).*

5.4 Discussion

The quality of the data collected made building and refinement of both crystal structures, but particularly Apo-ParA2$_{vc}$ a very taxing process. The calculated Matthews coefficient was strongly in favour of one molecule per asymmetric unit (asu) (**Figure 5.3**), with the probability being 0.9996 both for the resolution and overall. This made phasing slightly simpler, as it was already known that only one component copy was needed to be searched for, however finding a suitable molecular replacement model proved to be difficult. The list of models used and made for molecular replacement is extensive, including many homology models made from various softwares. However, the P1 ParA monomer was chosen over other type Ia solved structures for a few reasons. Firstly, it was solved in an APO conformation, with the pdb file only containing Mg^{+2}. This was useful as we expected that if there is similarity between how ParA2$_{vc}$ forms a dimer in the absence of nucleotide, especially the conformation of the N-terminal helix, then there was a higher probability that would be with this structure (3EZ9) than others. Although there was also an apo form of P1 ParA (3EZ7) available, to which ParA2$_{vc}$ shares a slightly higher sequence similarity, the structure exhibits a strange dimer conformation, presented as "domain swapping interactions". This non-traditional dimer conformation seems unlikely to be relevant to ParA2$_{vc}$, and is suspected of being non-physiological and as result of low pH conditions during crystallisation (Dunham et al., 2009).

When we compare the nucleotide bound structure to that of apo, there is a very minimal difference between the two (**Figure 5.13**). As described, the nucleotide binding site is in a more ordered conformation when bound to ADP, this made building into the electron density much easier than the apo map, despite the lower resolution. I therefore propose that the inherent flexibility of the apo dimer is the reason behind the low-quality electron density and therefore the difficulty in atomic model building. This is a feature which is also observed in type Ia apo orthologues, P1 and P7 ParA also exhibiting relatively poor refinement statistics. P1 at a 2.9 Å resolution having a high clashscore of 36 with 4.2% Ramachdran outliers and 13.5%

sidechain outliers, P7 at 2.8 Å with a clashscore of 24 with 2.5% Ramachandran outliers and 10.2% sidechain outliers. Despite the lower resolution of 3.2 Å, the ADP bound dimer has better electron density quality, which made building and refinement much easier. Thereby, I propose that the binding of nucleotide may help to stabilise the dimer conformation. This is also in agreement with thermal melting assay data, which suggests a stabilization of $ParA2_{vc}$ in the presence of nucleotide (Chodha et al., 2021).

Overall, $ParA2_{vc}$ adopts a very similar dimer architecture to other ParAs, both type Ia and Ib (**Figure 5.14**). The main body of the monomers encapsulating a β-sheet with α-helices, with the nucleotide binding pocket in the same position (**Figure 5.12**). ParAs dimerise along the same interface, with a slight differences in the chain orientations between orthologues. In the case of type Ia ParAs, the N-terminal domain shows a more varied positioning from the main body of the protein. The N-terminal helix is more unique to each individual species, $ParA2_{vc}$ being more flexible and unstructured compared to P7, while also positioned differently along the side of the monomer. Overall, this leads to differing chain orientations from each other, which can be seen when chain A from each orthologues are aligned and view the positioning of the B chains (**Figure 5.14**).

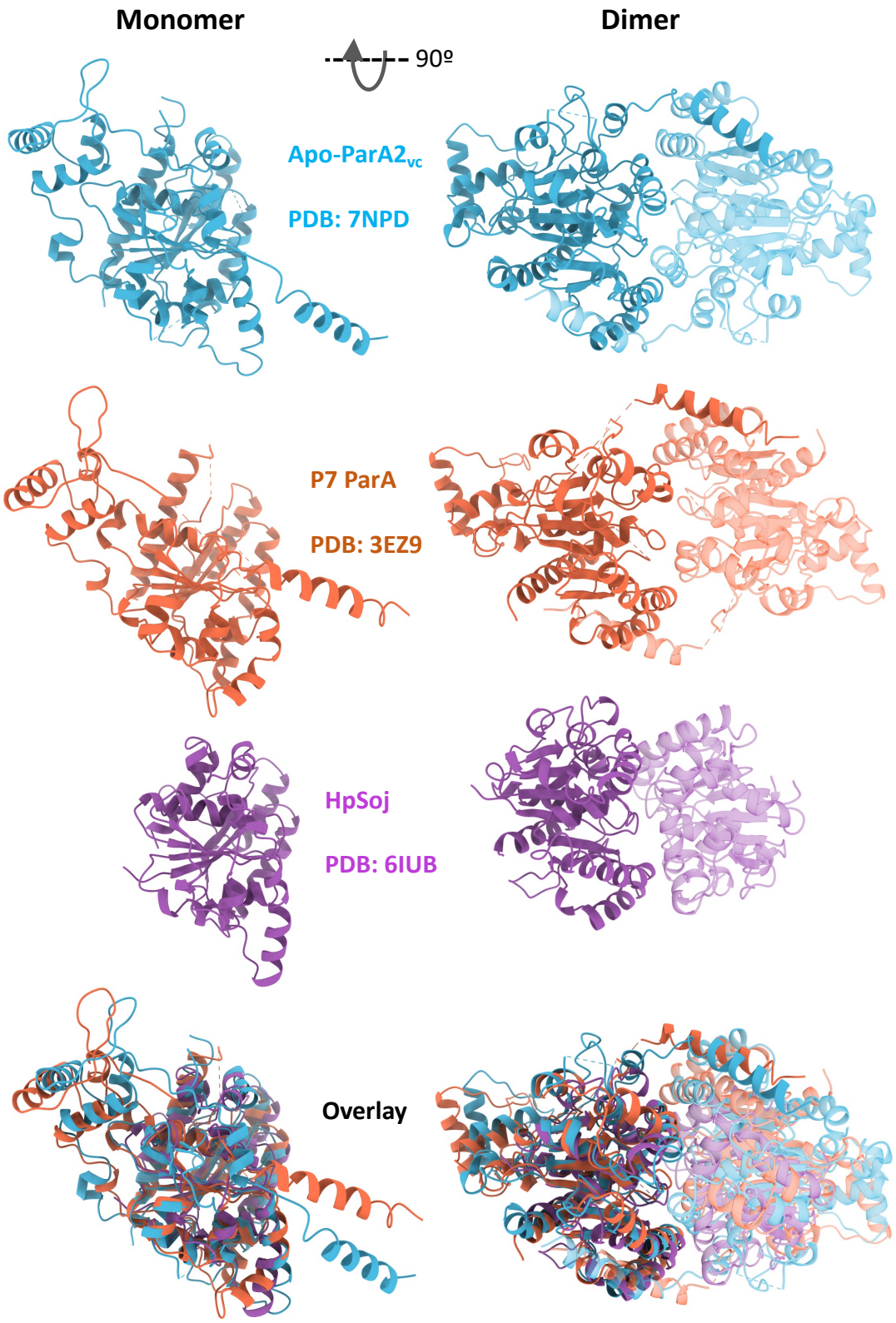

Figure 5.14. Comparison of ParA structures across bacterial species.
A monomer (left) and dimer (right) is shown for the structures of ParA2$_{VC}$ (cyan), the E.coli P7 plasmid ParA (orange), and $_{Hp}$Soj (purple). All three structures are aligned at the bottom, on the left chain for the dimer.

5.5 Conclusion

In this chapter I have discussed the process by which the apo and ADP bound state of $ParA2_{vc}$ dimers were solved by x-ray crystallography. From their similarity in structure we can conclude that $ParA2_{vc}$ is able to form a dimer in the absence of nucleotide, as evidenced by SEC-MALS (Chodha et al., 2021) and negative-stain EM. Furthermore, $ParA2_{vc}$ undergoes a very minimal conformational change under nucleotide binding and exhibits only a stabilisation of the already formed conformation. From the difficulty in model refinement, it could be understood that although ParA is able to form dimers independently, the resulting dimer may be flexible in nature and unstable, consistent with the theory ParA is able to dimerise and dissociate in equilibrium (Chodha et al., 2021; Vecchiarelli et al., 2010).

6 Results Chapter 4: Cryo-EM of ParA2$_{vc}$-ATPγS-DNA complexes

6.1 Introduction

ParA's ability to form filaments has been highly controversial. ParA filaments have been observed by negative-stain electron microscopy (EM) in the presence of nucleotide (Fogel & Waldor, 2006) and/or dsDNA (Chu et al., 2019; Hui et al., 2010; Leonard et al., 2005), but super-resolution fluorescence imaging in cells did not reveal filament formation in multiple systems, and a previously-reported crystal structures of ParA-DNA did not provide evidence for higher-order assembly (Chu et al., 2019; Zhang & Schumacher, 2017).

As reported in Chapter 4, no filament formation of ParA2$_{vc}$ was observed in the absence of DNA, regardless of nucleotide state. However, in the presence of both DNA and nucleotide, filaments were observed by negative-stain EM. Intriguingly, filaments with DNA were also not observed in the absence of nucleotide, contrary to a previous study (Hui et al., 2010). It was also noted that the ParA2$_{vc}$-DNA filaments could only be obtained at high protein concentration (protein-DNA ratio $\gtrsim$5:1 w/w), and that they dissociate at lower protein concentration (protein-DNA ratio $\lesssim$ 5:1 w/w). Furthermore, while the filaments are well ordered and with a clear helical architecture in the presence of ATP, when ADP was used, ParA was visibly bound to DNA, but lacked well-ordered filamentous architecture. In contrast, we were able to obtain stable filaments in the presence of the slow-hydrolysable ATP analogue ATPγS, which did not dissociate at lower protein concentration (Supplementary Figure 5a). From this negative stain data, it allowed us to understand that ParA2$_{vc}$ may differ in DNA binding, depending on nucleotide state, suggesting there may be a change in conformation between DNA binding and filament formation.

While filament formation of ParAs has been moderately studied using negative stain EM, further structural characterisation has been lacking. Currently, no type I ParAs have been solved forming higher order structures with DNA. This means however, that the most closely-related protein structure available in the filamentous form is the MinCD copolymeric filament, solved to 3.1 Å. As described in chapter 1, MinD is a part of the GTPase superfamily MinD/Mrb/ParA sub-family, adopting a deviant

Walker-A motif. This motif allows for homodimerization of the monomers; therefore, we might expect to see some similarity in dimer conformation between ParA and MinD. This makes the MinCD copolymeric filament the only comparable structure available, despite type II actin-like ParAs, for example AlfA, also being solved using cryo-EM (Szewczak-Harris & Löwe, 2018; Usluer et al., 2018).

In this chapter I am going to describe the process by which Cryo-electron microscopy was used to determine the structure of $ParA2_{vc}$ bound to DNA, to understand the interaction of ParA2 with DNA and with neighbouring dimers.

6.2 Grid optimisation and screening

From the work carried out in Chapter 4, it was concluded that ParA2$_{vc}$ filaments are more stable and able to survive negative-stain EM sample preparation while bound to the slowly hydrolysable analogue, ATPγS (**Method**). Using the same approach for sample preparation for cryo-EM, the ParA2-DNA mix was applied to carbon-coated copper grids varying in dilution from the from the non-diluted concentrated stock to a 10-fold dilution. However, even when the highest concentration was applied, no filaments could be seen in the ice. Instead, masses of aggregation were formed and DNA strands coating the carbon (**Figure 6.1**).

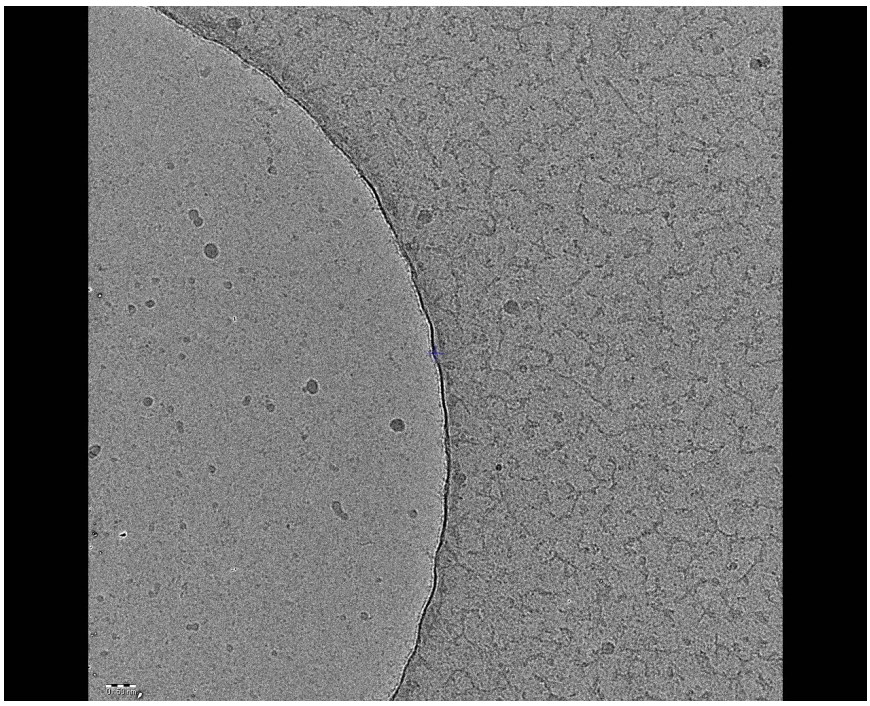

Figure 6.1. Cryo-electron micrograph of DNA attracted to the carbon.
Low magnification image of ParA2$_{vc}$-DNA sample on a quantifoil 2.1 holey carbon grid, the DNA in the sample is coating around the hole in the grid, lying on the carbon.

To obtain the ParA2$_{vc}$-DNA complexes into the ice and away from the carbon edges, numerous changes were attempted. These included lowering the glow-discharge time to reduce the charge attracting the DNA, introducing double-blotting, and adding detergent to sample prior to applying to the grid (**2.8.2.2**). Collectively, these changes were successful in viewing ParA2$_{vc}$-DNA filaments in the ice (**Figure 6.2**) and allowed for a data set to be collected (**2.8.2.3**). Despite filaments now being suspended in the vitreous ice, they are still at quite a low density and sample

preparation can be disruptive, causing shorter, segmented filaments (**Figure 6.2A**). The protein:DNA ratio was therefore increased along with the percentage of tween added to the sample (0.1% from 0.075%) (**2.8.2.1**), to reduce segmented filamentation and protect them during sample preparation. These filaments readily went into ice (**Figure 6.2B**), and a second dataset, using these improved conditions, was collected (**2.8.2.3**) (**Figure 6.2C**, **Table 6.1**).

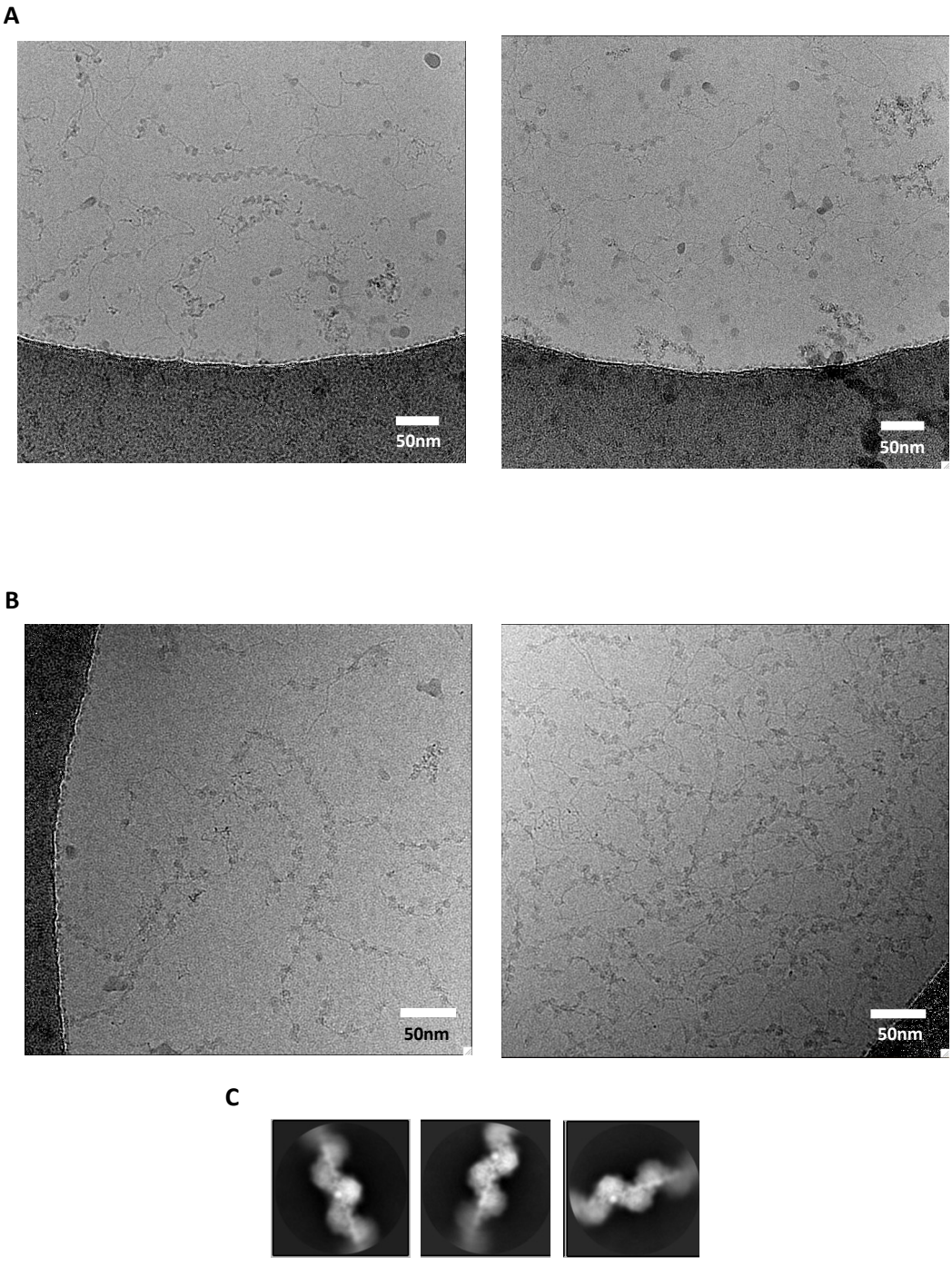

Figure 6.2. Representative cryo-electron micrographs from data collection taken at 105,000x and 130,000x magnification.
(A) *Micrographs taken at 105,000x magnification, showing an ideal ParA2$_{vc}$-DNA filament, surrounded by shorter segments (left), and a micrograph showing a more representative distribution of disturbed complexes (right).* ***(B)*** *Micrographs taken at 130,000x magnification, showing a clear formed ParA2$_{vc}$-DNA filament, with surrounding complexes (left), and a micrograph more representative to the complex distribution from the collection (right).* ***(C)*** *2D classification of manually picked particles from collection at 130,000x magnification (1.047 Å pixel size), the DNA can be seen down the middle of the classes.*

6.3 Cryo-EM data processing

6.3.1 Determining the helical symmetry

The initial data collection carried with a pixel size of 1.35 Å resulted in 3665 micrographs, which were motion-corrected, and the CTF for each micrograph was estimated. Following CTF estimation, particle picking was carried out manually followed by particle extraction using a range of box sizes (280 to 600 pixels) and helical rises. Each particle extraction was put into 2D and 3D classification to trial the above parameters and from this the particle extraction with a box size of 350pixels and helical rise of 90 Å was selected, due to the size of the ParA2 dimer, resulting in 28,310 extracted particles. 3D classification was carried out from this extraction, whereby multiple search ranges for helical twist and rise were applied (-80° and 25 Å to -190° and 80 Å). From this, 3D classification searching for a helical twist of -140° to -170° and rise of 50 to 65 Å produced the most promising reconstructions, producing 4 classes of low resolution (**Figure 6.3A**). Class 3 was selected for 3D refinement, converging on half-maps with an average helical twist of -159° and rise of 59 Å at 18.17 Å resolution (**Figure 6.3B**). Since the crystal structure of $ParA2_{vc}$ has not been solved yet, homology models of $ParA2_{vc}$ made using Phyre2 and were aligned to the map how I thought the dimers could be binding. Using the Eman script for converting atomic coordinates to volumes (Tang et al., 2007), a mask was created from the aligned molecules to be applied during refinement, however no increase in resolution was achieved.

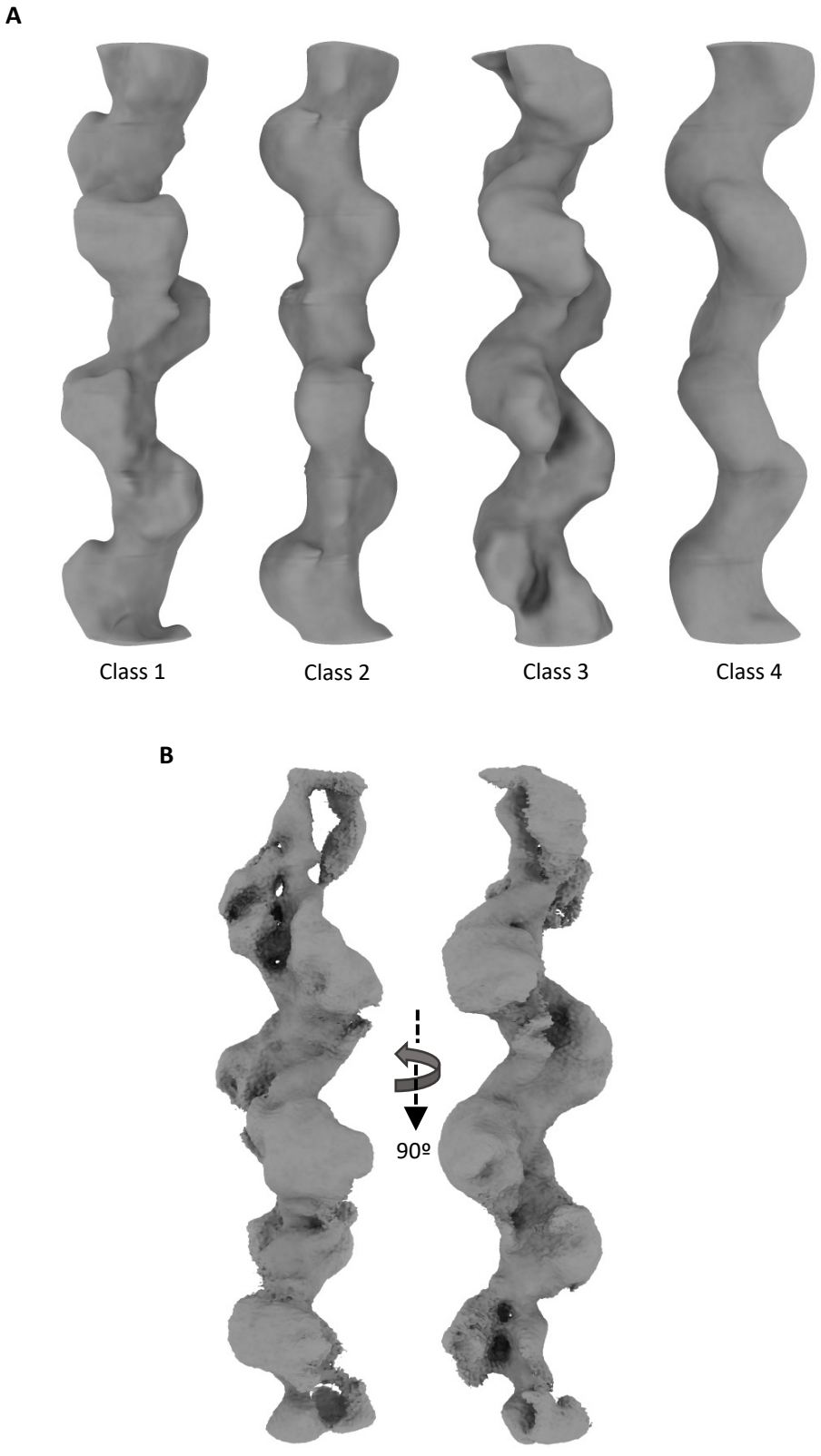

Figure 6.3. 3D classification and refinement of particles extracted with a 350pix box size from a 1.35 Å pixel size collection.
(A) *Classes produced from 3D classification applying helical reconstruction, particles from class 3 were selected for refinement.* ***(B)*** *Averaged helical reconstruction from 3D refinement, with a twist of -158.8 ° and rise of 59.8 Å at 18.17 Å resolution, the DNA can be seen down the centre of the reconstruction.*

Due to the low resolution and therefore uncertainty of the helical symmetry, a new particle extraction with a box size of 120pix was put into 3D classification, to classify without applying helical symmetry and/or undergoing helical reconstruction. This smaller box size and C1 symmetry classification resulted in a class which from one side preview presents a helical symmetry different to what was previously searched (**Figure 6.4A**). Suggesting the helical rise is smaller than 50 Å, a helical twist search of -70° to -90° and rise of 20 Å to 40 Å was applied to local searches of symmetry in 3D classification and 3D refinement. Applying this new search range on the smaller box sized particle resulted in a reconstruction with an average resolution of 8.35 Å (**Figure 6.4B**). After iterative refinement and post-processing, a map at 7.6 Å resolution is obtained (**Figure 6.4C**) with a helical twist of -80° and rise of 29.6 Å.

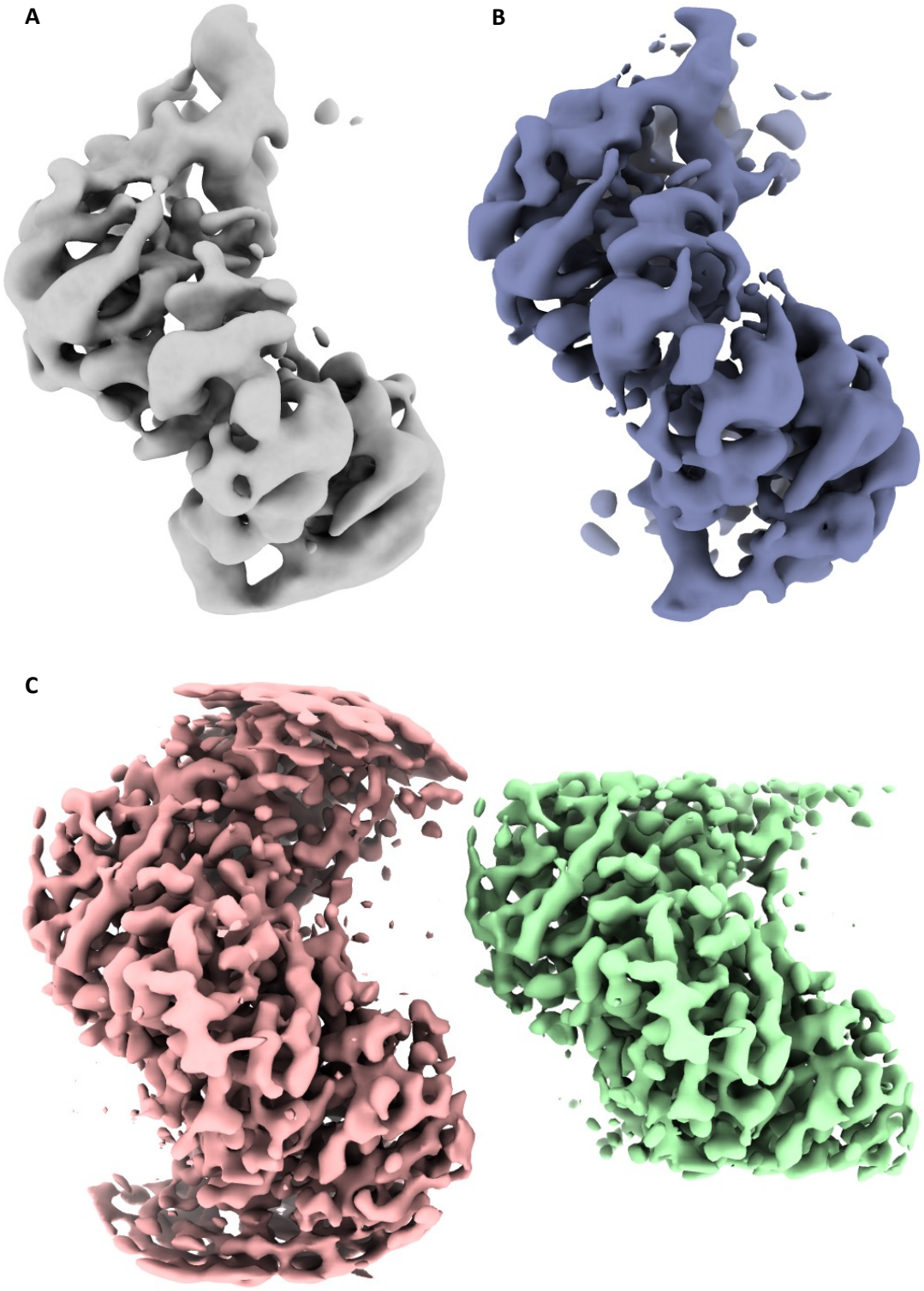

Figure 6.4. 3D classification, refinement and post-processing of ParA2$_{vc}$-DNA collected with a pixel size of 1.35 Å and box size of 120pix.
(A) *3D class obtained from 3D classification without searching or reconstructing with helical symmetry, initial features of dimers can be seen.* ***(B)*** *Averaged 3D refinement with helical reconstruction giving a resolution of 8.35 Å.* ***(C)*** *Post-processed helical reconstruction with (right) and without (left) applying a helical mask, both at 7.6 Å resolution.*

6.3.2 Processing the 1.047 Å pixel size dataset

From improvements made in sample preparation (**6.2**), data collection was carried out at a pixel size of 1.047 Å, resulting in 5786 micrographs. Structure determination was carried out as outlined in **Figure 6.5**. Particles were manually picked from motion-corrected micrographs, using relion's integrated helical-picker tool. During particle picking, 2D classification was ran, confirming that they are ordered, with the DNA backbone, nucleotide, and secondary structure elements of the protein easily identifiable (**Figure 6.2C**). Following particle extraction of the picked coordinates against CTF corrected aligned micrographs, 390,604 particles were extracted with a box size of 200 pixels (**2.8.3**). From 3D classification one of the six classes reconstructed was selected, at a resolution of 6.9 Å with a helical twist of -80.7° and rise of 27.8 Å, extracting 182,9997 particles (**Figure 6.5**). When applied to 3D refinement, the resolution was improved to 5.3 Å, producing a final helical symmetry of -80.57° and 28.68 Å for twist and rise, respectively. Creating a mask using relion's mask creation tool, low-pass filtered to 10 Å, the refinement half-maps were imported to Phenix for use on ResolveCryoEM for density modification applying a B factor of 250 $Å^2$, producing a final resolution of 4.5 Å (**Figure 6.6A, Figure 6.7, movie 1**).

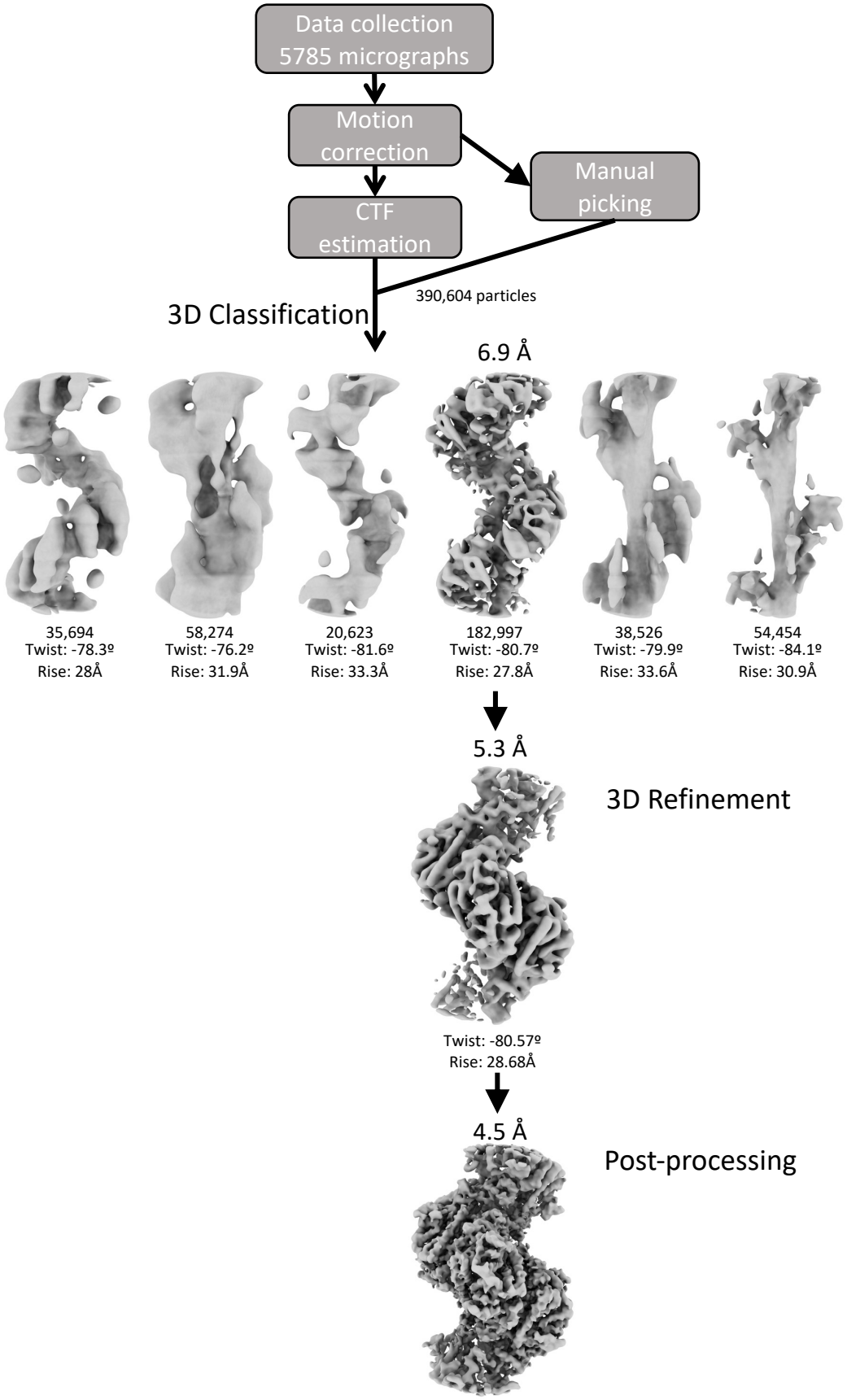

Figure 6.5. ParA2$_{vc}$-ATPγS-DNA filament cryo-EM structure determination.
Data processing pipeline of micrographs aquired with a pixel size of 1.047 Å

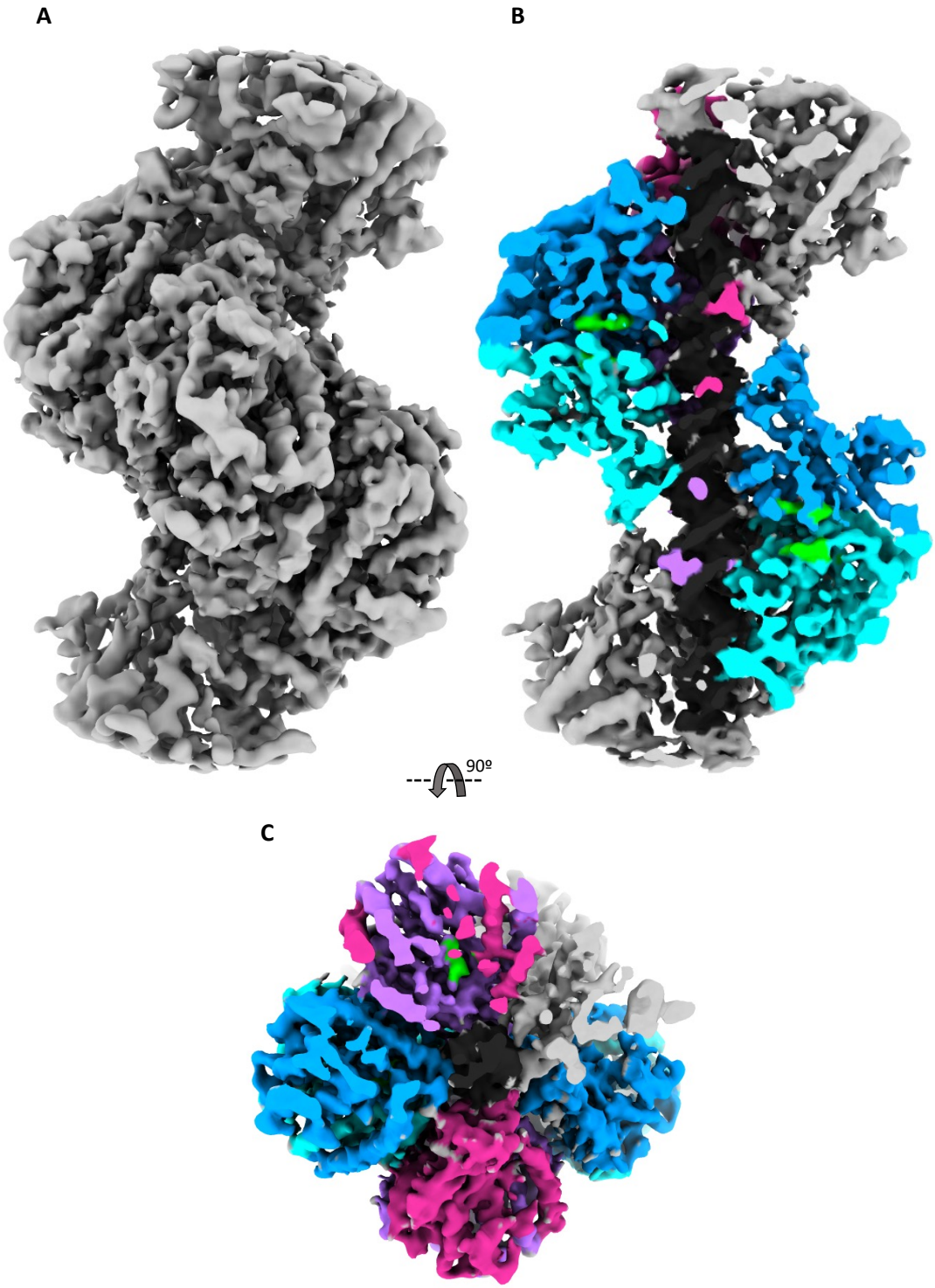

Figure 6.6. Structure of ParA2$_{vc}$-DNA at 4.5 Å resolution.
Electron potential map of ParA2$_{vc}$ bound to ATPγS in dimers forming a left-handed helix with a twist of -80.57° and rise of 28.68 Å, map post-processed and sharpened using Phenix. ***(A)*** *Final electron potential map produced.* ***(B)*** *Slap view of the map with map density coloured to show the ParA2 dimers and DNA, dimers are in blue and cyan and purple and pink with nucleotide and Mg^{2+} in neon green.* ***(C)*** *End on view of filament, map potential coloured as in (B).*

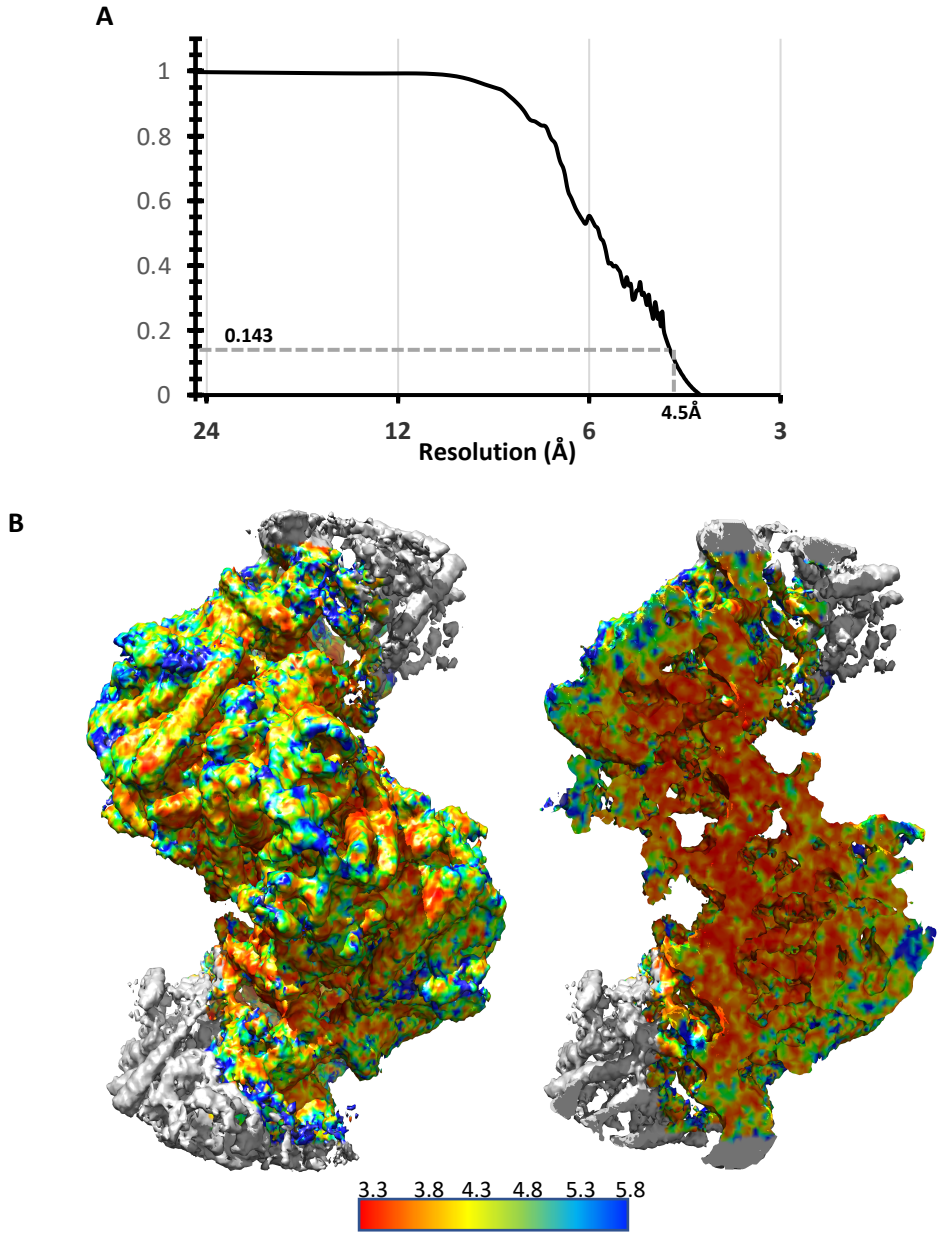

Figure 6.7. ParA2$_{vc}$-ATPγS-DNA filament cryo-EM structure resolution determination.
(A) *FSC curves for the masked post-processing refinement.* ***(B)*** *Local resolution of the electron potential map, calculated using ResMap with the scale bar in Å.*

	ParA2 ATPγS-DNA	ParA2 ATPγS-DNA
	Reconstruction 1	Reconstruction 2
Microscope	Titan Krios	Titan Krios
Magnification	105,000x	130,000x
Voltage (kV)	300	300
Camera	K2	K2
Pixel size (Å)	1.35	1.047
Defocus range (μm)	-3.25 - -1.5	-2.3 - -1.3
Total dose (e.Å-2)	49.92	52.02
Number of micrographs	3665	5785
Total segments used	23,209	182,997
Symmetry	Helical	Helical
Rise (Å)	29.62	28.68
Twist (º)	-80.29	-80.57
Map resolution (Å)	7.6	4.5

Table 6.1. Data collection and final map reconstruction parameters.

6.3.3 Building and refinement of the atomic model

To build the atomic model into the 4.5 Å map obtained via helical reconstruction, the crystal structure of $ParA2_{vc}$ bound to ADP (**Section 5.3)** was exploited. Docking a monomer into the map and replacing the ADP molecule with ATPγS, the N-terminal helix was deleted and manually re-build into the density using coot. The model was refined using the Phenix real-space refinement program (**Figure 6.9**). Following this, a second copy of the refined monomer was introduced into the map to form the dimer along with the dsDNA strand through the middle (**Figure 6.9D**), the model was then again put into real-space refinement. Further copies of the refined dimer were placed into their subsequent positions using Chimera, with the final model being real-space refined for all of the chains (**Figure 6.8**).

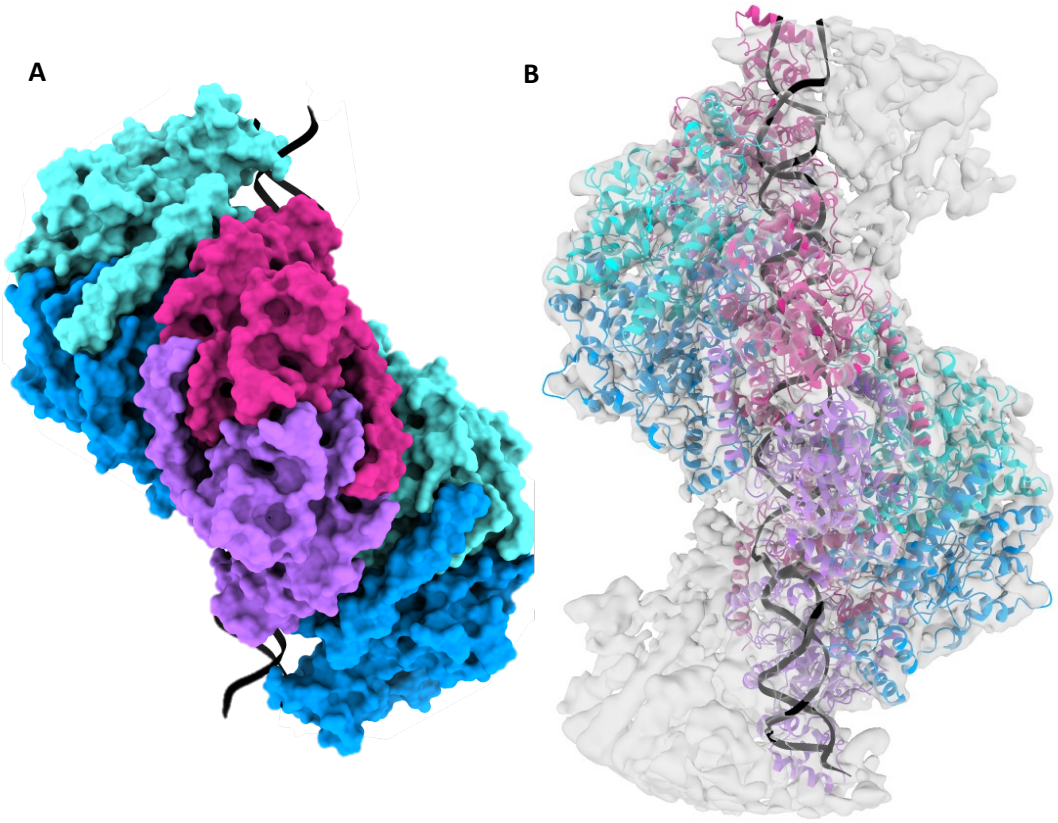

Figure 6.8. ParA2$_{vc}$-ATPγS-DNA filament and atomic modelling into map.
(A) *Surface view of ParA2 atomic model bound to DNA, each monomer coloured separately, dimers in pink and purple and blue and green.* ***(B)*** *ParA2 atomic model in cartoon view in transparent electron potential map with DNA.*

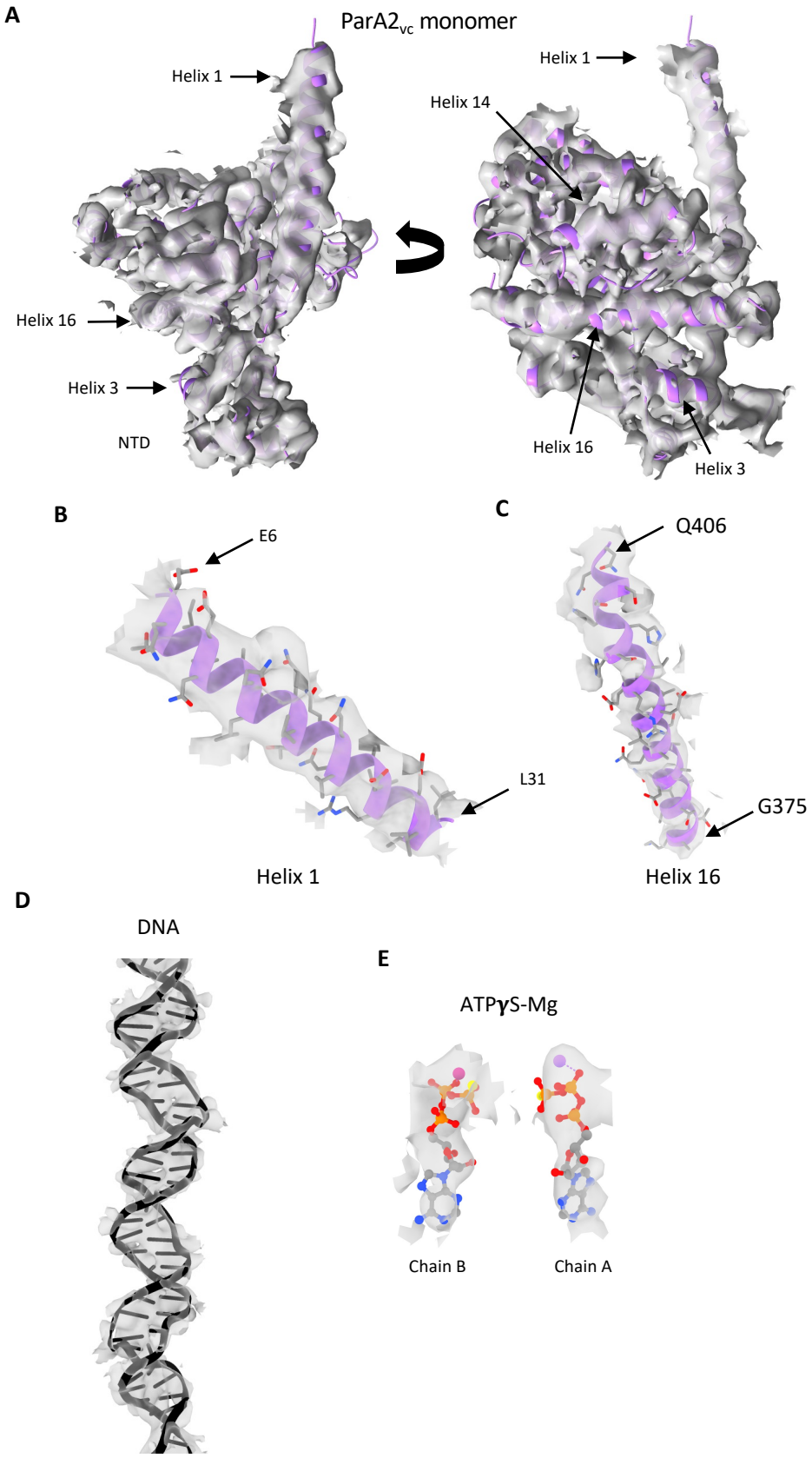

Figure 6.9. Fitting of atomic model to cryo-EM map.
(A) *fitting of ParA2$_{vc}$ monomer into map density following real-space refinement using Phenix.* ***(B)*** *Fitting of helix 1, showing side chains, into the electron potential map.* ***(C)*** *Fitting of helix 16, the last helix, into the map, showing side chains.* ***(D)*** *Fitting of dsDNA refined into map.* ***(E)*** *Fitting of ATPγS molecules in relation to eachother into the map, coloured via atom.*

From model building, the model refinement statistics are poor (**table 6.2**), producing a Ramachandran plot with only 80.48% in the favoured conformation and high clashscore of 39.62. To improve the quality of these, one of the dimers was removed from the model, due to the poor density near the edge of the map. The model was then put into ChimeraX for refinement using ISOLDE intermittent with Phenix's real-space refinement. Focusing on one chain at a time, the refinement statistics were improved (**table 6.2**), producing a Ramachandran plot with 91.1% favoured, 8.77% allowed and 0.13% disallowed with a reduced clashscore of 18.28. A map-to-model FSC curve was created using phenix (**appendix Figure 8.21**).

Model refinement		**ISOLDE**
Map sharpening B-iso (Å2)	40	40
Model composition		
Protein residues	4000	3216
Ligand	20	16
Nucleic acid	116	98
R.M.S deviation		
Bond length (Å)	0.008	0.004
Bond angle (∘)	1.445	0.917
Ramachandran plot		
Favoured (%)	80.48	91.1
Allowed (%)	19.52	8.77
Outliers (%)	0	0.13
Average B-factor		
macromolecules	185.48	111.36
ligands	150.79	90.37
Nucleic acid	129.68	137.96
Validation		
Rotamer outliers (%)	21.02	0.47
Clashscore	39.62	18.28
MolProbity score	3.81	2.28

Table 6.2. Refinement statistics from ParA2$_{vc}$-ATPγS-DNA cryo-EM structure.

6.4 ParA2-DNA-ATPyS structure

$ParA2_{vc}$ forms a left-handed helix, with a rise of 28.68 Å and a twist of -80.57° (**Figure 6.9A, movie 1**). This is consistent with the previously-reported filament architecture, based on low-resolution negative-stain data (Hui et al., 2010). The map includes density for five $ParA2_{vc}$ dimers, and a 48bp-long DNA fragment. Density for the DNA is clearly defined (**Figure 6.9D**), with notably some base pair separation in the best-resolved regions of the map. Density for the ATPγS and Mg molecules is also clearly delineated in the active site (**Figure 6.9E**).

6.4.1 $ParA2_{vc}$ interaction with DNA

Our structure of the $ParA2_{vc}$-DNA filament reveals that each $ParA2_{vc}$ molecule binds to DNA via two interaction sites (**Figure 6.10**, **movie 2**): (1) In the central ParA domain, three domain (residues 322-328, 345-353 and 376-382, **Figure 6.10A**) interact with the DNA backbone. In particular, a set of basic residues (K326, K327, R350, R352, K376 and K377) form salt bridges with the DNA phosphate. (2) In the N-terminal winged helix-turn-helix domain, the loop between residues 74 and 80 is inserted deep into the minor groove (**Figure 6.10A**). Similarly, several basic residues (K44, K74, H79) form salt bridges with the DNA backbone. Collectively, these basic residues, mostly present at the positively-charged end of helices, form a continuous positive surface at the bottom of the $ParA2_{vc}$ dimer, ideally suited for interaction with DNA (**Figure 6.10B**). To see whether these interaction sites are distorting the DNA, the atomic model is compared to B-form DNA (**Figure 6.10C**). When aligned to the right-hand side of the DNA models, you can see the DNA from the cryo-EM model initially looks the same as B-from. However, there is a slight stretching of the major grooves, which is evident by the shift seen between the two models on the left-hand side. Therefore, I can conclude that the DNA in the model is not B-form and is being distorted by ParA2 during the formation of the filament.

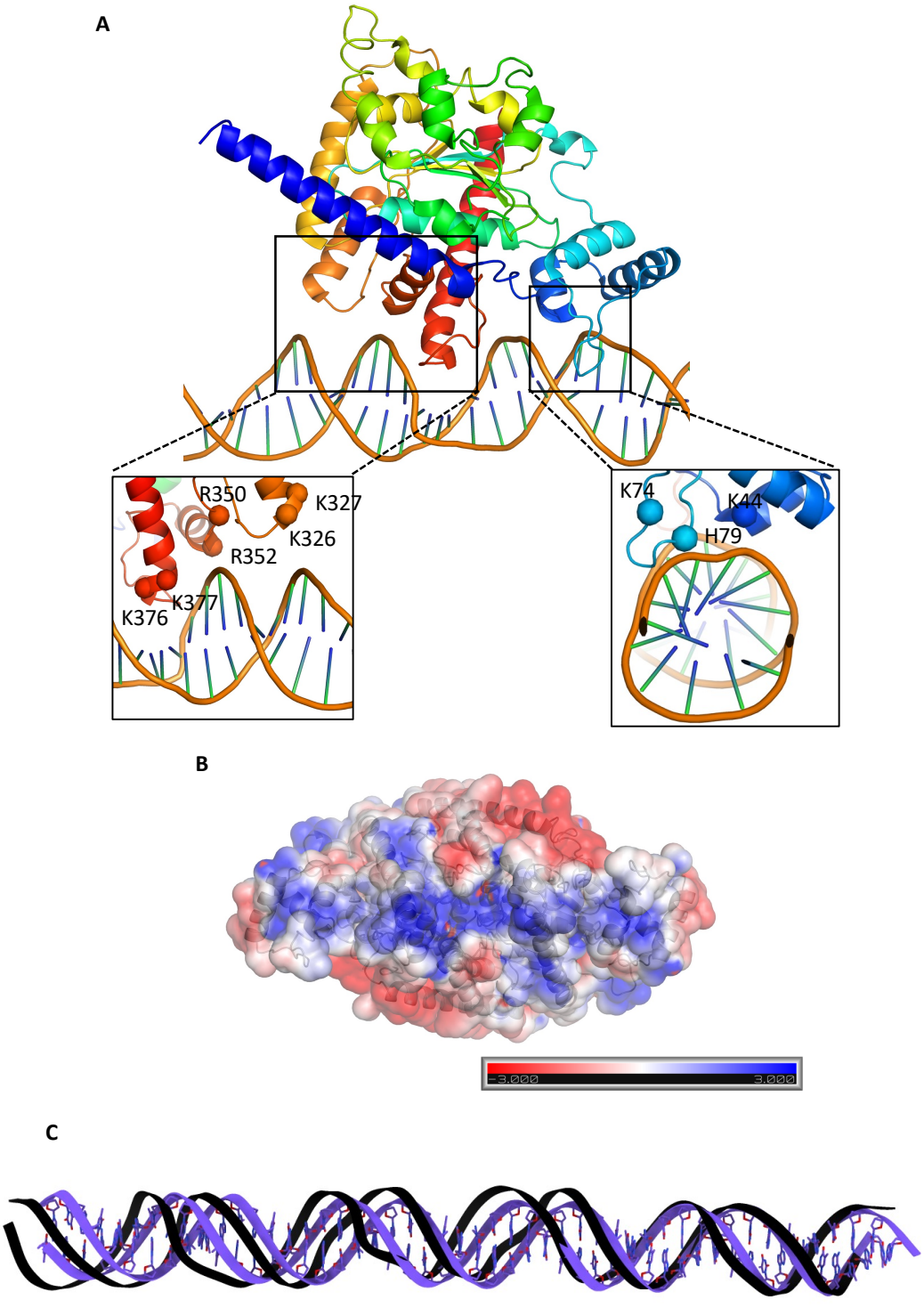

Figure 6.10. Binding of ParA2$_{vc}$ to DNA.
(A) *A ParA2$_{vc}$ monomer, and the DNA molecule, from the cryo-EM structure are shown in cartoon representation, in rainbow coloring. The two regions forming contacts with the DNA are in black boxes. Close-up views of these two regions are shown underneath, with the basic residues forming salt bridges with the DNA backbone indicated.* ***(B)*** *Electrostatic surface representation of the ParA2vc dimer. A positively charged stretch is clearly present, corresponding to the DNA-binding surface.* ***(C)*** *DNA from the cryo-EM atomic model (Black) in cartoon view compared to B-form DNA (Purple, with bases in atomic view), the models are aligned to the right-hand side of the strands.*

6.4.2 ParA2$_{vc}$ dimer-dimer interaction

In the structure of the ParA2$_{vc}$-DNA filament reported here, adjacent ParA dimers form extensive contacts (**Figure 6.11**), with a surface area of ~ 1,500 Å^2. This interface is largely mediated by three regions: two helices, located at the C-terminus (residues 325-339 and 381-405), and a helix-turn-helix motif from the N-terminal domain (**Figure 6.11A** movie 2), forming electrostatic contacts (**Figure 6.11B**). In particular, helices 14 and 16 possess a number of exposed charged residues at the oligomeric surface (**Figure 6.11C**), that form salt bridges with the adjacent subunits.

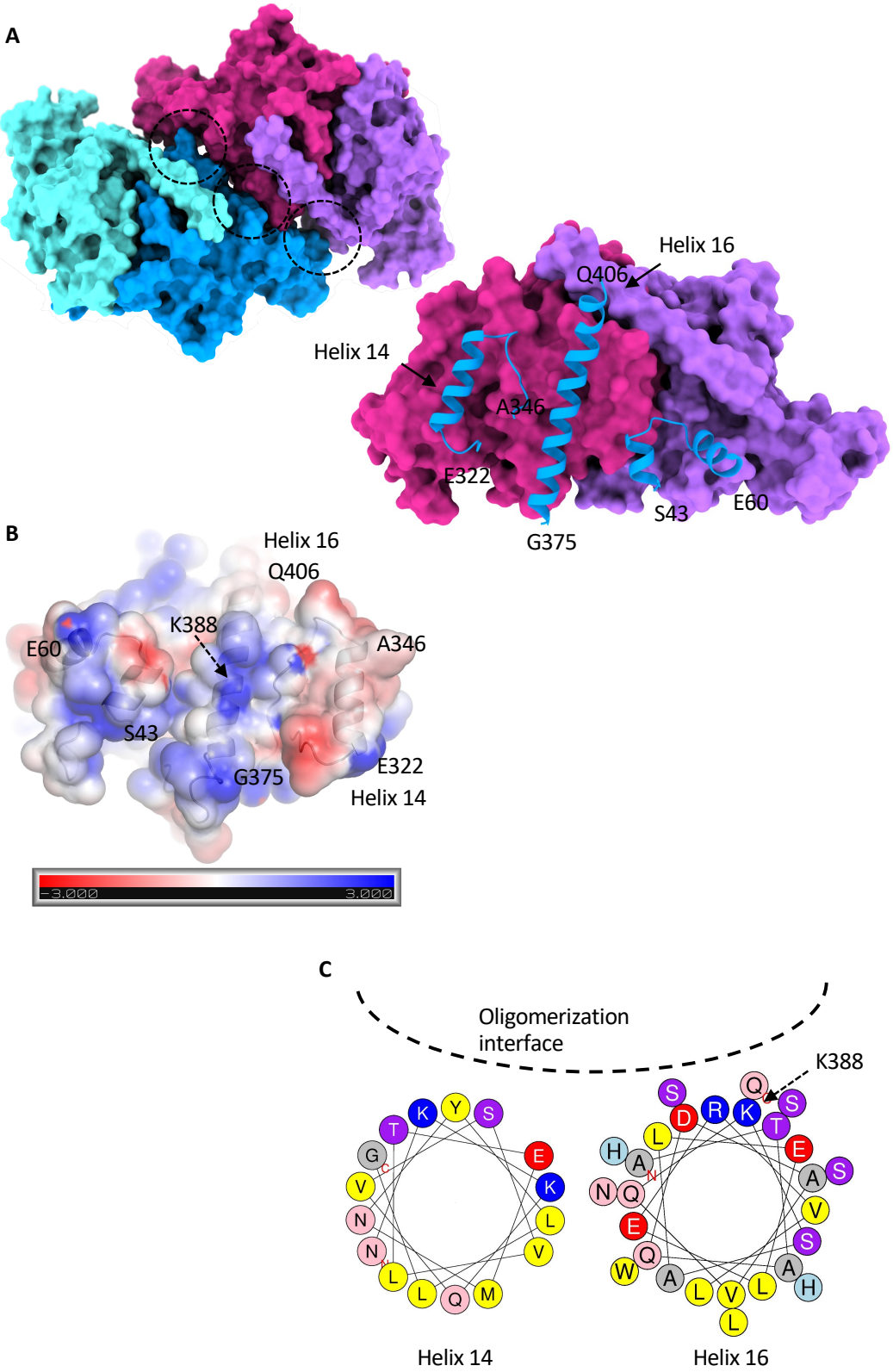

Figure 6.11. ParA2 filament interfaces.
(A) *Surface representation of two adjacent ParA2$_{vc}$ dimers (left) in the filament structure, colored as in Fig. 6.9. The interacting regions are indicated with black dotted circles. One dimer is shown (right) in surface representation, and the regions of the second dimer that are involved in the interaction are shown in cartoon. The residue boundaries are indicated.* ***(B)*** *Surface representation of a ParA2$_{vc}$ monomer in the filament structure, coloured by charge. The boundaries of the domains involved in dimer-dimer interaction are indicated.* ***(C)*** *Helical wheel plot of α-helices 14 and 16 of ParA2$_{vc}$, that form the filament oligomerization interface. The charged residues cluster on the interface side.*

6.5 Discussion

6.5.1 Particle distribution and picking

Grid optimisation for cryo-EM involved differing issues than from negative-stain (**section 4)**. Not needing to dilute the sample like with negative stain, dissociation due to dilution was not a problem. However, the relative charge of the ParA2:DNA complex provided a new hurdle along with the irreproducibility of cryo-EM grid plunging. To reduce the attraction of the DNA to the glow-discharged copper carbon-coated grid bars, glow-discharging was reduced to lower the charge applied to the carbon, along with introduction of detergent (Drulyte et al., 2018). Double-blotting made a large difference in the density of filaments seen In the ice, the first applied sample dampening the surface charge and reducing the attraction to the carbon, while allowing for a higher concentration of molecules to be forced into the holes (Snijder et al., 2017). Backwards blotting is a common suggestion among the community in regard to delicate samples and particularly filaments (Weissenberger et al., 2021), however this method was unsuccessful in increasing the concentration of complexes of my sample.

Despite mass advances in automated particle pickers over the past few years (Nguyen et al., 2021; Ohashi et al., 2021), both data collections of ParA2:DNA had to have the particles picked manually. This is due to the "messiness" of complex distribution, ParA2:DNA filaments not being straight and linear but instead entangled and considerably bent. However, manually picking has a number of advantages, for example, the number of falsely picked particles is minimal. In the case of helical reconstruction, this meant 2D classification is not as necessary since there are not many badly picked particles to remove from the extracted particles.

6.5.2 Helical reconstruction

As a 3D reconstruction of $ParA2_{vc}$ forming filaments along DNA was published in 2010 from negative stain data, some of the parameters of helical symmetry could already be seen, reporting "~4.4 subunits per turn of a ~120 Å pitch helix" (Hui et al., 2010). This corresponds to a helical twist of ~-81° and rise of ~27 Å. However, due to the low resolution of the reconstruction, there is a possibility that the symmetry stated

could be an artifact of reconstruction, so a wide search range was applied. During 3D classification, symmetry with a smaller twist and larger rise (~-150° and ~60 Å) was producing the most promising results, iteratively increasing in resolution, and revealing further features. However, the resolution of the reconstruction did not refine further than ~18 Å, suggesting the applied parameters were not correct. To solve what could be the right helical symmetry, it was decided to apply a single particle approach to see if the true twist and rise could be observed. The box size was therefore reduced to try to capture a dimer with only a neighbour bound to each side, and helical reconstruction was disabled. This was successful in that a reconstruction produced provided enough information to search for a more accurate helical twist and rise. When particles with the smaller box size were classified applying the calculated parameters from the single particle reconstruction, the classes produced surpassed the previous resolution and gave more confidence in the new correct symmetry. In the final reconstruction, the helical twist and rise (-80.57° and 28.68 Å) is similar to that published in 2010, however it is not clear why this was not found in the initial searches during classification.

6.5.3 ParA2$_{vc}$-DNA

From the cryo-EM map and atomic model obtained, ParA2$_{vc}$'s interactions with DNA and adjacent dimers can be observed. As described in **section 6.4.1**, ParA2$_{vc}$ molecules bind to DNA via two interaction sites: the N-terminal winged helix-turn helix domain binding to the minor groove, and a central ParA domain binding across a major and minor groove of the DNA. Interestingly, a C-terminal region (residues 376-382), covering a loop and beginning of helix 16, is inserting deep into the major groove of the DNA, causing distortion to the backbone. Since no other type Ia ParA structures are available to compare the N-terminal domain binding, we are only able to compare the binding of the central HTH domain, as viewed in type Ib ParA co-crystal structures with DNA. When ParA2$_{vc}$-DNA is aligned to $_{Hp}$Soj-DNA, they show a similar binding pattern regarding the central ParA domain (**Figure 6.12**), both binding to the major groove. However, HpSoj's C-terminal region (376-382 of ParA2) of the central binding domain isn't inserting into the major groove as far. There is also a

difference in binding orientation between the ParAs, HpSoj is seen to bind on a slight angle from ParA2$_{vc}$ (**Figure 6.12**)

The crystal structure of the archaeal plasmid pNOB8 ParA protein (Schumacher et al., 2015), however, revealed a completely different binding mode to both *Hp*Soj and ParA2$_{vc}$ (**Figure 6.12**). pNOB8 is seen to be binding to DNA through the "side" face of the dimer and is said to be able to bind DNA on both sides of the dimer. While this protein does not possess the N-terminal domain of type Ia ParA proteins, all three DNA-binding regions of the core domain are present in the pNOB8 protein, and like with ParA2, include several basic residues. It is not known if the difference in DNA interaction corresponds to a crystallization artefact or reflects biological differences in the interaction with DNA between archaeal and bacterial ParA proteins. From previous literature we can also compare the DNA binding affinities of ParA2$_{vc}$, pNOB8 ParA and *Hp*Soj. ParA2$_{vc}$ has the highest binding affinity at 45.9 nM (Chodha et al., 2021), while pNOB8 ParA and *Hp*Soj have similar affinities at 120 ($\pm$ 20) nM and 122 nM, respectively (Chu et al., 2019; Zhang & Schumacher, 2017). While these values do not correlate to the differing chromosome/plasmid size in each organism (1 Mbp for ParA2$_{vc}$, 41 Kbp for pNOB8 and 1.6 Mbp for *Hp*Soj), this increased affinity could be due to the N-terminal winged HTH domain possessed in Type Ia ParA proteins.

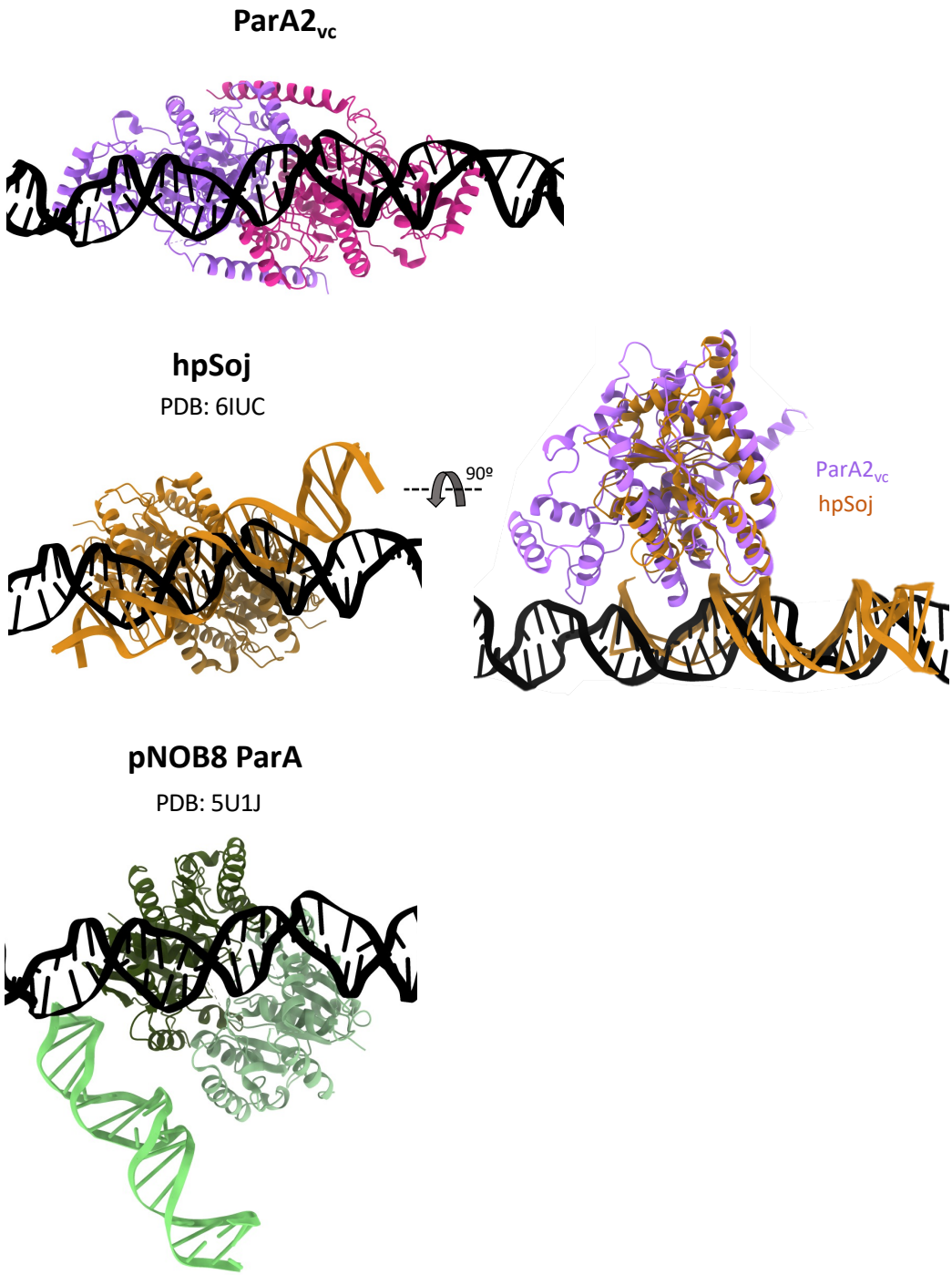

Figure 6.12. Comparison of the DNA binding in ParA orthologues.
The structure of the ParA dimer, from bottom, is shown for $ParA2_{vc}$, HpSoj, and pNOB8 ParA. The two $ParA2_{vc}$ molecules are colored as in Figure 6.9, with the DNA in black. For HpSoj and pNOB8 ParA, the position of the DNA in the filament structure reported here is shown in black, for comparison.

6.5.4 Nucleotide binding pocket

During hydrolysis, there is a nucleophilic attack of a lytic water molecule at the γ-phosphate on the ATP molecule, cleaving the phosphate bond resulting in proton transfer events and hydrogen bond rearrangements (Prieß et al., 2018). In canonical NTPases, the P-loop is the region that binds and facilitates this reaction. The Serine residue of the motif (Ser125 for $ParA2_{vc}$) coordinating the magnesium ion which is essential for enzymatic function, while the catalytic lysine (residue 124) makes interactions with the γ and β phosphates of the nucleotide (Romero Romero et al., 2018). Mutating this key lysine residue has been well characterised to modify ParA proteins abilities to bind, hydrolyse and release nucleotide, depending on the amino acid (as described in **4.6.2**) (Vecchiarelli, Havey, et al., 2013). Now that we have a resolved active site bound to nucleotide from this cryo-EM structure, it is possible to model how mutating K124 to Glutamic acid, Glutamine or Arginine changes this key interaction (**Figure 6.13**).

For each mutant, Serine 125 can be seen interacting with the magnesium ion, while residue 124 deviates from the wild-type (lysine). The Arginine residue (top right) can be seen extending further over the γ-phosphate of the nucleotide, consistent with the mutant phenotype of hydrolysis inhibition. However, there is no clear reasoning from the model for the K124E and K124Q mutant phenotypes. K124Q is still able to bind and hydrolyse ATP, however it has been described to inhibit an active state change which would allow for DNA binding, due to the shift in charge. K124E is positioned similarly, however it is clearer that the change in charge of the residue from positive to negative prevents the P-loop from being able to bind to ATP.

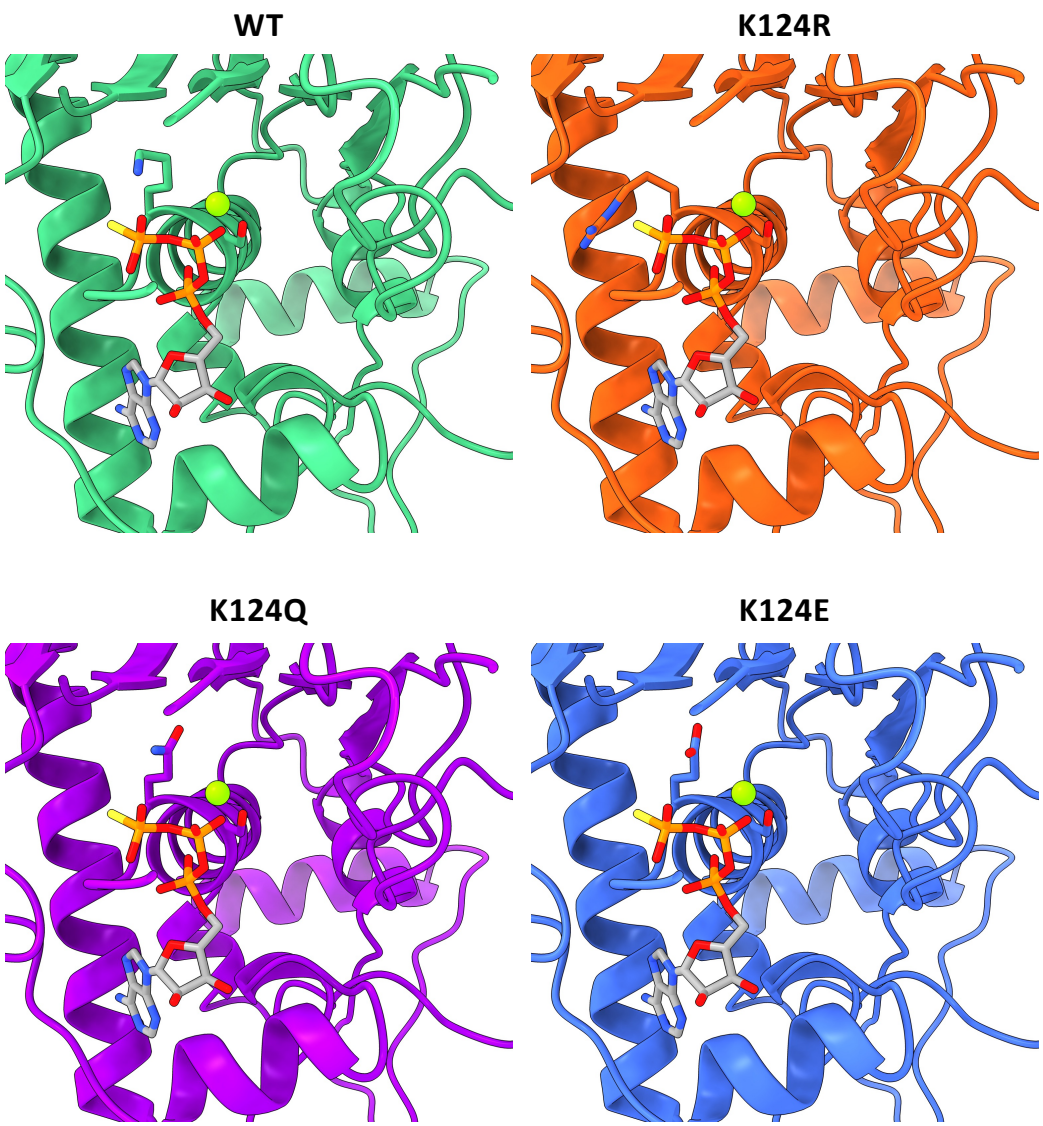

Figure 6.13. Modelling of catalytic lysine K124 mutants in the active site of the ParA2$_{vc}$-ATPγs-DNA cryo-EM structure.

Each panel shows the Serine 125 residue responsible for magnesium coordination and is coloured differently for each mutant. The residue side chains and ATPγS molecules are shown in atomic view coloured by element.

6.6 Conclusion

$ParA2_{vc}$ can form left-handed helical filaments using DNA has a backbone, the cryo-EM structure reported at 4.5 Å resolution shows a helical twist of -80.57° and rise of 28.68 Å. Despite the lack of atomic resolution, the structure shows ParA2's interactions with the DNA backbone, forming salt bridges in both the major and minor grooves, as well as highlighting the regions involved in the filament interface. The deletion mutation examined in **chapter 4** of the N-terminal helix (1) along with this filamentous structure conclude that filament formation isn't regulated through the N-terminal helix. Because of this, oligomerisation may not be a feature restricted to only type Ia ParAs. However, the structure revealed that a C-terminal helix and loop is involved in DNA binding, causing distortion to the DNA backbone. Since this section is missing in many type Ib sequences, this could explain differences in DNA binding seen among ParAs structures solved bound to DNA. From this cryo-EM structure it is therefore suggested that the role of the N-terminal helix may be more orientated around dimer stabilisation, outstretching across the partner monomer in the homodimer, as opposed to DNA binding and filament formation.

7 General Discussion and conclusion

In this study, the structure of the ParA2$_{vc}$ protein is reported in three states: apo, nucleotide-bound (ADP) and in a filamentous complex with nucleotide and DNA. Importantly, it reports the first structure of a ParA protein in the filamentous form. This structure allows us to identify how ParA molecules interact with the DNA, but also how they form higher-order structures. In particular, it is shown that the NTD forms additional contacts with the DNA compared to solved DNA-bound ParAs, revealing differences between type Ia and type Ib ParA proteins. I have also shown that the higher-order oligomerization is mostly mediated by the C-terminal region.

7.1 Conformational change of ParA2$_{vc}$

Having solved the structure of dimeric ParA2$_{vc}$ in multiple states, we are able to compare to see the extent of conformational change between states. Between the crystal structures (apo and ADP bound), as shown in **chapter** 4, there is a very minimal change in dimer conformation. The only observable feature being the increase in order of the nucleotide binding site with the ADP-bound structure compared to the apo. However, a considerable change in conformation of ParA molecules is observed between the crystal structures and the ParA2$_{vc}$-DNA filament structure (**Figure 7.1, movie 3**). Specifically, helix 1 undergoes a striking conformational change, merging with helix 2 to form a single, extended helix ~ 15 Å from its position in the structures obtained without DNA (**Figure 7.1A**). As indicated above, helix 1 forms a cross-dimer interaction, in the ParA2$_{vc}$ dimer. As a consequence, the angle between the two molecules in the filament structure is altered by ~ 30 degrees, compared to the crystal structures (**Figure 7.1B**). In **chapter 4** it was shown that the NTD helix is not required for DNA binding and/or filament formation, therefore it suggests the change in helix architecture is a consequence of DNA binding and filament formation, instead of a prerequisite.

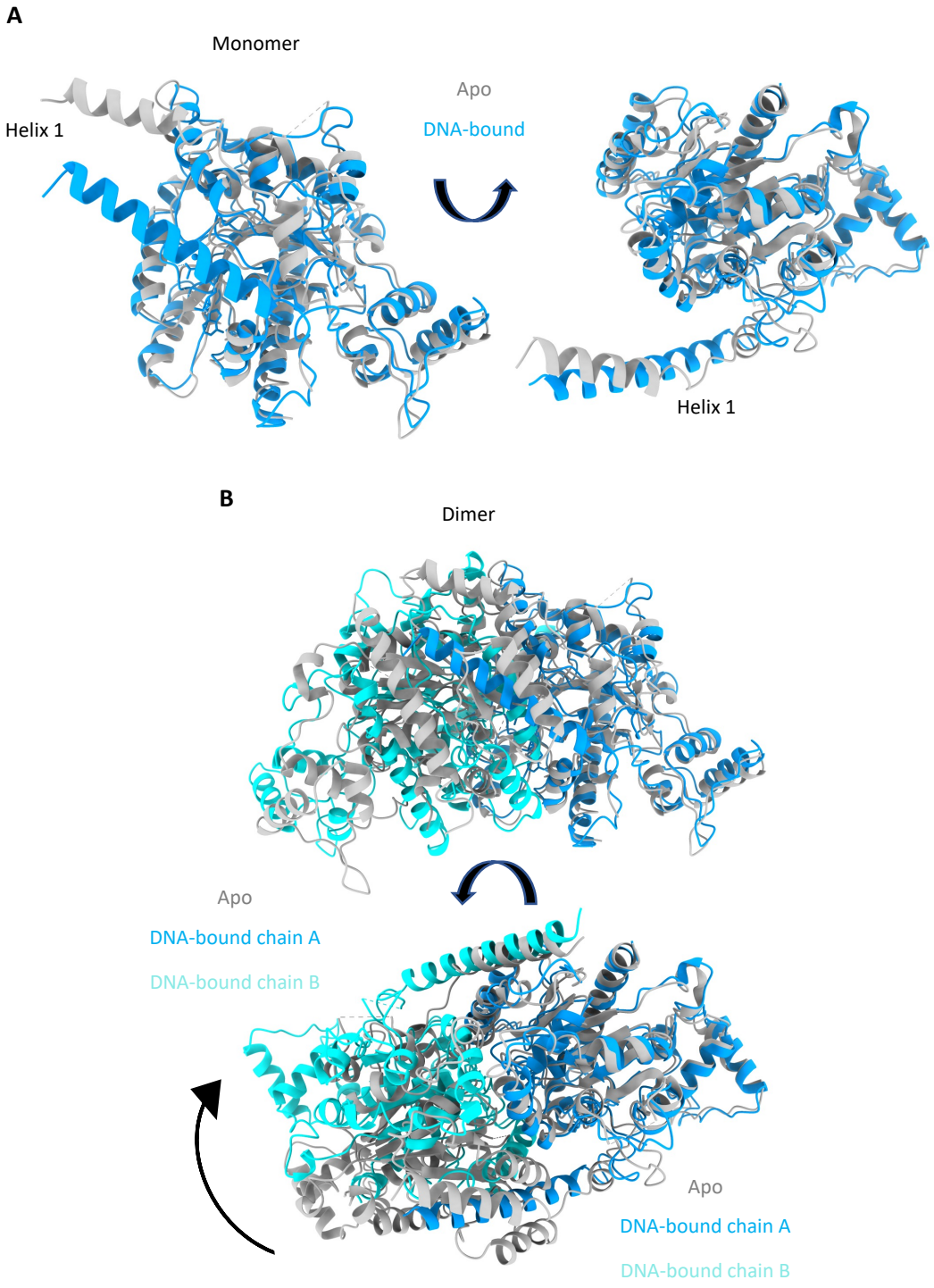

Figure 7.1. ParA2 conformational change upon binding DNA.
Comparison between ParA2$_{vc}$ structure in the free (grey) and DNA-bound (blue/cyan) conformations in cartoon representation. ***(A)*** *Conformational change of the monomer, illustrating the rearrangement of helix 1.* ***(D)*** *Dimer aligned on the blue subunit, to show the dramatic change in the dimer architecture.*

7.2 Conservation among ParAs

Sequence similarity across type I ParAs is very low, with the closest orthologue with a known structure, *E.coli* P1 plasmid ParA, having the highest sequence identity with $ParA2_{vc}$ of just 28%. When ParA sequences are aligned, we can visualise the extent to the lack of conservation (**Figure 7.2**). As expected, the P-loop deviant walker A motif is highly conserved across all species, between residues 125 to 199, allowing for nucleotide binding and dimerization (Koonin, 1993; Saraste et al., 1990). However, only sparse residues are conserved throughout the rest of the sequences, some of which line the nucleotide binding pocket and the rest form strands 5 and 6 of the β-sheet in the centre of the molecule. The sequence similarity seen over the β-sheet may explain why despite the lack of sequence homology, ParAs adopt an overall similar architecture. Therefore, many $ParA2_{vc}$ features observed are not conserved across type I ParAs, including the dimer interface, DNA binding interface and filament interface (**Figure 7.2**).

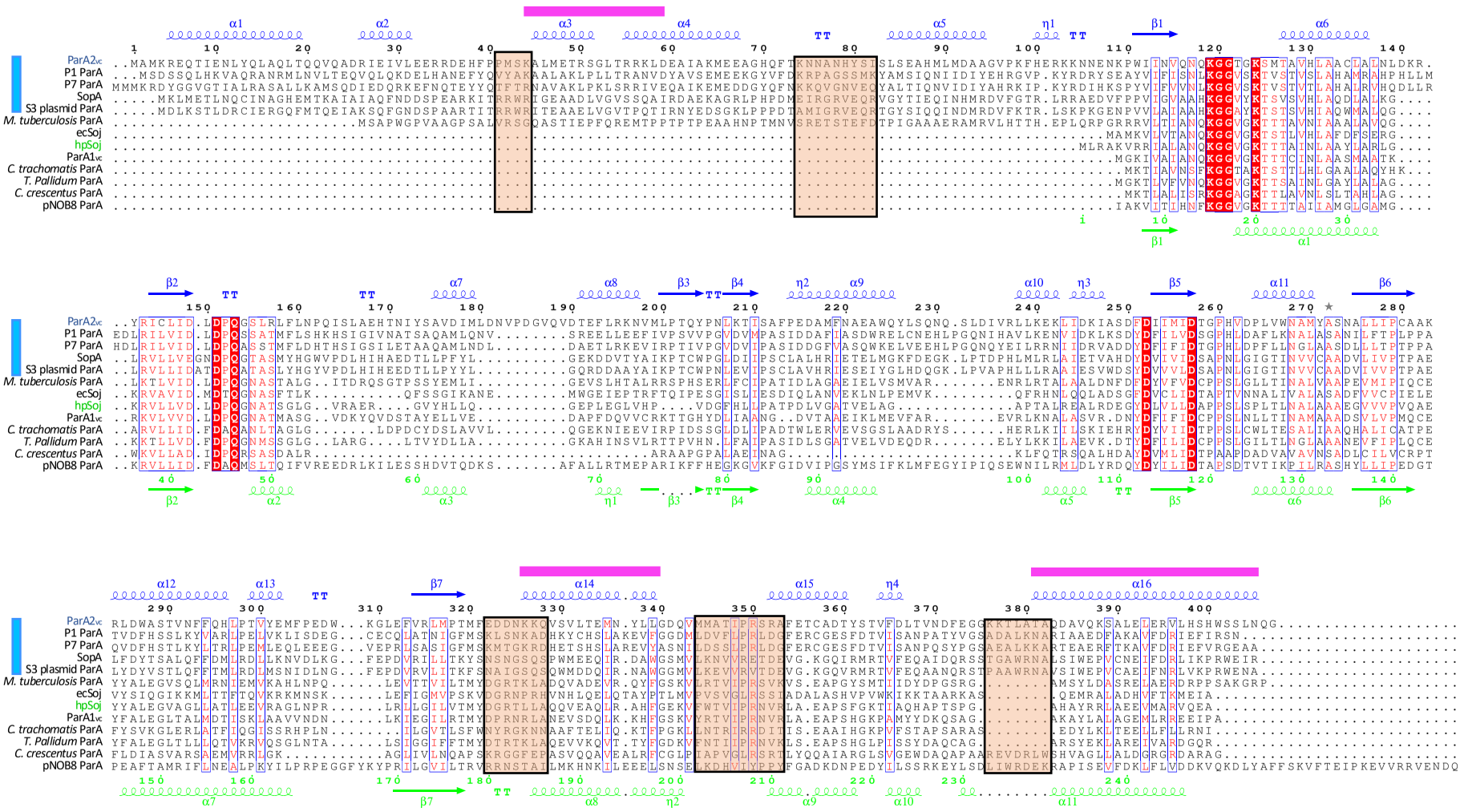

Figure 7.2. Multiple sequence alignment of various ParA orthologues.

The first six are Type Ia sequences, the next seven are type Ib sequences, and the bottom sequence is for the archaea pNOB8 plasmid ParA. The secondary structure elements for ParA2$_{vc}$ is in blue at the top, and for HpSoj in green at the bottom. Conserved residues are in red box, similar residues in red characters. The orange boxes indicate regions of ParA2$_{vc}$ that interact with DNA, and the purple bars indicate the filament oligomerization interfaces. The blue bar indicates the type-Ia ParA proteins, the remaining are type-Ib.

7.2.1 DNA binding

As described in **chapter 6**, 2 regions interact with the DNA upon binding, coressponding to five different loops across the molecule (**Figure 6.10A**). Interestingly, when viewed on the multiple sequence alignment, these regions are not conserved across orthologues (**Figure 7.2**). Nonetheless, for two of the corresponding regions (residues 322-328 and 345-353), basic residues are present in all ParA sequences, suggesting that the mode of binding is conserved.

In keeping with this, the recently published structure of a type Ib ParA protein (the *Helicobacter pylori* Soj protein, *Hp*Soj) bound to DNA (Chu et al., 2019), revealed a largely conserved set of interactions with the nucleic acid backbone between ParA2$_{vc}$ and *Hp*Soj (**Figure 6.10C**). However, the N-terminal domain is not present in type Ib ParA proteins, and accordingly this set of interactions is not present in the *Hp*Soj-DNA structure. Similarly, while a number of basic residues are found in region 376-382 of type Ia ParA proteins, this region (a loop and part of helix 16) is not found in type Ib ParA proteins, with the exception of the *C. crescentus* ParA orthologue (**Figure 6.12**). As shown on **Figure 6.10**, this loop forms a deep insertion within the major groove of the DNA, causing significant distortion of its backbone.

As a consequence, the relative orientation of the DNA molecule differs significantly between the *Hp*Soj-DNA crystal structure (Chu et al., 2019) and the ParA2$_{vc}$-DNA structure (**Figure 6.13**). Based on the sequence alignment, this difference in DNA orientation can likely be generalized between type Ia and type Ib ParA orthologues, and might be related to the transcription repression activity of type Ia ParA proteins (Baxter et al., 2020). As mentioned above, the *C. crescentus* ParA orthologue (which belongs to the type Ib family) possesses the additional DNA-binding region near the C-terminus normally found only in type Ia orthologues, and may therefore possess some common properties between the two families.

7.2.2 Filament formation

It had previously been proposed that only type Ia ParA orthologues could form filaments, which would be formed only by interactions via the N-terminal domain (Hui et al., 2010). However, our structure does not support this, and most of the filament oligomeric interface is located in the C-terminal region of the protein (**Figure 6.11**). To further investigate the role of the N-terminal region in filament formation, a deletion mutant of $ParA2_{vc}$ was engineered where the entire helix 1 was removed (Δ3-36) (**Chapter 4.4**). From this mutation it was observed that helix 1 does not play a crucial role in filament formation, as patterned filaments of ParA2 were still forming along DNA, despite missing the first ~30 amino acids. It could therefore be concluded from this that filament formation is not restricted to the presence of the N-terminal domain, exclusive to type Ia ParAs. To understand if the entire NTD plays a role in filament formation, a mutant was engineered with residues 4-106 removed. However, the protein wasn't soluble and was unable to be purified (**3.5.2.2**).

In order to verify the role of these C-terminal residues in the filamentous architecture of ParA, a helical wheel plot helped to identify which residues to target to engineer a point mutation (**Figure 6.11C**). Due to the low resolution of the electron potential map, confidence in the register and orientation of the residue side chains of helix 16 was low. The helical wheel plot therefore helped to confirm the positioning of charged residues along the oligomeric interface. Considering that residues 376-382 were identified, from the cryo-EM structure, to be a DNA binding region, K388 was therefore selected to mutate, to avoid disrupting DNA binding. Mutating K388 to alanine, as shown in **Chapter 4.4**, resulted in the protein not being able to form rigid filaments in the presence of ATP and DNA, confirming that this residue is critical to the dimer-dimer interface. Intriguingly, the residues involved in the interface between $ParA2_{vc}$ dimers, within the filament, are not conserved across orthologues, even within the type Ia family (**Figure 7.2**). This could indicate that the filament architecture differs in other bacteria, and/or that some ParA orthologues may not form filaments. Among ParAs solved bound to DNA, they show a variability in DNA binding orientation, for example, *Hp*Soj-DNA. Compared to $ParA2_{vc}$-DNA, *Hp*Soj binds on an angle to DNA, with no filaments being formed in the crystal. However it is unknown whether this is due to an artifact of crystallisation or if *Hp*Soj is unable to

form filaments altogether, as the negative stain data shown does not confirm if ordered filaments are forming or not (Chu et al., 2019).

Since no other type I ParA structures have been solved forming higher order oligomer, the closest orthologue available for comparison is the MinCD copolymeric filament. A fellow member of the MinD/Mrb/ParA family of ATPases, MinD is also a P-loop walker type ATPase, but involved in Z-ring localization (Lutkenhaus et al., 2012). MinD forms a dimer, structurally similar to ParA, but does not bind to DNA. Nonetheless, it was recently shown that MinD forms filaments, in the presence of its interacting partner MinC (Szewczak-Harris et al., 2019). However, comparison of the MinCD filament to the cryo-EM structure of the $ParA2_{vc}$-ATPγS-DNA filament (**Figure 7.3**) reveals that the filaments formed by these two proteins have a completely different architecture, and use different interfaces to form dimer-dimer contacts. Based on this, it is postulated that filament formation is not a general feature of this family of proteins either, but was adopted independently in ParA and MinD proteins, during evolution.

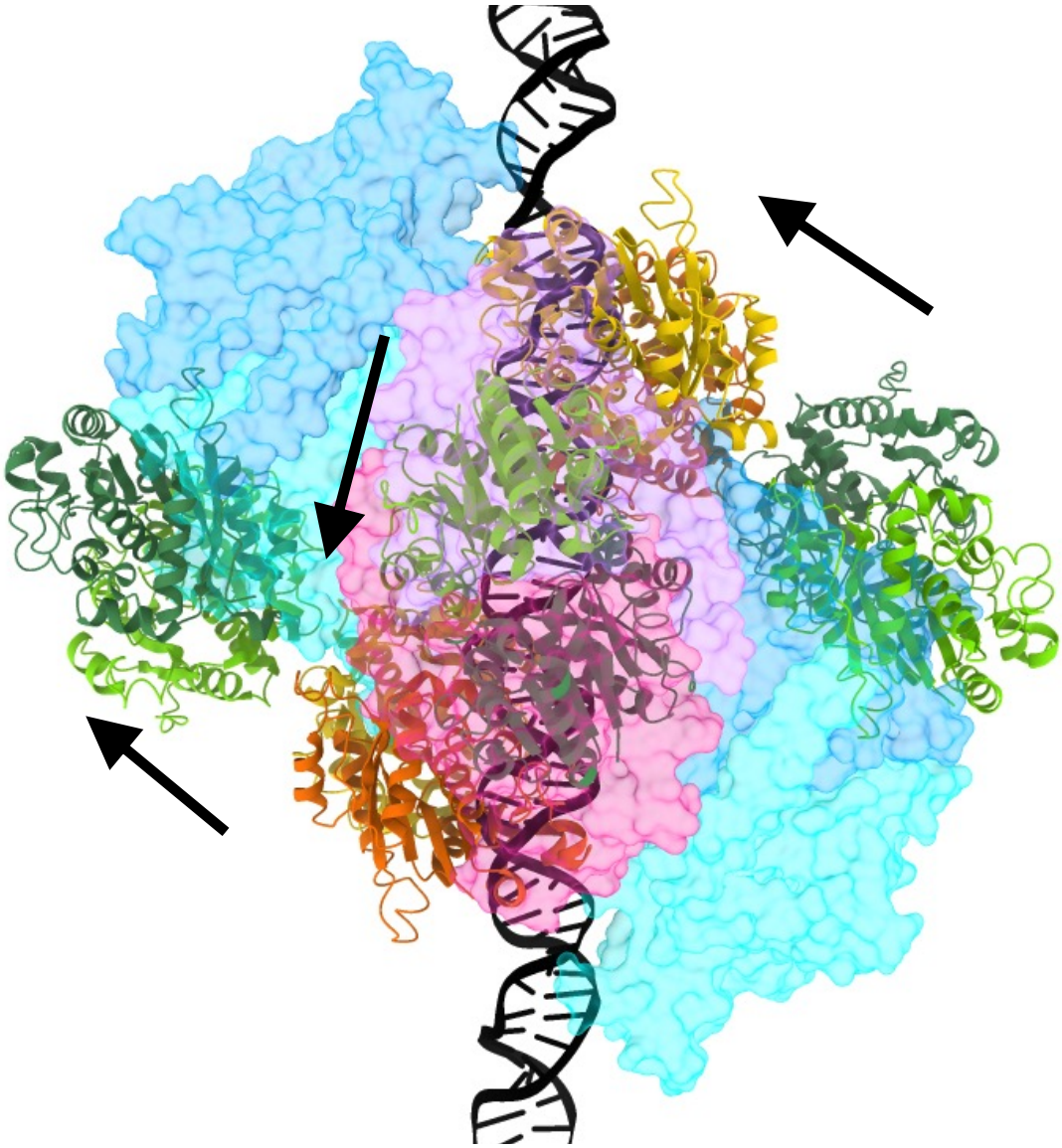

Figure 7.3. Comparison of the ParA2$_{vc}$-DNA filament to MinD in the MinCD filament.
A ParA2$_{vc}$ dimer bound to the DNA from the filament structure is shown, represented as in Figure 3c. Adjacent MinD dimers from the MinCD filament structure are in light and dark green for one dimer, yellow and orange for the other. The central green MinD dimer is aligned to ParA2$_{vc}$, the arrows indicate the direction of the MinD filament architecture.

7.3 Mechanistic model of ParA2$_{vc}$ filament assembly

From the three structures reported here, we are able to observe the conformational change occurring upon nucleotide binding and filament formation. Combined with prior biochemical and cell-based assays reported previously (Chodha et al., 2021; Hui et al., 2010), these structures allow us to propose a mechanistic model for ParA's higher-order assembly, shown in **Figure 7.4**: (a) At physiological concentrations, ParA is at equilibrium between monomeric and dimeric state in the absence of nucleotide. The recruitment of ATP stabilises the dimer. (b) A nucleotide-bound ParA dimer can bind to DNA, and this interaction induces a conformational change to the dimer architecture. (c) This change exposes the filament-forming surface of the DNA-bound ParA dimer, leading to the formation of a filament along the DNA. When encountering a *parS* bound ParB, this activates ParA's ATPase activity, leading to disassembly from the DNA, coupled with the release of hydrolysed nucleotide (**Figure 7.4**).

It's noted that previous biochemical data have shown that ParA2$_{vc}$ binds cooperatively to DNA (Chodha et al., 2021), as also observed in other ParA orthologues (Baxter et al., 2020)(Ebersbach et al., 2006)(Leonard et al., 2005). The structures reported here likely provide a mechanism for this cooperativity, with the structural changes associated with DNA binding allowing to form a charged surface that permits electrostatic interactions with adjacent dimers. This leads to an increased affinity for the binding of additional ParA2$_{vc}$ molecules adjacent to it. It remains to be verified if the change in dimer architecture is a result of the binding to ATPγS, or to DNA.

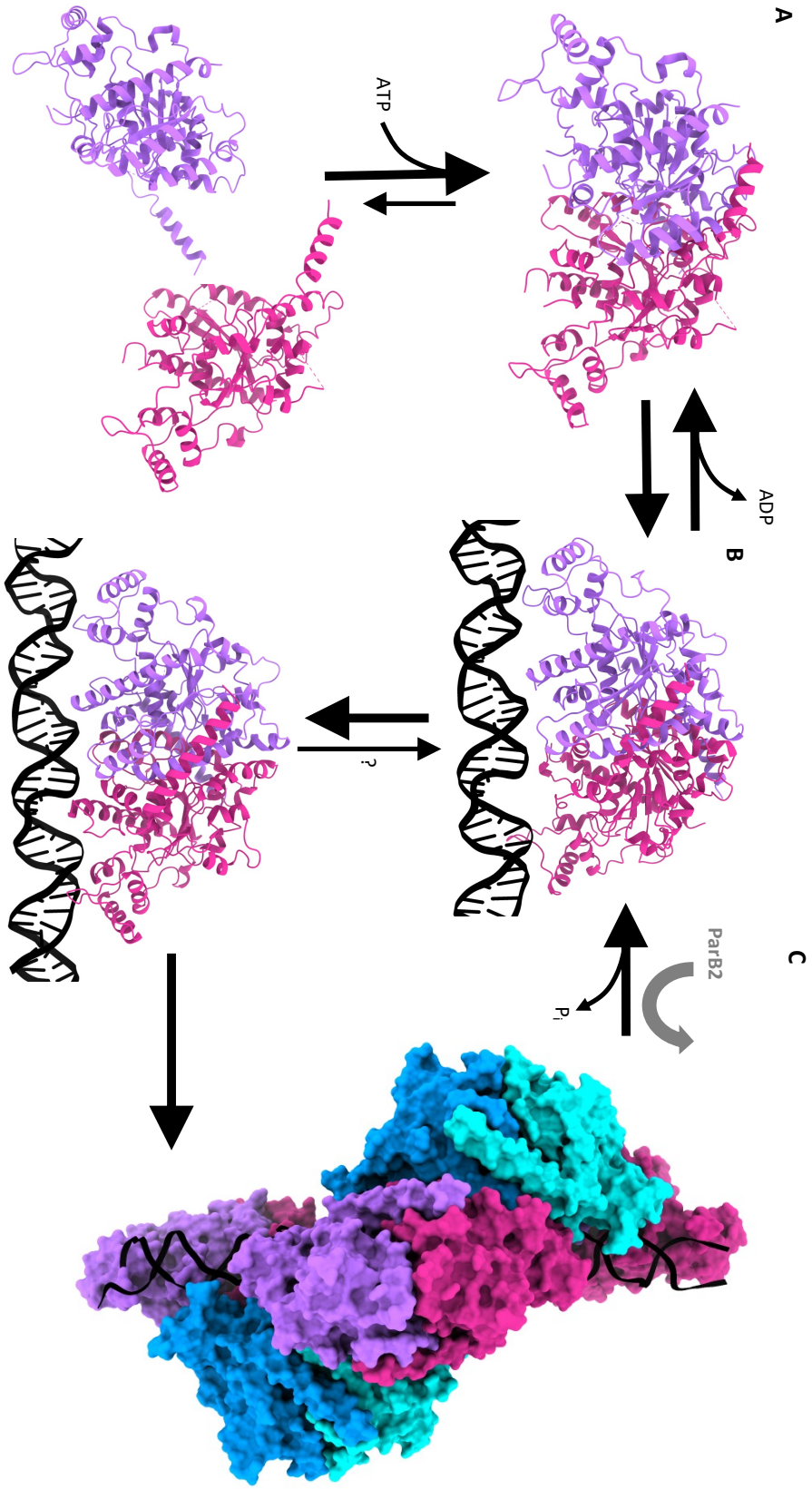

Figure 7.4. Proposed mechanism for ParA's cooperative binding to DNA, regulated by ParB.
(A) *in isolation, ParA is in equilibrium between monomer and dimer, with the dimer stabilized by the recruitment of nucleotide.* ***(B)*** *In the presence of DNA, the dimer undergoes a dramatic architecture change, exposing its oligomerization interface.* ***(C)*** *This leads to the formation of a higher-order assembly, in the form of a short filament segment. The presence of ParB-bound cargo stimulates ParA's ATPase activity, which leads to its return to the DNA-free conformation of the dimer. This in turn leads to the dissociation of ParA from the DNA, and the release of ADP.*

7.4 physiological relevance of the Cooperative binding to DNA

As mentioned above, whether ParA proteins do form filaments, and the role of such filaments, has remained controversial. Despite ParA filaments being formed *in vitro*, they probably do not exist as extended filaments in the cell, notably because of the low abundance of ParA in the cell. Since there is no evidence of extended filaments from fluorescence microscopy experiments, we can only predict that ParAs may form small filament patches on the DNA. Across species controlled by Par mediated segregation, there are mechanisms in place that may require for ParA clustering, and therefore a need for cooperative binding in these small regions.

7.4.1 High-density chromosomal regions (HDRs)

Multiple studies using fluorescently-tagged ParA orthologues in dividing cells, revealed that it clusters at high-density chromosomal regions (HDRs) (Baxter et al., 2020; Chodha et al., 2021; Le Gall et al., 2016; McLeod et al., 2017), and do not form filaments across the cell, as required for a mitotic-like mechanism. In keeping with this, the negative-stain EM experiments reported here suggests that at near-physiological concentration, the $ParA2_{vc}$ filaments can only form when bound to non-hydrolysed ATP. We therefore propose that *in-situ*, ParA proteins merely form small patches of filaments along the DNA, corresponding to those HDRs observed by super-resolution fluorescence microscopy. This likely helps forming high-density ParA regions in the nucleoid, as required in the proposed diffusion-ratchet model for segregation.

Nonetheless, a number of questions remain to be addressed to fully validate this mechanistic model. Specifically, while we observed major changes in the dimer architecture from the free ParA to the filament state, it remains to be established if these changes are induced by DNA binding, or by the recruitment of adjacent ParA molecules during filament formation. Furthermore, as indicated above, sequence similarity between ParA orthologue is low (**Figure 7.2**), and the residues at the DNA binding regions and filament interface are mostly not conserved.

7.4.2 Polar localisation proteins

As introduced in **Chapter 1**, polar localisation proteins are found among bacteria to help position the origin of replication (*oriC*) and maintain the directionality of segregation of native chromosomes (Bowman et al., 2008; Ebersbach et al., 2008; Ginda et al., 2013; Lin et al., 2017; Pióro et al., 2019; Pióro & Jakimowicz, 2020; Yamaichi et al., 2012). In *V. cholerae* and *C. crescentus*, HubP and PopZ are the respective proteins, having been identified to carry out their actions throughout sequestering ParA to the pole of the cell (Bowman et al., 2008; Ebersbach et al., 2008; Ptacin et al., 2014; Yamaichi et al., 2012). Since these regions have shown a condensed concentration of ParA, cooperative binding and filament formation could be relevant in these areas. Be more specific: Could HubP/PopZ induce filament formation/stabilize the filament? Do they interact directly with ParA?

7.4.3 Transcriptional repression

Another mechanism that has shown reliance on cooperative binding involves the specific binding capabilities of ParA. The N-terminal winged helix-turn-helix domain exclusive to type Ia ParAs exerts this specific binding capability, binding to their own promoter regions acting as transcriptional repressors (Biek & Strings, 1995; Friedman & Austin, 1988; Hayes et al., 1994). Recently, it has been uncovered in the *E.coli* F plasmid system that 3 $ParA_F$ (aka SopA) dimers bind cooperatively to overlapping motifs covering the promoter region (Boudsocq et al., 2021). Molecular dynamics from this study suggested how the winged-HTH domain is highly flexible, favouriting a cooperative binding hypothesis to the promoter region. However, the conformational changes observed between the different $ParA2_{vc}$ structures shows that the rotation of the dimer interface upon DNA binding causes the overall movement in the HTH domain. The N-terminal HTH domain itself remaining largely unchanged (**movie 3**).

7.5 Conclusion

$ParA2_{vc}$, like most ParAs, is a highly dynamic protein. Able to exist in both monomeric and dimeric states in the absence of nucleotide and showing an increased stability upon binding of ATP. ParA2 is established to bind cooperatively to DNA, like it's relatives, which could in turn be a feature of filament formation. Throughout the process of DNA binding and filament formation, there is a considerable change in dimer architecture. The N-terminal winged-HTH domain, being highly flexible, rotates out from the main body of the molecule, causing a twist over the dimer interface. However, it is unsure whether this is an adaption exerted over binding to DNA, or if it is a change triggered by cooperative binding and formation of the filament. The map obtained from cryo-EM has also revealed information on how ParA2 binds and interacts with the dsDNA. Showing a surprising third loop, located in the C-terminal, in the second DNA binding region binding deep into the major groove and distorting the DNA backbone, which has not be observed in other ParAs. Due to the low sequence homology among ParAs and members of the deviant walker A P-loop family, it is unsure whether filament formation is a feature shared among other members. This therefore requires further investigation, ideally with SopA ($ParA_F$) and P1 ParA, as these are other type Ia parAs which possess the C-terminal region discovered to be binding in the major groove. However, the mutagenesis work imaged via negative stain EM has suggested that filament formation may be controlled through the C-terminal α-helix (helix 16), of which there are a few conserved residues across all species examined. Since K388 is not conserved throughout ParAs, further mutagenesis work is required targeting the residues showing sequence similarity along the C-terminal α-helix. Despite years of research, we still largely don't understand how bacteria separate their DNA and the evolution between different species. However, from this work it has been highlighted the importance of the general fold seen across the MinD/ParA deviant walker-type family. All possessing the same general architecture, dimerising in a similar fashion along the nucleotide binding pocket with a β-sheet central to the molecule. Despite the lack of sequence conservation, this structural similarity must hold some significance. When we consider the diversity of action these proteins have, from

chromosome segregation to organelle positioning and flagella assembly, these proteins govern the overall arrangement of bacterial cells and are masters of cellular regulation. It is therefore intriguing to understand where this fold and assembly came from and how it has remained so prominent across many cellular mechanisms.

Data Availability

For the ParA2$_{vc}$ crystal structures, the coordinates have been deposited to the PDB, under the accession number 7NPD and 7NPE, for the apo and ADP bound state, respectively . For the ParA2-ATPγS-DNA cryo-EM atomic model, the coordinates have been deposited to the PDB, under the accession number 7NPF, and the map has been deposited to the EMDB, with the accession number 12515.

The majority of the contents of this thesis have been published under the reference: Parker, A. V, Mann, D., Tzokov, S. B., Hwang, L. C., & Bergeron, J. R. C. (2021). The structure of the bacterial DNA segregation ATPase filament reveals the conformational plasticity of ParA upon DNA binding. Nature Communications, 12(1), 5166. https://doi.org/10.1038/s41467-021-25429-2

Bibliography

Afonine, P. V., Grosse-Kunstleve, R. W., Echols, N., Headd, J. J., Moriarty, N. W., Mustyakimov, M., Terwilliger, T. C., Urzhumtsev, A., Zwart, P. H., & Adams, P. D. (2012). Towards automated crystallographic structure refinement with phenix.refine. *Acta Crystallographica Section D: Biological Crystallography*, *68*(4), 352–367. https://doi.org/10.1107/S0907444912001308

Afonine, P. V., Klaholz, B. P., Moriarty, N. W., Poon, B. K., Sobolev, O. V., Terwilliger, T. C., Adams, P. D., & Urzhumtsev, A. (2018). New tools for the analysis and validation of cryo-EM maps and atomic models. *Acta Crystallographica Section D: Structural Biology*, *74*(9), 814–840. https://doi.org/10.1107/S2059798318009324

Afonine, P. V., Poon, B. K., Read, R. J., Sobolev, O. V., Terwilliger, T. C., Urzhumtsev, A., & Adams, P. D. (2018). Real-space refinement in PHENIX for cryo-EM and crystallography. *Acta Crystallographica Section D: Structural Biology*, *74*(6), 531–544. https://doi.org/10.1107/S2059798318006551

Ah-Seng, Y., Lopez, F., Pasta, F., Lane, D., & Bouet, J.-Y. (2009). Dual role of DNA in regulating ATP hydrolysis by the SopA partition protein. *The Journal of Biological Chemistry*, *284*(44), 30067–30075. https://doi.org/10.1074/JBC.M109.044800

Akhtar, P., Anand, S. P., Watkins, S. C., & Khan, S. A. (2009). The tubulin-like RepX protein encoded by the pXO1 plasmid forms polymers in vivo in bacillus anthracis. *Journal of Bacteriology*, *191*(8), 2493–2500. https://doi.org/10.1128/JB.00027-09

Austin, S., & Abeles, A. (1983a). Partition of unit-copy miniplasmids to daughter cells: I. P1 and F miniplasmids contain discrete, interchangeable sequences sufficient to promote equipartition. *Journal of Molecular Biology*, *169*(2), 353–372. https://doi.org/10.1016/S0022-2836(83)80055-2

Austin, S., & Abeles, A. (1983b). Partition of unit-copy miniplasmids to daughter cells. II. The partition region of miniplasmid P1 encodes an essential protein and a centromere-like site at which it acts. *Journal of Molecular Biology*, *169*(2), 373–387. https://doi.org/10.1016/S0022-2836(83)80056-4

Baek, J. H., & Chattoraj, D. K. (2014). Chromosome I Controls Chromosome II Replication in *Vibrio cholerae*. *PLoS Genetics*, *10*(2), 1004184. https://doi.org/10.1371/journal.pgen.1004184

Barillà, D., Carmelo, E., & Hayes, F. (2007). The tail of the ParG DNA segregation protein remodels ParF polymers and enhances ATP hydrolysis via an arginine finger-like motif. *Proceedings of the National Academy of Sciences of the United States of America*, *104*(6), 1811–1816. https://doi.org/10.1073/PNAS.0607216104

Barillà, D., Rosenberg, M. F., Nobbmann, U., & Hayes, F. (2005). Bacterial DNA segregation dynamics mediated by the polymerizing protein ParF. *The EMBO Journal*, *24*(7), 1453. https://doi.org/10.1038/SJ.EMBOJ.7600619

Baxter, J. C., & Funnell, B. E. (2014). Plasmid Partition Mechanisms. *Microbiology Spectrum*, *2*(6). https://doi.org/10.1128/MICROBIOLSPEC.PLAS-0023-2014

Baxter, J. C., & Funnell, B. E. (2015). Plasmid Partition Mechanisms. In *Plasmids: Biology and Impact in Biotechnology and Discovery* (pp. 133–155). wiley. https://doi.org/10.1128/9781555818982.ch8

Baxter, J. C., Waples, W. G., & Funnell, B. E. (2020). Non-specific DNA binding by P1 ParA determines the distribution of plasmid partition and repressor activities. *Journal of Biological Chemistry*, jbc.RA120.015642. https://doi.org/10.1074/jbc.RA120.015642

Biek, D. P., & Strings, J. (1995). Partition Functions of Mini-F Affect Plasmid DNA Topology inEscherichia coli. *Journal of Molecular Biology*, *246*(3), 388–400. https://doi.org/10.1006/JMBI.1994.0094

Boudsocq, F., Salhi, M., Barbe, S., & Bouet, J.-Y. (2021). Three ParA Dimers Cooperatively Assemble on Type Ia Partition Promoters. *Genes 2021, Vol. 12, Page 1345*, *12*(9), 1345. https://doi.org/10.3390/GENES12091345

Bouet, J. Y., Ah-Seng, Y., Benmeradi, N., & Lane, D. (2007). Polymerization of SopA partition ATPase: Regulation by DNA binding and SopB. *Molecular Microbiology*, *63*(2), 468–481. https://doi.org/10.1111/j.1365-2958.2006.05537.x

Bowman, G. R., Comolli, L. R., Zhu, J., Eckart, M., Koenig, M., Downing, K. H., Moerner, W. E., Earnest, T., & Shapiro, L. (2008). A Polymeric Protein Anchors

the Chromosomal Origin/ParB Complex at a Bacterial Cell Pole. *Cell*, *134*(6), 945. https://doi.org/10.1016/J.CELL.2008.07.015

Brooks, A. C., & Hwang, L. C. (2017). Reconstitutions of plasmid partition systems and their mechanisms. In *Plasmid* (Vol. 91, pp. 37–41). Academic Press Inc. https://doi.org/10.1016/j.plasmid.2017.03.004

Caccamo, M., Dobruk-Serkowska, A., Rodríguez-Castañeda, F., Pennica, C., Barillà, D., & Hayes, F. (2020). Genome Segregation by the Venus Flytrap Mechanism: Probing the Interaction Between the ParF ATPase and the ParG Centromere Binding Protein. *Frontiers in Molecular Biosciences*, *7*, 108. https://doi.org/10.3389/fmolb.2020.00108

Castaing, J. P., Bouet, J.-Y., & Lane, D. (2008). F plasmid partition depends on interaction of SopA with non-specific DNA. *Molecular Microbiology*, *70*(4), 1000–1011. https://doi.org/10.1111/j.1365-2958.2008.06465.x

Chen, B. W., Lin, M. H., Chu, C. H., Hsu, C. E., & Sun, Y. J. (2015). Insights into ParB spreading from the complex structure of Spo0J and parS. *Proceedings of the National Academy of Sciences of the United States of America*, *112*(21), 6613–6618. https://doi.org/10.1073/pnas.1421927112

Chodha, S. S., Brooks, A. C., Davis, P., Ramachandran, R., Chattoraj, D. K., & Chin Hwang, L. (2021). Kinetic pathway of ATP-induced DNA interactions of ParA2, a protein essential for segregation of *Vibrio cholerae* chromosome 2. *BioRxiv*, 2021.02.27.433207. https://doi.org/10.1101/2021.02.27.433207

Chu, C. H., Yen, C. Y., Chen, B. W., Lin, M. G., Wang, L. H., Tang, K. Z., Hsiao, C. D., & Sun, Y. J. (2019). Crystal structures of HpSoj-DNA complexes and the nucleoid-adaptor complex formation in chromosome segregation. *Nucleic Acids Research*, *47*(4), 2113–2129. https://doi.org/10.1093/nar/gky1251

Croll, T. I., & Read, R. J. (2021). Adaptive Cartesian and torsional restraints for interactive model rebuilding. *Acta Crystallographica. Section D, Structural Biology*, *77*(Pt 4), 438. https://doi.org/10.1107/S2059798321001145

Dajkovic, A., & Lutkenhaus, J. (2006). Z ring as executor of bacterial cell division. In *Journal of Molecular Microbiology and Biotechnology* (Vol. 11, Issues 3–5, pp. 140–151). J Mol Microbiol Biotechnol. https://doi.org/10.1159/000094050

Davey, M., & Funnell, B. E. (1997). Modulation of the P1 plasmid partition protein

ParA by ATP, ADP, and P1 ParB. *The Journal of Biological Chemistry*, *272*(24), 15286–15292. https://doi.org/10.1074/JBC.272.24.15286

Davis, M. A., Martin, K. A., & Austin, S. J. (1992). Biochemical activities of the parA partition protein of the P1 plasmid. *Molecular Microbiology*, *6*(9), 1141–1147. https://doi.org/10.1111/J.1365-2958.1992.TB01552.X

Davis, M. A., Radnedge, L., Martin, K. A., Hayes, F., Youngren, B., & Austin, S. J. (1996). The P1 ParA protein and its ATPase activity play a direct role in the segregation of plasmid copies to daughter cells. *Molecular Microbiology*, *21*(5), 1029–1036. https://doi.org/10.1046/J.1365-2958.1996.721423.X

Drulyte, I., Johnson, R. M., Hesketh, E. L., Hurdiss, D. L., Scarff, C. A., Porav, S. A., Ranson, N. A., Muench, S. P., & Thompson, R. F. (2018). Approaches to altering particle distributions in cryo-electron microscopy sample preparation. *Acta Crystallographica. Section D, Structural Biology*, *74*(Pt 6), 560. https://doi.org/10.1107/S2059798318006496

Dunham, T. D., Xu, W., Funnell, B. E., & Schumacher, M. A. (2009). Structural basis for ADP-mediated transcriptional regulation by P1 and P7 ParA. *EMBO Journal*, *28*(12), 1792–1802. https://doi.org/10.1038/emboj.2009.120

Ebersbach, G., Briegel, A., Jensen, G. J., & Jacobs-Wagner, C. (2008). A Self-Associating Protein Critical for Chromosome Attachment, Division, and Polar Organization in Caulobacter. *Cell*, *134*(6), 956–968. https://doi.org/10.1016/J.CELL.2008.07.016

Ebersbach, G., & Gerdes, K. (2005). Plasmid segregation mechanisms. In *Annual Review of Genetics* (Vol. 39, pp. 453–479). Annu Rev Genet. https://doi.org/10.1146/annurev.genet.38.072902.091252

Ebersbach, G., Ringgaard, S., Møller-Jensen, J., Wang, Q., Sherratt, D. J., & Gerdes, K. (2006). Regular cellular distribution of plasmids by oscillating and filament-forming para ATPase of plasmid pB171. *Molecular Microbiology*, *61*(6), 1428–1442. https://doi.org/10.1111/j.1365-2958.2006.05322.x

Egan, E. S., Fogel, M. A., & Waldor, M. K. (2005). MicroReview: Divided genomes: negotiating the cell cycle in prokaryotes with multiple chromosomes. *Molecular Microbiology*, *56*(5), 1129–1138. https://doi.org/10.1111/J.1365-2958.2005.04622.X

Emsley, P., Lohkamp, B., Scott, W. G., & Cowtan, K. (2010). Features and development of Coot. *Acta Crystallographica Section D: Biological Crystallography*, *66*(4), 486–501. https://doi.org/10.1107/S0907444910007493

Evans, P. (2005). Scaling and assessment of data quality. *Urn:Issn:0907-4449*, *62*(1), 72–82. https://doi.org/10.1107/S0907444905036693

Faruque, S. M., Albert, M. J., & Mekalanos, J. J. (1998). Epidemiology, Genetics, and Ecology of Toxigenic *Vibrio cholerae*. *Microbiology and Molecular Biology Reviews*, *62*(4), 1301–1314. https://doi.org/10.1128/mmbr.62.4.1301-1314.1998

Fiebig, A., Keren, K., & Theriot, J. A. (2006). Fine-scale time-lapse analysis of the biphasic, dynamic behaviour of the two *Vibrio cholerae* chromosomes. *Molecular Microbiology*, *60*(5), 1164–1178. https://doi.org/10.1111/j.1365-2958.2006.05175.x

Fink, G., & Löwe, J. (2015). Reconstitution of a prokaryotic minus end-tracking system using TubRC centromeric complexes and tubulin-like protein TubZ filaments. *Proceedings of the National Academy of Sciences of the United States of America*, *112*(15), E1845–E1850. https://doi.org/10.1073/pnas.1423746112

Fisher, G. L. M., Pastrana, C. L., Higman, V. A., Koh, A., Taylor, J. A., Butterer, A., Craggs, T., Sobott, F., Murray, H., Crump, M. P., Moreno-Herrero, F., & Dillingham, M. S. (2017). The structural basis for dynamic DNA binding and bridging interactions which condense the bacterial centromere. *ELife*, *6*. https://doi.org/10.7554/eLife.28086

Fogel, M. A., & Waldor, M. K. (2005). Distinct segregation dynamics of the two *Vibrio cholerae* chromosomes. *Molecular Microbiology*, *55*(1), 125–136. https://doi.org/10.1111/j.1365-2958.2004.04379.x

Fogel, M. A., & Waldor, M. K. (2006). A dynamic, mitotic-like mechanism for bacterial chromosome segregation. *Genes and Development*, *20*(23), 3269–3282. https://doi.org/10.1101/gad.1496506

Friedman, S. A., & Austin, S. J. (1988). The P1 plasmid-partition system synthesizes two essential proteins from an autoregulated operon. *Plasmid*, *19*(2), 103–112. https://doi.org/10.1016/0147-619X(88)90049-2

Fung, E., Bouet, J. Y., & Funnell, B. E. (2001). Probing the ATP-binding site of P1 ParA: Partition and repression have different requirements for ATP binding and hydrolysis. *EMBO Journal*, *20*(17), 4901–4911. https://doi.org/10.1093/emboj/20.17.4901

Funnell, B. E. (2016). ParB partition proteins: Complex formation and spreading at bacterial and plasmid centromeres. In *Frontiers in Molecular Biosciences* (Vol. 3, Issue AUG, p. 44). Frontiers Media S.A. https://doi.org/10.3389/fmolb.2016.00044

Garner, E. C., Campbell, C. S., & Mullins, R. D. (2004). Dynamic instability in a DNA-segregating prokaryotic actin homolog. *Science*, *306*(5698), 1021–1025. https://doi.org/10.1126/science.1101313

Garner, E. C., Campbell, C. S., Weibel, D. B., & Mullins, R. D. (2007). Reconstitution of DNA segregation driven by assembly of a prokaryotic actin homolog. *Science*, *315*(5816), 1270–1274. https://doi.org/10.1126/science.1138527

Gerdes, K., Howard, M., & Szardenings, F. (2010). Pushing and pulling in prokaryotic DNA segregation. In *Cell* (Vol. 141, Issue 6, pp. 927–942). Elsevier B.V. https://doi.org/10.1016/j.cell.2010.05.033

Gerdes, K., Larsen, J. E. L., & Molin, S. (1985). Stable inheritance of plasmid R1 requires two different loci. *Journal of Bacteriology*, *161*(1), 292–298. https://doi.org/10.1128/jb.161.1.292-298.1985

Gerdes, K., & Molin, S. (1986). Partitioning of plasmid R1. Structural and functional analysis of the parA locus. *Journal of Molecular Biology*, *190*(3), 269–279. https://doi.org/10.1016/0022-2836(86)90001-X

Gerdes, K., Moller-Jensen, J., & Jensen, R. B. (2000). Plasmid and chromosome partitioning: Surprises from phylogeny. In *Molecular Microbiology* (Vol. 37, Issue 3, pp. 455–466). Blackwell Publishing Ltd. https://doi.org/10.1046/j.1365-2958.2000.01975.x

Ginda, K., Bezulska, M., Ziółkiewicz, M., Dziadek, J., Zakrzewska-Czerwińska, J., & Jakimowicz, D. (2013). ParA of Mycobacterium smegmatis co-ordinates chromosome segregation with the cell cycle and interacts with the polar growth determinant DivIVA. *Molecular Microbiology*, *87*(5), 998–1012. https://doi.org/10.1111/MMI.12146

Goddard, T. D., Huang, C. C., Meng, E. C., Pettersen, E. F., Couch, G. S., Morris, J. H., & Ferrin, T. E. (2018). UCSF ChimeraX: Meeting modern challenges in visualization and analysis. *Protein Science*, *27*(1), 14–25. https://doi.org/10.1002/pro.3235

Gordon, G. S., & Wright, A. (2000). DNA segregation in bacteria. In *Annual Review of Microbiology* (Vol. 54, pp. 681–708). Annu Rev Microbiol. https://doi.org/10.1146/annurev.micro.54.1.681

Graham, T. G. W., Wang, X., Song, D., Etson, C. M., van Oijen, A. M., Rudner, D. Z., & Loparo, J. J. (2014). ParB spreading requires DNA bridging. *Genes and Development*, *28*(11), 1228–1238. https://doi.org/10.1101/gad.242206.114

Havey, J. C., Vecchiarelli, A. G., & Funnell, B. E. (2012). ATP-regulated interactions between P1 ParA, ParB and non-specific DNA that are stabilized by the plasmid partition site, parS. *Nucleic Acids Research*, *40*(2), 801–812. https://doi.org/10.1093/nar/gkr747

Hayat, M. A. (1986). Glutaraldehyde: Role in electron microscopy. *Micron and Microscopica Acta*, *17*(2), 115–135. https://doi.org/10.1016/0739-6260(86)90042-0

Hayes, F., Radnedge, L., Davis, M. A., & Austin, S. J. (1994). The homologous operons for P1 and P7 plasmid partition are autoregulated from dissimilar operator sites. *Molecular Microbiology*, *11*(2), 249–260. https://doi.org/10.1111/j.1365-2958.1994.tb00305.x

He, S., & Scheres, S. H. W. (2017). Helical reconstruction in RELION. *Journal of Structural Biology*, *198*(3), 163–176. https://doi.org/10.1016/j.jsb.2017.02.003

Heidelberg, J. F., Elsen, J. A., Nelson, W. C., Clayton, R. A., Gwinn, M. L., Dodson, R. J., Haft, D. H., Hickey, E. K., Peterson, J. D., Umayam, L., Gill, S. R., Nelson, K. E., Read, T. D., Tettelin, H., Richardson, D., Ermolaeva, M. D., Vamathevan, J., Bass, S., Halving, Q., … Fraser, C. M. (2000). DNA sequence of both chromosomes of the cholera pathogen *Vibrio cholerae*. *Nature*, *406*(6795), 477–483. https://doi.org/10.1038/35020000

Hester, C. M., & Lutkenhaus, J. (2007). Soj (ParA) DNA binding is mediated by conserved arginines and is essential for plasmid segregation. *Proceedings of the National Academy of Sciences of the United States of America*, *104*(51),

20326–20331. https://doi.org/10.1073/pnas.0705196105

Hoshino, S., & Hayashi, I. (2012). Filament Formation of the FtsZ/Tubulin-like Protein TubZ from the Bacillus cereus pXO1 Plasmid. *The Journal of Biological Chemistry*, *287*(38), 32103. https://doi.org/10.1074/JBC.M112.373803

Hu, L., Vecchiarelli, A. G., Mizuuchi, K., Neuman, K. C., & Liu, J. (2017). Brownian ratchet mechanisms of ParA-mediated partitioning. In *Plasmid* (Vol. 92, pp. 12–16). Academic Press Inc. https://doi.org/10.1016/j.plasmid.2017.05.002

Hui, M. P., Galkin, V. E., Yu, X., Stasiak, A. Z., Stasiak, A., Waldor, M. K., & Egelman, E. H. (2010). ParA2, a *Vibrio cholerae* chromosome partitioning protein, forms left-handed helical filaments on DNA. *Proceedings of the National Academy of Sciences of the United States of America*, *107*(10), 4590–4595. https://doi.org/10.1073/pnas.0913060107

Hwang, L. C., Vecchiarelli, A. G., Han, Y. W., Mizuuchi, M., Harada, Y., Funnell, B. E., & Mizuuchi, K. (2013). ParA-mediated plasmid partition driven by protein pattern self-organization. *EMBO Journal*, *32*(9), 1238–1249. https://doi.org/10.1038/emboj.2013.34

Jacob, F., Brenner, S., & Cuzin, F. (1963). On the Regulation of DNA Replication in Bacteria. *Cold Spring Harbor Symposia on Quantitative Biology*, *28*(0), 329–348. https://doi.org/10.1101/sqb.1963.028.01.048

Jalal, A. S. B., & Le, T. B. K. (2020). Bacterial chromosome segregation by the ParABS system. *Open Biology*, *10*(6), 200097. https://doi.org/10.1098/rsob.200097

Jalal, A. S. B., Tran, N. T., & Le, T. B. K. (2020). ParB spreading on DNA requires cytidine triphosphate in vitro. *ELife*, *9*. https://doi.org/10.7554/eLife.53515

Jalal, A. S. B., Tran, N. T., Stevenson, C. E. M., Chimthanawala, A., Badrinarayanan, A., Lawson, D. M., & Le, T. B. K. (2021). A CTP-dependent gating mechanism enables ParB spreading on DNA in *Caulobacter crescentus*. *BioRxiv*, 816959. https://doi.org/10.1101/816959

Jindal, L., & Emberly, E. (2015). Operational Principles for the Dynamics of the In Vitro ParA-ParB System. *PLoS Computational Biology*, *11*(12), e1004651. https://doi.org/10.1371/journal.pcbi.1004651

Kabsch, W., T., B. A., K., D., A., K. P., K., D., S., M., G., R. R. B., P., E., S., F., K., W., W., K., W., K., W., K., W., K., P., K., & S., W. M. (2010). XDS. *Acta Crystallographica*

Section D Biological Crystallography, *66*(2), 125–132. https://doi.org/10.1107/S0907444909047337

Kadoya, R., & Chattoraj, D. K. (2012). Insensitivity of chromosome I and the cell cycle to blockage of replication and segregation of *Vibrio cholerae* chromosome II. *MBio*, *3*(3). https://doi.org/10.1128/mBio.00067-12

Kastner, B., Fischer, N., Golas, M. M., Sander, B., Dube, P., Boehringer, D., Hartmuth, K., Deckert, J., Hauer, F., Wolf, E., Uchtenhagen, H., Urlaub, H., Herzog, F., Peters, J. M., Poerschke, D., Lührmann, R., & Stark, H. (2007). GraFix: sample preparation for single-particle electron cryomicroscopy. *Nature Methods 2008 5:1*, *5*(1), 53–55. https://doi.org/10.1038/nmeth1139

Kepiro, I. E., Nardone, B., Page, A., & Ryadnov, M. G. (2020). Revealing Sources of Variation for Reproducible Imaging of Protein Assemblies by Electron Microscopy. *Micromachines*, *11*(3). https://doi.org/10.3390/MI11030251

Kirkup, B. C., Chang, L., Chang, S., Gevers, D., & Polz, M. F. (2010). Vibrio chromosomes share common history. *BMC Microbiology*, *10*. https://doi.org/10.1186/1471-2180-10-137

Kleckner, N., Fisher, J. K., Stouf, M., White, M. A., Bates, D., & Witz, G. (2014). The Bacterial Nucleoid: Nature, Dynamics and Sister Segregation. *Current Opinion in Microbiology*, *22*, 127. https://doi.org/10.1016/J.MIB.2014.10.001

Koonin, E. V. (1993). A superfamily of ATPases with diverse functions containing either classical or deviant ATP-binding motif. *Journal of Molecular Biology*, *229*(4), 1165–1174. https://doi.org/10.1006/jmbi.1993.1115

Krissinel, E., & Henrick, K. (2007). Inference of Macromolecular Assemblies from Crystalline State. *Journal of Molecular Biology*, *372*(3), 774–797. https://doi.org/10.1016/J.JMB.2007.05.022

Kucukelbir, A., Sigworth, F. J., & Tagare, H. D. (2014). Quantifying the local resolution of cryo-EM density maps. *Nature Methods*, *11*(1), 63–65. https://doi.org/10.1038/nmeth.2727

Larsen, R. A., Cusumano, C., Fujioka, A., Lim-Fong, G., Patterson, P., & Pogliano, J. (2007). Treadmilling of a prokaryotic tubulin-like protein, TubZ, required for plasmid stability in *Bacillus thuringiensis*. *Genes and Development*, *21*(11), 1340–1352. https://doi.org/10.1101/gad.1546107

Le Gall, A., Cattoni, D. I., Guilhas, B., Mathieu-Demazière, C., Oudjedi, L., Fiche, J. B., Rech, J., Abrahamsson, S., Murray, H., Bouet, J.-Y., & Nollmann, M. (2016). Bacterial partition complexes segregate within the volume of the nucleoid. *Nature Communications*, *7*. https://doi.org/10.1038/ncomms12107

Leipe, D. D., Wolf, Y. I., Koonin, E. V., & Aravind, L. (2002). Classification and evolution of P-loop GTPases and related ATPases. *Journal of Molecular Biology*, *317*(1), 41–72. https://doi.org/10.1006/jmbi.2001.5378

Leonard, T. A., Butler, P. J. G., & Löwe, J. (2004). Structural analysis of the chromosome segragation protein Spo0J from *Thermus thermophilus*. *Molecular Microbiology*, *53*(2), 419–432. https://doi.org/10.1111/j.1365-2958.2004.04133.x

Leonard, T. A., Butler, P. J. G., & Löwe, J. (2005). Bacterial chromosome segregation: structure and DNA binding of the Soj dimer--a conserved biological switch. *The EMBO Journal*, *24*(2), 270–282. https://doi.org/10.1038/sj.emboj.7600530

Lim, H. C., Surovtsev, I. V., Beltran, B. G., Huang, F., Bewersdorf, J., & Jacobs-Wagner, C. (2014). Evidence for a DNA-relay mechanism in ParABS-mediated chromosome segregation. *ELife*, *2014*(3). https://doi.org/10.7554/eLife.02758

Lin, L., Osorio Valeriano, M., Harms, A., Søgaard-Andersen, L., & Thanbichler, M. (2017). Bactofilin-mediated organization of the ParABS chromosome segregation system in *Myxococcus xanthus*. *Nature Communications 2017 8:1*, *8*(1), 1–16. https://doi.org/10.1038/s41467-017-02015-z

Livny, J., Yamaichi, Y., & Waldor, M. K. (2007). Distribution of centromere-like parS sites in bacteria: Insights from comparative genomics. *Journal of Bacteriology*, *189*(23), 8693–8703. https://doi.org/10.1128/JB.01239-07

Lutkenhaus, J. (2012). The ParA/MinD family puts things in their place. In *Trends in Microbiology* (Vol. 20, Issue 9, pp. 411–418). Elsevier. https://doi.org/10.1016/j.tim.2012.05.002

Lutkenhaus, J., Pichoff, S., & Du, S. (2012). Bacterial cytokinesis: from Z ring to divisome. *Cytoskeleton (Hoboken, N.J.)*, *69*(10), 778. https://doi.org/10.1002/CM.21054

Lutkenhaus, J., & Sundaramoorthy, M. (2003). MinD and role of the deviant Walker A motif, dimerization and membrane binding in oscillation. In *Molecular*

Microbiology (Vol. 48, Issue 2, pp. 295–303). John Wiley & Sons, Ltd. https://doi.org/10.1046/j.1365-2958.2003.03427.x

McCoy, A. J., Grosse-Kunstleve, R. W., Adams, P. D., Winn, M. D., Storoni, L. C., & Read, R. J. (2007). Phaser crystallographic software. *Journal of Applied Crystallography*, *40*(4), 658–674. https://doi.org/10.1107/S0021889807021206

McLeod, B. N., Allison-Gamble, G. E., Barge, M. T., Tonthat, N. K., Schumacher, M. A., Hayes, F., & Barillà, D. (2017). A three-dimensional ParF meshwork assembles through the nucleoid to mediate plasmid segregation. *Nucleic Acids Research*, *45*(6), 3158–3171. https://doi.org/10.1093/nar/gkw1302

Møller-Jensen, J., Borch, J., Dam, M., Jensen, R. B., Roepstorff, P., & Gerdes, K. (2003). Bacterial Mitosis: ParM of Plasmid R1 Moves Plasmid DNA by an Actin-like Insertional Polymerization Mechanism. *Molecular Cell*, *12*(6), 1477–1487. https://doi.org/10.1016/S1097-2765(03)00451-9

Nguyen, N. P., Ersoy, I., Gotberg, J., Bunyak, F., & White, T. A. (2021). DRPnet: automated particle picking in cryo-electron micrographs using deep regression. *BMC Bioinformatics 2021 22:1*, *22*(1), 1–28. https://doi.org/10.1186/S12859-020-03948-X

Ni, L., Xu, W., Kumaraswami, M., & Schumacher, M. A. (2010). Plasmid protein TubR uses a distinct mode of HTH-DNA binding and recruits the prokaryotic tubulin homolog TubZ to effect DNA partition. *Proceedings of the National Academy of Sciences of the United States of America*, *107*(26), 11763–11768. https://doi.org/10.1073/PNAS.1003817107

Ogasawara, N., & Yoshikawa, H. (1992). Genes and their organization in the replication origin region of the bacterial chromosome. *Molecular Microbiology*, *6*(5), 629–634. https://doi.org/10.1111/J.1365-2958.1992.TB01510.X

Ogura, T., & Hiraga, S. (1983). Partition mechanism of F plasmid: Two plasmid gene-encoded products and a cis-acting region are involved in partition. *Cell*, *32*(2), 351–360. https://doi.org/10.1016/0092-8674(83)90454-3

Ohashi, M., Hosokawa, F., Shinkawa, T., & Iwasaki, K. (2021). Evaluation of automated particle picking for cryogenic electron microscopy using high-precision transmission electron microscope simulation based on a multi-slice method. *Urn:Issn:2059-7983*, *77*(7), 966–979.

https://doi.org/10.1107/S2059798321005106

Ohi, M., Li, Y., Cheng, Y., & Walz, T. (2004). Negative Staining and Image Classification-Powerful Tools in Modern Electron Microscopy. *Biological Procedures Online* •, *6*(1), 23–34. www.biologicalprocedures.com

Osorio-Valeriano, M., Altegoer, F., Das, C. K., Steinchen, W., Panis, G., Connolley, L., Giacomelli, G., Feddersen, H., Corrales-Guerrero, L., Giammarinaro, P., Hanßmann, J., Bramkamp, M., Viollier, P. H., Murray, S., Schäfer, L. V, Bange, G., & Thanbichler, M. (2021). The CTPase activity of ParB acts as a timing mechanism to control the dynamics and function of prokaryotic DNA partition complexes. *BioRxiv*, 2021.05.05.442810. https://doi.org/10.1101/2021.05.05.442810

Osorio-Valeriano, M., Altegoer, F., Steinchen, W., Urban, S., Liu, Y., Bange, G., & Martin Thanbichler. (2019). ParB-type DNA Segregation Proteins Are CTP-Dependent Molecular Switches. *Cell*, *179*. https://doi.org/10.1016/j.cell.2019.11.015

Pióro, M., & Jakimowicz, D. (2020). Chromosome Segregation Proteins as Coordinators of Cell Cycle in Response to Environmental Conditions. In *Frontiers in Microbiology* (Vol. 11, p. 588). Frontiers Media S.A. https://doi.org/10.3389/fmicb.2020.00588

Pióro, M., Małecki, T., Portas, M., Magierowska, I., Trojanowski, D., Sherratt, D. J., Zakrzewska-Czerwińska, J., Ginda, K., & Jakimowicz, D. (2019). Competition between DivIVA and the nucleoid for ParA binding promotes segrosome separation and modulates mycobacterial cell elongation. *Molecular Microbiology*, *111*(1), 204–220. https://doi.org/10.1111/mmi.14149

Possoz, C., Junier, I., & Espeli, O. (2012). Bacterial chromosome segregation. *Frontiers in Bioscience*, *17*(3), 1020–1034. https://doi.org/10.2741/3971

Pratto, F., Cicek, A., Weihofen, W., Lurz, R., Saenger, W., & Alonso, J. C. (2008). *Streptococcus pyogenes* pSM19035 requires dynamic assembly of ATP-bound ParA and ParB on parS DNA during plasmid segregation. *Nucleic Acids Research*, *36*(11), 3676–3689. https://doi.org/10.1093/NAR/GKN170

Prieß, M., Göddeke, H., Groenhof, G., & Schäfer, L. V. (2018). Molecular Mechanism of ATP Hydrolysis in an ABC Transporter. *ACS Central Science*, *4*(10), 1334–

1343. https://doi.org/10.1021/ACSCENTSCI.8B00369/SUPPL_FILE/OC8B00369_LIVESLIDES.MP4

Ptacin, J. L., Gahlmann, A., Bowman, G. R., Perez, A. M., Von Diezmann, A. R. S., Eckart, M. R., Moerner, W. E., & Shapiro, L. (2014). Bacterial scaffold directs pole-specific centromere segregation. *Proceedings of the National Academy of Sciences of the United States of America*, *111*(19), E2046. https://doi.org/10.1073/pnas.1405188111

Ptacin, J. L., Lee, S. F., Garner, E. C., Toro, E., Eckart, M. R., Comolli, L. R., Moerner, W. E., & Shapiro, L. (2010). A spindle-like apparatus guides bacterial chromosome segregation. *Nature Cell Biology*, *12*(8), 791–798. https://doi.org/10.1038/ncb2083

Ramachandran, R., Jha, J., & Chattoraj, D. K. (2014). Chromosome segregation in *Vibrio cholerae*. In *Journal of Molecular Microbiology and Biotechnology* (Vol. 24, Issues 5–6, pp. 360–370). S. Karger AG. https://doi.org/10.1159/000368853

Ramachandran, R., Jha, J., Paulsson, J., & Chattoraj, D. K. (2017). Random versus Cell Cycle-Regulated Replication Initiation in Bacteria: Insights from Studying *Vibrio cholerae* Chromosome 2. *Microbiology and Molecular Biology Reviews*, *81*(1). https://doi.org/10.1128/mmbr.00033-16

Reyes-Lamothe, R., Nicolas, E., & Sherratt, D. J. (2012). Chromosome replication and segregation in bacteria. *Annual Review of Genetics*, *46*, 121–143. https://doi.org/10.1146/annurev-genet-110711-155421

Ringgaard, S., Van Zon, J., Howard, M., & Gerdes, K. (2009). Movement and equipositioning of plasmids by ParA filament disassembly. *Proceedings of the National Academy of Sciences of the United States of America*, *106*(46), 19369–19374. https://doi.org/10.1073/pnas.0908347106

Rodionov, O., ŁObocka, M., & Yarmolinsky, M. (1999). Silencing of genes flanking the P1 plasmid centromere. *Science*, *283*(5401), 546–549. https://doi.org/10.1126/science.283.5401.546

Rohou, A., & Grigorieff, N. (2015). CTFFIND4: Fast and accurate defocus estimation from electron micrographs. *Journal of Structural Biology*, *192*(2), 216–221. https://doi.org/10.1016/j.jsb.2015.08.008

Romero Romero, M. L., Yang, F., Lin, Y. R., Toth-Petroczy, A., Berezovsky, I. N., Goncearenco, A., Yang, W., Wellner, A., Kumar-Deshmukh, F., Sharon, M., Baker, D., Varani, G., & Tawfik, D. S. (2018). Simple yet functional phosphate-loop proteins. *Proceedings of the National Academy of Sciences of the United States of America*, *115*(51), E11943–E11950. https://doi.org/10.1073/PNAS.1812400115/SUPPL_FILE/PNAS.1812400115.SAPP.PDF

Sanchez, A., Cattoni, D. I., Walter, J. C., Rech, J., Parmeggiani, A., Nollmann, M., & Bouet, J. Y. (2015). Stochastic Self-Assembly of ParB Proteins Builds the Bacterial DNA Segregation Apparatus. *Cell Systems*, *1*(2), 163–173. https://doi.org/10.1016/J.CELS.2015.07.013/ATTACHMENT/07C760A9-BA91-4FDC-B04D-3E11FB6E3B07/MMC1.PDF

Saraste, M., Sibbald, P. R., & Wittinghofer, A. (1990). The P-loop - a common motif in ATP- and GTP-binding proteins. In *Trends in Biochemical Sciences* (Vol. 15, Issue 11, pp. 430–434). Elsevier Current Trends. https://doi.org/10.1016/0968-0004(90)90281-F

Schofield, W. B., Lim, H. C., & Jacobs-Wagner, C. (2010). Cell cycle coordination and regulation of bacterial chromosome segregation dynamics by polarly localized proteins. *EMBO Journal*, *29*(18), 3068–3081. https://doi.org/10.1038/emboj.2010.207

Schumacher, M. A. (2008). Structural biology of plasmid partition: Uncovering the molecular mechanisms of DNA segregation. In *Biochemical Journal* (Vol. 412, Issue 1, pp. 1–18). Portland Press. https://doi.org/10.1042/BJ20080359

Schumacher, M. A., & Funnell, B. E. (2005). Structures of ParB bound to DNA reveal mechanism of partition complex formation. *Nature*, *438*(7067), 516–519. https://doi.org/10.1038/nature04149

Schumacher, M. A., Tonthat, N. K., Lee, J., Rodriguez-Castañeda, F. A., Chinnam, N. B., Kalliomaa-Sanford, A. K., Ng, I. W., Barge, M. T., Shaw, P. L. R., & Barillà, D. (2015). Structures of archaeal DNA segregation machinery reveal bacterial and eukary otic linkages. *Science*, *349*(6252), 1120–1124. https://doi.org/10.1126/science.aaa9046

Snijder, J., Borst, A. J., Dosey, A., Walls, A. C., Burrell, A., Reddy, V. S., Kollman, J. M.,

& Veesler, D. (2017). Vitrification after multiple rounds of sample application and blotting improves particle density on cryo-electron microscopy grids. *Journal of Structural Biology*, *198*(1), 38. https://doi.org/10.1016/J.JSB.2017.02.008

Soh, Y.-M., Davidson, I. F., Zamuner, S., Basquin, J., Bock, F. P., Taschner, M., Veening, J.-W., De Los Rios, P., Peters, J.-M., & Gruber, S. (2019). Self-organization of parS centromeres by the ParB CTP hydrolase. *Science (New York, N.Y.)*. https://doi.org/10.1126/science.aay3965

Surovtsev, I. V., Campos, M., & Jacobs-Wagner, C. (2016). DNA-relay mechanism is sufficient to explain ParA-dependent intracellular transport and patterning of single and multiple cargos. *Proceedings of the National Academy of Sciences of the United States of America*, *113*(46), E7268–E7276. https://doi.org/10.1073/pnas.1616118113

Szardenings, F., Guymer, D., & Gerdes, K. (2011). ParA ATPases can move and position DNA and subcellular structures. In *Current Opinion in Microbiology* (Vol. 14, Issue 6, pp. 712–718). Curr Opin Microbiol. https://doi.org/10.1016/j.mib.2011.09.008

Szewczak-Harris, A., & Löwe, J. (2018). Cryo-EM reconstruction of AlfA from *Bacillus subtilis* reveals the structure of a simplified actin-like filament at 3.4-Å resolution. *Proceedings of the National Academy of Sciences*, *115*(13), 3458–3463. https://doi.org/10.1073/PNAS.1716424115

Szewczak-Harris, A., Wagstaff, J., & Löwe, J. (2019). Cryo-EM structure of the MinCD copolymeric filament from *Pseudomonas aeruginosa* at 3.1 Å resolution. *FEBS Letters*, *593*(15), 1915–1926. https://doi.org/10.1002/1873-3468.13471

Tang, G., Peng, L., Baldwin, P. R., Mann, D. S., Jiang, W., Rees, I., & Ludtke, S. J. (2007). EMAN2: An extensible image processing suite for electron microscopy. *Journal of Structural Biology*, *157*(1), 38–46. https://doi.org/10.1016/J.JSB.2006.05.009

Taylor, J. A., Pastrana, C. L., Butterer, A., Pernstich, C., Gwynn, E. J., Sobott, F., Moreno-Herrero, F., & Dillingham, M. S. (2015). Specific and non-specific interactions of ParB with DNA: Implications for chromosome segregation. *Nucleic Acids Research*, *43*(2), 719–731. https://doi.org/10.1093/nar/gku1295

Taylor, J. A., Seol, Y., Budhathoki, J., Neuman, K. C., & Mizuuchi, K. (2021). Ctp and pars coordinate parb partition complex dynamics and para-atpase activation for parabs-mediated dna partitioning. *ELife*, *10*. https://doi.org/10.7554/ELIFE.65651

Tickle, I. J., Flensburg, C., Keller, P., Paciorek, W., Sharff, A., Vonrhein, C., & Bricogne, G. (2018). *STARANISO*. https://staraniso.globalphasing.org/cgi-bin/staraniso.cgi

Toro, E., Hong, S. H., McAdams, H. H., & Shapiro, L. (2008). Caulobacter requires a dedicated mechanism to initiate chromosome segregation. *Proceedings of the National Academy of Sciences of the United States of America*, *105*(40), 15435–15440. https://doi.org/10.1073/pnas.0807448105

Toro, E., & Shapiro, L. (2010). Bacterial chromosome organization and segregation. In *Cold Spring Harbor perspectives in biology* (Vol. 2, Issue 2). https://doi.org/10.1146/annurev-cellbio-100814-125211

Usluer, G. D., DiMaio, F., Yang, S. K., Hansen, J. M., Polka, J. K., Mullins, R. D., & Kollman, J. M. (2018). Cryo-EM structure of the bacterial actin AlfA reveals unique assembly and ATP-binding interactions and the absence of a conserved subdomain. *Proceedings of the National Academy of Sciences*, *115*(13), 3356–3361. https://doi.org/10.1073/PNAS.1715836115

Van den Ent, F., Møller-Jensen, J., Amos, L. A., Gerdes, K., & Löwe, J. (2002). F-actin-like filaments formed by plasmid segregation protein ParM. *EMBO Journal*, *21*(24), 6935–6943. https://doi.org/10.1093/emboj/cdf672

Vecchiarelli, A. G., Han, Y. W., Tan, X., Mizuuchi, M., Ghirlando, R., Biertümpfel, C., Funnell, B. E., & Mizuuchi, K. (2010). ATP control of dynamic P1 ParA-DNA interactions: A key role for the nucleoid in plasmid partition. *Molecular Microbiology*, *78*(1), 78–91. https://doi.org/10.1111/j.1365-2958.2010.07314.x

Vecchiarelli, A. G., Havey, J. C., Ing, L., Wong, E., Waples, W. G., & Funnell, B. E. (2013). Dissection of the ATPase active site of P1 ParA reveals multiple active forms essential for plasmid partition. *The Journal of Biological Chemistry*, *288*(24), 17823–17831. https://doi.org/10.1074/JBC.M113.469981

Vecchiarelli, A. G., Hwang, L. C., & Mizuuchi, K. (2013). Cell-free study of F plasmid partition provides evidence for cargo transport by a diffusion-ratchet

mechanism. *Proceedings of the National Academy of Sciences of the United States of America*, *110*(15). https://doi.org/10.1073/pnas.1302745110

Vecchiarelli, A. G., Mizuuchi, K., & Funnell, B. E. (2012). Surfing biological surfaces: Exploiting the nucleoid for partition and transport in bacteria. In *Molecular Microbiology* (Vol. 86, Issue 3, pp. 513–523). John Wiley & Sons, Ltd. https://doi.org/10.1111/mmi.12017

Venkatesan, M. M., Goldberg, M. B., Rose, D. J., Grotbeck, E. J., Burland, V., & Blattner, F. R. (2001). Complete DNA sequence and analysis of the large virulence plasmid of Shigella flexneri. *Infection and Immunity*, *69*(5), 3271–3285. https://doi.org/10.1128/IAI.69.5.3271-3285.2001

Viollier, P. H., Thanbichler, M., McGrath, P. T., West, L., Meewan, M., McAdams, H. H., & Shapiro, L. (2004). Rapid and sequential movement of individual chromosomal loci to specific subcellular locations during bacterial DNA replication. *Proceedings of the National Academy of Sciences of the United States of America*, *101*(25), 9257–9262. https://doi.org/10.1073/PNAS.0402606101

Volante, A., & Alonso, J. C. (2015). Molecular anatomy of ParA-ParA and ParA-ParB interactions during plasmid partitioning. *Journal of Biological Chemistry*, *290*(30), 18782–18795. https://doi.org/10.1074/jbc.M115.649632

Vonrhein, C., Flensburg, C., Keller, P., Sharff, A., Smart, O., Paciorek, W., Womack, T., & Bricogne, G. (2011). Data processing and analysis with the autoPROC toolbox. *Urn:Issn:0907-4449*, *67*(4), 293–302. https://doi.org/10.1107/S0907444911007773

Watanabe, E., Wachi, M., Yamasaki, M., & Nagai, K. (1992). ATPase activity of SopA, a protein essential for active partitioning of F plasmid. *Molecular & General Genetics : MGG*, *234*(3), 346–352. https://doi.org/10.1007/BF00538693

Webb, C. D., Graumann, P. L., Kahana, J. A., Teleman, A. A., Silver, P. A., & Losick, R. (1998). Use of time-lapse microscopy to visualize rapid movement of the replication origin region of the chromosome during the cell cycle in *Bacillus subtilis*. *Molecular Microbiology*, *28*(5), 883–892. https://doi.org/10.1046/J.1365-2958.1998.00808.X

Weissenberger, G., Henderikx, R. J. M., & Peters, P. J. (2021). Understanding the

invisible hands of sample preparation for cryo-EM. *Nature Methods 2021 18:5*, *18*(5), 463–471. https://doi.org/10.1038/s41592-021-01130-6

Yamaichi, Y., Bruckner, R., Ringgaard, S., Möll, A., Ewen Cameron, D., Briegel, A., Jensen, G. J., Davis, B. M., & Waldor, M. K. (2012). A multidomain hub anchors the chromosome segregation and chemotactic machinery to the bacterial pole. *Genes and Development*, *26*(20), 2348–2360. https://doi.org/10.1101/gad.199869.112

Yamaichi, Y., Fogel, M. A., Mcleod, S. M., Hui, M. P., & Waldor, M. K. (2007). Distinct Centromere-Like parS Sites on the Two Chromosomes of Vibrio spp. *JOURNAL OF BACTERIOLOGY*, *189*(14), 5314–5324. https://doi.org/10.1128/JB.00416-07

Yamaichi, Y., Fogel, M. A., & Waldor, M. K. (2007). par genes and the pathology of chromosome loss in *Vibrio cholerae*. *Proceedings of the National Academy of Sciences of the United States of America*, *104*(2), 630–635. https://doi.org/10.1073/pnas.0608341104

Yanagida, M. (2005). Basic mechanism of eukaryotic chromosome segregation. *Philosophical Transactions of the Royal Society B: Biological Sciences*, *360*(1455), 609. https://doi.org/10.1098/RSTB.2004.1615

Zhang, H., & Schumacher, M. A. (2017). Structures of partition protein para with nonspecific dna and parb effector reveal molecular insights into principles governing walker-box dna segregation. *Genes and Development*, *31*(5), 481–492. https://doi.org/10.1101/gad.296319.117

Zheng, S. Q., Palovcak, E., Armache, J. P., Verba, K. A., Cheng, Y., & Agard, D. A. (2017). MotionCor2: Anisotropic correction of beam-induced motion for improved cryo-electron microscopy. In *Nature Methods* (Vol. 14, Issue 4, pp. 331–332). Nature Publishing Group. https://doi.org/10.1038/nmeth.4193

Zivanov, J., Nakane, T., Forsberg, B. O., Kimanius, D., Hagen, W. J. H., Lindahl, E., & Scheres, S. H. W. (2018). New tools for automated high-resolution cryo-EM structure determination in RELION-3. *ELife*, *7*. https://doi.org/10.7554/eLife.42166

Appendix Figures

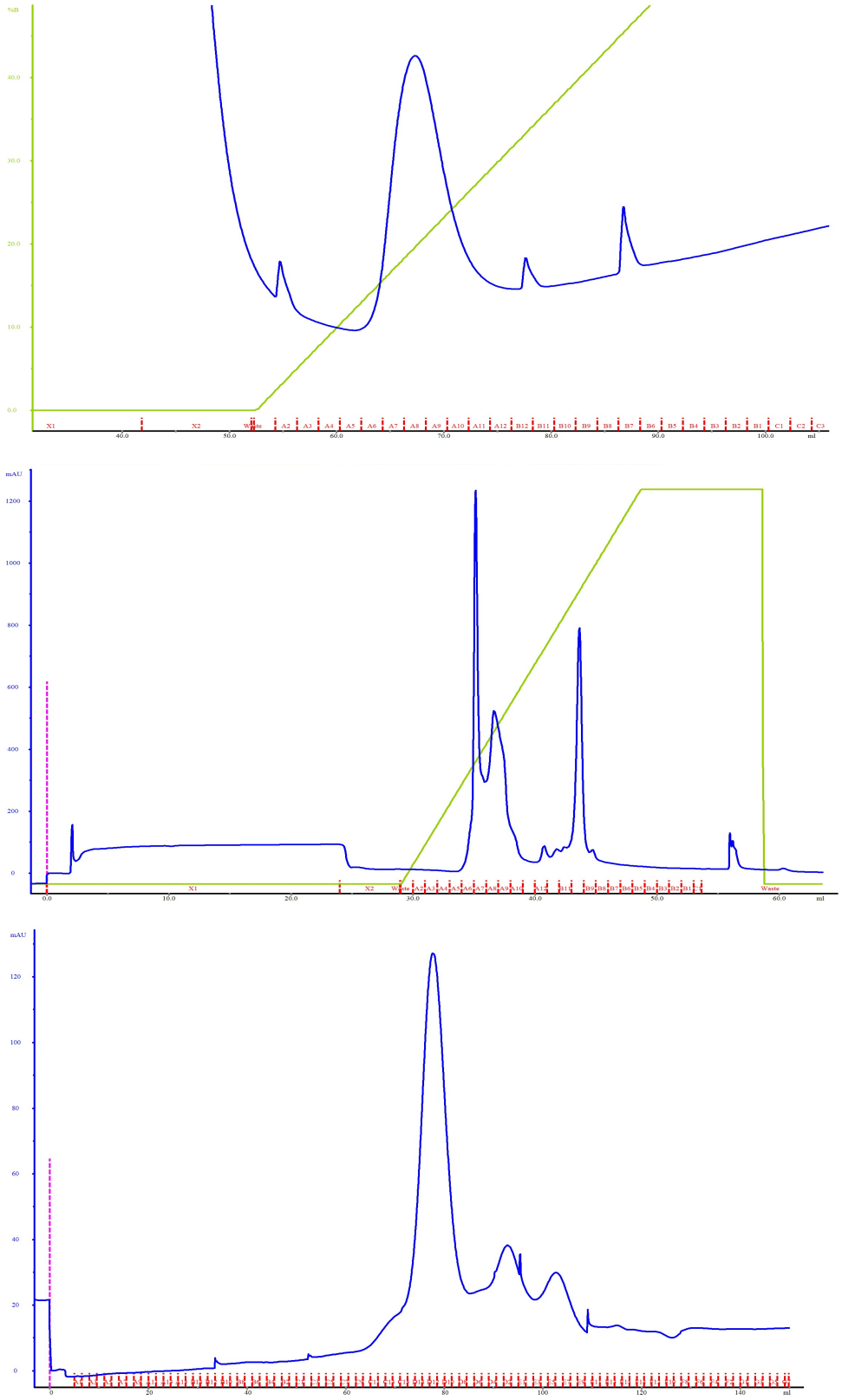

Figure 8.1 – Chromatograms of ParA1-GFP purifications, showing a nickel affinity column, a mono Q column and a Superdex gel filtration column.

K124Q

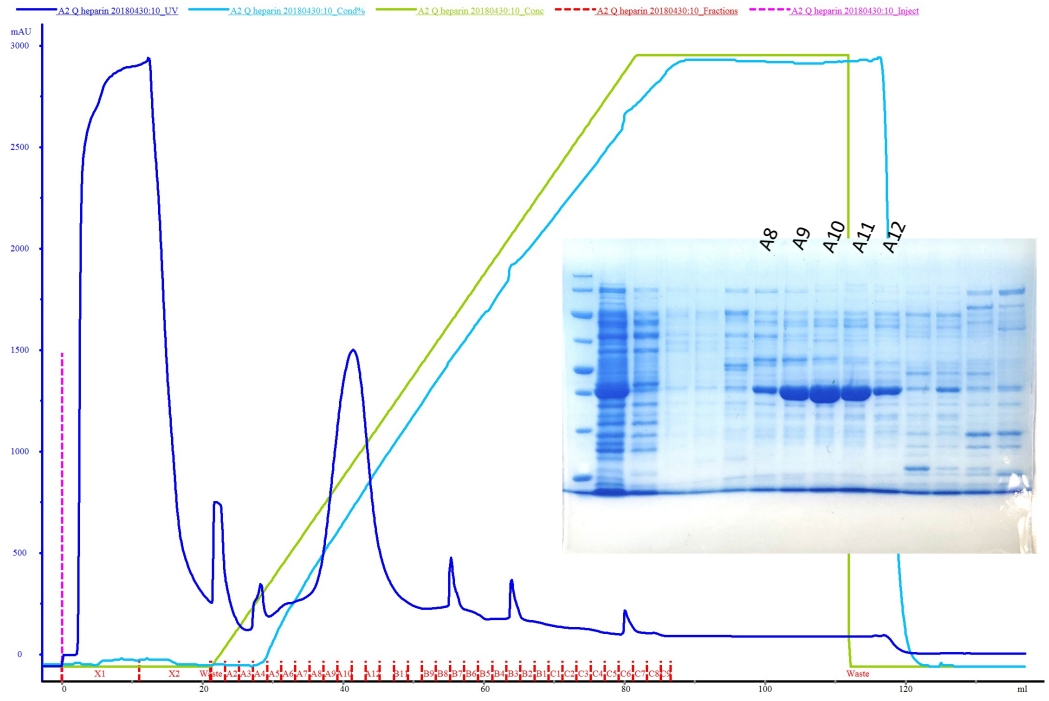

K124R

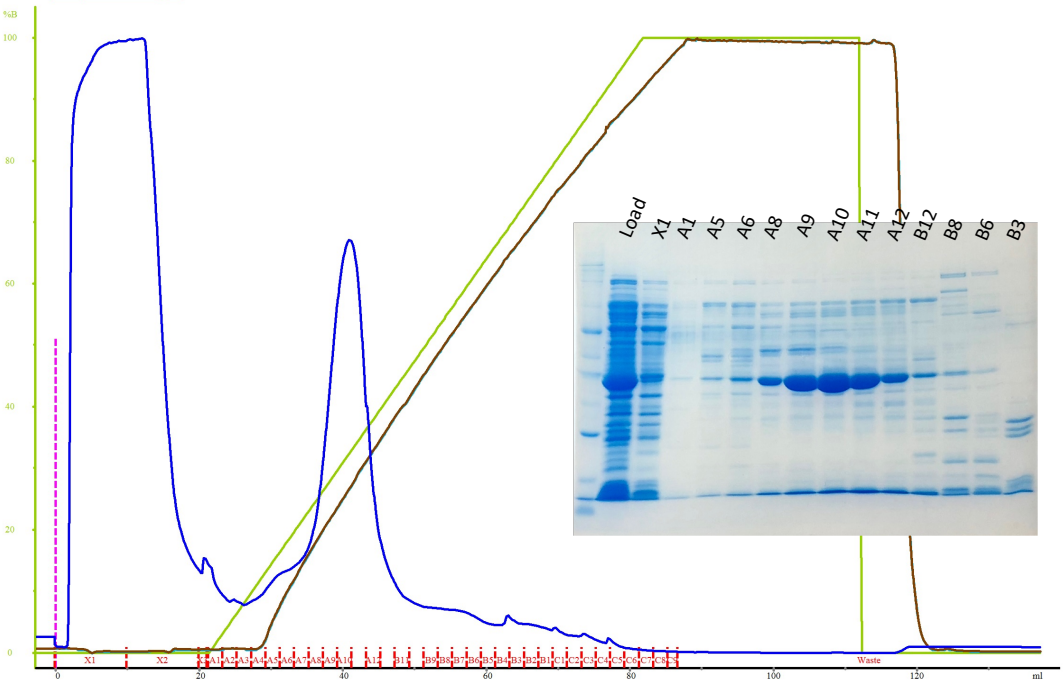

Figure 8.2 – Chromatograms of heparin affinity column chromatogrpahy of catalytic mutants.

K124Q

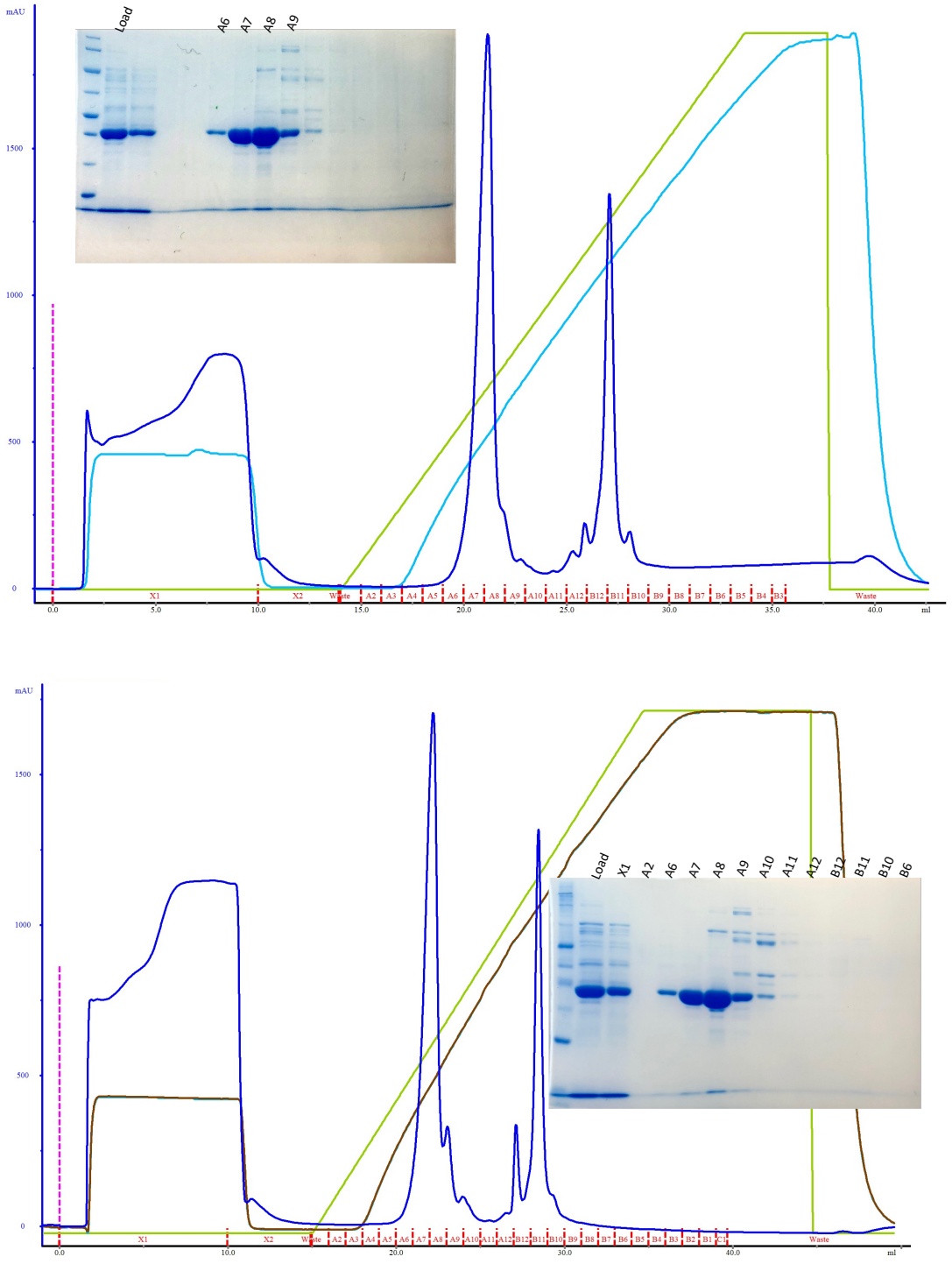

Figure 8.3 - Chromatograms of MonoQ ion exchange column chromatography of catalytic mutants.

K124Q

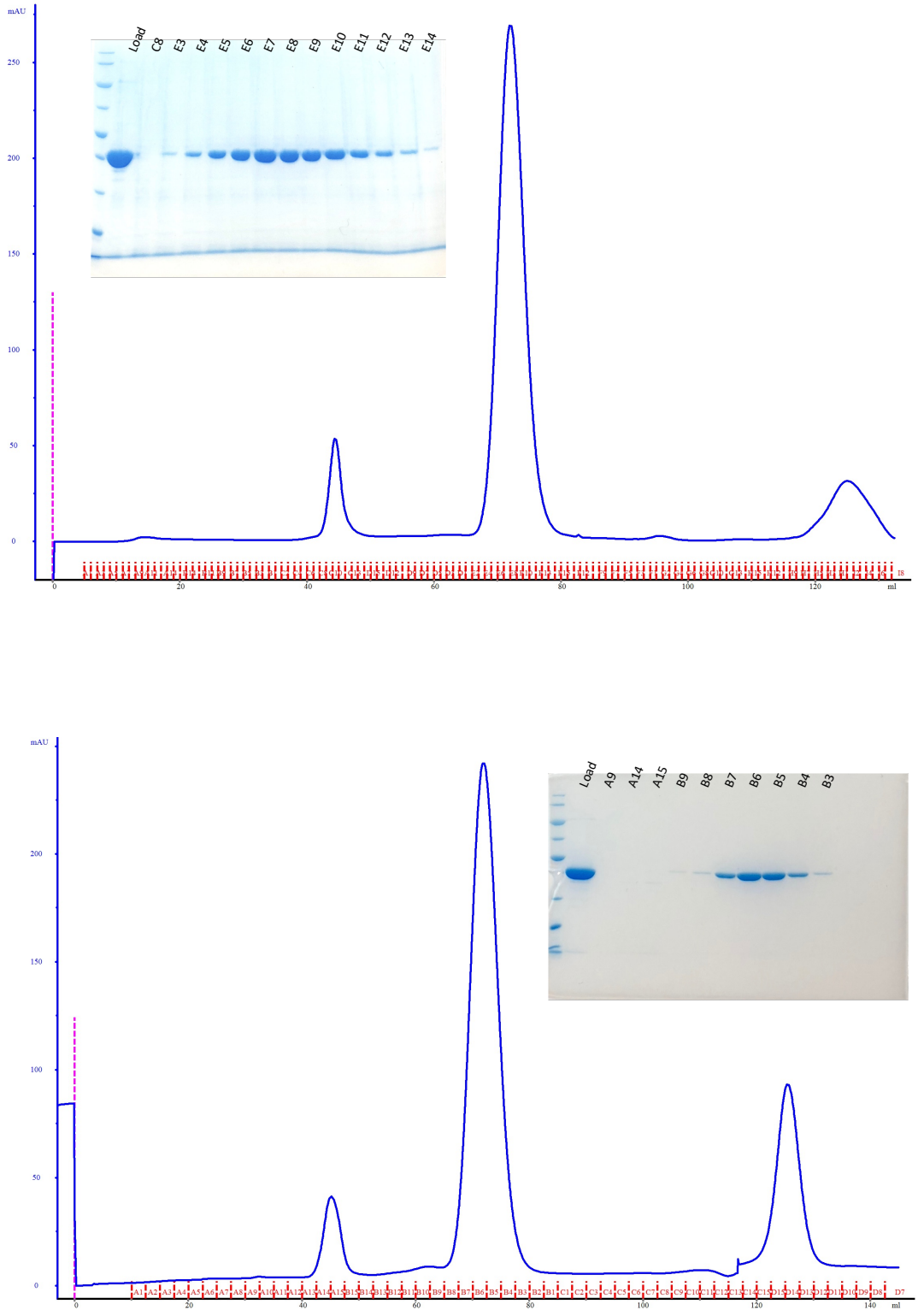

Figure 8.4 - Chromatograms of Superdex size exclusion column chromatography of catalytic mutants.

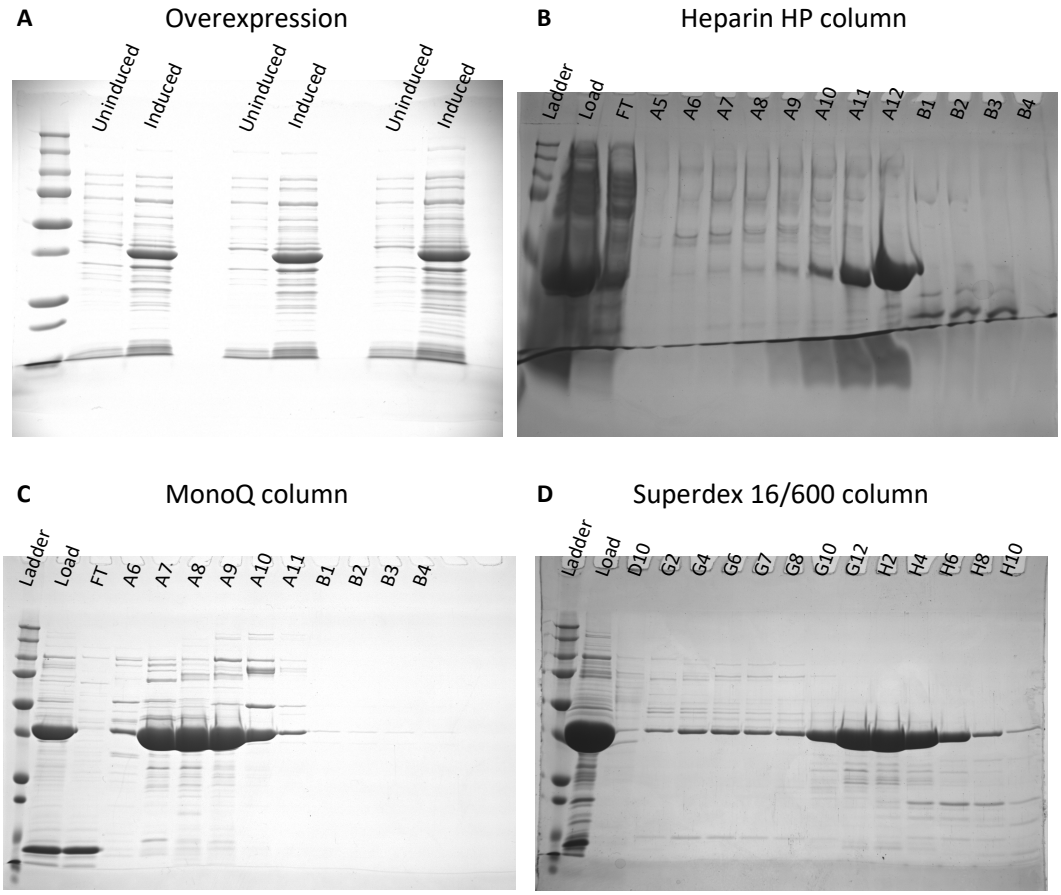

Figure 8.5 – Purification gels of ParA2-Δ4-35

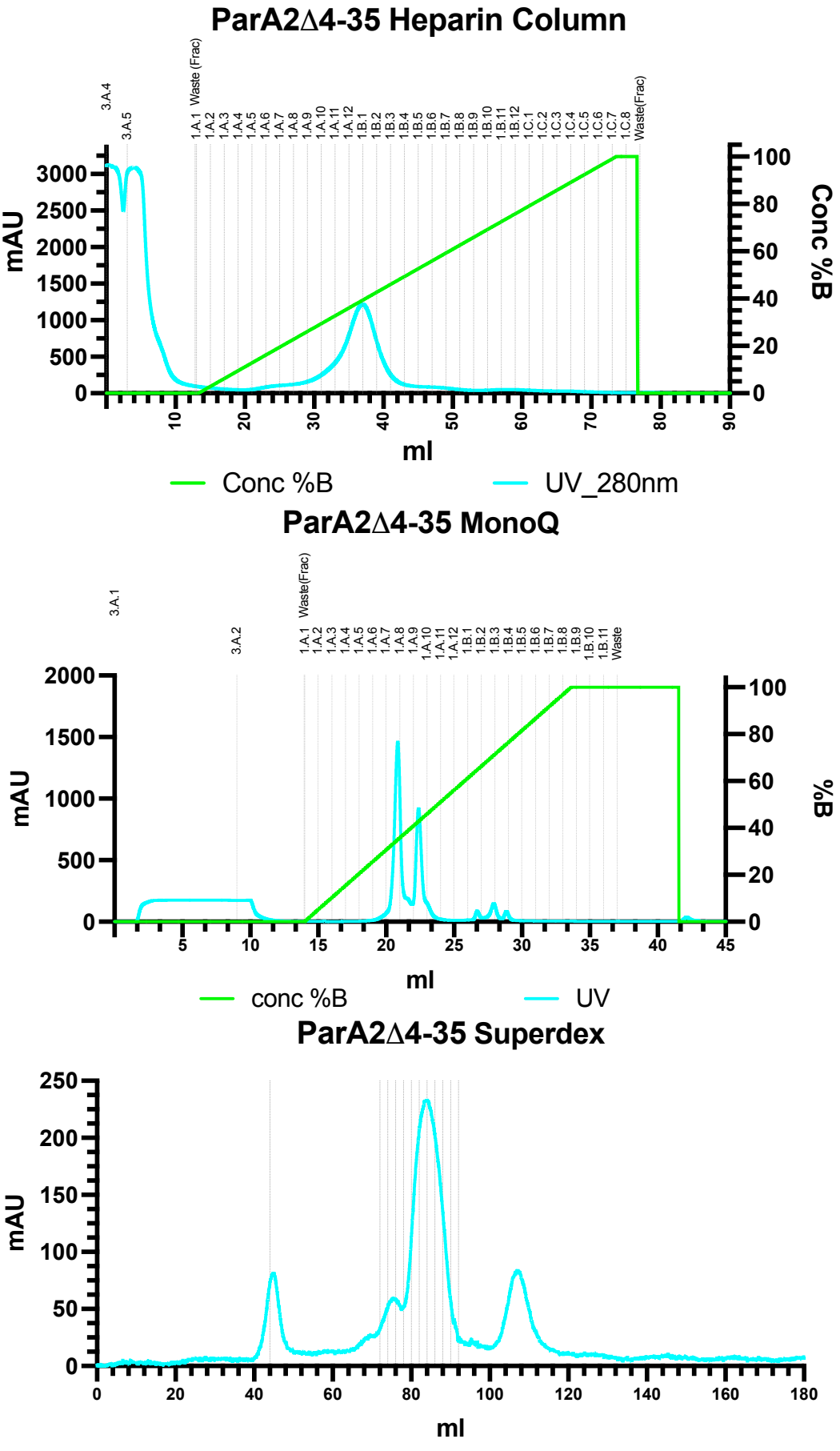

Figure 8.6 – Chromatograms of ParA2-Δ4-35 purification

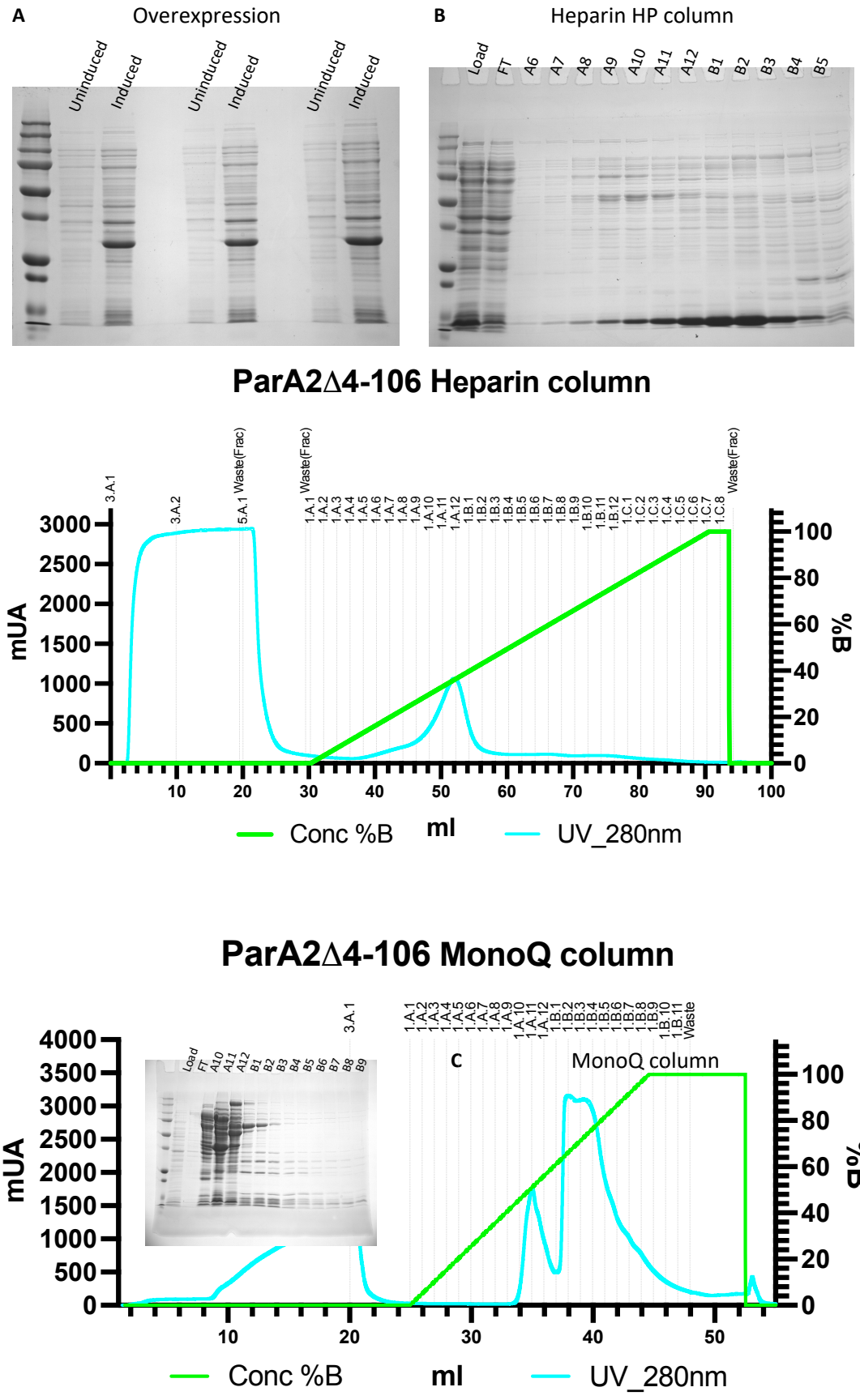

Figure 8.7 - Chromatograms and SDS-PAGE analysis of ParA2Δ4-106 purification\

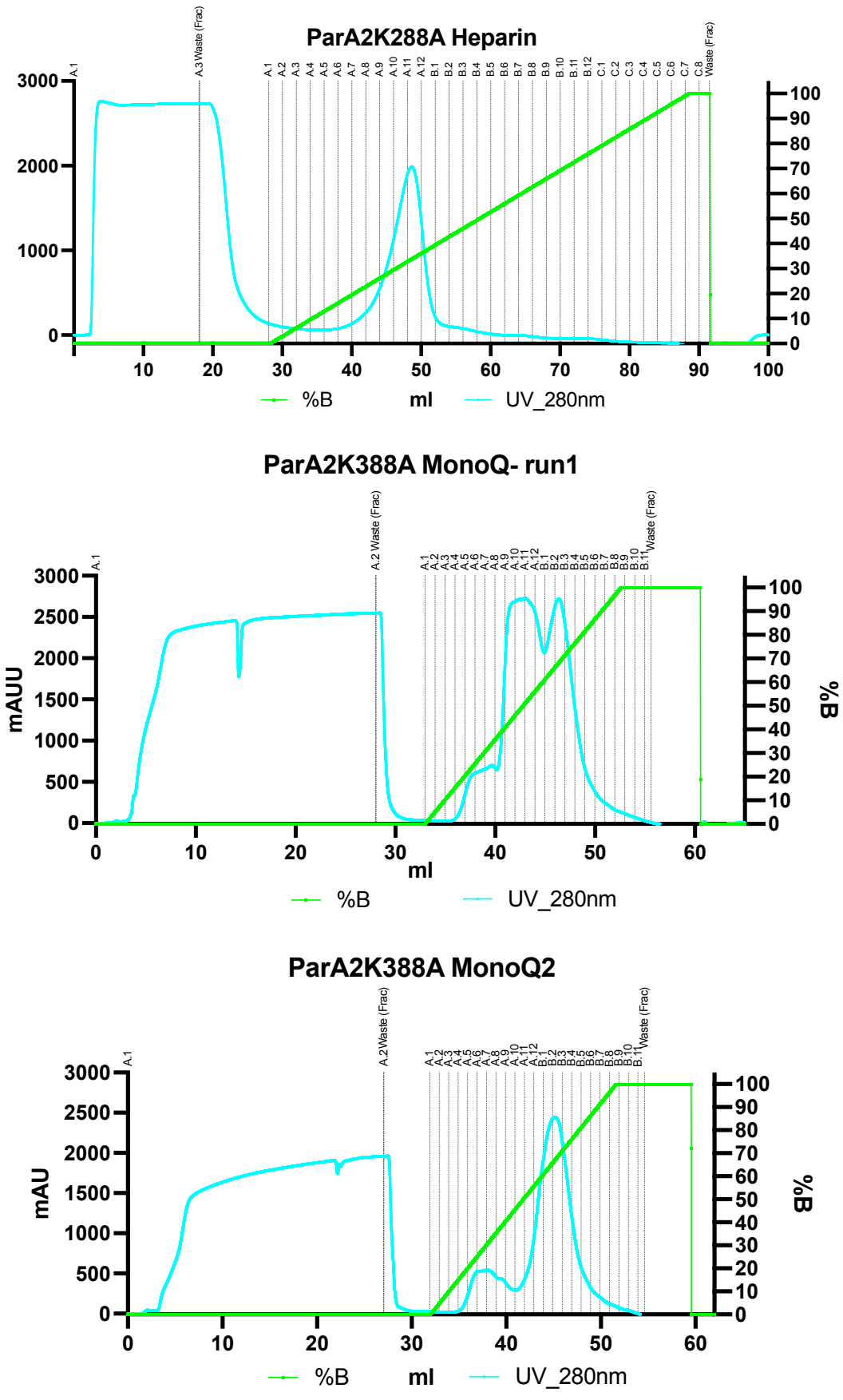

Figure 8.8 – Chromatograms of ParA2K388A purification

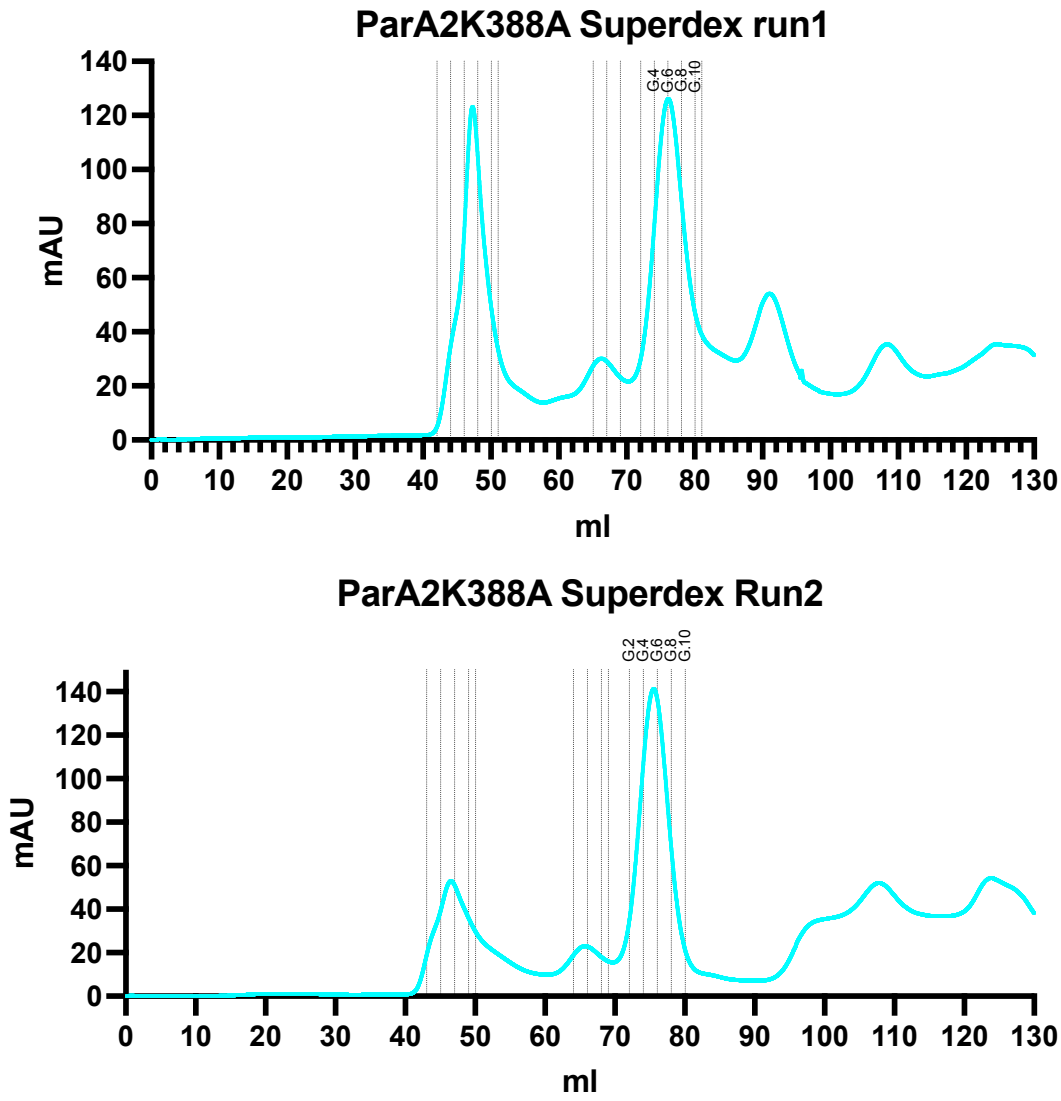

Figure 8.9 – Chromatograms of ParA2K388A purification

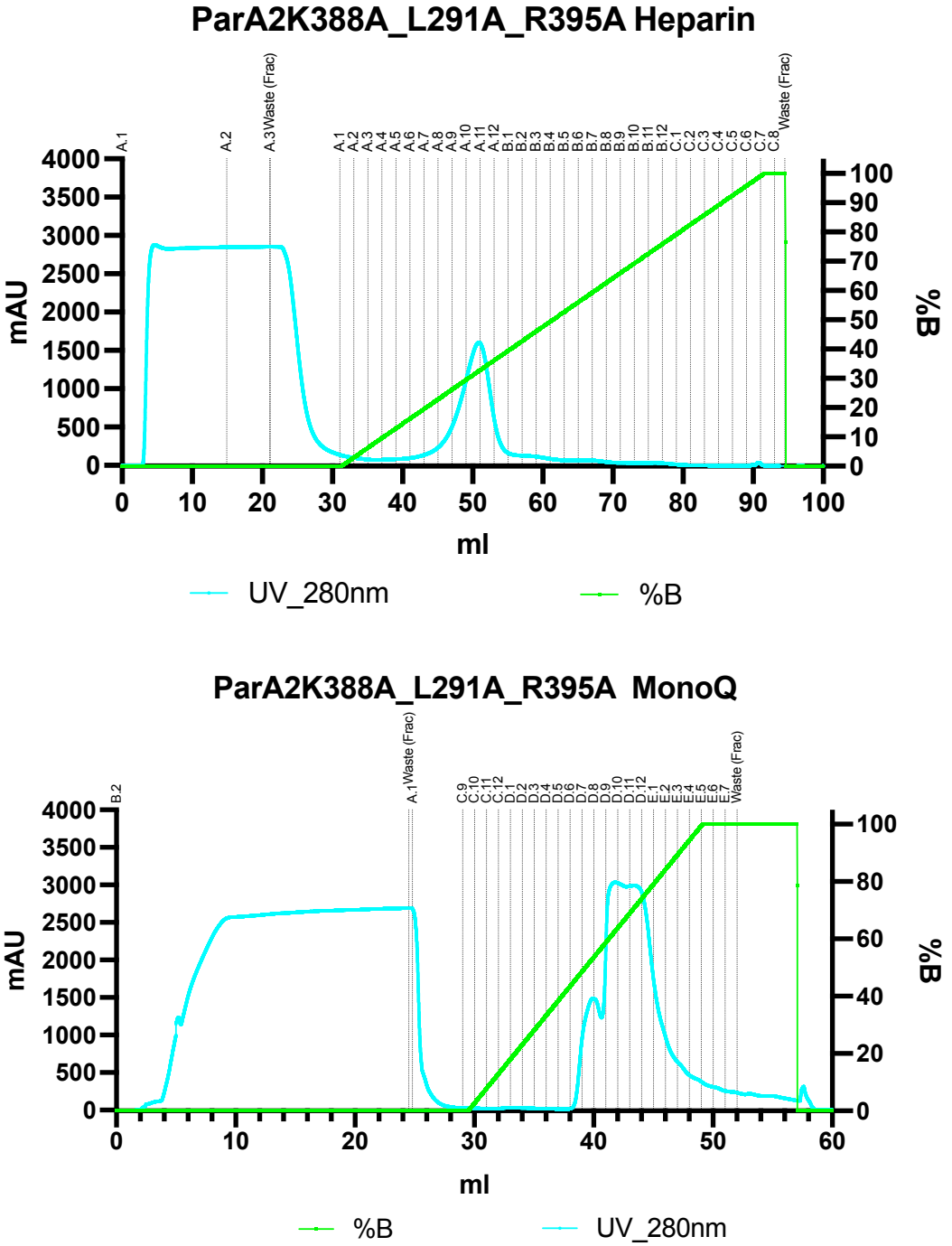

Figure 8.10 – Chromatograms of ParA2K388A_L291A_R395A purification using a Heparin affinity column and a MonoQ ion exchange column.

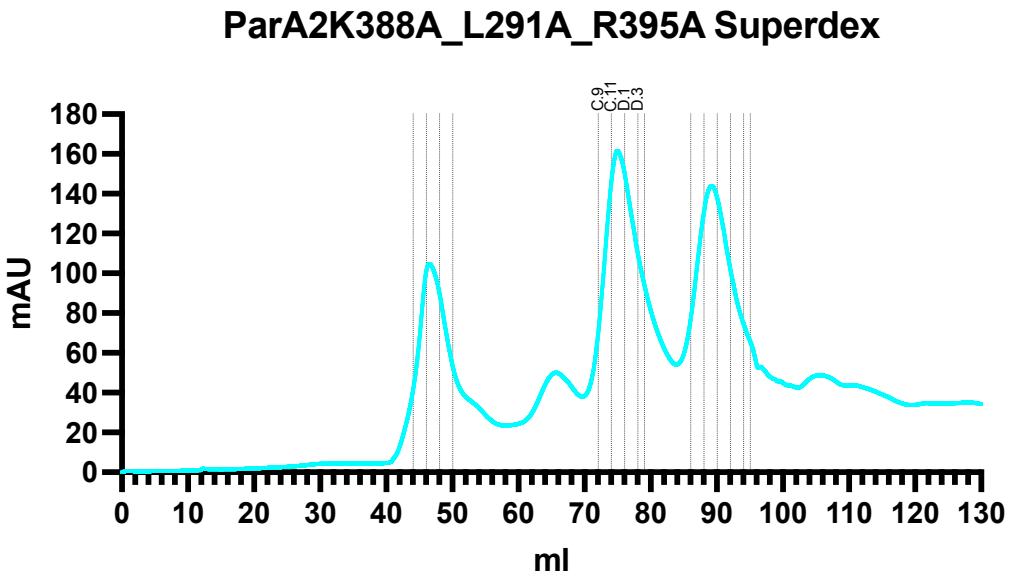

Figure 8.11 – Chromatogram of ParA2K388A_L291A_R395A size exclusion column chromatography

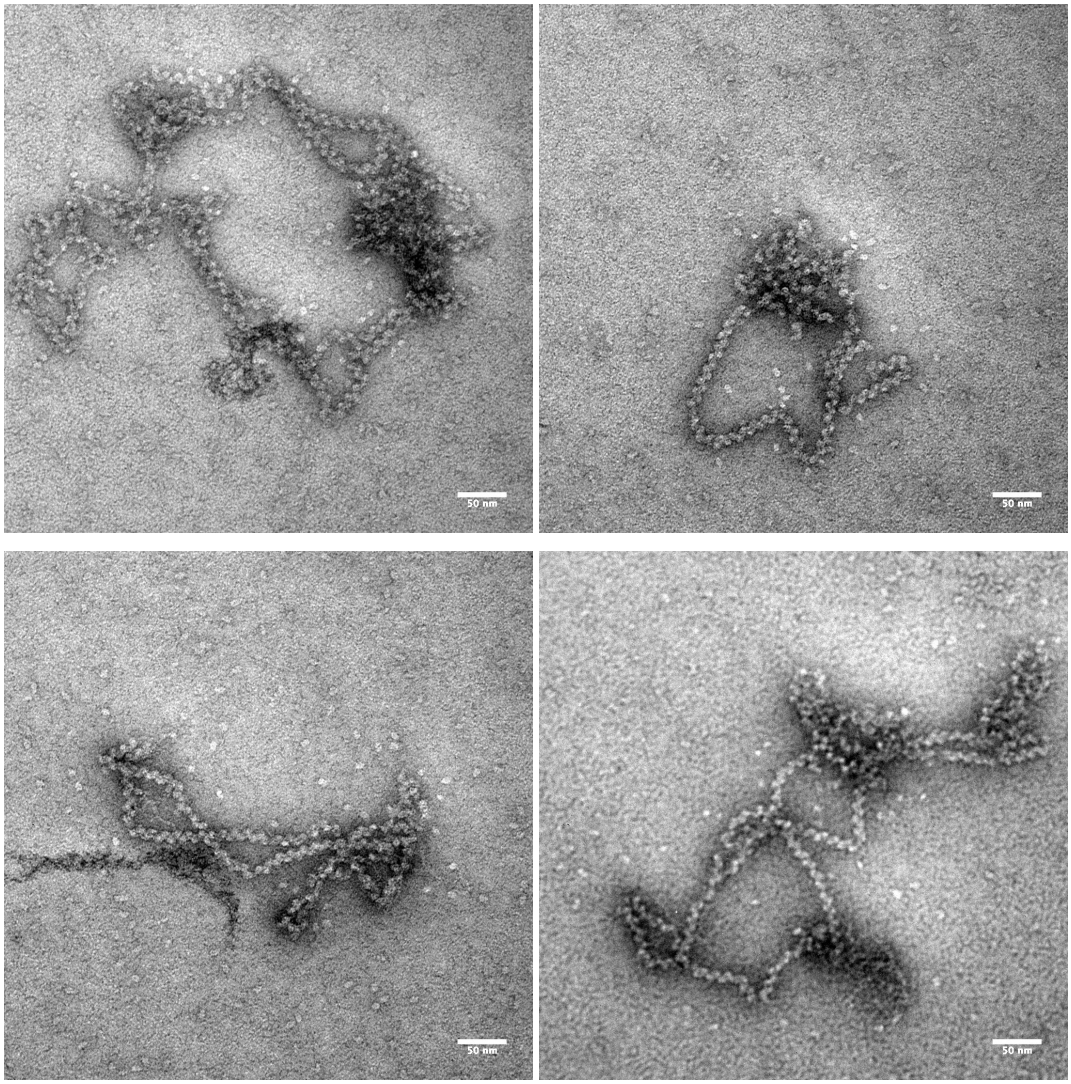

Figure 8.12 – Negative stain EM micrographs of $ParA2_{vc}$-DNA in the presence of ATP. Scale bar is 50nm

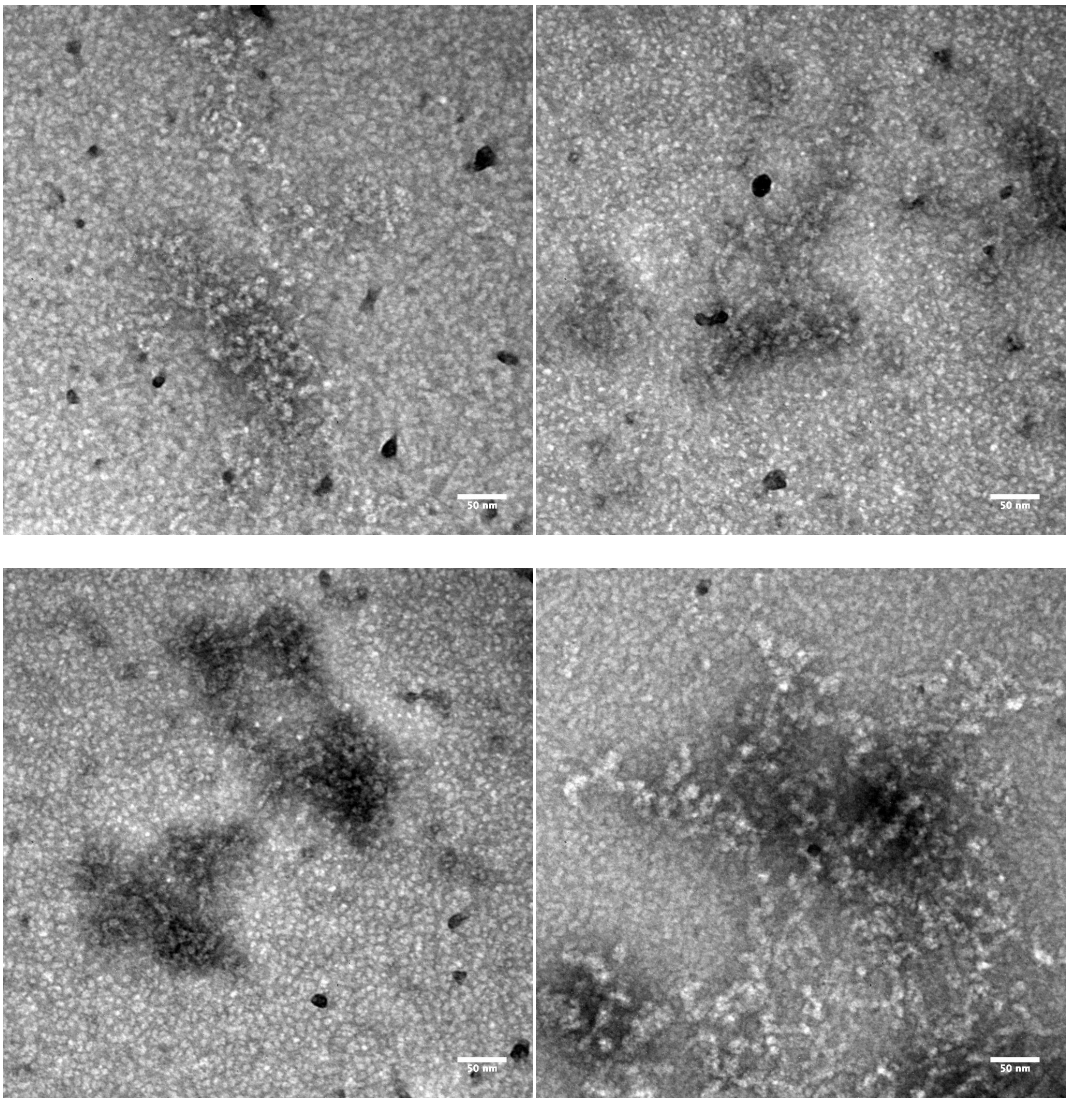

Figure 8.13 – Negative stain EM micrographs of $ParA2_{vc}$-DNA in the presence of ADP. Scale bar is 50nm

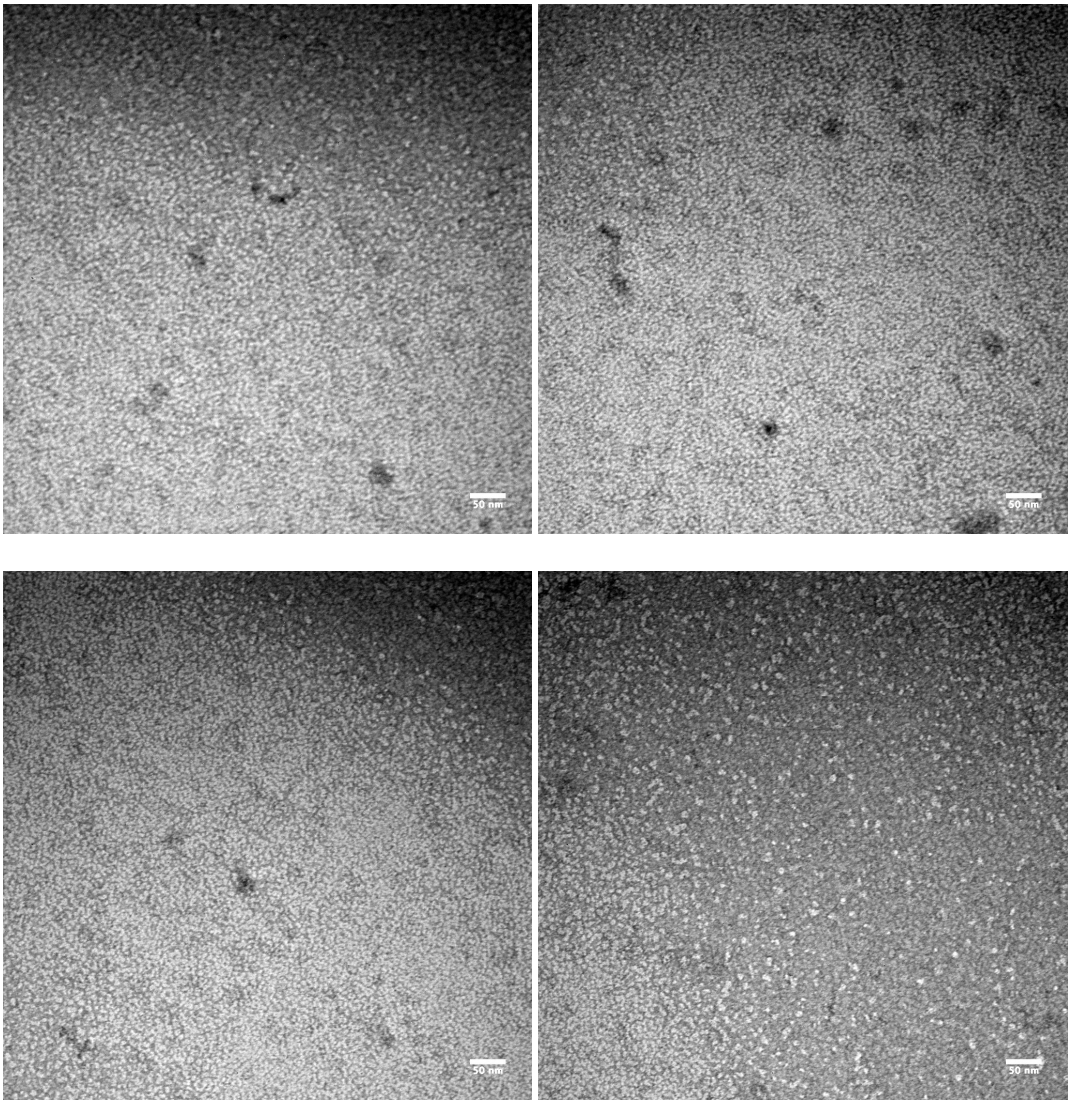

Figure 8.14 – Negative stain EM micrographs of $ParA2_{vc}$ with DNA in the absence of nucleotide. Scale bar is 50nm

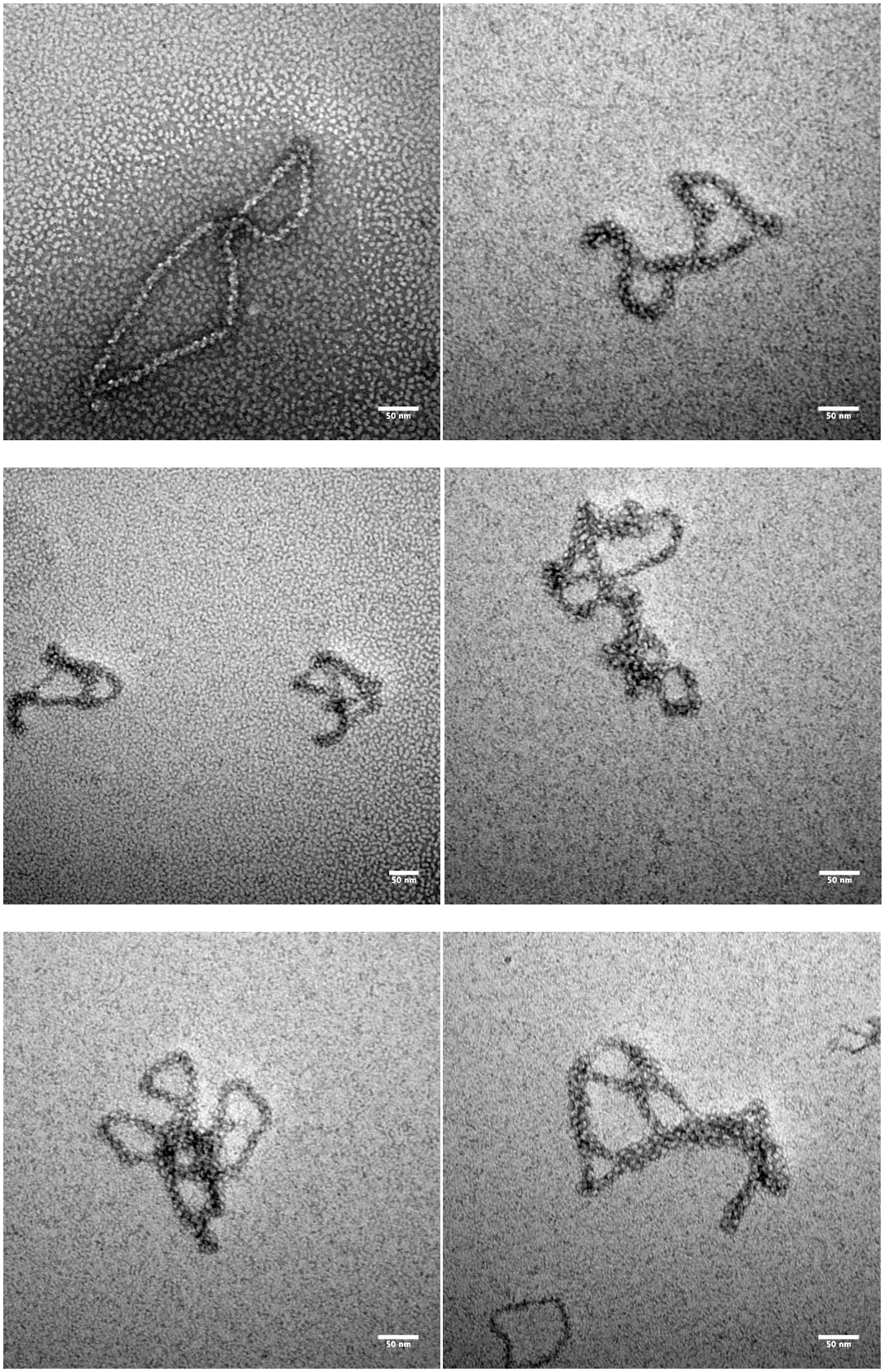

Figure 8.15 – Negative stain EM micrographs of ParA2$_{vc}$Δ4-35-DNA in the presence of ATP. Scale bar is 50nm

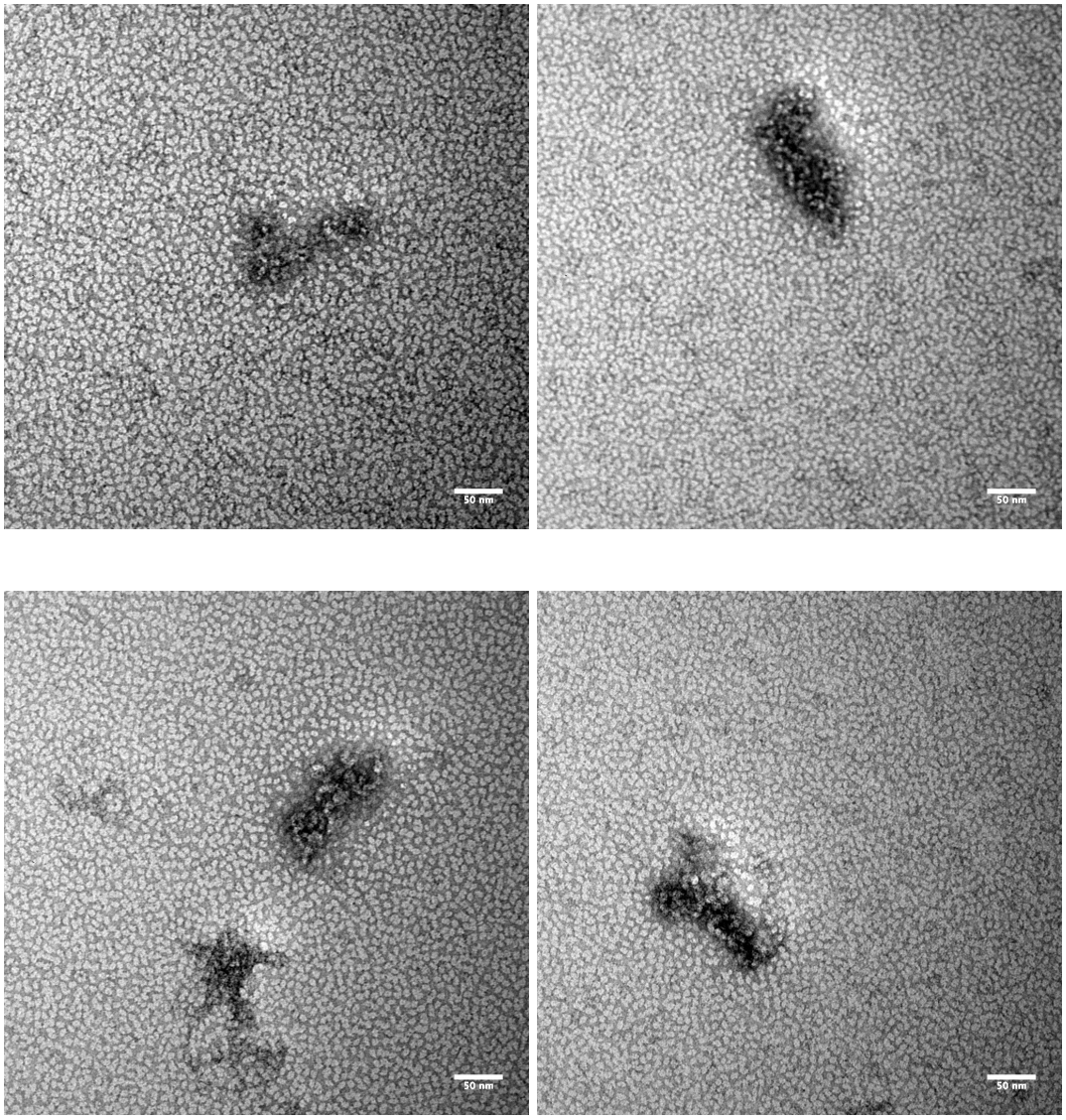

Figure 8.16 – Negative stain EM micrographs of ParA2$_{vc}$K388A-DNA in the presence of ATP. Scale bar is 50nm

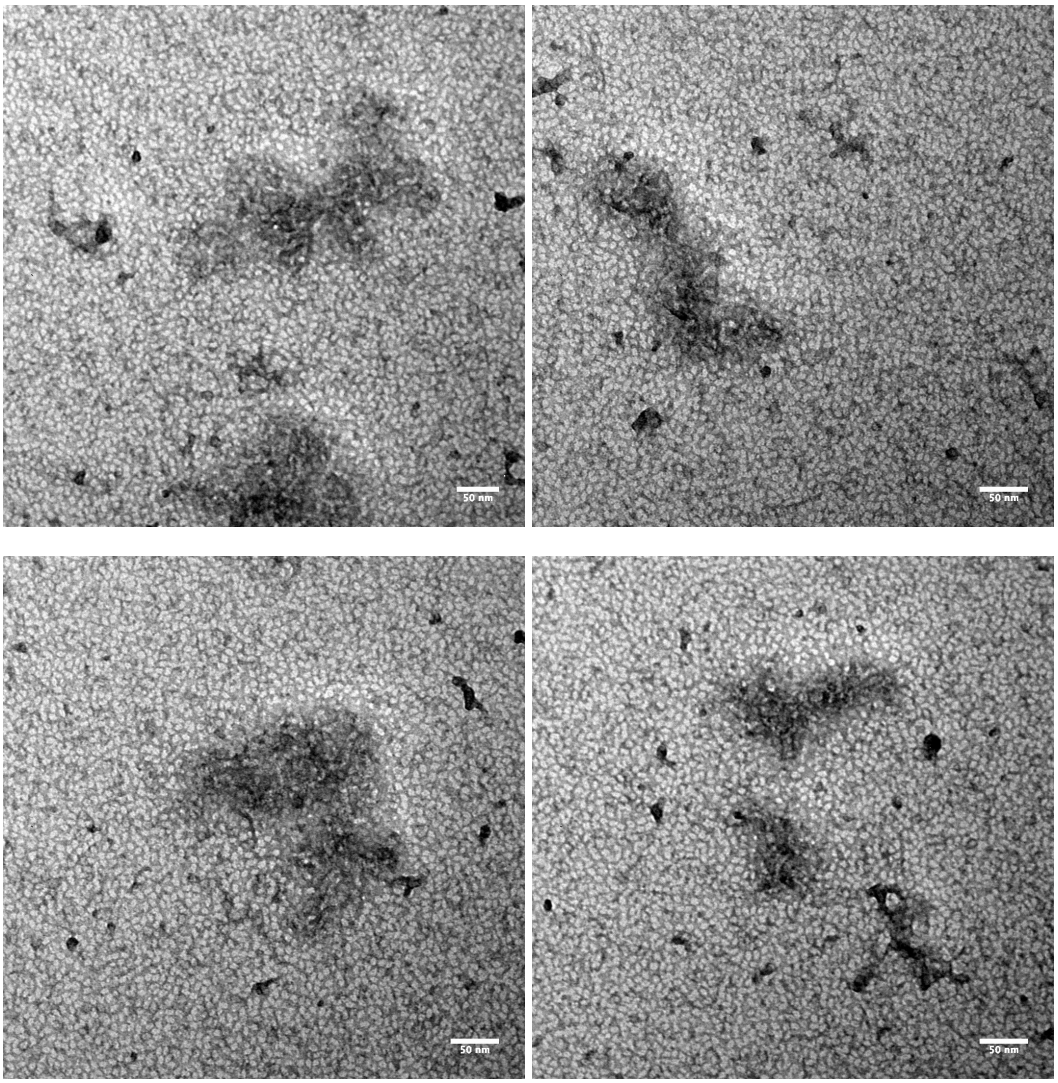

Figure 8.17 – Negative stain EM micrographs of ParA2K388A_L291A_R395A in the presence of ATP. Scale bar is 50nm

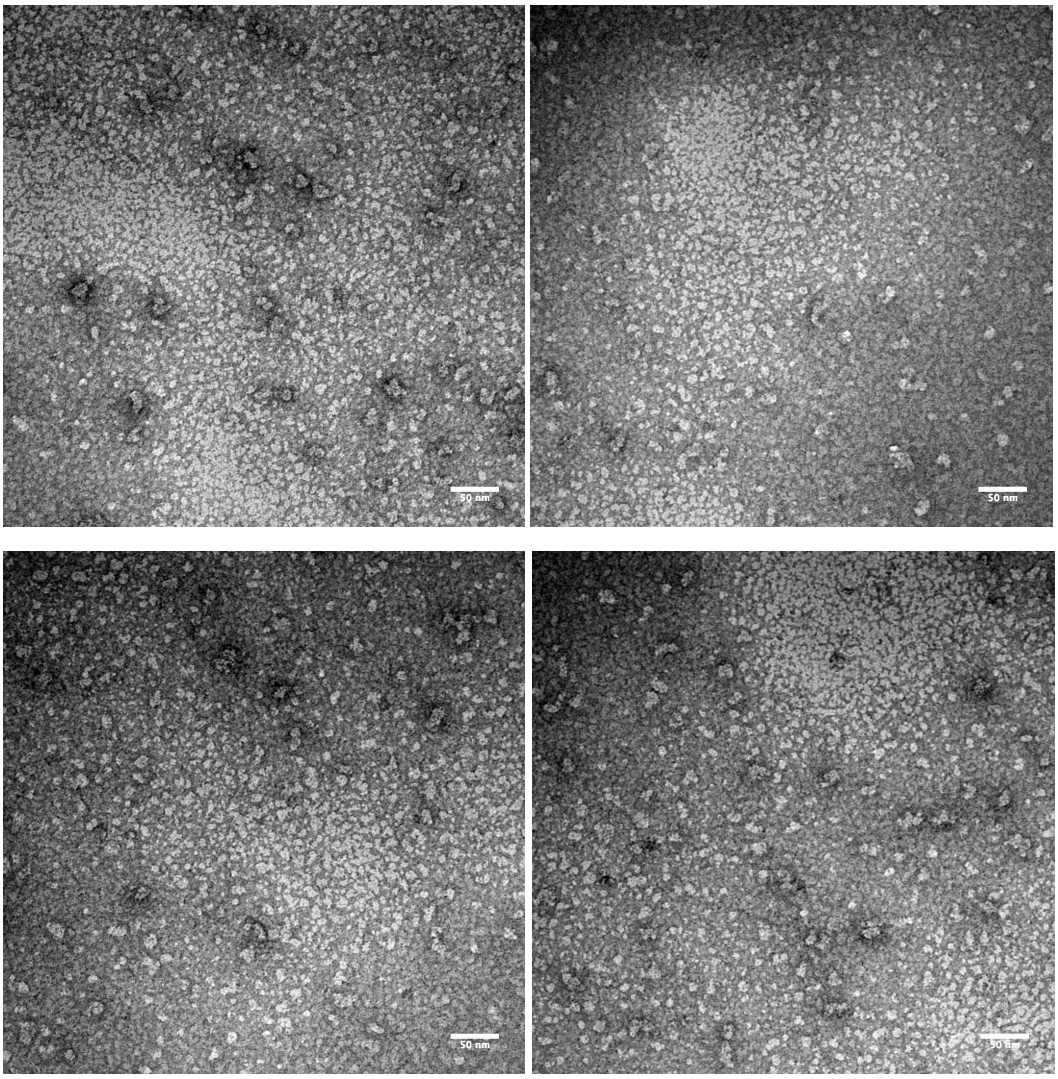

Figure 8.18 – Negative stain EM micrographs of ParA2K124E in the presence of ATP. Scale bar is 50nm

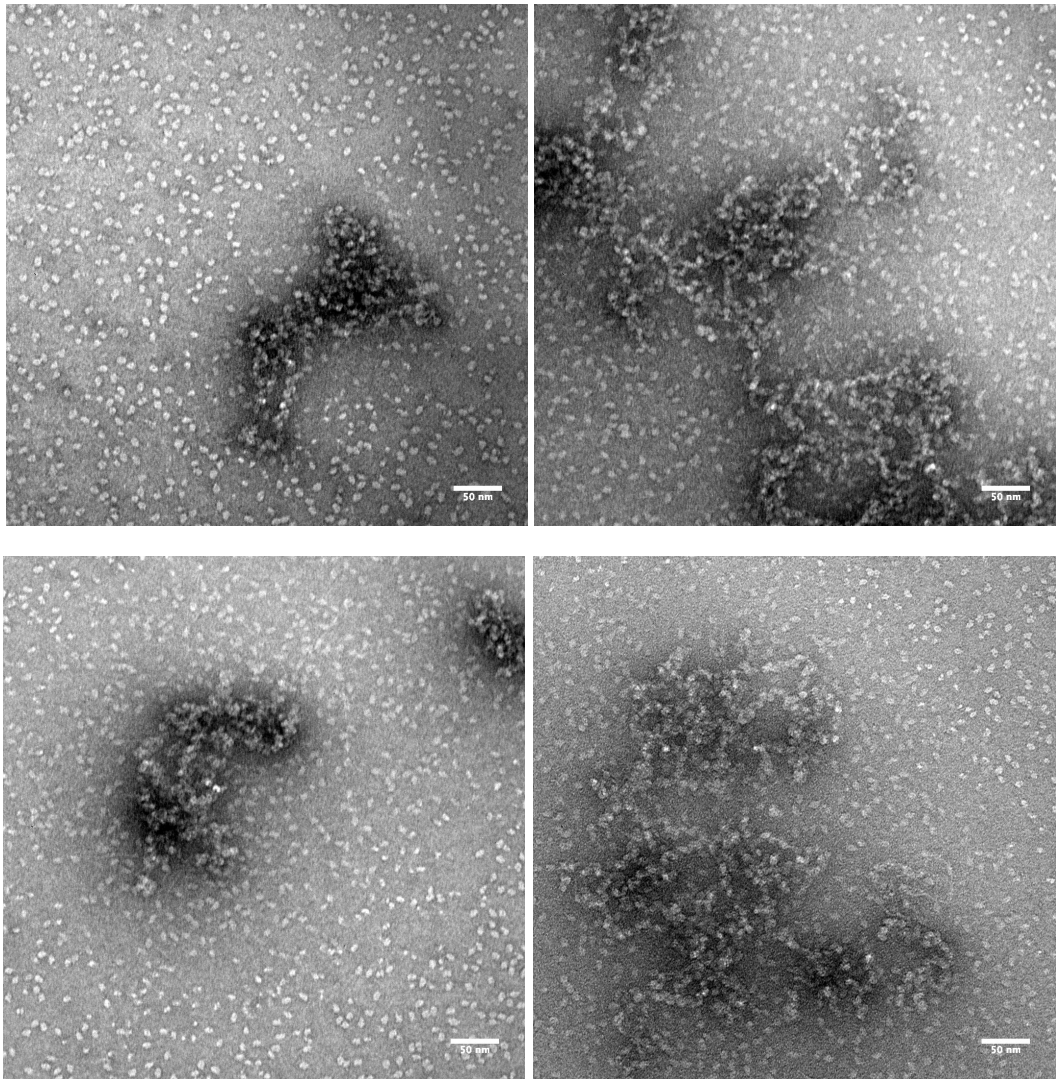

Figure 8.19 – Negative stain EM micrographs of ParA2K124R in the presence of ATP. Scale bar is 50nm

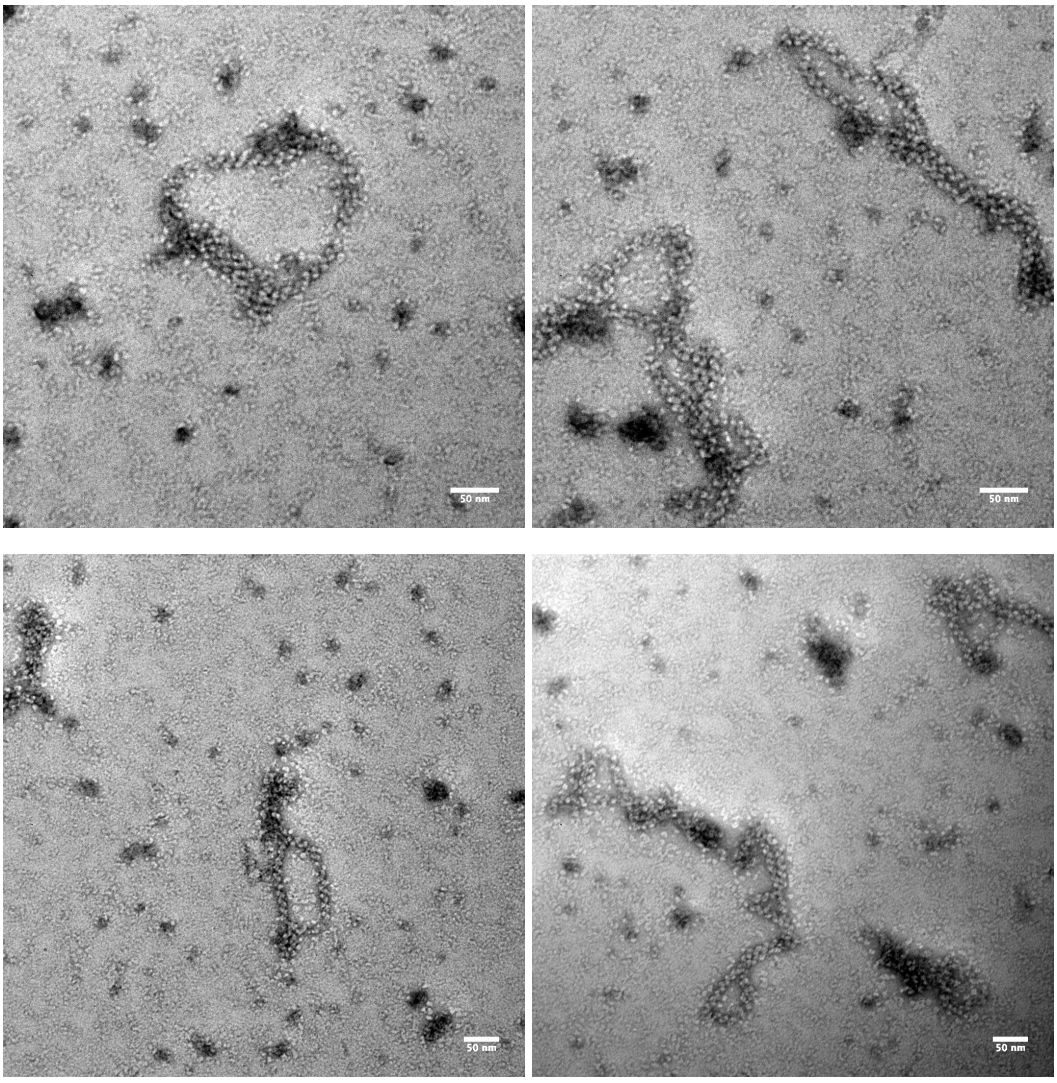

Figure 8.20 – Negative stain EM micrographs of ParA2K124Q in the presence of ATP. Scale bar is 50nm

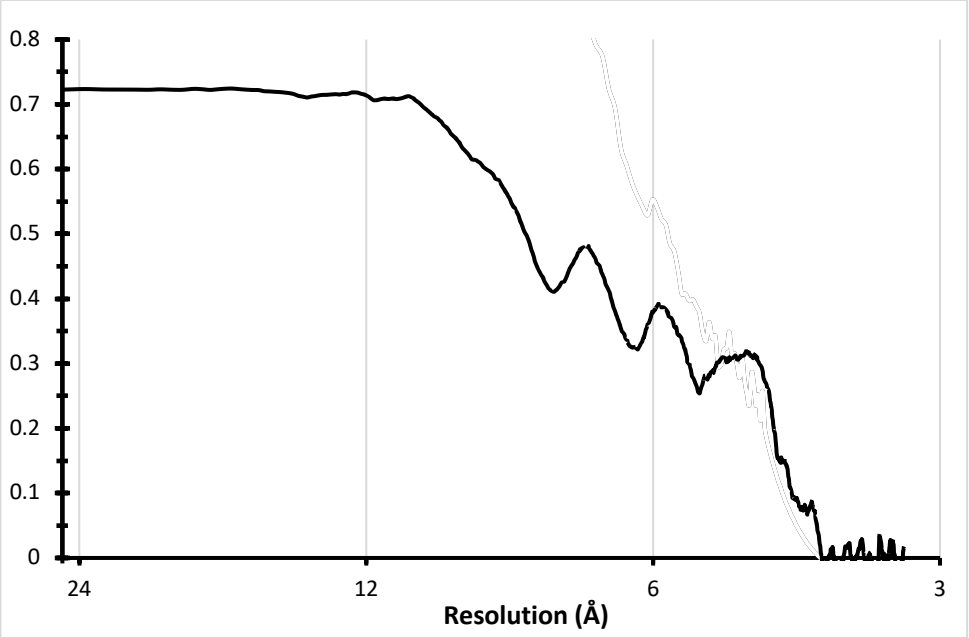

Figure 8.21 – ParA2$_{vc}$-ATPγS-DNA map-to-model fsc curve